UNIVERSITY OF ALBERTA

INVESTIGATING ENVIRONMENTAL ENGINEERING REACTORS USING LASER MEASUREMENT TECHNIQUES AND ADVANCED MODELLING

BY

MAHAD SAID ALI BAAWAIN

A THESIS SUBMITTED TO THE FACULTY OF GRADUATE STUDIES AND RESEARCH IN PARTIAL FULFILLMENT OF THE REQUIREMENTS FOR THE DEGREE OF

DOCTOR OF PHILOSOPHY

IN

ENVIRONMENTAL ENGINEERING

DEPARTMENT OF CIVIL AND ENVIRONMENTAL ENGINEERING

EDMONTON, ALBERTA

FALL, 2007

Library and
Archives Canada

Published Heritage
Branch

395 Wellington Street
Ottawa ON K1A 0N4
Canada

Bibliothèque et
Archives Canada

Direction du
Patrimoine de l'édition

395, rue Wellington
Ottawa ON K1A 0N4
Canada

Your file Votre référence
ISBN: 978-0-494-32912-2
Our file Notre référence
ISBN: 978-0-494-32912-2

NOTICE:
The author has granted a non-exclusive license allowing Library and Archives Canada to reproduce, publish, archive, preserve, conserve, communicate to the public by telecommunication or on the Internet, loan, distribute and sell theses worldwide, for commercial or non-commercial purposes, in microform, paper, electronic and/or any other formats.

The author retains copyright ownership and moral rights in this thesis. Neither the thesis nor substantial extracts from it may be printed or otherwise reproduced without the author's permission.

AVIS:
L'auteur a accordé une licence non exclusive permettant à la Bibliothèque et Archives Canada de reproduire, publier, archiver, sauvegarder, conserver, transmettre au public par télécommunication ou par l'Internet, prêter, distribuer et vendre des thèses partout dans le monde, à des fins commerciales ou autres, sur support microforme, papier, électronique et/ou autres formats.

L'auteur conserve la propriété du droit d'auteur et des droits moraux qui protège cette thèse. Ni la thèse ni des extraits substantiels de celle-ci ne doivent être imprimés ou autrement reproduits sans son autorisation.

In compliance with the Canadian Privacy Act some supporting forms may have been removed from this thesis.

While these forms may be included in the document page count, their removal does not represent any loss of content from the thesis.

Conformément à la loi canadienne sur la protection de la vie privée, quelques formulaires secondaires ont été enlevés de cette thèse.

Bien que ces formulaires aient inclus dans la pagination, il n'y aura aucun contenu manquant.

Canada

"and say: My Lord! Increase me in knowledge"

[Quran, 20:114]

ABSTRACT

This thesis includes three experimental studies and three modelling approaches to selected two-phase flow Environmental Engineering systems. A two-dimensional laser flow map particle image velocimetry coupled with planar laser-induced fluorescence (PIV/PLIF) was used to study the hydrodynamic characteristics of an impinging jets bubble column, a horizontal inline multi-jets ozone contactor, and an inclined surface plunging jets aeration system. The PIV/PLIF system provided a combination of simultaneous whole-field velocity and concentration measurements of the two phases (liquid and gas) under different operating conditions for both the bubble column and the multi-jets contactor. The PLIF results were used to determine the axial liquid dispersion coefficient (D_L, m^2/s) for each operating condition. The overall mass transfer coefficient (k_La, s^{-1}) was then determined. Both systems showed high ozone transfer rates with a relatively low dispersion effect compared to that of conventional ozone contactors. The third experimental study utilized the PIV system to analyze the velocity profiles of two inclined water jets intersecting on the surface of an aeration tank. The effect of the nozzle diameter, plunging angle and jets' length was evaluated. The system showed a smaller Sauter mean bubble diameter (d_S, m) and higher penetration depth (z_p, m) and gas holdup (ε_G) compared to those of vertical plunging jets systems.

The artificial neural network (ANN) modelling approach was used to characterize different types of bubble columns by predicting k_La, ε_G, and d_S. The ANN results showed very good agreement between the modelled and the measured parameters. Transient and steady-state back flow cell models (BFCM) were used successfully to model the hydrodynamic behaviour and the dissolved ozone concentration profiles of an impinging-

jet ozone bubble column. Two computation fluid dynamics (CFD) models were utilized to characterize a recycled water pond and a storage reservoir. The first CFD model was used to simulate the pond's dissolved oxygen resulting from the turbulent surface plunging jets and to predict the resulting dissolved oxygen when submerged inlets were used under different operational and atmospheric conditions. The second model was employed to evaluate the effect of the internal geometry and inlet configuration on the reactor's effective contact time (t_{10}).

DEDICATION

This manuscript is dedicated to:

My wife and sons
(For the love and support which were a continuous inspiration)

My mother and grandmother
(For all those prayers which made the difference)

My brothers and sisters
(For believing on me which provided that final push)

That very special person; my father
(May Allah grant you His mercy)

ACKNOWLEDGEMENTS

All praise and thanks are due to Allah, the Lord of the Worlds. I would like to express my genuine gratitude and appreciation to my supervisor Dr. M. Gamal El-Din for his guidance, encouragement, endurance, and continuous support all through the course of this work. A very special thank you goes to my co-supervisor Dr. D.W. Smith for his continuous support and encouragement. The friendly environment and the talented research mentality provided by my supervisors were the major keys for this work to be accomplished.

I am very grateful to my thesis committee members Dr. C. Adams, Dr. J. Feddes, Dr. N. Rajaratnam, and Dr. I. D. Buchanan for their valuable suggestions that enhanced the quality of this thesis.

I am thankful to by Dr N. Rajaratnam for providing the experimental data used in the CFD model of the storage reservoir. Also, I greatly acknowledge Dr C. Lange for allowing me to use his CFX 5.6® to model the storage reservoir. The technical support provided by the technical staff (Mr. N. Chernuka, Mrs. M. Demeter, and Mr. G. Solonynko) at the Environmental Engineering Laboratory of the University of Alberta is greatly appreciated.

I would like to acknowledge the financial support I received from the Sultan Qaboos University, Oman, during my study here at the University of Alberta. I want also to acknowledge the research funds provided by the Natural Sciences and Engineering Research Council of Canada (NSERC), Canada Foundation for Innovation (CFI), Alberta Ingenuity, Syncrude Canada Ltd., and Mazzei Injector Corporation.

I would like to acknowledge all my friends for their support and encouragement throughout my study at the University of Alberta. Mohamed Nour and Tarek Abdelaziz were those special friends who were always available with their sincere advices, support and encouragements. I am very honoured to gain their friendship.

Finally, my special thanks go to my beloved family, especially my mother, my grandmother, my wife, my sons (Said, Alaiham, and Aban), my brothers, and my sisters. This manuscript became a reality with your prayers, support, encouragements, and considerations. I love you all.

TABLE OF CONTENTS

CHAPTER 1

INTRODUCTION 1

1.1 GENERAL 1

1.2 ORGANIZATION OF THE THESIS 3

CHAPTER 2

ARTIFICIAL NEURAL NETWORKS MODELLING OF OZONE BUBBLE COLUMNS: MASS TRANSFER COEFFICIENT, GAS HOLD-UP, AND BUBBLE SIZE 8

2.1 INTRODUCTION 8

2.2 OZONE BUBBLE COLUMNS 10

2.3 ANN MODELS PREPARATION 13

2.4 RESULTS AND DISCUSSION 16

2.5 CONCLUSIONS 20

2.6 REFERENCES 31

CHAPTER 3

IMPINGING-JET OZONE BUBBLE COLUMN MODELLING: HYDRODYNAMICS, GAS HOLD-UP, BUBBLE CHARACTERISTICS, AND OZONE MASS TRANSFER 41

3.1 INTRODUCTION 41

  3.1.1 Modelling Ozone Contactors 42

  3.1.2 Bubble Columns Ozone Contactors 43

3.2 TRANSIENT BACK FLOW CELL MODEL 47

3.3 STEADY STATE BACK FLOW CELL MODEL 48

3.4 EXPERIMENTAL PROCEDURES 51

  3.4.1 Operation of the Impinging-Jet Ozone Bubble Column 51

  3.4.2 Hydrodynamic and Gas Hold-up Experiments 52

  3.4.3 Bubble Diameter Measurements 53

3.4.4 Ozone Mass Transfer Experiments 53
3.5 EXPERIMENTAL DATA ANALYSIS METHODS 54
3.5.1 Liquid-Phase Backmixing 54
3.5.2 Gas Hold-up 55
3.5.3 Gas Bubble Characteristics 56
3.5.4 Ozone Mass Transfer 58
3.6 RESULTS AND DISCUSSION 59
3.6.1 Liquid-Phase Backmixing 59
3.6.2 Gas Hold-up 61
3.6.3 Gas Bubble's Properties 62
3.6.4 Ozone Mass Transfer 64
3.7 CONCLUSION 68
3.8 REFERENCES 80

CHAPTER 4

PIV/PLIF STUDY OF IMPINGING JET BUBBLE COLUMN WITH MIXING NOZZLES 88
4.1 INTRODUCTION 88
4.2 LASER MEASUREMENT TECHNIQUES 89
4.3 EXPERIMENTAL SET-UP 91
4.2.1 Flow Facility 91
4.2.2 PIV/PLIF Set-up 92
4.2.3 PDA Set-up 94
4.3 MEASUREMENT DESCRIPTION 94
4.4 RESULTS AND DISCUSSION 96
4.4 CONCLUSIONS 102
4.5 REFERENCES 117

CHAPTER 5

HYDRODYNAMIC CHARACTERIZATION AND MASS TRANSFER ANALYSIS OF AN IN-LINE MULTI-JETS OZONE CONTACTOR 120

5.1 INTRODUCTION 120
5.2 EXPERIMENTAL SET-UP 122
5.2.1 Flow Facility 122
5.2.2 PIV/PLIF Set-up 124
5.2.3 Gas Mass Transfer Set-up 125
5.3 MEASUREMENT DESCRIPTION 126
5.4 RESULTS AND DISCUSSION 128
5.4.1 Reactor's Hydrodynamics 128
5.4.2 Gas Mass Transfer 135
5.5 CONCLUSIONS 139
5.6 REFERENCES 155

CHAPTER 6
THE EFFECT OF TWO INCLINED CIRCULAR PLUNGING JETS ON AIR ENTRAINMENT IN AN AERATION TANK 160
6.1 INTRODUCTION 160
6.2 EXPERIMENTAL SET-UP 163
6.2.1 Flow Facility 163
6.2.2 PIV Set-up 164
6.3 MEASUREMENT DESCRIPTION 165
6.4 RESULTS AND DISCUSSION 167
6.3.1 Air entrainment measurements 167
6.3.2 Velocity measurements 169
6.3.3 Penetration depth 170
6.3.4 Gas hold-up and mass transfer coefficient 171
6.5 CONCLUSIONS 173
6.6 REFERENCES 186

CHAPTER 7
COMPUTATIONAL FLUID DYNAMICS MODELLING OF DISSOLVED OXYGEN IN A RECYCLED WATER POND 190

7.1 INTRODUCTION 190
7.2 MODEL FORMULATION 191
    7.2.1 Inlets' Boundary Conditions 194
    7.2.2 Surface Boundary Condition 197
    7.2.3 Bottom Boundary Condition 200
7.3 CFD MODEL 202
7.4 RESULTS AND DISCUSSION 204
    7.4.1 Current Inlet Conditions 204
    7.4.2 Submerged Inlet Condition 206
7.5 CONCLUSIONS 209
7.6 REFERENCES 219

CHAPTER 8

CFD APPLICATION IN MODELING AND IMPROVING THE PERFORMANCE OF A STORAGE RESERVOIR USED AS A CONTACT CHAMBER FOR MICROORGANISM INACTIVATION 223
8.1 INTRODUCTION 223
    8.1.1 Storage Tanks as Contact Chambers 226
    8.1.2 Study Objectives 229
8.2 CFD MODEL 229
8.3 RESULTS AND DISCUSSION 235
    8.3.1 Results of CFD Models' Simulations 235
    8.3.2 Effect of Different Inlet Configurations 238
    8.3.3 Effect of a New Arrangement of Baffle Walls 240
8.4 CONCLUSIONS AND RECOMMENDATIONS 241
8.5 REFERENCES 253

CHAPTER 9

GENERAL CONCLUSIONS AND RECOMMENDATIONS 258
9.1 GENERAL CONCLUSIONS 258
9.2 RECOMMENDATIONS 263

LIST OF TABLES

Table 2.1 Summary of ANN applications in reactor modelling. 21
Table 2.2 Sources of data used in training and validating the developed ANN models... 22
Table 2.3 Ranges of input and output parameters of the ANN models. 23
Table 3.1 Parameters pertaining to the steady-state BFCM.. 70
Table 3.2 Operating conditions of the impinging-jet bubble column experiments. 71
Table 4.1 Summary of PDA configuration and operational settings. 104
Table 4.2 Summary of the operating conditions used for the PIV, PLIF and PDA .... experiments. 105
Table 5.1 Summary of the operating conditions during PLIF experiments................ 141
Table 5.2 Summary of the operating conditions during PIV experiments.................. 142
Table 5.3 Summary of the operating conditions during gas mass transfer experiments... 143
Table 6.1 Summary of the operating conditions for entrained air flow rate runs. 175
Table 6.2 Summary of the operating conditions for PIV runs. 176
Table 6.3 Summary of the air entrainment results. 177
Table 7.1 Measured and predicted DO levels at the outflow of the current inlets...... 211
Table 7.2 Summary of data collected for the RCW pond. 211
Table 8.1 Input and output conditions and assumptions used for the CFD models.... 243

LIST OF FIGURES

Figure 2.1 A schematic of a typical ozone bubble column reactor. 24

Figure 2.2 Architecture of the multi-layer artificial neural network model. 25

Figure 2.3 ANN Predicted versus experimental results for k_La. 26

Figure 2.4 ANN Predicted versus experimental results for ε_G. 27

Figure 2.5 ANN Predicted versus experimental results for d_S. 28

Figure 2.6 Relative contribution weights of the input parameters in the ANN models. 29

Figure 2.7 Predicted (using developed ANN models) versus experimental results for k_L. 30

Figure 3.1 Schematic diagram representing the transient back flow cell model for the co-current operation of a bubble column reactor (Adapted from Gamal El-Din and Smith (2001b)). 72

Figure 3.2 Bubble column pilot-scale set-up (Adapted from Gamal El-Din and Smith (2001c)). 73

Figure 3.3 Bubble dimensions (adapted from Yamashita et al. (1979)). 74

Figure 3.4 Effect of the number of cells on the TBFCM predictions of the RTDs.... 74

Figure 3.5 Comparison between the use of one mixing zone and two mixing zones to characterize the backmixing in the impinging-jet bubble column. 75

Figure 3.6 Comparison between the TBFCM-fitted and regression-fitted backmixing ratios for the impinging-jet bubble column. 75

Figure 3.7 Comparison between the experimentally-measured and the regression-fitted gas hold-ups. 76

Figure 3.8 Comparison between published gas hold-up correlations at $u_L = 0.02$ m/s. 76

Figure 3.9 Comparison between measured and predicted Sauter mean bubble diameters for approach (1). 77

Figure 3.10 Sum of the squares of the residuals (SSR) plot for injection and ejection modes. 77

Figure 3.11 Dissolved ozone concentration profiles for injection and ejection modes.78
Figure 3.12 Comparison between the BFCM predicted and the regression-fitted k_La. 78
Figure 3.13 Comparison between correlations predicting k_La in a number of bubble column designs. 79
Figure 4.1 Critical dimensions and geometry of Mazzei injector and nozzle. 106
Figure 4.2 Experimental setup. 107
Figure 4.3 PLIF images showing concentration distribution for different liquid flow rates. 108
Figure 4.4 PLIF images showing concentration distribution of two different gas flow rates for the same liquid flow rate. 109
Figure 4.5 PLIF images showing concentration distribution of two different liquid flow rates for the same gas flow rate. 110
Figure 4.6 Velocity vectors for different liquid flow rates without gas injection. 111
Figure 4.7 Velocity vectors for liquid and gas phases under different gas flow rates ($Q_L = 1.26 \times 10^{-4}$ m^3/s). 112
Figure 4.8 Step response curve from PLIF images ($u_L = 0.016$ m/s, $u_G = 0.001$ m/s). 113
Figure 4.9 Comparison between the predicted and the experimental D_L. 113
Figure 4.10 Bubble size distributions under different liquid flow rates. 114
Figure 4.11 Bubble size distributions under different gas flow rates. 115
Figure 4.12 Comparison between the predicted and the experimental d_S. 116
Figure 4.13 Comparison between the predicted and the experimental ε_G. 116
Figure 5.1 Experimental setup. 144
Figure 5.2 Critical dimensions and geometry of Mazzei injector and nozzle. 145
Figure 5.3 PLIF images showing concentration distribution for different liquid flow rates without side stream injection. 146
Figure 5.4 PLIF images showing concentration distribution for 1-phase side stream jets ($Q_L = 0.01$ m^3/s). 147
Figure 5.5 PLIF images showing concentration distribution for 2-phase side stream jets ($Q_L = 0.01$ m^3/s, $Q_G = 2.0 \times 10^{-4}$ m^3/s). 148

Figure 5.6 Velocity vectors at the contactor end for different pipe flow rates without side stream injection. 149
Figure 5.7 Velocity vectors at the mixing zone of the side stream injection for liquid-phase jets (without gas injection). 150
Figure 5.8 Velocity vectors at the mixing zone of the side stream injection for gas-phase jets. 150
Figure 5.9 Step response curve from PLIF images ($Q_L = 0.01$ m^3/s, no side jets)... 151
Figure 5.10 Probability plot of the step response signal ($Q_L = 0.01$ m^3/s, no side jets)... 151
Figure 5.11 Comparison between the measured dispersion parameter and published data for turbulent pipe flows. 152
Figure 5.12 Liquid dispersion coefficient versus number of side jets for different phases and jet alignments. 152
Figure 5.13 Liquid dispersion coefficient versus superficial gas velocity for alternating and opposing jets. 153
Figure 5.14 Overall mass transfer coefficient for alternating and opposing jets........ 153
Figure 5.15 Experimental versus predicted overall mass transfer coefficient for 2 opposing jets. 154
Figure 6.1 Schematic of characteristic lengths of plunging jets. 178
Figure 6.2 Experimental setup (flow facility). 179
Figure 6.3 PIV Setup. 180
Figure 6.4 Comparison between measured and calculated air entrainment ratio..... 180
Figure 6.5 Lateral distributions of the axial mean velocity. 181
Figure 6.6 Variation of penetration depth with nozzle diameter and outlet velocity..... 182
Figure 6.7 Comparison between measured and calculated penetration depth.......... 183
Figure 6.8 Variation of the gas hold-up with nozzles diameter and outlet velocity. 184
Figure 6.9 Comparison between measured and calculated gas hold-up. 185
Figure 6.10 Comparison between measured and calculated bubble diameter............ 185
Figure 7.1 Current inlet configurations of the RCW pond. 212
Figure 7.2 Variation of free water jets at the inlets of the RCW pond. 212

Figure 7.3 Carbonaceous biochemical oxygen demand test results. 213
Figure 7.4 Sediment oxygen demand test results. 213
Figure 7.5 CFD simulation of DO for current inlet conditions (21-12-05). 214
Figure 7.6 CFD simulations versus measured outlet DO for current inlet conditions. .. 214
Figure 7.7 Predicted outlet DO concentrations with time under current inlet conditions for different flow rates and water depths. 215
Figure 7.8 CFD model results of DO for the submerged inlet (21-12-05). 215
Figure 7.9 Comparison between CFD model of DO under current and submerged inlet conditions. 216
Figure 7.10 Outlet DO concentration versus time under different inlet conditions for average Q of 6.5 m^3/s and h of 2.3 m. 217
Figure 7.11 Predicted outlet DO concentrations versus wind velocity at different inlet temperatures and DO levels for submerged inlet condition. 217
Figure 7.12 Monthly outlet DO prediction for submerged inlet condition using Q of 6.5 m^3/s and h of 2.3 m. 218
Figure 8.1 A plan view of the original reservoir design; a reservoir with one baffle wall (after Hurtig (2003)). 244
Figure 8.2 A plan view of the modified reservoir design; a reservoir with nine baffle walls (after Hurtig (2003)). 244
Figure 8.3 Velocity vectors in the influent flow region of the one-baffle-wall reservoir model. 245
Figure 8.4 Rhodamine WT concentration distribution on an XY plane at 50 mm above the bottom of the one-baffle-wall reservoir model. 246
Figure 8.5 Velocity vectors in the influent flow region of the nine-baffle-wall reservoir model. 247
Figure 8.6 Rhodamine WT concentration distribution on an XY plane at 50 mm above the bottom of the nine-baffle wall reservoir model. 248
Figure 8.7 Rhodamine WT experimental and simulated concentration profiles at the outlet of the reservoir models. 249

Figure 8.8 Effect of inlet configuration on Rhodamine WT simulated concentration profiles at the outlet of the nine-baffle-wall pilot-scale reservoir........... 249

Figure 8.9 A plan view of a proposed reservoir design; with a new arrangement of five baffle walls... 250

Figure 8.10 Rhodamine WT concentration distribution on an XY plane at 50 mm above the bottom of the proposed one-inlet reservoir design. 251

Figure 8.11 Effect of inlet configuration on Rhodamine WT simulated concentration profiles at the outlet of two proposed reservoir designs. 252

CHAPTER 1

INTRODUCTION

1.1 GENERAL

One of the major problems facing water and wastewater treatment plants is to achieve, at relatively low costs, the water quality standards required to protect public and environmental health. Doing so requires detailed knowledge of the mechanisms responsible for separating, coagulating, precipitating, or oxidizing the contaminants in the influent water to the treatment units. Since these treatment mechanisms involve different combinations of physical unit operations, and chemical and biological unit processes; knowledge of chemical kinetics, fluid mechanics, and mass transfer are also essential for understanding these units. However, due to the difficulty and cost of accurately estimating the parameters needed to solve mathematical representations of the treatment systems, environmental engineers rely upon empirical and semi-empirical relationships for developing the design of needed reactors. However, these relationships cannot be considered reliable, valid or both over the wide range of applications encountered in practice. Therefore, design procedures which improve the accuracy of water treatment reactors and reduce the errors in the empirical relationships are essential for a good design. The prediction of performance requires accurate prediction of both the hydrodynamic conditions in the reactor and the performance of the unit operations and processes. Generally, the predictions of hydrodynamic conditions are best where near plug flow or complete mixing flow conditions prevail. However, the reactors' size and the range of flows often lead to mixed flow conditions which then challenge the efficiency of the required kinetics processes.

The advent of non-intrusive (i.e., no direct interaction with the flow field) laser measurement techniques such as those involving the laser Doppler anemometer (LDA), the particle dynamics analyzer (PDA), the particle image velocimetry (PIV), and the planer laser-induced fluorescence (PLIF) can be utilized to accurately measure reactor hydrodynamics. The use of computation fluid dynamics (CFD) can provide more freedom in predicting hydraulic conditions in complex geometry configurations after they have been calibrated with results obtained from some measuring techniques for simpler geometries.

Among the water and wastewater treatment units, gas-liquid exchange systems, such as aeration tanks and ozone contactors, are complex in their natures and their behaviour can vary substantially depending on the reactor's design, configuration, and operating conditions. Conducting experimental measurements inside gas-liquid flows is very difficult because of their sensitivity to any disturbances caused by intrusive measuring methods. Accordingly, laser measurement techniques can be very useful for characterizing and improving our understanding of flow phenomena in gas-liquid systems.

This work explores the application of single- and two-phase multiple mixing jets entering water and wastewater reactors by using laser measurement techniques and several modelling methods. PIV and PLIF systems were used to characterize the hydrodynamics of two special types of ozone contactors, an impinging-jets bubble column and an inline multi-jets ozone contactor. The PDA system was used to characterize the bubble sizes of the impinging-jets bubble column. The PIV system was used to study the air entrainment and bubble characteristics of surface jets plunging into an aeration tank. Three different modelling methods were employed in this work: the artificial neural network (ANN), the steady-state and transient backflow cell model (BFCM), and computation fluid dynamics (CFD). The ANN modelling technique was applied to different types of ozone bubble columns. The steady-state and transient BFCM model was used to evaluate the performance of the impinging-jets bubble column. The CFD modelling approach was used to model two water systems, a recycled water pond and a storage reservoir used as a microorganism reduction unit.

1.2 ORGANIZATION OF THE THESIS

The effect of two-phase turbulent jets on the hydrodynamics and mass transfer in five selected water systems was investigated by using advanced laser measurement techniques and modelling approaches. The experimental and the modelling results are presented in seven chapters. A brief introduction to each chapter is provided below.

Chapter 2 presents a review of the published data for the overall mass transfer coefficient (k_La, s^{-1}), the gas hold-up (ε_G, dimensionless), and the Sauter mean bubble diameter (d_S, m) of different types of ozone bubble columns operated under variable continuous flow regimes. Three multi-layer perceptron (MLP) artificial neural network (ANN) models were used to simulate and predict k_La, ε_G, and d_S in the bubble columns by utilizing simple inputs such as the bubble column's geometry and operating conditions.

The results obtained from the ANN models were then used to determine the local mass transfer coefficient (k_L, m.s^{-1}).

Chapter 3 presents a transient BFCM used to characterize the hydrodynamic behaviour of an impinging-jet ozone bubble column. A steady-state back flow cell model was developed to analyze the dissolved ozone concentration profiles measured in the bubble column. The effect of varying the superficial gas and liquid velocities, u_G (from 0.002 to 0.012 m/s) and u_L (from 0.008 to 0.028 m/s) on the column-average k_La (s^{-1}) was investigated. Concurrently, the specific interfacial area, a (m^{-1}), was evaluated by measuring the column average ε_G and d_S (m) of the bubbles. The local mass transfer coefficient, k_L (m.s^{-1}), was determined subsequently.

Chapter 4 introduces the results obtained from a PIV/PLIF system used in characterizing an impinging jet bubble column with mixing nozzles. This research aimed at evaluating the mixing effect resulting from the nozzle diffusers attached to the outlets of the impinging jets' injectors. The PIV system was used to study the flow patterns of the liquid and gas phases under different u_G and u_L values (from 0.002 to 0.017 m/s and from 0.008 to 0.024 m/s, respectively). Furthermore, the PDA system was used to characterize the bubble sizes under the same operating conditions. A PLIF system was used to determine the liquid axial dispersion coefficient (D_L, m^2/s) for the mentioned range of operating conditions. The column average ε_G and a were then determined in order to evaluate the column's mass transfer efficiency.

Chapter 5 presents the results of the hydrodynamics and gas mass transfer analyses of a pilot-scale inline multi-jets horizontal ozone contactor. The hydrodynamic characteristics of the contactor were studied by using a PIV/PLIF system. All hydrodynamic measurements were conducted under a total liquid flow rate of about 0.01 m^3/s with a gas flow rate ranging from 5.0×10^{-5} to 4.0×10^{-4} m^3/s. The gas was introduced into the system through a series of side stream injectors. The side injectors were tested under opposing and alternating modes. The mass transfer study was conducted under a liquid flow rate range of 7.6×10^{-3} to 0.01 m^3/s and a gas flow rate range of 5.0×10^{-5} m^3/s to 4.0×10^{-4} m^3/s. The effect of the number of side jets and the jets' alignment on both D_L and k_La was studied.

Chapter 6 introduces the results of an experimental study of the air entrainment resulting from surface jets plunging into an aeration tank. In this study, experiments were conducted to explore some properties of the bubble plumes of two inclined circular plunging water jets on a water surface in a cubic tank by utilizing particle image velocimetry (PIV). Different combinations of two-inclined water jets with nozzle size ranging from 2.5×10^{-3} to 0.01 m and operated under different liquid flow rates (3.15×10^{-5} to 12.6×10^{-5} m^3/s) and plunging angles (60° to 80°) were used to study the air entrainment in the aeration tank. The vertical distance from the jets' nozzles to the water's free surface was varied from 0.05 to 0.55 m. The PIV system was used to measure the two-phase jet velocities in both the lateral and axial positions. Other parameters of interest, such as ε_G, penetration depths and the height and width of the two-phase mixture due to the air entrainment, were also monitored. The value of d_S under each operating condition was determined by using images captured by the PIV system. By using ε_G and d_S, the values of a and k_La under each operating condition were determined. The obtained results were compared to the results obtained under similar operating conditions for vertically aligned jets in the same tank and from other published studies.

Chapter 7 presents a practical case study of the high aeration rates resulting from surface water jets plunging into a recycled water pond. The pond received water from two different inlets (in the form of turbulent plunging jets). The flow rate from both inlets ranged from 6.0 to 7.0 m^3/s. The surface area of the pond was about 1.5 x 10^5 m^2 with a varying depth of 0.4 to 4.8 m. The average theoretical hydraulic retention time (HRT) was around 18 h. The DO rates were minimized by altering the configurations of the inlets. A CFD model was first used to simulate the dissolved oxygen (DO) concentration in the recycled water pond under the current inlet configurations. The DO concentration and water temperature were collected for 9 months at the pond's inlets and outlets and used for model verification. Other important parameters influencing the DO in the pond, such as the biochemical oxygen demand (BOD) and the sediment oxygen demand (SOD), were obtained experimentally. The CFD model was then tested for a new submerged impinging jet inlet configuration to evaluate the resulting DO levels in the pond. Different ranges of the water flow rate, water depth, inlet DO concentration, temperature, and wind velocity were tested.

Chapter 8 presents a CFD model used to simulate two tracer studies conducted, in scaled-down physical models of an existing storage tank, to investigate the effect of the tank configuration on the effective contact time (t_{10}). One of the scaled-down physical models of the storage tank was equipped with one submerged inlet and one baffle wall at the middle length, and the other was equipped with one submerged inlet with nine baffle walls distributed evenly along the reservoir length. The developed CFD model was then applied to different inlet reservoir configurations for further investigation in order to improve the t_{10} value. The effect of using fewer baffle walls with different inlet arrangements on the t_{10} value was also tested.

Chapter 9 presents this thesis' general conclusions and final remarks. For each of the studies, in Chapters 3 to 8, Chapter 9 provides a brief summary and suggests recommendations for possible future research.

CHAPTER 2

ARTIFICIAL NEURAL NETWORKS MODELLING OF OZONE BUBBLE COLUMNS: MASS TRANSFER COEFFICIENT, GAS HOLD-UP, AND BUBBLE SIZE*

2.1 INTRODUCTION

Bubble columns are commonly used in chemical, biochemical and environmental industries as gas-liquid mass transfer systems due to their simple construction, operation and maintenance. More details on the applications and advantages of bubble columns have been reviewed recently by Kantarci et al. (2005). It is evident that precise knowledge of the hydrodynamics is required for accurate design of such contactors in order to evaluate their performance. The overall performance of bubble columns is often limited by the gas-liquid mass transfer (Cramers et al., 1992), which is controlled by the gas hold-up, specific interfacial area, and bubble-size distribution in the contactors (Patel et al., 1989; Weisweiler and Rosch, 1978). Therefore, many empirical correlations have been introduced to estimate these key design parameters of bubble columns (Akita and Yoshida, 1973; Akita and Yoshida, 1974; Deckwer and Schumpe, 1993; Hughmark, 1967; Kawase et al., 1992; Koide, 1996; Kumar et al., 1997; Kundu et al., 2003; Lau et al., 2004; Nakao et al., 1983; Patel et al., 1989; Poulsen and Iversen, 1998; Shah et al., 1982; Vasconcelos et al., 2003; Winterton, 1994; Yamashita et al., 1979). However, all these correlations were obtained for specific experimental conditions and cannot be used for the wide range of operating conditions, physical properties and reactor geometries. Hence, a need for new empirical correlations arises whenever a new bubble column is to be designed and run under new operating conditions.

---

* A version of this chapter has been accepted for publication. Baawain, M.B., M. Gamal El-Din, and D.W. Smith, *Ozone Sci. & Eng.* (March 2007)

Good experimental techniques are costly and require qualified personal. Therefore, a general modelling approach that can be implemented easily with satisfactory efficiency is necessary to obtain reliable designs of bubble columns. Artificial neural network (ANN) models appear to be a good choice as they have been recognized to perform exceptionally well in capturing complex interactions within the used input parameters without prior knowledge about the nature of the problem. They can tolerate imprecise data, and approximate results with less vulnerability to outliers compared to that of deterministic models (Haykin, 1999). They are based on the decomposition of input-output relationship into a series of linearly separable steps by using hidden layer(s) neurons (Haykin, 1999). Generally, ANN models are developed in four steps: (1) data transforming (scaling); (2) network architecture defining (setting the number of hidden layers, the number of neurons in each layer, and the connectivity between the neurons); (3) training (calibrating) the network to respond adequately to a given set of inputs; and (4) validating the network to a set of inputs to insure the generality of the ANN model's prediction ability. Although several architectures of neural networks are available, the feed-forward multilayer perceptron (MLP) ANNs trained with a backpropagation algorithm (BP) are considered among the most commonly used networks. MLP-BP ANNs with only one hidden layer have been reported to be universal approximators of any non-linear functions and can be sufficient for most important applications (Hornik et al., 1989).

A review of the available literature illustrated that ANNs have been applied successfully to predict the values of the overall mass transfer coefficient (k_La, s^{-1}), the gas hold-up (ε_G, dimensionless), gas bubbles specific interfacial area (a, m^{-1}), and the bubble diameter (d_b, m) in a number of industrial reactors (see Table 2.1). The presented models cover a wide range of gas-liquid systems. These developed ANN models are based on the reactors' geometry, operating conditions, and/or physicochemical properties (viscosity, density, surface tension and diffusivity). According to the provided statistical measures, ANNs can provide a promising tool for predicting the important design parameters of gas-liquid systems.

The aim of this study is to develop general, simple and relatively accurate ANN models that can be used to design and evaluate ozone bubble columns operating under different experimental conditions. The aim of the developed ANN models is to adequately predict k_La, ε_G, and the Sauter mean bubble diameter (d_S, m) by using simple inputs such as the bubble columns' geometry and operational parameters. Once these parameters are successfully predicted, the local mass transfer coefficient (k_L, $m.s^{-1}$) can be estimated.

2.2 OZONE BUBBLE COLUMNS

Bubble columns are used in environmental engineering as ozone contactors to degrade (oxidize) the organic constituents in wastewater and/or to inactivate pathogenic microorganisms in treated water. A typical ozone bubble column is shown in Figure 2.1

where ozone gas is injected into the system through gas diffusers. The ozone gas can be sparged into a stagnant liquid (semi-batch system) or a continuous flowing system. Ozone bubble columns have received relatively high attention from researchers in both chemical and environmental engineering studies aimed at obtaining accurate design and scale-up approaches (Bin et al., 2001; Chen et al., 2002a; Farooq and Ahmed, 1989; Gamal El-Din and Smith, 2001; Gamal El-Din and Smith, 2003a; Herbrechtsmeier et al., 1987; Huang et al., 1998; Huber et al., 2005; Kallas et al., 1995; Lesauze et al., 1993; Mitani et al., 2005; Roustan et al., 1996; Wright et al., 1998; Xu and Liu, 1990; Zhou and Smith, 2000). These research studies showed that the design and modelling of ozone bubble columns are based on the accurate determination of k_La, ε_G, and d_S.

The overall mass transfer coefficient (k_La) is used to describe the absorbance of ozone gas into the liquid phase. This absorbance can be described by the following equation:

$$\Psi = k_L a\left(C_L^* - C_L\right) \qquad [2.1]$$

where Ψ is ozone absorption rate (mg.L^{-1}.s^{-1}), $C_L{}^*$ is the dissolved ozone concentration in equilibrium with the bulk ozone (mg.L^{-1}), and C_L is the dissolved ozone concentration in the bulk liquid (mg.L^{-1}). The value of k_La can be determined by obtaining the dissolved ozone concentrations in the bubble column with time in order to solve Equation 2.1 under specific operating conditions. Then k_La is usually correlated with the operating conditions and/or the physicochemical characteristics (viscosity, density, surface tension and diffusivity) to generalize the outcomes of the experimental procedure of the studied column. An example of such correlations is the expression of k_La as a function of the superficial gas velocity (u_G (m.s^{-1}), the ratio of the gas flow rate to the bubble column's cross-sectional area) and the superficial liquid velocity (u_L (m.s^{-1}), the ratio of the liquid flow rate to the bubble column's cross-sectional area) (Huynh et al., 1991):

$$k_L a = c_1 u_G^{c_2} u_L^{c_3} \qquad [2.2]$$

where k_La is in s^{-1}, u_G and u_L are in m.s^{-1}, while c_1, c_2, and c_3 are constants that can be obtained empirically through a nonlinear regression analysis.

Although the determination of k_La is useful for design purposes, it is important in many cases to determine the local mass transfer coefficient (k_L, m.s^{-1}) in order to evaluate the enhancement factor for gas absorption with a chemical reaction or gas-liquid reaction (Akita and Yoshida, 1974). Therefore, one must know the value of the gas bubbles specific interfacial area (a, m^2/m^3), which is equal to the ratio between the bubbles' surface area (A, m^2) and the volume of the dispersed phases (V, m^3). However, due to the difficulties associated with determining A, the value of a can be calculated using the following relationship:

$$a = \frac{6\varepsilon_G}{d_S} \qquad [2.3]$$

where a is in m^{-1}, ε_G is the dimensionless gas hold-up, and d_S is Sauter mean bubble diameter (m). The values of ε_G for any bubble column can be obtained by determining the pressure profile in the bubble column experimentally, using pressure taps or transducers, and then applying the following equation:

$$\varepsilon_G = 1 - \frac{\Delta P}{\rho_L g \Delta x} \qquad [2.4]$$

where ΔP is the pressure difference (Pa), ρ_L is the liquid density (kg.m^{-3}), g is the acceleration due to gravity (9.81 m.s^{-2}), and Δx is the axial distance between two measuring points (m). Furthermore, d_S can be expressed as

$$d_S = \frac{\sum_{i=1}^{N} d_i^3}{\sum_{i=1}^{N} d_i^2} \qquad [2.5]$$

where d_i is the diameter of the i^{th} bubble (m), and N is the number of bubbles measured. The values of d_i can be determined by using several measuring techniques such as those involving optical fibre probes, digital photography, and laser particle dynamics analyzers.

2.3 ANN MODELS PREPARATION

As Table 2.1 shows, the majority of the ANN models were developed for semi-batch systems (which sparge gas into a stagnant liquid) because of the relative ease in controlling the experimental conditions and in measuring the parameter(s) of interest. However, practical conditions require the use of continuous liquid and gas flow conditions. Only three studies have considered systems with a continuous flow mode, two of which are not relevant to this work. Baawain et al. (2005) provided a preliminary study of the applicability of the ANN modelling technique in predicting k_La in continuous flow bubble columns. The current work modifies this previous study's k_La ANN model and develops two more ANN models to predict ε_G and d_S.

The data used for developing the three ANN models was obtained from 18 research studies performed on different bubble columns operating under continuous flow conditions (see Table 2.2). Almost every study used a unique bubble column with a different geometry and gas-injection method. Also, the operating conditions (liquid and gas flow rates) varied from one column to the other. Among the 18 research studies summarized in Table 2.2, only five examined ozone-water bubble columns under continuous flow conditions (Beltran et al., 1995; Chen et al., 2002b; Gamal El-Din and Smith, 2003a; Roustan et al., 1996; Xu and Liu, 1990). The other studies considered oxygen-water bubble columns operating under continuous flow conditions. This study assumes that the gas type has a negligible effect on the values of ε_G and d_S. However, according to the surface renewal theory, the values of oxygen-based k_La have to be converted to an ozone-based k_La (Danckwerts, 1970). The k_La values were first corrected for the water temperature using the following modified Arrhenius' equation (Roustan et al., 1996):

$$(k_L a)_{20} = (k_L a)_T 1.024^{(20-T)} \qquad [2.6]$$

where $(k_La)_{20}$ is the overall mass transfer coefficient at 20 °C (s^{-1}), and $(k_La)_T$ is the overall mass transfer coefficient (s^{-1}) at the water temperature in the bubble column (T, °C). Then, the surface renewal theory introduced by Danckwerts (1970) and validated by Sherwood et al. (1975) and Beltran et al. (1998) was used to convert the oxygen-based k_La to an ozone-based k_La as follows:

$$\frac{(k_L a)_{O_3}}{(k_L a)_{O_2}} = \sqrt{\frac{D_{O_3}}{D_{O_2}}} \qquad [2.7]$$

where D_{O_3} is the molecular diffusivity of ozone gas in water (= 1.74×10^{-9} m^{2}s^{-1}), and D_{O_2} is the molecular diffusivity of oxygen gas in water (= 2.50×10^{-9} m^{2}s^{-1}).

After the parameters of interest (k_La, ε_G, and d_S) were collected, three MLP-BP ANN models were developed by utilizing NeuroShell 2 Software™ from Ward Systems Group Inc. A typical architecture of the used MLP ANN model is shown in Figure 2.2. The parameters cross-sectional area (A_{cs}, m^2), effective water height in the bubble column (H_{bc}, m), ozone diffuser diameter (d_{dif}, m), diffuser pore size (d_{pore}, m), flow direction (α; +1 for the co-current flow condition and -1 for the counter-current flow conditions), u_L (m.s^{-1}), and u_G (m.s^{-1}) were used as inputs for the three MLP-BP ANN models, while the k_La, ε_G and d_S were set to be the models' outputs. Table 2.3 shows the ranges of input and output parameters used in the developed ANN models. The collected data for each ANN model (378 data points for the k_La network, 278 data points for the ε_G network, and 138 data points for the d_S network) was divided randomly into training and validation data sets at a ratio of 3:1 (training to validation). The input parameters for all networks were scaled with a linear scaling function over an open interval from 0 to 1 to overcome the large variation in the input data, which can slow if not prevent the calibration of the network. One hidden layer with a number of hidden neurons was employed in developing the networks. The output layer of each ANN model consisted of one neuron to resemble the value of the predicted parameter. The neurons in the input layer were related to the hidden layer neurons, which were in turn related to the output layer by using connection weights (Figure 2.2). The input data was propagated, during the training process of a network, by using a feed-forward method to produce output data according to the connection weights and activation functions. The outputs from the neurons in a preceding layer were multiplied by the connecting weights to the neuron in the next layer. An activation function was then applied to the sum of these products, and the result was introduced in the neuron of the succeeding layer. Different activation functions were explored in both the hidden and the output layers in order to obtain the best model network. The training process was propagated by using a number of iterations (epochs) and automatic adjustment of the connection weights until the minimum mean square error (*MSE*) was achieved. Further details regarding the MLP-BP ANN's structure and activation functions can be found elsewhere (Haykin, 1999; Hornik et al., 1989).

2.4 RESULTS AND DISCUSSION

The MLP-BP ANN architecture that yielded the best training and validation results for k_La consisted of one hidden layer with 20 hidden neurons with logistic activation functions in both the hidden and the output layers. This network was trained with 4000 epochs with TurboProbe weight updates (by updating the weight size independently for each different weight with an adaptive adjustment of the step size as the learning progressed) and rotation pattern selection (by selecting the training pattern as they appeared in the provided file according to the training to validation ratio mentioned above). The developed MLP-BP ANN model simulated the k_La values very well, as the coefficient of multiple determination (R^2) was 0.99 and 0.98 for the training and validation data sets, respectively. Furthermore, the performance of the developed model was evaluated by determining the average absolute relative error (*AARE*), which was found to be 9 % for the training data set and 13 % for the validation data set. The high performance of the developed ANN model is strongly supported by Figure 2.3, which shows an excellent agreement between the experimentally measured k_La values and the ANN predicted ones in both the training and validation data sets. The values of the *AARE* are relatively small (compared to most *AARE* values shown in Table 2.1; only the ANN models developed for specific experiments yielded lower *AARE* than those obtained in this study). The small difference between the ANN model's predictions and the measured k_La values is probably due to the wide range of some operating conditions such as the range of H_{bc} (7.2 m used by Deckwer et al. (1983) and 0.11 m used by Alvarezcuenca et al. (1980)).

The MLP-BP ANN architecture that resulted in the minimum *MSE* of ε_G simulations for both the training and validation data sets consisted of 12 hidden neurons and used logistic activation functions in both the hidden and output layers. The ε_G ANN model was trained with 5000 epochs with TurboProbe weight updates and rotation pattern selection. The model predicted ε_G values in both the training and validation data sets excellently, as R^2 and *AARE* were 0.99 and 6 %, respectively. Figure 2.4 illustrates the high performance of the developed ε_G ANN model through the excellent agreement shown between the measured and the ANN-predicted ε_G values in both the training and validation data sets. Although previous ANN models that aimed at predicting ε_G were developed for semi-batch systems (with simpler operating conditions than those of the continuous flow systems considered in this study), the current ε_G ANN model outperformed most of them.

The MLP-BP ANN architecture developed for modelling d_S values consisted of 3 hidden neurons and used a symmetric logistic activation function in the hidden layer and a logistic activation function in the output layer. This model was trained with 3500 epochs with TurboProbe weight updates and rotation pattern selection. Figure 2.5 depicts an excellent agreement between the measured and the ANN-predicted d_S values in both the training and validation data sets. The obtained R^2 and *AARE* values were 0.99 and 5 %, respectively, for both the training and validation data sets, which demonstrate the validity of the developed model in predicting d_S in bubble columns. The slightly higher *AARE* associated with d_S compared to that of the ANN models of d_S in semi-batch systems (Table 2.1) can be related to the uncertainty associated with the turbulence intensity induced by u_L in the bubble columns.

As Table 2.2 shows, most researchers explored the use of only one gas diffuser in their bubble columns. Therefore, their experimental procedures were based on relating k_La, ε_G, and/or d_S to the operating conditions (i.e., u_G and/or u_L) and/or the physiochemical properties through nonlinear regressions for the bubble column design under investigation. As a result, each regression model (developed for k_La, ε_G, and/or d_S) was case-sensitive as it excluded the effects of several other factors including the bubble column's geometry and the gas sparging technique. Figure 2.6 shows the contribution weights of the input parameters on the prediction of k_La, ε_G, and d_S in the developed ANN models. The effect of u_G is higher than u_L for the k_La (Figure 2.6a) and ε_G (Figure 2.6b) models. This finding agrees with the findings in most of the available literature. Moreover, the variables d_{pore}, d_{dif}, and H_{bc} have a relatively high effect on k_La and ε_G, and this finding also agrees with several researchers' observations (Alvarezcuenca et al., 1980; Alvarezcuenca and Nerenberg, 1981; Huynh et al., 1991). Figure 2.6c shows that the effect of u_G is lower than u_L for d_S model. This finding also concurs with those in some previous studies (Akita and Yoshida, 1974; Unno and Inoue, 1980; Varley, 1995). The variables d_{pore}, and d_{dif} have a relatively high effect on d_S as Unno and Inoue (1980) also found. On the other hand, the flow direction was found to have minimal effect on the predicted parameters in bubble columns. This finding agrees with those of Gamal El-Din and Smith (2001) and Roustan et al. (1996).

After the determination of k_La, ε_G, and d_S by utilizing the developed ANN models, the values of k_L were calculated by combining Equation 2.3 and k_La as follows:

$$k_L = \frac{k_L a \cdot d_S}{6\varepsilon_G} \qquad [2.8]$$

The k_L values predicted by using the results obtained from the three developed ANN models and Equation 2.8 were then plotted against the experimental values of k_L, as shown in Figure 2.7. The overall prediction for k_L is very good as the obtained R^2 and *AARE* values are 0.85 and 20 %, respectively. The relatively high error in k_L values is due to the propagation of the errors in predicting k_La, ε_G, and d_S. Nevertheless, the combination of the three ANN models and Equation 2.8 provide an adequate tool to predict k_L when compared to the cumbersome experimental methods.

2.5 CONCLUSIONS

This study demonstrated the validity of the artificial neural network (ANN) modelling approach in predicting the key parameters required for designing and evaluating ozone bubble columns. Three multilayer perceptron (MLP) ANN models, trained with a BP algorithm, were developed to predict the overall mass transfer coefficient (k_La), the gas hold-up (ε_G), and the Sauter mean bubble diameter (d_S) in different bubble columns with different operating conditions. The three MLP-BP ANN models used the following input parameters: the cross-sectional area (A_{cs}), the water height in the bubble column (H_{bc}), the ozone diffuser diameter (d_{dif}), the diffuser pore size (d_{pore}), the flow direction (α), the superficial liquid velocity (u_L, m.s^{-1}), and the superficial gas velocity (u_G, m.s^{-1}).

The ANN models showed excellent prediction ability as the respective values of the coefficient of multiple determination (R^2) and the average absolute relative error (*AARE*) were 0.98 and 13 % for k_La, 0.99 and 6 % for ε_G, and 0.99 and 5 % for d_S. The local mass transfer coefficient (k_L) was then calculated by using the ANN models' results and Equation 2.8. The results showed very good agreement between the calculated and the experimental k_L values as the R^2 and *AARE* values were 0.85 and 20 %, respectively.

Table 2.1 Summary of ANN applications in reactor modelling.

Authors	Reactor type[‡]	Flow mode	Data points	Predicted parameter	Statistical measures *MSE*	*AARE*	R^2
Al-Masry and Abdennour (2006)	BCs	*	200	ε_G	2 %	-	-
Alvarez et al. (2000)	BCs	*	-	k_La	-	1 %	-
Baawain et al. (2005)	BCs	+	300	k_La	-	-	0.85
Behkish et al. (2005)	BCs	*	3880	ε_G	-	16 %	0.90
Djebbar and Narbaitz (2002)	ASPTs	+	1078	k_La	-	24 %	-
Fonseca et al. (2000)	SPECs	*	60	k_La	-	7 %	-
García-Ochoa and Castro (2001)	STRs	*	450	k_La	-	10 %	-
Iliuta et al. (1999)	TBRs	+	3200	k_La, a	-	29 %	-
Jamialahmadi et al. (2001)	BCs	*	200	d_b	-	2 %	-
Lemoine et al. (2003)	SGRs	*	4435	k_La	-	-	0.91
Shaikh and Al-Dahhan (2003)	BCs	*	3500	ε_G	-	15 %	-
Supardan et al. (2004)	BCs	*	178	k_La, ε_G	-	15 %	-
Utomo et al. (2001)	BCs	*	102	ε_G, d_b	-	1 %	-
Wu et al. (2003)	BCs	*	3000	ε_G	-	6 %	0.89
Yang et al. (1999)	STRs	*	824	k_La	-	25 %	-

‡ BCs: Bubble columns; ASPTs: air stripping packed towers; SPECs: spray and packed extraction columns; STRs: stirred tank reactors; TBRs: trickle-bed reactors; SGRs: surface aeration and gas-induced reactors

* Semi-batch flow mode (injection of gas into a constant liquid volume)

+ Continuous flow mode (both gas and liquid are injected continuously into the reactor)

Table 2.2 Sources of data used in training and validating the developed ANN models.

Authors	Data points	Gas diffuser*	Flow direction+	Measured parameter(s)
Akita and Yoshida (1973)	28	SN	1, -1	k_La, ε_G
Akita and Yoshida (1974)	28	SN	1, -1	d_S
Akosman et al. (2004)	10	SN	1	k_La, ε_G, d_S
Alvarezcuenca et al. (1980)	32	SSN	1	k_La
Alvarezcuenca et al. (1981)	32	SSN	1	k_La
Beltran et al. (1995)	4	DP	1	k_La, ε_G
Briens et al. (1992)	13	NVT	1	k_La, ε_G
Chen et al. (2002b)	7	PCP	-1	k_La, ε_G
Deckwer et al. (1974)	48	CwO, SP	1, -1	ε_G
Deckwer et al. (1983)	48	CwO, SP	1, -1	k_La
Gamal El-Din and Smith (2003a)‡	12	VI	1	k_La, ε_G, d_S
Hikita et al. (1981)	12	SN	1	k_La, ε_G
Huynh et al. (1991)	31	NVT	1	k_La, ε_G
Kulkarni and Shah (1984)§	11	RD	1	k_La, ε_G, d_S
Kulkarni et al. (1983)	25	RD	1	k_La, ε_G, d_S
Roustan et al. (1996)	52	PCP	1, -1	k_La, ε_G, d_S
Wang and Fan (1978)	25	SN	1	k_La, ε_G
Xu and Liu. (1990)	36	MPTP	-1	k_La

* SN: single nozzle; SSN: stainless steel nozzle, DP: diffuser plate; NVT: nozzle with venture throat; PCP: perforated ceramic plate; CwO: cross with orifices; SP: sintered plate; VI: venture injector; RD: ring type distributor; MPTP: micro-porous titanium plate

+ 1 = co-current flow, -1 = counter-current flow

‡ Values of ε_G were obtained from Gamal El-Din and Smith (2003b)

§ Values of d_S were obtained from Kulkarni et al. (1983)

Table 2.3 Ranges of input and output parameters of the ANN models.

Variable	Minimum	Maximum	Mean	Standard deviation
A_{cs} (m^2)*	0.002	0.031	0.013	0.009
H_{bc} (m)*	0.112	7.2	2.4	1.86
d_{dif} (m)*	0.003	0.18	0.052	0.047
d_{pore} (m)*	0	0.019	0.005	0.006
α*	-1	1	0.523	0.853
u_L (m.s^{-1})*	0	0.399	0.095	0.114
u_G (m.s^{-1})*	0.0003	0.4	0.063	0.086
k_La (s^{-1})‡	0.001	1.038	0.11	0.175
ε_G‡	0.004	0.348	0.084	0.073
d_S (m)‡	0.001	0.028	0.006	0.006

* Input variables ‡ Actual outputs

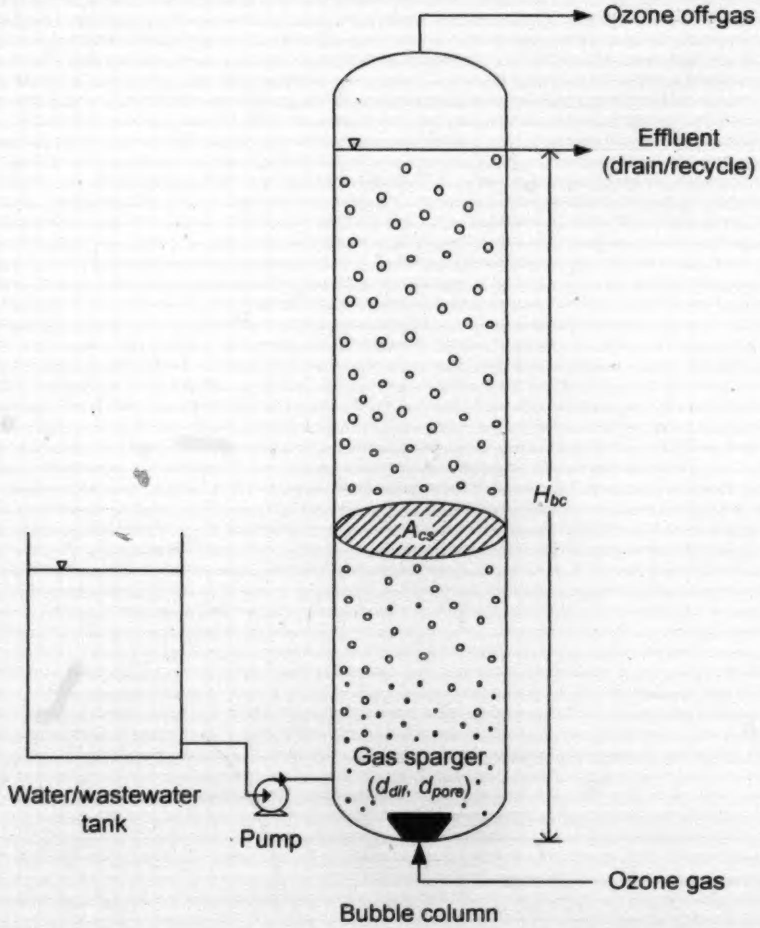

Figure 2.1 A schematic of a typical ozone bubble column reactor.

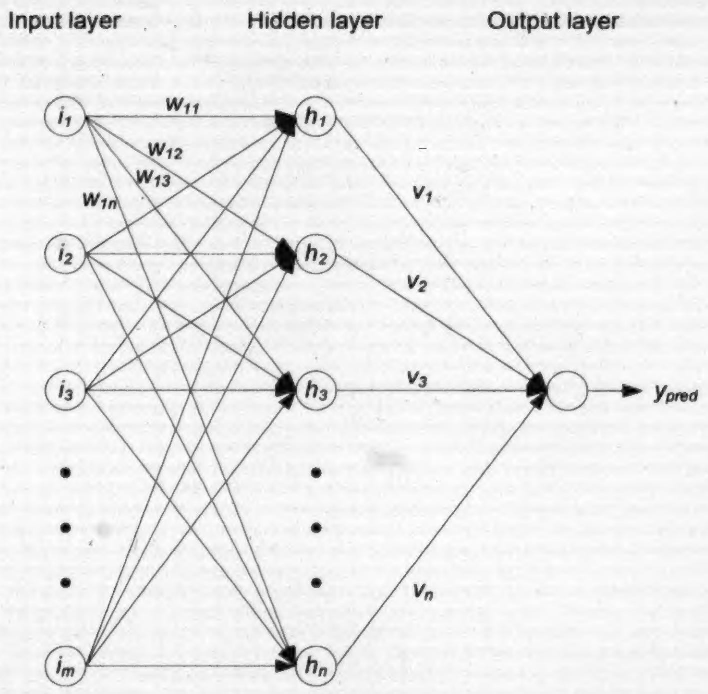

Figure 2.2 Architecture of the multi-layer artificial neural network model.

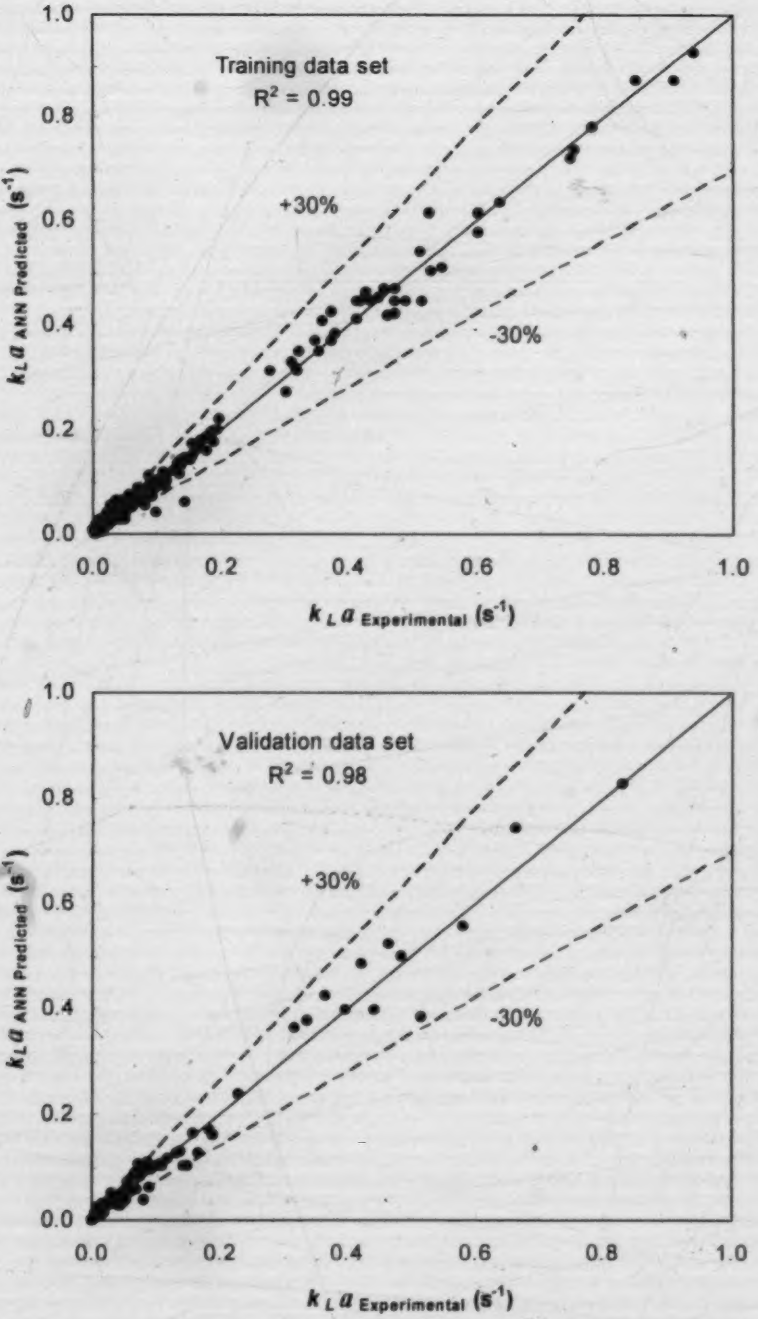

Figure 2.3 ANN Predicted versus experimental results for $k_L a$.

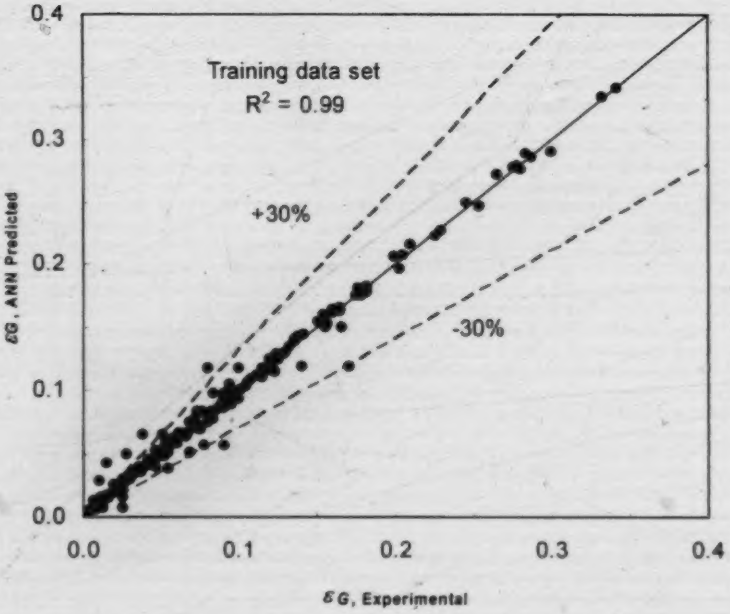

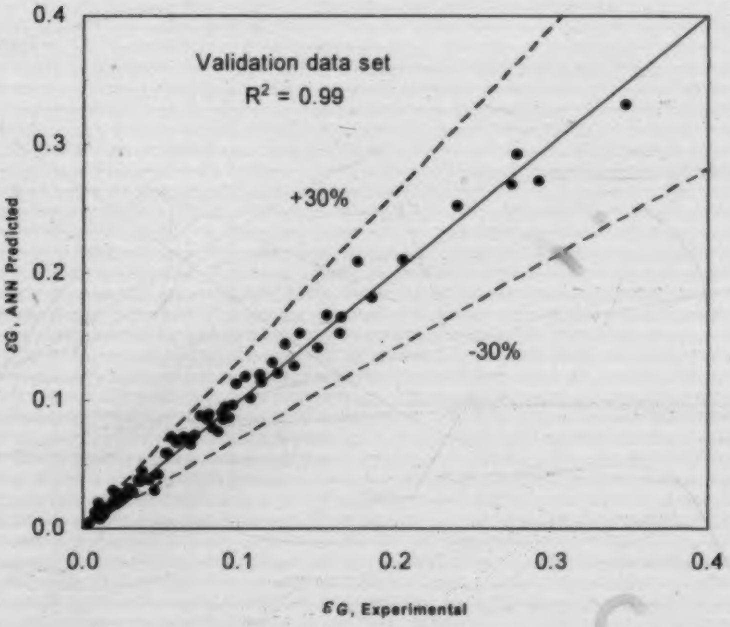

Figure 2.4 ANN Predicted versus experimental results for ε_G.

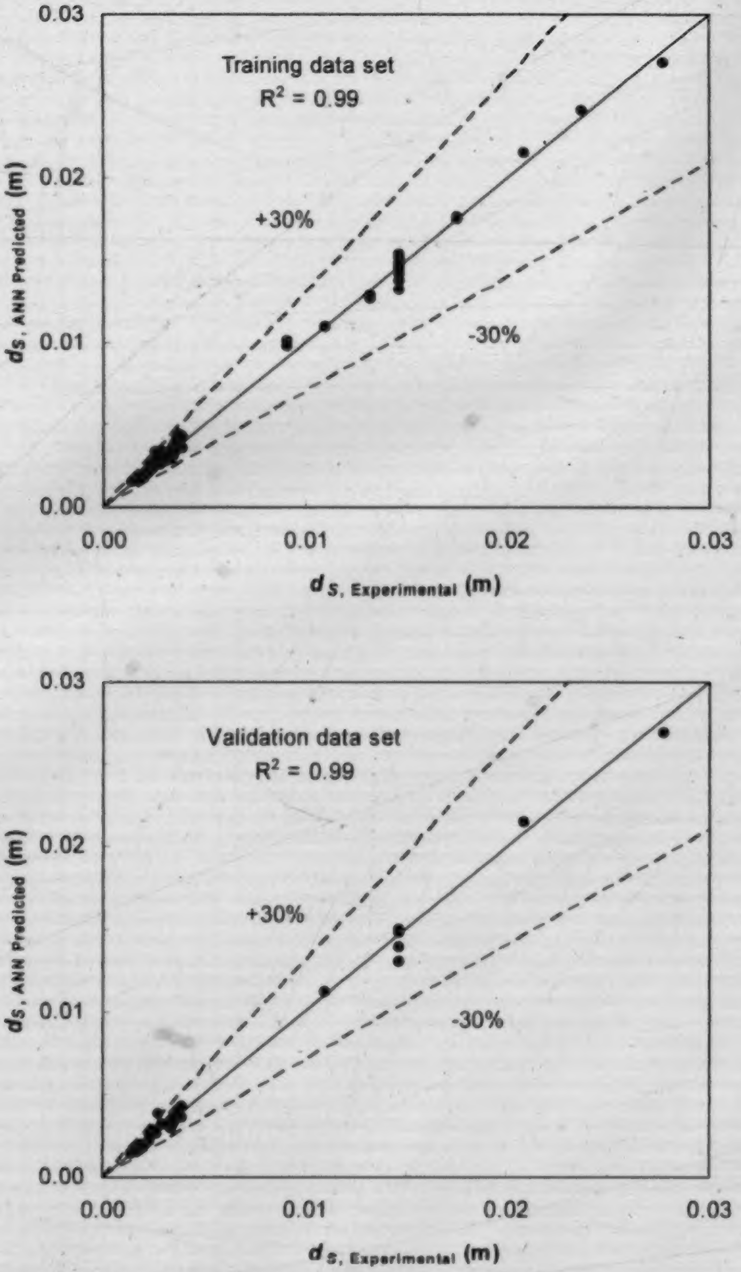

Figure 2.5 ANN Predicted versus experimental results for d_S.

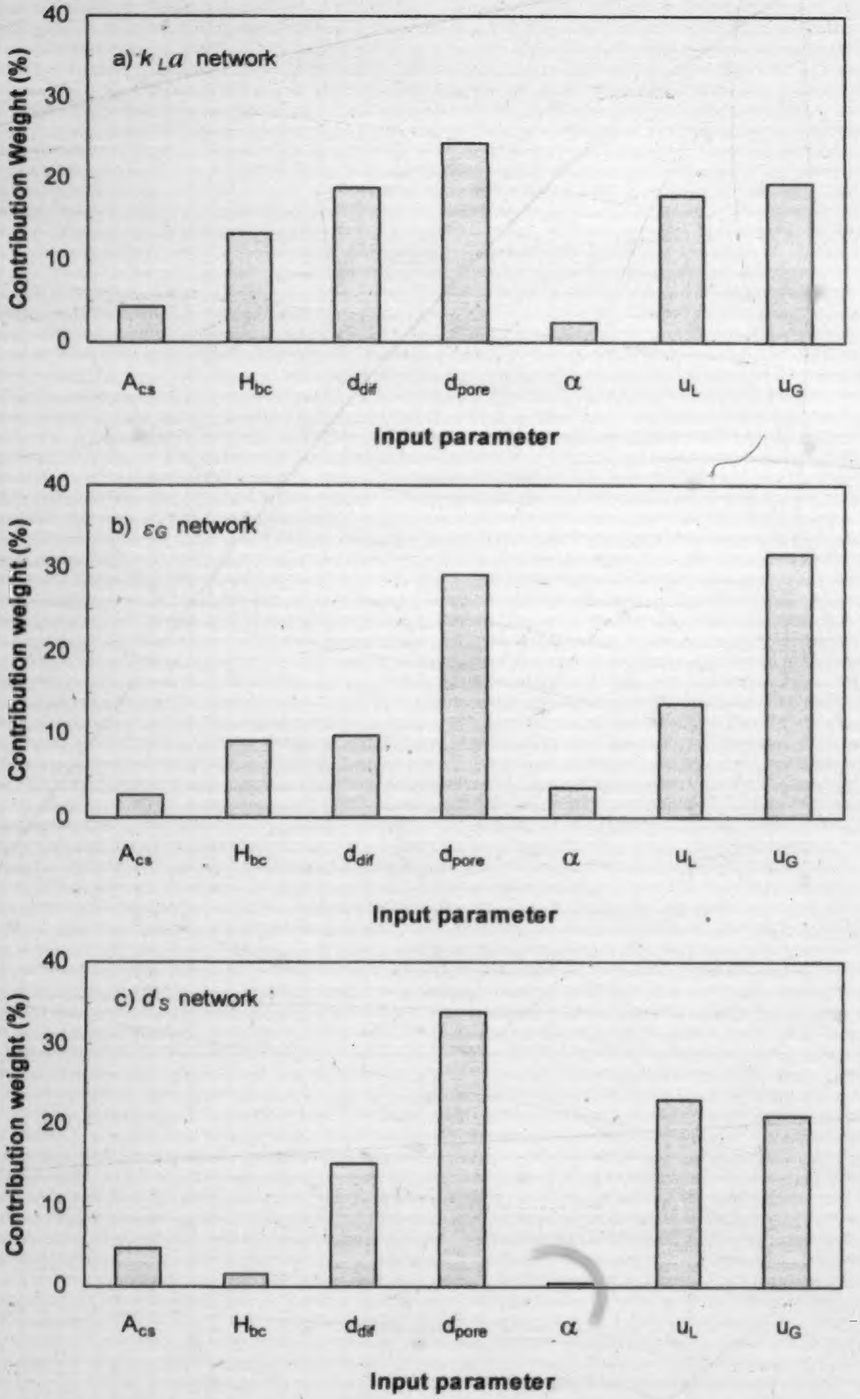

Figure 2.6 Relative contribution weights of the input parameters in the ANN models.

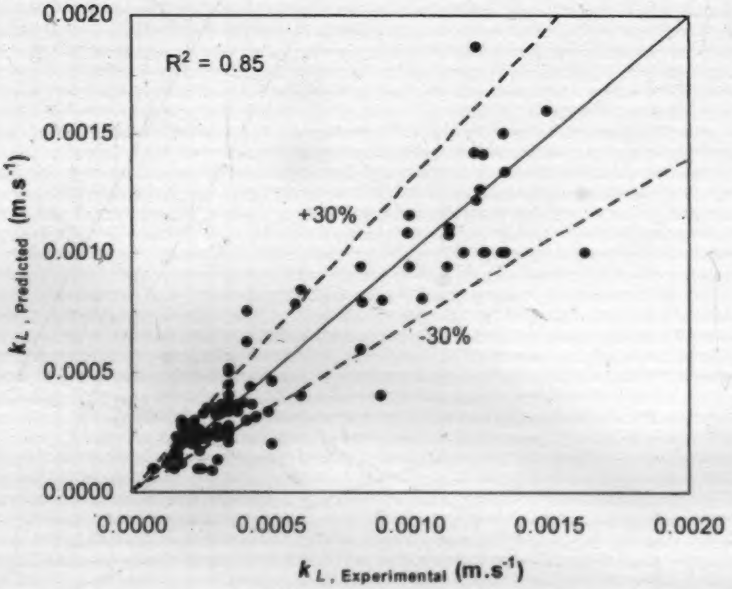

Figure 2.7 Predicted (using developed ANN models) versus experimental results for k_L.

2.6 REFERENCES

1. Akita, K., and F. Yoshida, "Gas Holdup and Volumetric Mass-Transfer Coefficient in Bubble Columns - Effects of Liquid Properties", *Industrial & Engineering Chemistry Process Design and Development*, 12(1): 76-80 (1973).
2. Akita, K., and F. Yoshida, "Bubble Size, Interfacial Area, and Liquid-Phase Mass Transfer Coefficient in Bubble Columns", *Industrial & Engineering Chemistry Process Design and Development*, 13(1): 84-91 (1974).
3. Akosman, C., R. Orhan, and G. Dursun, "Effects of Liquid Property on Gas Holdup and Mass Transfer in Co-Current Downflow Contacting Column", *Chemical Engineering and Processing*, 43(4): 503-509 (2004).
4. Al-Masry, W.A., and A. Abdennour, "Gas Hold-up Estimation in Bubble Columns Using Passive Acoustic Waveforms with Neural Networks", *Journal of Chemical Technology and Biotechnology*, 81(6): 951-957 (2006).
5. Alvarez, E., J.M. Correa, C. Riverol, and J.M. Navaza, "Model Based in Neural Networks for the Prediction of the Mass Transfer Coefficients in Bubble Columns. Study in Newtonian and Non-Newtonian Fluids", *International Communications in Heat and Mass Transfer*, 27(1): 93-98 (2000).
6. Alvarezcuenca, M., C.G.J. Baker, and M.A. Bergougnou, "Oxygen Mass-Transfer in Bubble-Columns", *Chemical Engineering Science*, 35(5): 1121-1127 (1980).
7. Alvarezcuenca, M., and M.A. Nerenberg, "Oxygen Mass-Transfer in Bubble-Columns Working at Large Gas and Liquid Flow-Rates", *AIChE Journal*, 27(1): 66-73 (1981).

8. Baawain, M.S., M. Gamal El-Din, and D.W. Smith, "Mass Transfer Analysis in Ozone Bubble Columns Using Artificial Neural Netwroks", *in Proceedings of the Eighth International Conference on the Application of Artificial Intelligence to Civil, Structural and Environmental Engineering*, Stirling, United Kingdom. (2005).

9. Behkish, A., R. Lemoine, L. Sehabiague, R. Oukaci, and B. Morsi, "Prediction of the Gas Holdup in Industrial-Scale Bubble Columns and Slurry Bubble Column Reactors Using Back-Propagation Neural Networks", *International Journal of Chemical Reactor Engineering*, 3 (2005).

10. Beltran, F.J., J.M. Encinar, and J.F. Garciaaraya, "Modeling Industrial Waste-Water Ozonation in Bubble Contactors .2. Scale-up from Bench to Pilot-Plant", *Ozone-Science & Engineering*, 17(4): 379-398 (1995).

11. Beltran, F.J., L.A. Fernandez, P. Alvarez, and E. Rodriguez, "Comparison of Ozonation Kinetic Data from Film and Danckwerts Theories", *Ozone-Science & Engineering*, 20(5): 403-420 (1998).

12. Bin, A.K., B. Duczmal, and P. Machniewski, "Hydrodynamics and Ozone Mass Transfer in a Tall Bubble Column", *Chemical Engineering Science*, 56(21-22): 6233-6240 (2001).

13. Briens, C.L., L.X. Huynh, J.F. Large, A. Catros, J.R. Bernard, and M.A. Bergougnou, "Hydrodynamics and Gas-Liquid Mass-Transfer in a Downward Venturi-Bubble Column Combination", *Chemical Engineering Science*, 47(13-14): 3549-3556 (1992).

14. Chen, Y.H., C.Y. Chang, C.Y. Chiu, W.H. Huang, Y.H. Yu, P.C. Chiang, Y. Ku, and J.N. Chen, "Dynamic Model of Ozone Contacting Process with Oxygen Mass Transfer in Bubble Columns", *Journal of Environmental Engineering-ASCE*, 128(11): 1036-1045 (2002a).

15. Chen, Y.H., C.Y. Chang, Y.H. Yu, P.C. Chiang, C.Y. Chiu, Y. Ku, and J.N. Chen, "A Dynamic Model of Ozone Disinfection in a Bubble Column with Oxygen Mass Transfer", *Journal of the Chinese Institute of Chemical Engineers*, 33(3): 253-265 (2002b).

16. Cramers, P., A. Beenackers, and L.L. Vandierendonck, "Hydrodynamics and Mass-Transfer Characteristics of a Loop-Venturi Reactor with a Downflow Liquid Jet Ejector", *Chemical Engineering Science*, 47(13-14): 3557-3564 (1992).

17. Danckwerts, P., *Gas-Liquid Reaction*. (New York: McGraw-Hill, 1970).

18. Deckwer, W.D., R. Burckhart, and G. Zoll, "Mixing and Mass Transfer in Tall Bubble Columns", *Chemical Engineering Science*, 29: 2177-2188 (1974).

19. Deckwer, W.D., K. Nguyentien, B.G. Kelkar, and Y.T. Shah, "Applicability of Axial-Dispersion Model to Analyze Mass-Transfer Measurements in Bubble-Columns", *AIChE Journal*, 29(6): 915-922 (1983).

20. Deckwer, W.D., and A. Schumpe, "Improved Tools for Bubble Column Reactor Design and Scale-Up", *Chemical Engineering Science*, 48(5): 889-911 (1993).

21. Djebbar, Y., and R.M. Narbaitz, "Neural Network Prediction of Air Stripping K(L)A", *Journal of Environmental Engineering-ASCE*, 128(5): 451-460 (2002).

22. Farooq, S., and M. Ahmed, "Modeling of an Ozone Waste-Water Systems Kinetics", *Water Research*, 23(7): 809-815 (1989).

23. Fonseca, A.P., J.V. Oliveira, and E.L. Lima, "Neural Networks for Predicting Mass Transfer Parameters in Supercritical Extraction", *Brazilian Journal of Chemical Engineering*, 17(4-7): 517-524 (2000).

24. Gamal El-Din, M., and D.W. Smith, "Maximizing the Enhanced Ozone Oxidation of Kraft Pulp Mill Effluents in an Impinging-Jet Bubble Column", *Ozone-Science & Engineering*, 23(6): 479-493 (2001).

25. Gamal El-Din, M., and D.W. Smith, "Mass Transfer Analysis in Ozone Bubble Columns", *Journal of Environmental Engineering and Science*, 2(1): 63-76 (2003a).

26. Gamal El-Din, M., and D.W. Smith, "Measurements of the Size, Rise Velocity, and Specific Interfacial Area of Bubbles in an Impinging-Jet Bubble Column", *Journal of Environmental Engineering and Science*, 2(2): 127-138 (2003b).

27. Garcia-Ochoa, F., and E.G. Castro, "Estimation of Oxygen Mass Transfer Coefficient in Stirred Tank Reactors Using Artificial Neural Networks", *Enzyme and Microbial Technology*, 28(6): 560-569 (2001).

28. Haykin, S., *Neural Networks a Comprehensive Foundation*. (New Jersey: Prentice Hall, Inc., 1999).

29. Herbrechtsmeier, P., H. Schafer, and R. Steiner, "Ozone and Oxygen Absorption in Downflow Bubble-Columns", *Ozone-Science & Engineering*, 9(3): 217-232 (1987).

30. Hikita, H., S. Asai, K. Tanigawa, K. Segawa, and M. Kitao, "The Volumetric Liquid-Phase Mass-Transfer Coefficient in Bubble-Columns", *Chemical*

Engineering Journal and the Biochemical Engineering Journal, 22(1): 61-69 (1981).

31. Hornik, K., M. Stinchcombe, and H. White, "Multilayer Feedforward Networks Are Universal Approximators", *Neural Networks*, 2(5): 359-366 (1989).

32. Huang, W.H., C.Y. Chang, C.Y. Chiu, S.J. Lee, Y.H. Yu, H.T. Liou, Y. Ku, and J.N. Chen, "A Refined Model for Ozone Mass Transfer in a Bubble Column", *Journal of Environmental Science and Health Part a-Toxic/Hazardous Substances & Environmental Engineering*, 33(3): 441-460 (1998).

33. Huber, M.M., A. Gobel, A. Joss, N. Hermann, D. Loffler, C.S. McArdell, A. Ried, H. Siegrist, T.A. Ternes, and U. von Gunten, "Oxidation of Pharmaceuticals During Ozonation of Municipal Wastewater Effluents: A Pilot Study", *Environmental Science & Technology*, 39(11): 4290-4299 (2005).

34. Hughmark, G.A., "Holdup and Mass Transfer in Bubble Columns", *Industrial & Engineering Chemistry Process Design and Development*, 6(2): 218-& (1967).

35. Huynh, L.X., C.L. Briens, J.F. Large, A. Catros, J.R. Bernard, and M.A. Bergougnou, "Hydrodynamics and Mass-Transfer in an Upward Venturi Bubble Column Combination", *Canadian Journal of Chemical Engineering*, 69(3): 711-722 (1991).

36. Iliuta, I., F. Larachi, B.P.A. Grandjean, and G. Wild, "Gas-Liquid Interfacial Mass Transfer in Trickle-Bed Reactors: State-of-the-Art Correlations", *Chemical Engineering Science*, 54(23): 5633-5645 (1999).

37. Jamialahmadi, M., M.R. Zehtaban, H. Muller-Steinhagen, A. Sarrafi, and J.M. Smith, "Study of Bubble Formation under Constant Flow Conditions", *Chemical Engineering Research & Design*, 79(A5): 523-532 (2001).

38. Kallas, J., R. Munter, A. Viiroja, and M. Korvits, "Simulation and Parameter Estimation of Ozonation Column Models", *ACh-Models in Chemistry*, 132(5): 807-829 (1995).

39. Kantarci, N., F. Borak, and K.O. Ulgen, "Bubble Column Reactors", *Process Biochemistry*, 40(7): 2263-2283 (2005).

40. Kawase, Y., S. Umeno, and T. Kumagai, "The Prediction of Gas Hold-up in Bubble Column Reactors - Newtonian and Non-Newtonian Fluids", *Chemical Engineering Journal and the Biochemical Engineering Journal*, 50(1): 1-7 (1992).

41. Koide, K., "Design Parameters of Bubble Column Reactors with and without Solid Suspensions", *Journal of Chemical Engineering of Japan*, 29(5): 745-759 (1996).

42. Kulkarni, A., and Y. Shah, "Gas Phase Dispersion in a Downflow Bubble Column", *Chemical Engineering Communications*, 28: 311-326 (1984).

43. Kulkarni, A., Y. Shah, and A. Schumpe, "Hydrodynamics and Mass Transfer in Downflow Bubble Column", *Chemical Engineering Communications* 24: 307-337 (1983).

44. Kumar, S.B., D. Moslemian, and M.P. Dudukovic, "Gas-Holdup Measurements in Bubble Columns Using Computed Tomography", *AIChE Journal*, 43(6): 1414-1425 (1997).

45. Kundu, A., E. Dumont, A.M. Duquenne, and H. Delmas, "Mass Transfer Characteristics in Gas-Liquid-Liquid System", *Canadian Journal of Chemical Engineering*, 81(3-4): 640-646 (2003).

46. Lau, R., W. Peng, L.G. Velazquez-Vargas, G.Q. Yang, and L.S. Fan, "Gas-Liquid Mass Transfer in High-Pressure Bubble Columns", *Industrial & Engineering Chemistry Research*, 43(5): 1302-1311 (2004).

47. Lemoine, R., B. Fillion, A. Behkish, A.E. Smith, and B.I. Morsi, "Prediction of the Gas-Liquid Volumetric Mass Transfer Coefficients in Surface-Aeration and Gas-Inducing Reactors Using Neural Networks", *Chemical Engineering and Processing*, 42(8-9): 621-643 (2003).

48. Lesauze, N., A. Laplanche, N. Martin, and G. Martin, "Modeling of Ozone Transfer in a Bubble Column", *Water Research*, 27(6): 1071-1083 (1993).

49. Mitani, M.M., A.A. Keller, O.C. Sandall, and R.G. Rinker, "Mass Transfer of Ozone Using a Microporous Diffuser Reactor System", *Ozone-Science & Engineering*, 27(1): 45-51 (2005).

50. Nakao, K., H. Takeuchi, H. Kataoka, H. Kaji, T. Otake, and T. Miyauchi, "Mass-Transfer Characteristics of Bubble-Columns in Recirculation Flow Regime", *Industrial & Engineering Chemistry Process Design and Development*, 22(4): 577-582 (1983).

51. Patel, S.A., J.G. Daly, and D.B. Bukur, "Holdup and Interfacial Area Measurements Using Dynamic Gas Disengagement", *Aiche Journal*, 35(6): 931-942 (1989).

52. Poulsen, B.R., and J.J.L. Iversen, "Characterization of Gas Transfer and Mixing in a Bubble Column Equipped with a Rubber Membrane Diffuser", *Biotechnology and Bioengineering*, 58(6): 633-641 (1998).

53. Roustan, M., R.Y. Wang, and D. Wolbert, "Modeling Hydrodynamics and Mass Transfer Parameters in a Continuous Ozone Bubble Column", *Ozone-Science & Engineering*, 18(2): 99-115 (1996).

54. Shah, Y.T., B.G. Kelkar, S.P. Godbole, and W.D. Deckwer, "Design Parameters Estimations for Bubble Column Reactors", *AIChE Journal*, 28(3): 353-379 (1982).

55. Shaikh, A., and M. Al-Dahhan, "Development of an Artificial Neural Network Correlation for Prediction of Overall Gas Holdup in Bubble Column Reactors", *Chemical Engineering and Processing*, 42(8-9): 599-610 (2003).

56. Sherwood, T.K., L.P. Robert, and R.W. Charles, *Mass Transfer* (New York: McGraw-Hill, 1975).

57. Supardan, M.D., Y. Masuda, A. Maezawa, and S. Uchida, "Local Gas Holdup and Mass Transfer in a Bubble Column Using an Ultrasonic Technique and a Neural Network", *Journal of Chemical Engineering of Japan*, 37(8): 927-932 (2004).

58. Unno, H., and I. Inoue, "Size Reduction of Bubbles by Orifice Mixer", *Chemical Engineering Science*, 35: 1571-1579 (1980).

59. Utomo, M.B., T. Sakai, S. Uchida, and A. Maezawa, "Simultaneous Measurement of Mean Bubble Diameter and Local Gas Holdup Using Ultrasonic Method with Neural Network", *Chemical Engineering & Technology*, 24(5): 493-500 (2001).

60. Varley, J., "Submerged Gas-Liquid Jets: Bubble Size Prediction", *Chemical Engineering Science*, 50(5): 901-905 (1995).

61. Vasconcelos, J.M.T., J.M.L. Rodrigues, S.C.P. Orvalho, S.S. Alves, R.L. Mendes, and A. Reis, "Effect of Contaminants on Mass Transfer Coefficients in Bubble Column and Airlift Contactors", *Chemical Engineering Science*, 58(8): 1431-1440 (2003).

62. Wang, K.B., and L.T. Fan, "Mass Transfer in Bubble Columns Packed with Motionless Mixers", *Chemical Engineering Science*, 33: 945-952 (1978).

63. Weisweiler, W., and S. Rosch, "Interfacial Area and Bubble-Size Distribution in Jet Reactors", *German Chemical Engineering*, 1: 212-218 (1978).

64. Winterton, R.H.S., "A Simple Method of Predicting Bubble-Size in Bubble-Columns", *Chemical Engineering and Processing*, 33(1): 1-5 (1994).

65. Wright, P.C., V. Meeyoo, and W.K. Soh, "A Study of Ozone Mass Transfer in a Cocurrent Downflow Jet Pump Contactor", *Ozone-Science & Engineering*, 20(1): 17-33 (1998).

66. Wu, Y.X., X.H. Luo, Q.M. Chen, D.H. Li, S.R. Li, M.H. Al-Dahhan, and M.P. Dudukovic, "Prediction of Gas Holdup in Bubble Columns Using Artificial Neural Network", *Chinese Journal of Chemical Engineering*, 11(2): 162-165 (2003).

67. Xu, F.C., and C.L. Liu, "Mass Balance Analysis of Ozone in a Conventional Bubble Column", *Ozone-Science & Engineering*, 12(3): 269-279 (1990).

68. Yamashita, F., Y. Mori, and S. Fujita, "Sizes and Size Distributions of Bubbles in a Bubble Column - Comparison between the 2 Point Electric Probe Method and the Photographic Method", *Journal of Chemical Engineering of Japan*, 12(1): 5-9 (1979).

69. Yang, H., B.S. Fang, and M. Reuss, "K(L)a Correlation Established on the Basis of a Neural Network Model", *Canadian Journal of Chemical Engineering*, 77(5): 838-843 (1999).

70. Zhou, H.D., and D.W. Smith, "Ozone Mass Transfer in Water and Wastewater Treatment: Experimental Observations Using a 2d Laser Particle Dynamics Analyzer", *Water Research*, 34(3): 909-921 (2000).

CHAPTER 3

IMPINGING-JET OZONE BUBBLE COLUMN MODELLING: HYDRODYNAMICS, GAS HOLD-UP, BUBBLE CHARACTERISTICS, AND OZONE MASS TRANSFER*

3.1 INTRODUCTION

The process of ozonation is usually conducted in bubble column contactors operating under co-current or counter-current upflow or downflow conditions. Several studies have been conducted to evaluate and compare the mass transfer efficiency under such conditions (Briens et al., 1992; Huynh et al., 1991; Kulkarni et al., 1983; Otake et al., 1981; Roustan et al., 1987; Roustan et al., 1992b; Sotiriadis et al., 2005; Wright et al., 1998). Generally, the ozonation process is composed of four activities carried out simultaneously: ozone auto-decomposition reactions, competitive reactions of other water or wastewater matrix constituents with ozone, the mass transfer of ozone from the gas phase into the liquid phase, and the convection and backmixing of the liquid and gas phases (Zhou et al., 1994). Optimizing the ozone treatment process depends the reactor's ability to efficiently transfer ozone gas into the liquid being treated (Finch et al., 2001; Gamal El-Din and Smith, 2002). Reliable models can be very useful in optimizing the performance of ozone contactors as they can provide high flexibility in evaluating the ozone process under different operational and geometrical configurations.

---

* A version of this chapter has been accepted for publication. Baawain, M.B., M. Gamal El-Din, K. Clarke, and D.W. Smith, *Ozone Sci. & Eng.* (May 2007)

3.1.1 Modelling Ozone Contactors

Accurate modelling of contactor hydrodynamics should take into account the geometry of the reactor, the retention time of the liquid phase, the operational conditions of the reactor, and the mixing characteristics of the gas and liquid phases, with the latter being the most difficult parameter to model, as the actual flow pattern of the liquid phase typically deviates from the assumed ideal flow regimes (Bellamy, 1995; Deckwer et al., 1983). Previous investigators have determined that the intensity of the liquid-phase backmixing occurring at the inlet of a reactor is quite high and must, therefore, be modelled appropriately (Deckwer et al., 1983; Salazar et al., 1993). In general, bubble column reactors are modelled based on variations of the axial dispersion model (ADM) and the cell-based models.

The basis of the ADM assumes that the flow inside the reactor resembles an ideal plug flow with some degree of backmixing superimposed on top (Zhou et al., 1994). The ADM assumes that the dispersion is represented by diffusion laws, the concentration profile is uniform in the radial direction, and the axial dispersion is uniform throughout the water column (Marinas et al., 1993). Kawagoe et al. (1989) and Shetty et al. (1992) applied the ADM model to describe the flow of gas bubbles through their bubble column reactors. Other researchers have successfully applied the model in characterizing the flow of liquids in bubble column reactors (Deckwer et al., 1974; Deckwer et al., 1983; Gamal El-Din and Smith, 2001a; Houzelot et al., 1985; Kantak et al., 1994; Marinas et al., 1993).

Cell-based models generally assume four types of liquid flow zones: the zone of plug flow, the zone of axial dispersed flow, the zone of perfect mixing, and the dead zones (Kastánek et al., 1993). These zones of liquid flow are interconnected by the main flow of the liquid, the cross-flow stream, the circulation-flow stream (backmixing and exchange flows), or a by-pass flow stream (Kastánek et al., 1993). Several investigators have studied the backmixing in the liquid phase to understand and explain the mixing behaviour of bubble columns (Deckwer et al., 1973; Hikita and Kikukawa, 1974; Houzelot et al., 1985; Lesauze et al., 1992; Ohki and Inoue, 1970). Moreover, several researchers have studied the gas phase backmixing in bubble columns (Deckwer, 1976; Kawagoe et al., 1989; Reith et al., 1968; Shetty et al., 1992; Wachi and Nojima, 1990; Zahradnik and Fialova, 1996).

3.1.2 Bubble Columns Ozone Contactors

In bubble columns with diameters larger than 140 mm, the gas-phase dispersion coefficient is usually high due to the occurrence of large-scale eddies. In bubble columns with diameters less than 140 mm and large aspect ratios (length/diameter ratio (L/D) >> 1), the gas-phase dispersion coefficient is usually less than the liquid-phase dispersion coefficient by an order of magnitude (Reith et al., 1968). Based on the theoretical calculations of Deckwer (1976), the gas-phase backmixing can be neglected in bubble columns with diameters less than 500 mm. Therefore, the gas-phase flow can be considered in the plug flow regime.

The effect of liquid-phase backmixing can be studied by using the dimensionless back flow ratio (r), which can be represented by the following equation:

$$r = \frac{N_{BFCM}}{Pe_L} - 0.5 = \frac{D_L \cdot \varepsilon_L \cdot N_{BFCM}}{u_L \cdot L} - 0.5 \qquad [3.1]$$

where N_{BFCM} = number of cells in series, Pe_L = dimensionless liquid-phase Peclet number, D_L = liquid-phase axial dispersion coefficient (m^2/s), ε_L = dimensionless liquid-phase hold-up, u_L = superficial liquid velocity (m/s), and L = length (or height) of the reactor (m). Researchers have applied cell-based models in an attempt to describe the hydrodynamics of bubble column reactors (Gamal El-Din and Smith, 2001b; Roustan et al., 1996; Zahradnik and Fialova, 1996; Zhou and Smith, 1995).

Depending on the degree of mixing, the gas properties in a gas-liquid reactor will be affected. For example, in a co-current bubble column reactor, an increase in the liquid-phase turbulence leads to higher shear stresses affecting the gas bubbles' sizes (Gamal El-Din and Smith, 2003a). Consequently, the large gas bubbles are sheared into smaller bubbles. The rise velocity for the small bubble sizes is slower in an upflow reactor and faster (less drag) in a downflow reactor. In turn, the smaller bubbles display a smaller rise velocity in the upflow bubble column and are thus retained for longer periods of time than large bubbles, resulting in a larger amount of gas being retained in the reactor. The ratio of the volumetric fraction of gas to the total volume of the reactor, the gas hold-up (ε_G), is a parameter essential to achieve an efficient reactor design. This parameter reflects the amount of gas available for transfer into the liquid phase and, hence, available for the treatment of water and wastewater (Kastánek et al., 1993).

The diameter of the gas bubble is also affected by the bubbles' coalescence and breakup rates, which are influenced by the superficial liquid and gas velocities and the properties of the liquid (Akita and Yoshida, 1974). Smaller bubbles are more desirable, as they increase the surface area available for the transfer of ozone gas into the liquid phase. By knowing the bubble diameter and the gas hold-up, an important parameter recognized as the specific bubble interfacial area (a) can be determined based on the following relationship:

$$a = \frac{6 \cdot \varepsilon_G}{d_{S.}} \qquad [3.2]$$

where a = mean specific interfacial area (m^2/m^3), ε_G = dimensionless gas hold-up, and d_S = Sauter mean bubble diameter (m). An increase in the interfacial area can result in an increase in the overall mass transfer coefficient (k_La). The absorption of gas via diffusion at the gas-liquid interface is governed by diffusion through the liquid film, as the diffusivity of ozone gas in the liquid phase is much smaller than that in the gas phase. The surface renewal theory proposed by Dankwerts (1970) indicates that an increase in turbulence can cause an increase in the rate of mass transfer. This increase occurs because, with increased turbulence, the elements of liquid at the interface are replaced more frequently, allowing for those fluid elements not saturated with ozone gas to absorb more gas at an increased rate. This increase in turbulence also causes the liquid film thickness to decrease, allowing gas to diffuse through the film at an increased rate (Danckwerts, 1970; Gamal El-Din and Smith, 2003b).

Some of the factors influencing the mass transfer of ozone gas into the liquid phase in bubble columns include the ability of ozone to diffuse into the liquid solution, the rate of the auto-decomposition of ozone (influenced by liquid temperature and pH), and the occurrence of any chemical reactions between the ozone and other dissolved and/or undissolved constituents in the water or wastewater matrix (Sotelo et al., 1989). In the case of deep ozone contactors (e.g., deep U-tubes), the static water pressure can significantly impact the mass transfer of ozone (Roustan et al., 1992a). The type of gas distributor also plays a significant role. In trying to improve the performance of reactors, researchers have attempted to maximize the rate of gas absorption by changing the type of distributor used. Huynh et al. (1991) found an increased rate of mass transfer when using a venturi injector compared with that obtained from a porous plate distributor. Zhou and Smith (2000) found that venturi injectors produced significantly smaller bubbles than those generated when the bubble column was fitted with glass discs or a crystalline aluminia diffusing stone. These researchers speculated that these smaller bubble sizes would subsequently increase the rate of mass transfer.

Gas injectors are gaining popularity as effective means of dissolving ozone gas into liquids because of the high mixing intensity they generate (Zhou and Smith, 2000). Gamal El-Din and Smith (2001a; 2003a) also used venturi injectors in their bubble column and noticed a marked increase in the mass transfer of the system when compared with that of other bubble column designs.

The current study investigates the mass transfer of ozone in an impinging-jet bubble column. A transient back flow cell model (TBFCM) was used to model the hydrodynamics of the bubble column while a steady-state back flow cell model (BFCM) was developed to model the dissolved ozone concentrations. The gas hold up was also characterized in this contactor. Accordingly, the overall mass transfer coefficient was modelled. A photographic technique was employed to study the bubbles' characteristics in terms of their shapes and sizes inside the bubble column in order to determine the specific interfacial area and, consequently, the local mass transfer coefficient in the contactor.

3.2 TRANSIENT BACK FLOW CELL MODEL

The liquid-phase hydrodynamics of bubble column reactors are difficult to characterize; however, a model has been developed that is able to accurately represent the hydrodynamic behaviour of the flow of the liquid phase inside an impinging-jet bubble column reactor. One primary assumption is that the liquid-phase flow follows the axially dispersed flow regime, which is characterized by a back flow ratio (r) and an exchange flow ratio (r'), with the gas phase flowing in the plug flow regime.

In essence, the transient back flow cell model (TBFCM) consists of two series of completely mixed cells: one series representing the gas phase and the other representing the liquid phase. With respect to the cells describing the liquid phase, there exists a main flow stream (exchange flow) of the liquid and a backmixed flow (i.e., back flow) of the liquid. With respect to the gas-phase flow, due to the buoyancy of gas bubbles, the gas-phase flow is assumed to follow the plug flow regime. Zhou (1995) developed a version of the TBFCM that was applied to fine-diffuser bubble columns. Gamal El-Din and Smith (2001b) later modified and expanded this model to account for variable backmixing, cross-sectional area, and cell volume along the bubble columns and/or ozone contactors. A representation of the basis of the TBFCM for a bubble column operating in a co-current flow mode is shown in Figure 3.1.

The TBFCM's ability to predict a variable backmixing parameter or back flow ratio (*r*) along the height of the reactor is unique. This feature allows an accurate representation of the mixing occurring along the height of the reactor, as it is known that there is a larger degree of mixing occurring at the inlet of the reactor than at its outlet. Therefore, it is prudent, when modelling a bubble column reactor, to include a variable degree of mixing along its height, especially for tall or long bubble columns.

Another unique feature of the transient back flow cell model is its ability to accommodate a varying cell volume along the height of the reactor. This feature allows for easy use of the model when dealing with ozone reactors (or contactors) with multiple chambers of variable dimensions. The governing assumptions and details regarding the development of the TBFCM and the equations used to describe it can be found in Gamal El-Din and Smith (2001b).

3.3 STEADY STATE BACK FLOW CELL MODEL

Similar to the TBFCM, the steady-state back flow cell model (BFCM) can predict the hydrodynamics inside a reactor with a variable cell volume and/or with variable mixing conditions along the height of the reactor. Furthermore, the steady-state BFCM can account for a variable cross-sectional area, variable pressure along the height of the bubble column, and a variable rate of mass transfer. The assumptions governing the steady-state BFCM and the details of the model's development can be found elsewhere

(Gamal El-Din and Smith, 2001d). Zhou (1995) developed a version of the steady-state BFCM that was applied to fine-diffuser bubble columns. This model was later modified and expanded by Gamal El-Din and Smith (2001d) to account for variable backmixing, the cross-sectional area, and the cell volume along the bubble columns and/or ozone contactors. The steady-state BFCM developed by Gamal El-Din and Smith (2001d) has been modified to simulate and model bubble columns that have a variable cross-sectional area and mixing coefficient.

Applying mass balance equations to the co-current operation of the impinging-jet bubble column, shown in Figure 3.2 and represented by the schematic shown in Figure 3.1, will lead to sets of equations describing the dissolved ozone, the gaseous ozone, and the total gas within each cell. These equations differ slightly from those published in Gamal El-Din and Smith (2001d). The following equations account for a variable mass transfer coefficient along the height of the reactor, as described by the varying liquid-phase Stanton number (St_L), which changes the assumption of a constant rate of mass transfer to that of a variable rate of mass transfer. Also, the following equations take into account the variable cell volume (as reflected in the parameter f_j), the variable cross-sectional area (as reflected in the parameter $f_{A,j}$), and the variable pressure (as reflected in the parameter $f_{Z,j}$) occurring along the height of the bubble column.

Dissolved Ozone

For cell: $j = 1$

$$X_0 - \left(1 + r_1' + f_j \cdot f_{A.j} \cdot D_{A.j} + f_j \cdot f_{A.j} \cdot St_{L.j}\right) \cdot X_1 + r_1 \cdot X_2 + \\ f_j \cdot f_{A.j} \cdot St_{L.j} \cdot \left(1 + \alpha \cdot f_{z.j} \cdot 0.5\right) \cdot Y_1 = 0 \qquad [3.3]$$

For cells: $2 \le j \le N_{BFCM}-1$

$$\left(1 + r_{j-1}\right) \cdot X_{j-1} - \left(1 + r_j' + r_j + f_j \cdot f_{A.j} \cdot D_{A.j} + f_j \cdot f_{A.j} \cdot St_{L.j}\right) \cdot X_j + \\ r_{j+1}' \cdot X_{j+1} + f_j \cdot f_{A.j} \cdot St_{L.j} \cdot \left(1 + \alpha \cdot f_{z.j} \cdot (j - 0.5)\right) \cdot Y_j = 0 \qquad [3.4]$$

For cell: $j = N_{BFCM}$

$$\left(1 + r_{N_{BFCM}}\right) \cdot X_{N_{BFCM}} - \left(1 + r_{N_{BFCM}}' + f_j \cdot f_{A.j} \cdot D_{A.N_{BFCM}} + f_j \cdot f_{A.j} \cdot St_{L.N_{BFCM}}\right) \cdot X_{N_{BFCM}} \\ + f_j \cdot f_{A.j} \cdot St_{L.N_{BFCM}} \cdot \left(1 + \alpha \cdot f_{z.j} \cdot \left(N_{BFCM} - 0.5\right)\right) \cdot Y_{N_{BFCM}} = 0 \qquad [3.5]$$

Gaseous Ozone

For cells: $1 \le j \le N_{BFCM}$

$$q_{G.j-1} \cdot Y_{j-1} \cdot \left(1 + \alpha \cdot f_{z.j} \cdot (j - 1.5)\right) - q_{G.j} \cdot Y_j \left(1 + \alpha \cdot f_{z,j} (j - 0.5)\right) \\ - f_j \cdot f_{A.j} \cdot St_{G.j} \cdot \left(\left(1 + \alpha \cdot f_{z.j} \cdot (j - 0.5)\right) \cdot Y_j - X_j\right) = 0 \qquad [3.6]$$

Total Gas

For cells: $1 \le j \le N_{BFCM}$

$$q_{G.j-1} \cdot \left(1 + \alpha \cdot f_{z.j} \cdot (j - 1.5)\right) - q_{G.j} \cdot \left(1 + \alpha \cdot f_{z.j} \cdot (j - 0.5)\right) \\ - f_j \cdot f_{A.j} \cdot St_{G.j} \cdot y_0 \cdot \left(\left(1 + \alpha \cdot f_{z.j} \cdot (j - 0.5)\right) \cdot Y_j - X_j\right) = 0 \qquad [3.7]$$

The parameters in Equations 3.3 to 3.7 are shown in Table 3.1.

3.4 EXPERIMENTAL PROCEDURES

3.4.1 Operation of the Impinging-Jet Ozone Bubble Column

Pilot-scale tracer tests were conducted in the impinging-jet bubble column reactor operated in a co-current flow regime. A schematic diagram of the experimental set-up is shown in Figure 3.2. The bubble column was made of PVC and had an inside diameter of 100 mm and a total height of 1,520 mm. The water level inside the column was maintained at 1,315 mm with the use of an overflow weir at the top of the bubble column. A ring tube with a hole of 20 mm in diameter and facing downwards was also placed at the top of the column to drain and/or recycle the water exiting the bubble column. Its base was elliptical in shape, and the sidewalls of its bottom had a conical shape. Although this geometry is not used in full-scale contactor designs due to manufacturing difficulties, it was selected to reduce the effects of the backward fluid jet created as a result of the jet impingement, and to minimize any possible short-circuiting that might occur (Gamal El-Din and Smith, 2001c; Gamal El-Din and Smith, 2003b).

Mazzei® venturi injectors, model type 384, were used as gas injectors. The venturi injectors were placed 25 mm above the bottom of the bubble column, and at an intersecting angle of 125°. The distance between the centres of the nozzles was 60 mm. More details regarding the experimental set-up of the impinging-jet bubble column are found in Gamal El-Din and Smith (2001c; 2003b). It should be mentioned that the details of the studied bubble column are provided for the reproducibility of the data and are not intended for scale-up issues, as further investigations are needed to generalize the findings to full-scale contactors.

The impinging-jet bubble column was operated under the operating conditions shown in Table 3.2 in order to study the hydrodynamics, the gas hold-up, bubbles' characteristics, and ozone mass transfer in the column. The superficial liquid velocity was varied from 0.008 to 0.028 m/s, and the superficial gas velocity was varied from 0.002 to 0.014 m/s.

3.4.2 Hydrodynamic and Gas Hold-up Experiments

Tracer tests were conducted on the impinging-jet bubble column in an attempt to characterize the backmixing of the non-ideal flow conditions. Pulse-input tracer tests were applied by using an inert tracer of potassium chloride (KCl) solution of known concentration (70 g/L). The test liquid was clean de-ionized water. The conductivity was monitored every second at four locations along the height of the bubble column, until the total tracer mass was recovered. The resulting theoretical hydraulic residence time (τ) ranged between 48 and 190 s (Gamal El-Din and Smith, 2003a).

The gas hold-up measurements were carried simultaneously with the concentration measurements during the tracer study by determining the pressure every 10 seconds at the static head levels of 348 mm, 830 mm, and 1,297 mm from the bottom of the bubble column reactor. Initially measured in volts, the static head was then used to calculate the gas hold-up.

3.4.3 Bubble Diameter Measurements

A digital photographic technique was employed to determine the shapes and sizes of the bubbles produced in the impinging-jet bubble column. Experiments were carried out in the impinging-jet bubble column by using clean de-ionized water for the liquid phase and extra-dry air for the gas phase. To minimize the distortion caused by the curved surface of the bubble column, a clear acrylic jacket (150 mm x 150 mm) with flat surfaces was placed around the bubble column. Clean de-ionized water was placed in the gap between the bubble column and the square jacket. The photographic images were taken around the middle height of the column, as done by Roustan et al. (1996), to resemble the average bubble sizes under different operating conditions. For purposes of scaling, a measuring tape displaying a known scale was placed in the vicinity where the photographic images were taken. Bubble sizes were measured by selecting several sharply focused bubbles, the shapes and dimensions of which could be determined. The size measurements of the bubbles were corrected by using the proper scale factor.

3.4.4 Ozone Mass Transfer Experiments

The impinging-jet bubble column was operated in the co-current flow mode, with the venturi injectors operating under injection (positive pressure) and ejection (negative pressure) modes. The bubble column was allowed to operate for approximately eight times the reactor's theoretical hydraulic retention time, to ensure that the column reached the steady-state condition. Measurement of the constant off-gas concentration verified that the bubble column had reached this condition. The liquid's temperature ranged from

19.5 to 24.5 °C (Gamal El-Din and Smith, 2003a). Water samples were withdrawn from the five bell-shaped sampling taps (used to avoid bubble entrainment in the sample tube) located along the height of the column. The samples were withdrawn directly into volumetric flasks. The flow of the liquid was such as to minimize any loss of ozone. The concentration of ozone was measured by using the Indigo method (Gamal El-Din and Smith, 2003a).

3.5 EXPERIMENTAL DATA ANALYSIS METHODS

3.5.1 Liquid-Phase Backmixing

Once it had been determined that the tracer concentration profiles could be most accurately predicted by using eight cells in the TBFCM (as described later in the paper), the predicted concentrations were compared with those obtained experimentally. For each of the conductivity probes, the sum of squares of the residuals (*SSR*) between the model-predicted and the experimental RTDs was determined. The sum of the SSR for all the four probes (SSR_{total}) was minimized by changing the back flow and exchange flow ratios (r and r', respectively) between every two adjacent cells. This minimization technique was employed in two separate situations: (1) in the presence of two mixing zones (r_1 and r_2) and (2) in the presence of one mixing zone ($r_1 = r_2 = r$).

Within the impinging-jet bubble column, two zones of mixing can be distinguished. The first zone is representative of the intense mixing caused in the bottom zone of the column represented by the first cell of the model where the impinging jets are located, and is represented by the back flow ratio (r_1). The remainder of the column is represented by a second zone of mixing, displaying less intense mixing conditions along the height of the column represented by the back flow ratio (r_2). For the purpose of comparison, the presence of only one mixing zone ($r_1 = r_2 = r$) in the bubble column was also investigated. The most accurate and reliable method of characterizing the hydrodynamics inside the impinging-jet bubble column was determined. Linear regression analysis was applied to the back flow ratios, obtained through the TBFCM predictions, to determine a possible relationship that would correlate the back flow ratio(s) (r or r_1 and r_2) with the superficial gas velocity (u_G) and the superficial liquid velocity (u_L).

3.5.2 Gas Hold-up

Each day that a tracer study was carried out, the pressure sensors were calibrated. Experimental data from the three pressure sensors was taken every 10 seconds over a given period of time, and was immediately downloaded into a data logger. For each pressure sensor, the average reading was calculated and then used to determine the pressure along the height of the column. A linear regression analysis was used to produce a calibration curve for each of the pressure sensors, while at the same time producing an equation describing the actual hydrostatic pressure based on the pressure readings (recorded in volts) obtained from the sensors. The pressure data collected during the tracer experiments was standardized by using the equations determined through the calibration of the pressure sensors. The calibrated data was then used to determine the gas hold-up between the top and middle sensors, and the middle and bottom sensors. The gas hold-up between every two sensors was determined based on the following equation (Deckwer, 1992):

$$\varepsilon_G = 1 - \frac{\Delta P}{\Delta x} \qquad [3.8]$$

where ε_G = dimensionless gas hold-up, ΔP = change in measured pressure between the locations of two pressure sensors (m), and Δx = height difference between the locations of two pressure sensors (m). Under each set of operating conditions, the two gas hold-up values determined for the two regions (top to middle and middle to bottom) were averaged, resulting in one column-average gas hold-up. For the sake of comparison with different ozone bubble columns, a linear regression technique was used to produce a correlation equation representing ε_G of the impinging-jet bubble column as a function of u_G and u_L.

3.5.3 Gas Bubble Characteristics

The diameters of individual bubbles were measured by using the following two methods. The first method assumes that the bubble has the shape of an oblate sphere, and, thus, gives the diameter of the bubble as an average between two bubble's characteristic lengths, d_a and d_b:

$$\text{Approach 1: } d_{a1} = \frac{d_a + d_b}{2} \qquad [3.9]$$

where: d_a = longest length of the bubble (mm), and d_b = shortest length of the bubble (mm).

The second method assumes that the bubble is an ellipsoid, and thus the diameter of the bubble takes into account all measurable lengths. This three-dimensional technique is often simplified by assuming that shortest length of the bubble, d_b, and the width of the bubble, d_c, are of equal length, thus reducing this measurement to a two dimensional approach:

Approach 2: $d_{a2} = \sqrt[3]{d_a d_b d_c} = \sqrt[3]{d_a d_b^2}$ [3.10]

where d_c = width of the bubble (mm).

Following the determination of the diameters of each individual bubble by using the above two methods, each individual bubble's diameter was further used to determine the count mean bubble diameter, d_B, and the Sauter mean bubble diameter (d_S) as follows:

$$d_B = \frac{\sum_{i=1}^{i=N} d_i^3}{N} \qquad [3.11]$$

$$d_S = \frac{\sum_{i=1}^{i=N} d_i^3}{\sum_{i=1}^{i=N} d_i^2} \qquad [3.12]$$

where d_B = count mean bubble diameter (mm), d_S = Sauter mean bubble diameter (mm), N = number of the bubbles analyzed, d_i = i^{th} bubble diameter (mm) determined by either Equation 3.9 or 3.10, and i = bubble number ($1 \le i \le N$).

An area on the photograph, containing between 50 and 80 bubbles, was sectioned off for better measurements of the bubbles' diameters. Linear regression was employed to determine the relationship between the superficial liquid and gas velocities (u_G and u_L, respectively), and the diameters of the bubbles (d_B and d_S). These relationships were then combined with the gas hold-up (ε_G) regression model to determine the mean specific interfacial area (a) of the gas bubbles by using Equation 3.2.

3.5.4 Ozone Mass Transfer

The analysis of the dissolve ozone concentration data was carried out by using the equations describing the steady-state BFCM (Equations 3.3 to 3.7). These equations were solved simultaneously by using TKSOLVER® software. The solution for each run was reached within a maximum of 200 iterations. The relative error in these cases was set to be less than or equal to 1 x 10^{-6}. The output data was used in a simple spreadsheet, where single parameter minimization techniques were employed by changing the overall mass transfer coefficient k_La by comparing the modelled versus the dissolved ozone concentration profiles. This procedure was performed by minimizing the sum of the squared residuals (SSR) between the measured and the predicted dissolved ozone concentrations ($C_{O_3,measured}$ and $C_{O_3,predicted}$, respectively):

$$SSR = \sum \left(C_{O_3,measured} - C_{O_3,predicted} \right)^2 \qquad [3.13]$$

Next, a linear regression technique was employed to determine the relationship between k_La and u_G and u_L. The obtained relationship was used, in conjunction with knowledge of the gas hold-up and bubble properties of the impinging jet bubble column, to determine the local mass transfer coefficient, k_L.

3.6 RESULTS AND DISCUSSION

3.6.1 Liquid-Phase Backmixing

To accurately characterize the liquid-phase backmixing in the impinging-jet bubble column, it was necessary to determine the most appropriate number of cells (N_{BFCM}) required for the modelling of this reactor, based on the TBFCM. The determination of N_{BFCM} was accomplished by using residence time distribution (RTD) curves. For each of the conductivity probes, the sum of squares of the residuals (SSR) between the model-predicted and the experimental RTDs was determined. The sum of the SSR for all the four probes (SSR_{total}) was minimized by changing the back flow and exchange flow ratios (r' and r) between every two adjacent cells within the mixing zone(s), and as such, the number of cells producing the minimum SSR_{total} was deemed to be the most appropriate number of cells. Figure 3.4 shows a comparison of the TBFCM predictions of the RTDs for six, eight, and 10 cells in the TBFCM. From the minimum SSR_{total}, the most appropriate N_{BFCM} for the accurate representation of the impinging-jet bubble column reactor hydrodynamics was found to be that based on the presence of eight cells.

To determine the most appropriate approach for characterizing the liquid-phase hydrodynamics of the impinging-jet bubble column, two methods were investigated. The first one assumed a single mixing zone with a constant backmixing ratio (r) along the bubble column's height. The second approach assumed the presence of two mixing zones (r_1 and r_2). The TBFCM was tested for both cases, as shown in Figure 3.5, which reveals that (1) little difference exists in the modelling of this reactor when either two mixing zones or one mixing zone are present, and (2) a slight phase shift exists between the two RTDs predicted by using the two approaches. Furthermore, the use of the two-mixing-zone approach predicted the onset of the tracer peak compared to the one-mixing-zone approach (which showed an early peak). This result demonstrates the validity of using multi mixing zones in bubble columns modelling. The overestimating of the peak's magnitude by both approaches can be related to a possible fractional loss of the tracer during the injection process in the experimental runs. However, as the two approaches differed slightly for this bubble column (due to its short height, i.e., less effect of the static water pressure), and for the sake of simplicity, the reactor was modelled according to the presence of an average degree of backmixing (i.e., one mixing zone) occurring along the height of the bubble column reactor. The dependence of the column-average backmixing ratio (r) on the superficial gas and liquid velocities was quantified as

$$Log(r+0.5) = -0.88 + 0.08 \cdot Log(u_G) - 0.97 \cdot Log(u_L) \qquad [3.14]$$

where r = dimensionless backflow ratio, u_G = superficial gas velocity ($m.s^{-1}$), and u_L = superficial liquid velocity ($m.s^{-1}$). The coefficient of multiple determination (R^2) of Equation 3.14 is 0.91. The developed model's (Equation 3.14) accuracy is confirmed by Figure 3.6, which shows that the majority of the data appear between the upper and lower 95% confidence intervals (Upper CI and Lower CI). Equation 3.14 indicates that an increase in the superficial gas velocity (u_G) combined with a decrease in the superficial liquid velocity (u_L) will result in increasing the degree of backmixing. Similar observations have been noted in other research studies conducted on different bubble columns with different bubble diffusers (Marinas et al., 1993; Wachi et al., 1987; Zhou, 1995).

3.6.2 Gas Hold-up

Regression analysis was carried out, and a relationship between the gas hold-up and the superficial gas and liquid velocities was determined. This equation, as a representation of the column-average gas hold-up (ε_G) along the reactor height, is as follows:

$$\varepsilon_G = 4.67 \cdot u_G^{1.109} \cdot u_L^{-0.046} \qquad [3.15]$$

The coefficient of multiple determination (R^2) of Equation 3.15 is 0.92. Equation 3.15 depicts a pronounced relationship with the superficial gas velocity (u_G) in the bubble column reactor, as previously noted by other investigators (Deckwer, 1992; Gamal El-Din and Smith, 2003b; Kastánek et al., 1993; Roustan et al., 1996; Zhou and Smith, 2000). Meanwhile, as u_L increases, higher shear stresses are induced in the liquid phase due to the increased turbulence intensity. As a result, large gas bubbles tend to shear off into small bubbles, which lead to smaller gas hold-up. The decrease in ε_G as u_L increases was observed by Akita and Yoshida (1973), who used a bubble column with a single hole gas sparger; Bin et al. (2001), who used a bubble column with porous gas distributors; and Jakubowski et al. (2003), who used a confined plunging liquid jet contactor. An indication of Equation 3.15's ability to accurately model the gas hold-up in the impinging-jet bubble column reactor is shown in Figure 3.7, where the regression-fitted gas hold-up is plotted against the experimentally-measured gas hold-up. 178 data points were used to carry out the regression analysis. The majority of them lie within the 95% confidence interval, indicating that the model is able to accurately predict the gas hold-up of the impinging-jet bubble column.

Figure 3.8 compares the gas hold-up predicted for the impinging-jet bubble column reactor, with the predictions for the other reactors investigated in previous studies. This figure shows that the impinging-jet bubble column reactor produced a gas hold-up comparable to that achieved with other bubble column designs. In all noted cases, the gas hold-up increased with an increase in the superficial gas velocity.

3.6.3 Gas Bubble's Properties

The majority of the bubbles were observed to have the shape of an oblate sphere, rather than having a purely spherical shape. Yamishita et al. (1979), who carried out experiments in a rectangular bubble column equipped with a porous plate, made similar observations. As previously discussed, two methods of determining the arithmetic mean of the bubble diameter were conducted, and a linear regression technique was applied to develop a power-law regression model representing the count mean bubble diameter, d_B, as a function of the superficial gas and liquid velocities for the two methods. Furthermore, the Sauter mean bubble diameter (d_S) was determined, and a linear regression technique was again employed to determine the relationship between the

Sauter mean bubble diameter and the superficial gas and liquid velocities. The regression correlation equations for both approaches and for d_B and d_S are as follows:

Count mean bubble diameter (d_B in mm):

Approach (1): $$d_B = 6.93 \cdot u_G^{0.223} \cdot u_L^{-0.034} \quad [3.16]$$

Approach (2): $$d_B = 7.72 \cdot u_G^{0.224} \cdot u_L^{-0.020} \quad [3.17]$$

Sauter mean bubble diameter (d_S in mm):

Approach (1): $$d_S = 7.78 \cdot u_G^{0.207} \cdot u_L^{-0.008} \quad [3.18]$$

Approach (2): $$d_S = 8.22 \cdot u_G^{0.207} \cdot u_L^{-0.007} \quad [3.19]$$

The coefficients of multiple determination (R^2) of Equations 3.16 to 3.19 are 0.90, 0.89, 0.89, and 0.89, respectively. Equations 3.16 to 3.19 predict an increase in the bubble diameter with an increase in the superficial gas velocity. Roustan et al. (1996) reported a similar observation. Meanwhile, the bubble diameter decreased with an increase in the superficial liquid velocity. This finding is most likely the result of a higher degree of turbulence shear stresses as u_L increased, resulting in the shearing off of the large bubbles into bubbles with smaller diameters. Gamal El-Din and Smith (2003b) made a similar observation.

For the count mean and the Sauter mean bubble diameters (d_B and d_S, respectively), the first approach yielded smaller values, thus implying that the gas bubbles' interfacial area available for the mass transfer of ozone from the gas phase into the liquid phase was larger. Evaluating the adequacy of the proposed models is prudent. Figure 3.9 plots the experimentally-measured Sauter mean bubble diameter against the regression-fitted Sauter mean bubble diameter. The data lie on either side of the 1:1 line, and the majority of the data lie within the 95% confidence interval, indicating a good fit.

From the determined Sauter mean bubble diameters, the specific interfacial area (*a*) of the bubbles was further calculated. The two approaches for determining the diameters will remain as individual approaches, and will be analyzed as such. Equation 3.15, for the gas hold-up, and Equations 3.18 and 3.19, for the Sauter mean bubble diameter (approaches 1 and 2, respectively), were substituted into Equation 3.2, and the resultant equations are as follows (*a* in m^{-1}):

Approach (1): $$a = 3.61 \times 10^{3} \cdot u_G^{0.902} \cdot u_L^{-0.038} \qquad [3.20]$$

Approach (2): $$a = 3.40 \times 10^{3} \cdot u_G^{0.901} \cdot u_L^{-0.039} \qquad [3.21]$$

As was the case with the diameters of the bubbles, the specific interfacial area is predicted to increase with an increase in the superficial gas velocity, and to decrease with an increase in the superficial liquid velocity. Kulkarni et al. (1983) and Gamal El-Din and Smith (2003b) have made a similar observation.

3.6.4 Ozone Mass Transfer

The steady-state BFCM, developed to predict the dissolved ozone concentration profiles along the contactor, incorporates in its equations the equations used to predict the backmixing coefficient (*r*) and the gas hold-up (ε_G) in the impinging-jet bubble column reactor. The specific ozone utilization rate (k_w) was also required for solving the steady-state BFCM. The value used was $k_w\big|_{20^\circ C} = 2.61\times10^{-4}\ \mathrm{s}^{-1}$, as suggested by Gamal El-Din and Smith (2001a). The developed system of equations was then set up within the TKSOLVER® software, and solved by using the iterative Newton-Raphson method.

The measured ozone concentration profiles allowed for the estimation of the overall mass transfer coefficient (k_La), which was then input into the mass balance equations as an initial value. Minimization techniques were employed to minimize the *SSR* between the predicted and measured dissolved ozone concentrations, by changing the overall mass transfer coefficient (k_La). Figure 3.10 shows a plot produced to depict the minimum *SSR* and the corresponding k_La value for the injection and ejection modes. The corresponding concentration profile plot is depicted in Figure 3.11, which clearly shows that the model was able to accurately predict the dissolved ozone concentration profiles along the impinging-jet bubble column. A more rapid increase in the dissolved ozone concentration occurred at the entrance of the bubble column, which is attributed to the higher degree of turbulence and higher shear rates, which ultimately resulted in smaller bubbles, and subsequently, a larger bubbles' interfacial area was available for the mass transfer of ozone gas into the liquid phase. The use of the column-averaged mass transfer coefficient to simulate the model's performance (in terms of predicting the dissolved ozone concentration profiles) was sufficient for simplicity's case, yet this method produced mass transfer coefficient values that are probably lower than the actual ones in the inlet zone of the bubble column and higher than the actual ones in the later stages of the column. The effect of the mixing induced by the impinging jets on enhancing the ozone mass transfer efficiency at the inlet zone was verified by Bale et al.

(2005) by using a small cell system (equivalent to the inlet zone of the bubble column). Deckwer et al. (1974), Alvarezcuenca and Nerenberg (1981), and Salazar et al. (1993) made similar observations in studies where the gas was introduced into the liquid phase through a type of jet stream.

Based on the collected minimum *SSR* data and the corresponding k_La values, a regression technique correlated k_La with u_G and u_L as follows:

$$k_L a = 55.58 \cdot u_G^{1.256} \cdot u_L^{0.080} \qquad [3.22]$$

where k_La is in s^{-1}. Equation 3.22 has R^2 of 0.86. For the studied range of volumetric gas to liquid flow ratios (Q_G/Q_L up to 0.6), as the superficial gas velocity increases, a resulting increase occurs in k_La. This increase can be related to the higher gas hold-up exerted by the increase in u_G and the increased mixing and subsequent increase in the local mass transfer coefficient (as shown below) and decrease in film thickness. Researchers utilizing injectors as distributors (Briens et al., 1992; Deckwer et al., 1974; Havelka et al., 2000; Zahradnik et al., 1985) made similar observations of the increase of k_La with u_G. Similarly, modifications to the distributors resulted in similar relationship between u_G and k_La in studies by Alvarezcuenca (1980), who used nozzle injectors; Bin et al. (2001), who used a porous distributor; Chen et al. (2002), who used a perforated plate; Jakubowski et al. (2003), who studied a confined plunging liquid jet contactor with a nozzle as an injector; Kulkarni et al. (1983), who employed a ring type distributor; and Roustan et al. (1996), who used a porous distributor. Moreover, k_La increases as u_L increases, although the effect of u_L is much smaller than that of u_G. Huynh et al. (1991) showed similar effects on k_La at high u_L. However, Equation 3.22 needs further verifications before extrapolating it to other volumetric gas to liquid flow ratios (e.g. $Q_G/Q_L > 1$). As Briens et al. (1992) and Wright et al. (1998) suggested, the increase in k_La may fall off significantly at increased Q_G/Q_L.

To display the adequacy of the proposed relationship (Equation 3.22), Figure 3.12 plots the regression-fitted k_La against the steady state BFCM fitted k_La. The data lie within close proximity to the 1:1 line, and the majority of the data points are within the 95% confidence interval. Figure 3.13 compares the k_La values predicted for the impinging-jet bubble column with those predicted for other bubble column designs. The impinging-jet bubble column reactor displays greater mass transfer capabilities, within comparable ranges of superficial gas velocities.

After k_La and a are known, the local liquid mass transfer coefficient, k_L can be determined. Based on the two approaches used to estimate a, two equations for k_L ($m.s^{-1}$) can be developed as follows:

Approach (1) $k_L = 0.0154 \cdot u_G^{0.354} \cdot u_L^{0.118}$ [3.23]

Approach (2) $k_L = 0.0164 \cdot u_G^{0.355} \cdot u_L^{0.119}$ [3.24]

Both approaches show that k_L is predicted to increase when u_G and u_L are increased, with the effect of u_G being more pronounced.

3.7 CONCLUSION

The TBFCM, which is easy to formulate and solve, can adequately describe the liquid-phase backmixing in the impinging-jet bubble column over a wide range of operating conditions. The TBFCM can account for variable backmixing coefficient (i.e., variable Pe_L or r) along the column height while predicting simultaneously the RTD curves at various locations. However, because the short column height results in a low effect of the static water pressure, a slight difference between the reactor modelling based on the presence of two mixing zones and the presence of one mixing zone was observed. Nevertheless, this approach can be very useful when modelling deep ozone bubble columns. The number of cells in-series, as one of the mixing parameters to be considered for the TBFCM simulations, has to be chosen carefully so that the TBFCM predictions of the hydrodynamic behaviour in the ozone contactors under various operating conditions are closer to the actual backmixing conditions.

Gas hold-up (ε_G) was measured and found to be dependent on the superficial gas and liquid velocities (u_G and u_L, respectively). The bubbles produced in the impinging-jet bubble column reactor were investigated by using a digital photographic technique. The determination of bubble diameters (count mean of the bubble diameter (d_B) and the Sauter mean bubble diameter (d_S)) was based on two approaches: the assumption that the bubble is an oblate sphere, and the assumption that the bubble is an ellipsoid. Both approaches showed that d_B and d_S are dependent mainly on u_G and increase as u_G increases. Consequently, the specific bubbles' interfacial area (a) was determined.

The steady-state BFCM was used to model ozone mass transfer in the impinging-jet bubble column. Under varied gas and liquid flow rates, the impinging-jet bubble column resulted in an increased ability to transfer ozone into the liquid phase compared to that of other contactor designs. The model showed the high dependency of k_La on u_G. The local liquid mass transfer coefficient, k_L, was then represented as $k_L = 0.0154 \cdot u_G^{0.354} \cdot u_L^{0.118}$ (oblate sphere bubbles assumption) and $k_L = 0.0164 \cdot u_G^{0.355} \cdot u_L^{0.119}$ (ellipsoid bubbles assumption). The two approaches depict that k_L increases with both u_G and u_L.

Table 3.1 Parameters pertaining to the steady-state BFCM.

Parameter	Equation	Parameter	Equation
X_j	$\frac{C_{L.j}}{C^{*}_{L.0}}$	$q_{G.j}$	$\frac{Q_{G.j}}{Q_{G.0}}$
$C^{*}_{L.j_{j}}$ (mg.L^{-1})	$\frac{P_j}{H} \cdot y_j$	$St_{G.j}$	$\frac{k_L a \cdot L}{N_{BFCM} \cdot u_{G.0}} \cdot \frac{R \cdot T}{H}$
r_j	$\frac{Q_{B.j}}{Q_L}$	$u_{G.0}$ (m.s^{-1})	$\frac{Q_G}{A_{BC}}$
r'_j	$\frac{Q'_{B.j}}{Q_L}$	f_j	$\frac{V_{C.j}}{V/N_{BFCM}}$
$D_{A.j}$	$\frac{k_w \cdot \varepsilon_L \cdot L}{N_{BFCM} \cdot u_L}$	$f_{A.j}$	$\frac{V_{COMB}}{L \cdot A_{COMB}}$
u_L (m.s^{-1})	$\frac{Q_L}{A_{BC}}$	V_{COMB} (m^3)	$V_1 + V_2$
$St_{L.j}$	$\frac{k_L a \cdot L}{N_{BFCM} \cdot u_L}$	$f_{z.j}$	$\frac{Z_{j.act}}{Z_{j.avg}}$
α	$\frac{-\rho \cdot g \cdot \varepsilon_L \cdot L}{N_{BFCM} \cdot P_0}$	$Z_{j.avg}$	$\frac{j - 0.5}{N_{BFCM}}$
Y_j	$\frac{y_j}{y_0}$		

Table 3.2 Operating conditions of the impinging-jet bubble column experiments.

					Approach 1		Approach 2		
Experiment No.	u_L (m.s^{-1})	u_G (m.s^{-1})	Measured ε_G	Measured $\log(r + 0.5)$	d_B (mm)	d_S (mm)	d_B (mm)	d_S (mm)	Measured $k_La_{(T=20)}$ (s^{-1})
1	7.7E-03	2.4E-03	7.5E-03	0.93	2.16	2.07	2.00	2.17	1.2E-02
2	7.7E-03	3.7E-03	1.1E-02	1.02	2.22	2.42	2.32	2.54	2.6E-02
3	1.1E-02	2.4E-03	6.4E-03	0.88	2.13	2.35	2.24	2.46	-
4	1.1E-02	3.7E-03	1.2E-02	-	2.23	2.44	2.34	2.56	-
5	1.1E-02	7.3E-03	2.2E-02	-	2.74	3.02	2.88	3.17	-
6	1.4E-02	1.8E-03	6.8E-03	0.63	2.31	2.50	2.42	2.63	2.1E-02
7	1.4E-02	2.3E-03	5.6E-03	0.76	2.22	2.38	2.34	2.52	1.7E-02
8	1.9E-02	3.4E-03	1.1E-02	0.64	2.17	2.65	2.26	2.74	-
9	1.9E-02	7.0E-03	2.2E-02	-	2.57	2.83	2.70	2.98	-
10	1.9E-02	1.2E-02	4.4E-02	0.63	2.95	3.28	3.09	3.45	-
11	2.3E-02	2.0E-03	3.1E-03	0.54	1.99	2.10	2.09	2.20	1.1E-02
12	2.3E-02	3.2E-03	9.2E-03	0.52	2.18	2.46	2.29	2.60	1.5E-02
13	2.3E-02	6.8E-03	2.0E-02	0.54	2.58	2.78	2.71	2.91	4.9E-02
14	2.3E-02	1.2E-02	4.1E-02	0.52	3.10	3.40	3.24	3.59	9.9E-02
15	2.8E-02	1.7E-03	2.6E-03	0.43	1.89	2.11	1.97	2.22	
16	2.8E-02	6.2E-03	1.7E-02	0.45	2.59	2.81	2.73	2.96	7.6E-02
17	2.8E-02	1.1E-02	5.7E-02	0.43	3.07	3.35	3.23	3.53	9.1E-02
18	2.8E-02	1.4E-02	-	0.43	-	-	-	-	1.2E-01

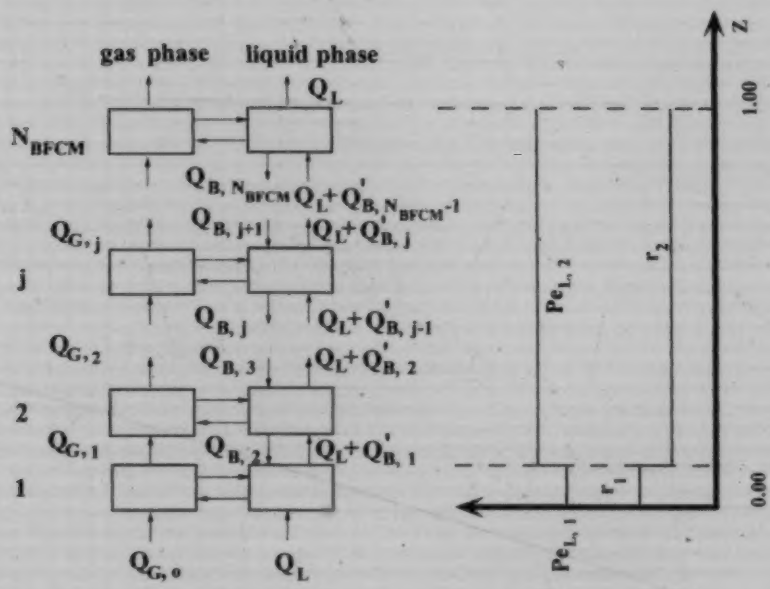

Figure 3.1 Schematic diagram representing the transient back flow cell model for the co-current operation of a bubble column reactor (Adapted from Gamal El-Din and Smith (2001b)).

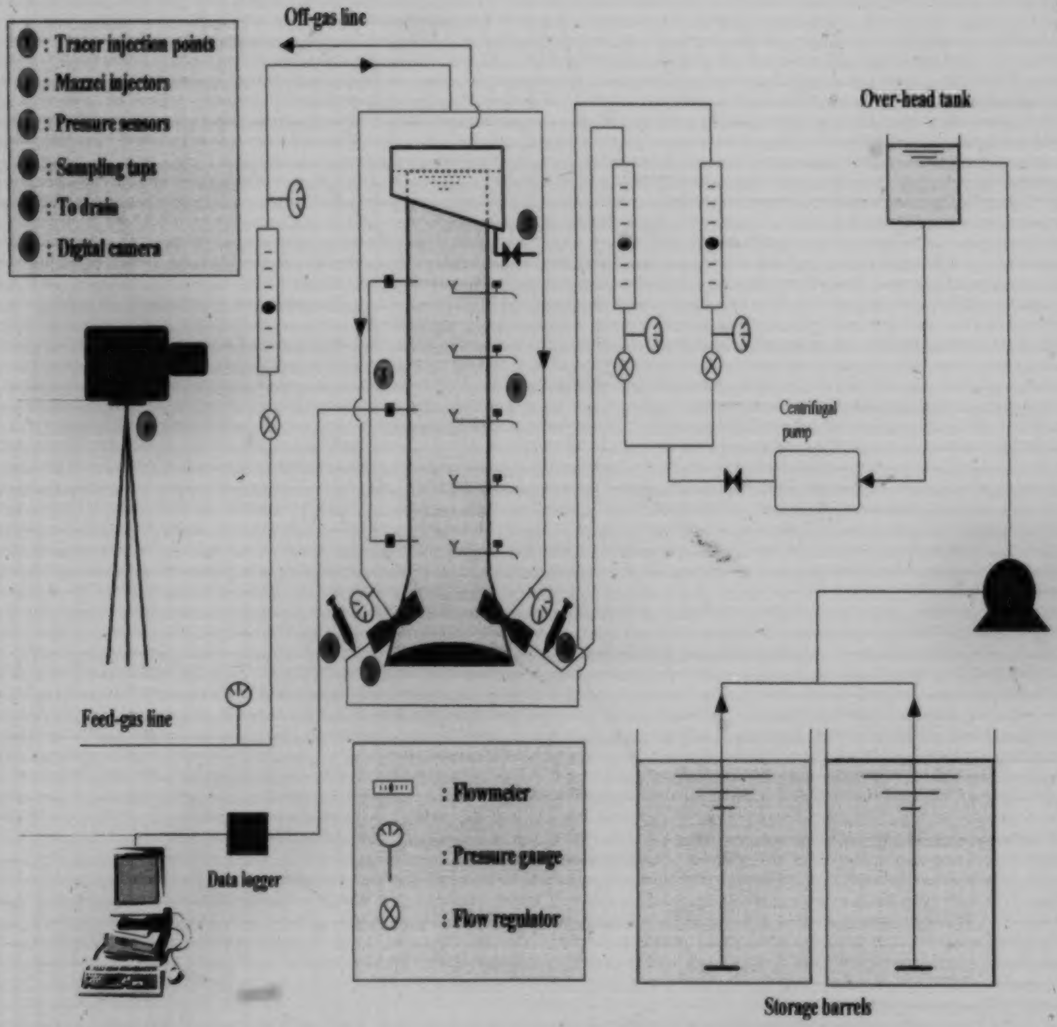

Figure 3.2 Bubble column pilot-scale set-up (Adapted from Gamal El-Din and Smith (2001c)).

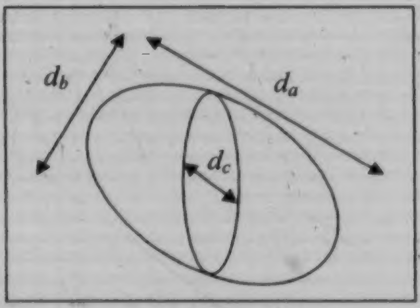

Figure 3.3 Bubble dimensions (adapted from Yamashita et al. (1979)).

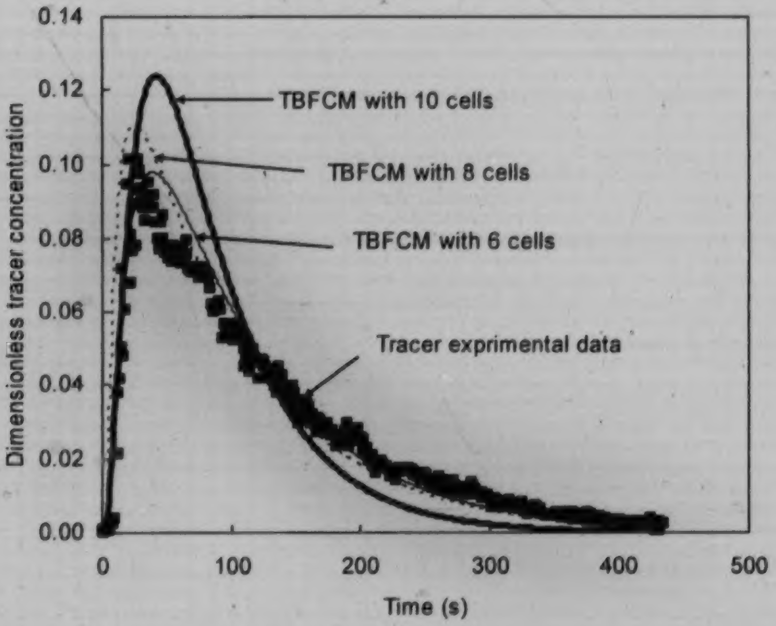

Figure 3.4 Effect of the number of cells on the TBFCM predictions of the RTDs.

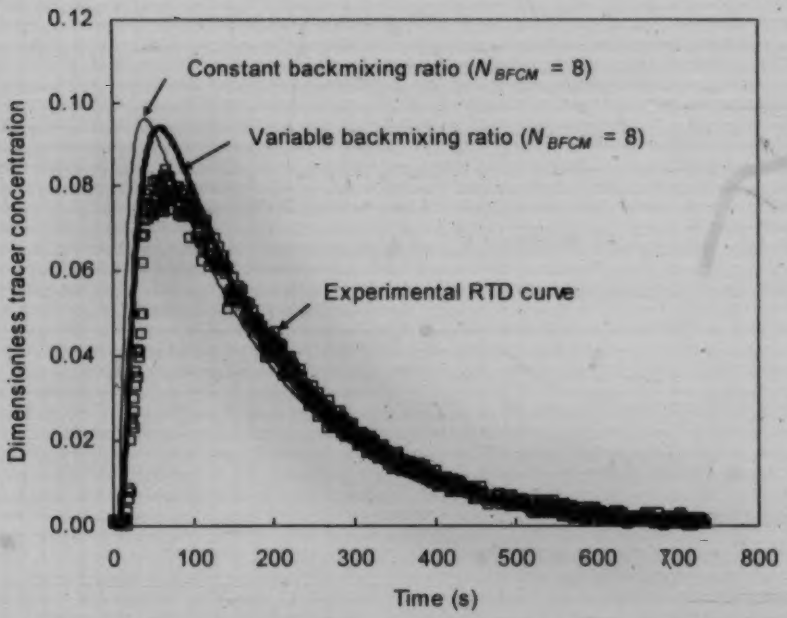

Figure 3.5 Comparison between the use of one mixing zone and two mixing zones to characterize the backmixing in the impinging-jet bubble column.

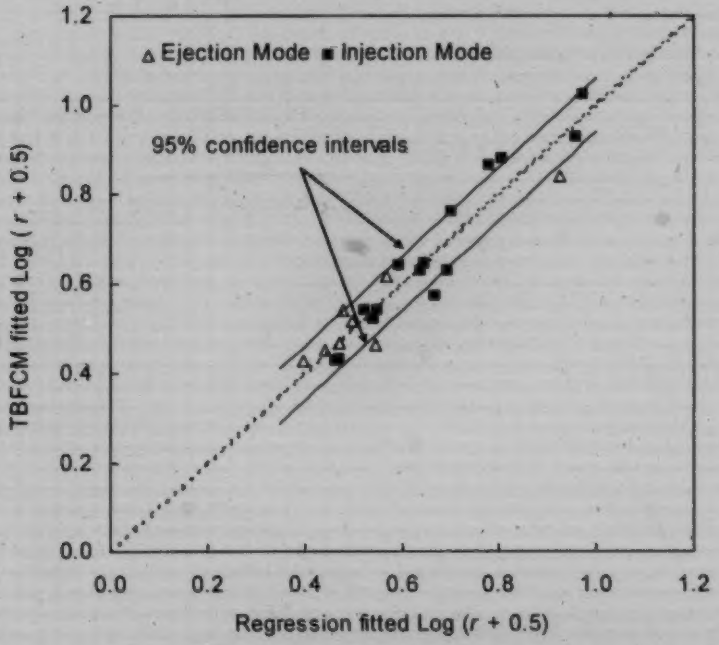

Figure 3.6 Comparison between the TBFCM-fitted and regression-fitted backmixing ratios for the impinging-jet bubble column.

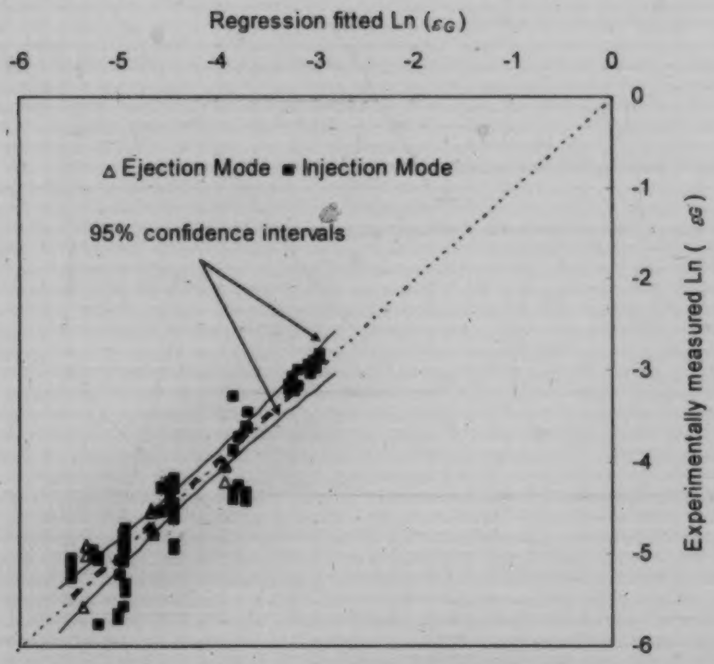

Figure 3.7 Comparison between the experimentally-measured and the regression-fitted gas hold-ups.

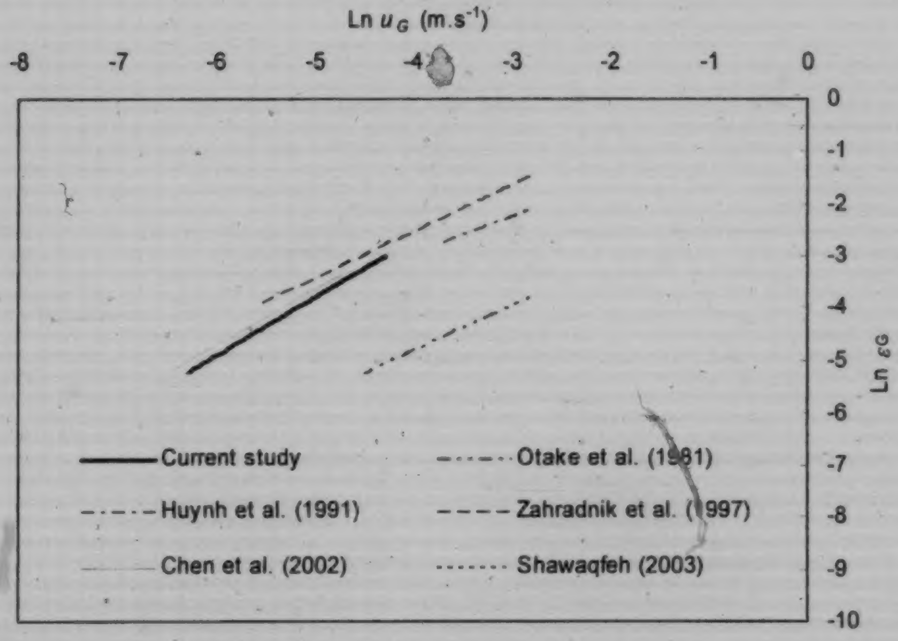

Figure 3.8 Comparison between published gas hold-up correlations at $u_L = 0.02$ m/s.

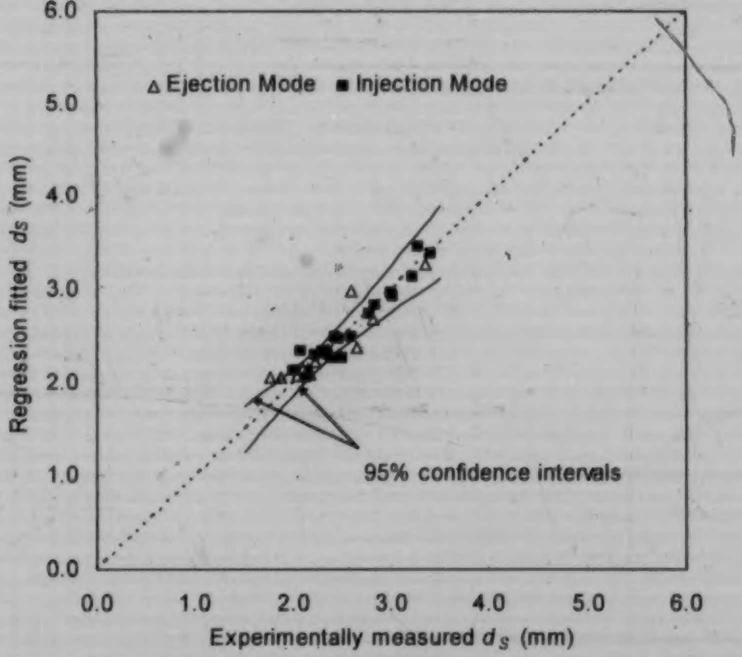

Figure 3.9 Comparison between measured and predicted Sauter mean bubble diameters for approach (1).

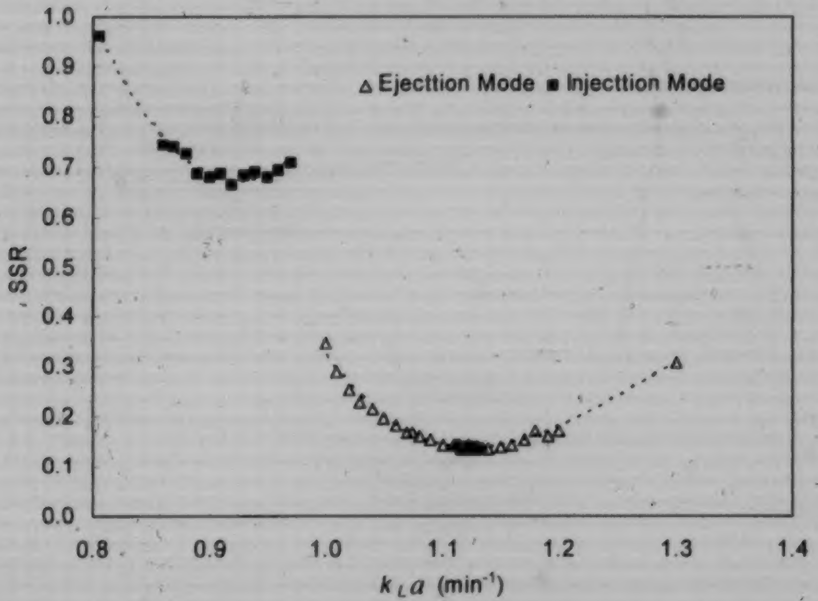

Figure 3.10 Sum of the squares of the residuals (SSR) plot for injection and ejection modes.

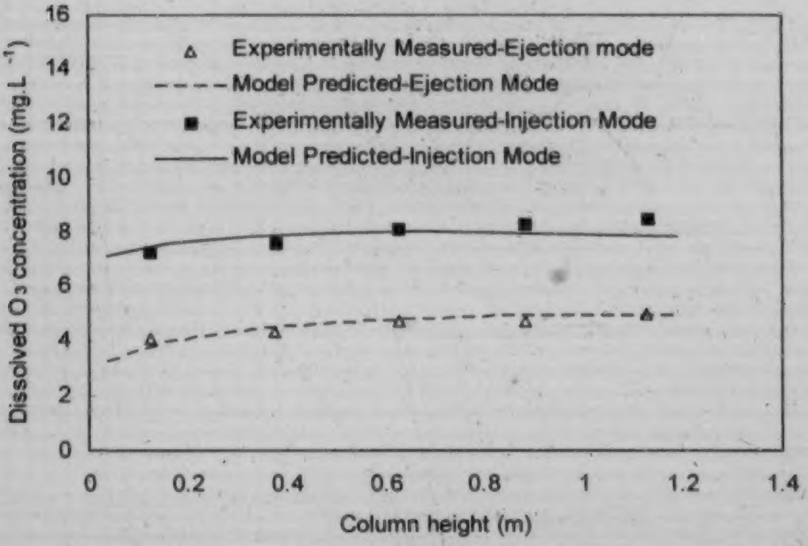

Figure 3.11 Dissolved ozone concentration profiles for injection and ejection modes.

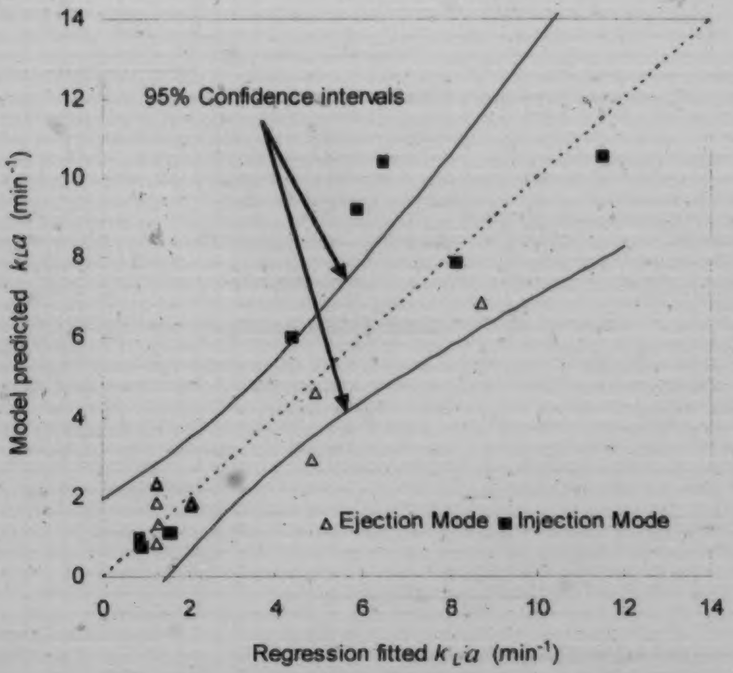

Figure 3.12 Comparison between the BFCM predicted and the regression-fitted k_La.

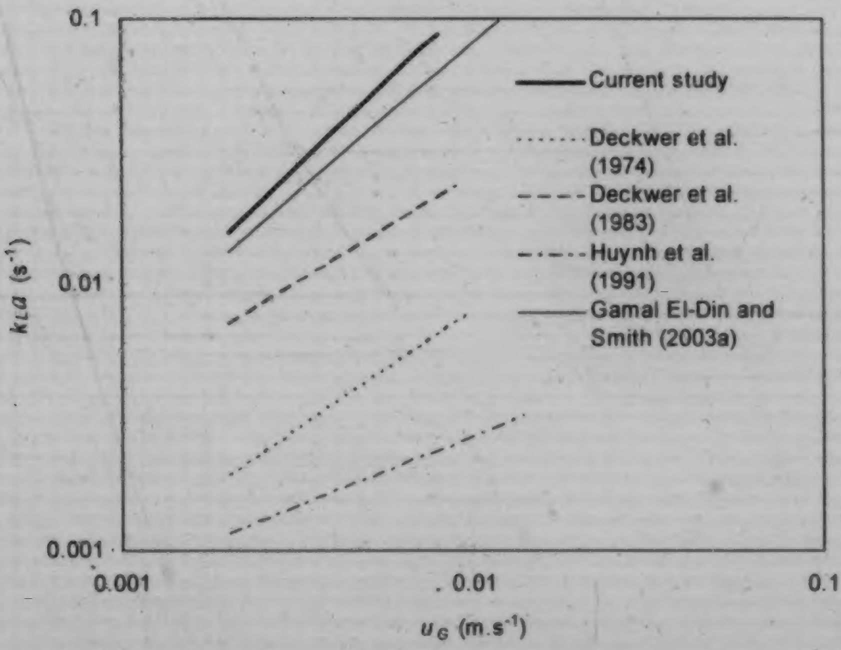

Figure 3.13 Comparison between correlations predicting k_La in a number of bubble column designs.

3.8 REFERENCES

1. Akita, K., and F. Yoshida, "Gas Holdup and Volumetric Mass-Transfer Coefficient in Bubble Columns - Effects of Liquid Properties", *Industrial & Engineering Chemistry Process Design and Development*, 12(1): 76-80 (1973).
2. Akita, K., and F. Yoshida, "Bubble Size, Interfacial Area, and Liquid-Phase Mass-Transfer Coefficient in Bubble Columns", *Industrial & Engineering Chemistry Process Design and Development*, 13(1): 84-91 (1974).
3. Alvarezcuenca, M., C.G.J. Baker, and M.A. Bergougnou, "Oxygen Mass-Transfer in Bubble-Columns", *Chemical Engineering Science*, 35(5): 1121-1127 (1980).
4. Alvarezcuenca, M., and M.A. Nerenberg, "Oxygen Mass-Transfer in Bubble-Columns Working at Large Gas and Liquid Flow-Rates", *Aiche Journal*, 27(1): 66-73 (1981).
5. Bale, A., M. Gamal El-Din, D.W. Smith, A. Mazzei, and P. Overbeck, "Ozone Mass Transfer Analysis of Two New Ozone Reactor Designs", *17th World Congress of the International Ozone Association*, Starsbour, France. (2005).
6. Bellamy, W.D., *Full-Scale Ozone Contactor Study*. (Denver: A.W.W.A. Research Foundation, 1995).
7. Bin, A.K., B. Duczmal, and P. Machniewski, "Hydrodynamics and Ozone Mass Transfer in a Tall Bubble Column", *Chemical Engineering Science*, 56(21-22): 6233-6240 (2001).
8. Briens, C.L., L.X. [illegible]uynh, J.F. Large, A. Catros, J.R. Bernard, and M.A. Bergougnou, "Hydrodynamics and Gas-Liquid Mass-Transfer in a Downward

Venturi-Bubble Column Combination", *Chemical Engineering Science*, 47(13-14): 3549-3556 (1992).

9. Chen, Y.H., C.Y. Chang, C.Y. Chiu, W.H. Huang, Y.H. Yu, P.C. Chiang, Y. Ku, and J.N. Chen, "Dynamic Model of Ozone Contacting Process with Oxygen Mass Transfer in Bubble Columns", *Journal of Environmental Engineering-Asce*, 128(11): 1036-1045 (2002).

10. Danckwerts, P.V., *Gas-Liquid Reactions*. (New York, U.S.A: McGraw-Hill, Inc., 1970).

11. Deckwer, W., U. Graeser, Langeman.H, and Y. Serpemen, "Zones of Different Mixing in Liquid-Phase of Bubble Columns", *Chemical Engineering Science*, 28(5): 1223-1225 (1973).

12. Deckwer, W.D., "Non-Isobaric Bubble-Columns with Variable Gas Velocity", *Chemical Engineering Science*, 31(4): 309-317 (1976).

13. Deckwer, W.D., *Bubble Column Reactors*. (Chichester, England: John Wiley & Sons Ltd, Inc., 1992).

14. Deckwer, W.D., Burckhar.R, and G. Zoll, "Mixing and Mass-Transfer in Tall Bubble Columns", *Chemical Engineering Science*, 29(11): 2177-2188 (1974).

15. Deckwer, W.D., K. Nguyentien, B.G. Kelkar, and Y.T. Shah, "Applicability of Axial-Dispersion Model to Analyze Mass-Transfer Measurements in Bubble-Columns", *Aiche Journal*, 29(6): 915-922 (1983).

16. Finch, G.R., C.N. Haas, J.A. Oppenheimer, G. Gordon, and R.R. Trussell, "Design Criteria for Inactivation of Cryptosporidium by Ozone in Drinking Water", *Ozone-Science & Engineering*, 23(4): 259-284 (2001).

17. Gamal El-Din, M., and D.W. Smith, "Designing Ozone Bubble Columns: A Spreadsheet Approach to Axial Dispersion Model", *Ozone-Science & Engineering*, 23(5): 369-384 (2001a).

18. Gamal El-Din, M., and D.W. Smith, "Development of Transient Back Flow Cell Model (Bfcm) for Bubble Columns", *Ozone-Science & Engineering*, 23(4): 313-326 (2001b).

19. Gamal El-Din, M., and D.W. Smith, "Maximizing the Enhanced Ozone Oxidation of Kraft Pulp Mill Effluents in an Impinging-Jet Bubble Column", *Ozone-Science & Engineering*, 23(6): 479-493 (2001c).

20. Gamal El-Din, M., and D.W. Smith, "Ozone Mass Transfer in Water Treatment: Hydrodynamics and Mass Transfer Modelling of Ozone Bubble Columns", *Water Science and Technology: Water Supply*, 1(2): 123-130 (2001d).

21. Gamal El-Din, M., and D.W. Smith, "Comparing Different Designs and Scales of Bubble Columns for Their Effectiveness in Treating Kraft Pulp Mill Effluents", *Ozone-Science & Engineering*, 24(5): 307-320 (2002).

22. Gamal El-Din, M., and D.W. Smith, "Mass Transfer Analysis in Ozone Bubble Columns", *Journal of Environmental Engineering and Science*, 2(1): 63-76 (2003a).

23. Gamal El-Din, M., and D.W. Smith, "Measurements of the Size, Rise Velocity, and Specific Interfacial Area of Bubbles in an Impinging-Jet Bubble Column", *Journal of Environmental Engineering and Science*, 2(2): 127-138 (2003b).

24. Havelka, P., V. Linek, J. Sinkule, J. Zahradnik, and M. Fialova, "Hydrodynamic and Mass Transfer Characteristics of Ejector Loop Reactors", *Chemical Engineering Science*, 55(3): 535-549 (2000).

25. Hikita, H., and H. Kikukawa, "Liquid-Phase Mixing in Bubble Columns: Effect of Liquid Properties", *The Chemical Engineering Journal*, 8(3): 191-197 (1974).

26. Houzelot, J.L., M.F. Thiebaut, J.C. Charpentier, and J. Schiber, "Contribution to the Hydrodynamic Study of Bubble Columns", *International Chemical Engineering*, 25(4): 645-650 (1985).

27. Huynh, L.X., C.L. Briens, J.F. Large, A. Catros, J.R. Bernard, and M.A. Bergougnou, "Hydrodynamics and Mass-Transfer in an Upward Venturi Bubble Column Combination", *Canadian Journal of Chemical Engineering*, 69(3): 711-722 (1991).

28. Jakubowski, C.A., B.W. Atkinson, P. Dennis, and G.M. Evans, "Ozone Mass Transfer in a Confined Plunging Liquid Jet Contactor", *Ozone-Science & Engineering*, 25(1): 1-12 (2003).

29. Kantak, M.V., S.A. Shetty, and B.G. Kelkar, "Liquid-Phase Backmixing in Bubble-Column Reactors - a New Correlation", *Chemical Engineering Communications*, 127: 23-34 (1994).

30. Kastánek, F., J. Zahradník, J. Kratochvíl, and J. Čermák, *Chemical Reactors for Gas-Liquid Systems*. (Chichester, West Sussex, England: Ellis Horwood Limited, 1993).

31. Kawagoe, M., T. Otake, and C.W. Robinson, "Gas-Phase Mixing in Bubble-Columns", *Journal of Chemical Engineering of Japan*, 22(2): 136-142 (1989).

32. Kulkarni, A., Y. Shah, and A. Schumpe, "Hydrodynamics and Mass Transfer in Downflow Bubble Column", *Chemical Engineering Communications*, 24: 307-337 (1983).

33. Lesauze, N., A. Laplanche, M.T.O. Develasquez, G. Martin, B. Langlais, and N. Martin, "The Residence Time Distribution of the Liquid-Phase in a Bubble Column and Its Effect on Ozone Transfer", *Ozone-Science & Engineering*, 14(3): 245-262 (1992).

34. Marinas, B.J., S. Liang, and E.M. Aieta, "Modeling Hydrodynamics and Ozone Residual Distribution in a Pilot-Scale Ozone Bubble-Diffuser Contactor", *Journal American Water Works Association*, 85(3): 90-99 (1993).

35. Ohki, Y., and H. Inoue, "Longitudinal Mixing of Liquid Phase in Bubble Columns", *Chemical Engineering Science*, 25(1): 1-& (1970).

36. Otake, T., S. Tone, and K. Shinohara, "Gas Holdup in the Bubble Column with Cocurrent and Countercurrent Gas-Liquid Flow", *Journal of Chemical Engineering of Japan*, 14(4): 338-340 (1981).

37. Reith, T., S. Renken, and B.A. Israel, "Gas Hold-up and Axial Mixing in Fluid Phase of Bubble Columns", *Chemical Engineering Science*, 23(6): 619-& (1968).

38. Roustan, M., J.P. Duguet, B. Brette, E. Brodard, and J. Mallevialle, "Mass Balance Analysis of Ozone in Conventional Bubble Contactors", *Ozone-Science & Engineering*, 9(3): 289-298 (1987).

39. Roustan, M., A. Line, J.P. Duguet, J. Mallevialle, and O. Wable, "Practical Design of a New Ozone Contactor - the Deep U-Tube", *Ozone-Science & Engineering*, 14(5): 427-438 (1992a).

40. Roustan, M., A. Line, and O. Wable, "Modeling of Vertical Downward Gas-Liquid Flow for the Design of a New Contactor", *Chemical Engineering Science*, 47(13-14): 3681-3688 (1992b).

41. Roustan, M., R.Y. Wang, and D. Wolbert, "Modeling Hydrodynamics and Mass Transfer Parameters in a Continuous Ozone Bubble Column", *Ozone-Science & Engineering*, 18(2): 99-115 (1996).

42. Salazar, J.A., K.D. Wisecarver, Y.T. Shah, and B. Solari, "Gas-Liquid Mass-Transfer in Jet Bubble-Column", *Chemical Engineering Communications*, 124: 177-188 (1993).

43. Shawaqfeh, A.T., "Gas Holdup and Liquid Axial Dispersion under Slug Flow Conditions in Gas-Liquid Bubble Column", *Chemical Engineering and Processing*, 42(10): 767-775 (2003).

44. Shetty, S.A., M.V. Kantak, and B.G. Kelkar, "Gas-Phase Backmixing in Bubble-Column Reactors", *Aiche Journal*, 38(7): 1013-1026 (1992).

45. Sotelo, J.L., F.J. Beltran, F.J. Benitez, and J. Beltranheredia, "Henrys Law Constant for the Ozone Water-System", *Water Research*, 23(10): 1239-1246 (1989).

46. Sotiriadis, A.A., R.B. Thorpe, and J.M. Smith, "Bubble Size and Mass Transfer Characteristics of Sparged Downwards Two-Phase Flow", *Chemical Engineering Science*, 60(22): 5917-5929 (2005).

47. Wachi, S., H. Morikawa, and K. Ueyama, "Gas Holdup and Axial Dispersion in Gas-Liquid Cocurrent Bubble Column", *Journal of Chemical Engineering of Japan*, 20(3): 309-316 (1987).

48. Wachi, S., and Y. Nojima, "Gas-Phase Dispersion in Bubble Columns", *Chemical Engineering Science*, 45(4): 901-905 (1990).

49. Wright, P.C., V. Meeyoo, and W.K. Soh, "A Study of Ozone Mass Transfer in a Cocurrent Downflow Jet Pump Contactor", *Ozone-Science & Engineering*, 20(1): 17-33 (1998).

50. Yamashita, F., Y. Mori, and S. Fujita, "Sizes and Size Distributions of Bubbles in a Bubble Column - Comparison between the 2 Point Electric Probe Method and the Photographic Method", *Journal of Chemical Engineering of Japan*, 12(1): 5-9 (1979).

51. Zahradnik, J., and M. Fialova, "The Effect of Bubbling Regime on Gas and Liquid Phase Mixing in Bubble Column Reactors", *Chemical Engineering Science*, 51(10): 2491-2500 (1996).

52. Zahradnik, J., M. Fialova, V. Linek, J. Sinkule, J. Reznickova, and F. Kastanek, "Dispersion Efficiency of Ejector-Type Gas Distributors in Different Operating Modes", *Chemical Engineering Science*, 52(24): 4499-4510 (1997).

53. Zahradnik, J., J. Kratochvil, and M. Rylek, "Gas Holdup and Interfacial Mass-Transfer in Gas-Liquid Tower Contactors with Ejector-Type Gas Distributors", *Collection of Czechoslovak Chemical Communications*, 50(11): 2535-2544 (1985).

54. Zhou, H., "Investigation of Ozone Disinfection Kinetics and Contactor Performance Modelling", Ph.D. , University of Alberta, Edmonton, Alberta, Canada., (1995).

55. Zhou, H., and D.W. Smith, "Modelling of Mass Transfer and Ozone Decomposition in a Bubble Column: Experimental Verification", *12th World Congress of the International Ozone Association*, Lille, France. (1995).

56. Zhou, H.D., and D.W. Smith, "Ozone Mass Transfer in Water and Wastewater Treatment: Experimental Observations Using a 2d Laser Particle Dynamics Analyzer", *Water Research*, 34(3): 909-921 (2000).

57. Zhou, H.D., D.W. Smith, and S.J. Stanley, "Modeling of Dissolved Ozone Concentration Profiles in Bubble-Columns", *Journal of Environmental Engineering-Asce*, 120(4): 821-840 (1994).

CHAPTER 4

PIV/PLIF STUDY OF IMPINGING JET BUBBLE COLUMN WITH MIXING NOZZLES

4.1 INTRODUCTION

Ozone is normally applied to water and wastewater by introducing the on-site generated ozone gas into the liquid phase by utilizing conventional techniques such as the use of bubble diffusers, turbine mixers, and gas injectors. Bubble columns are probably the most common ozone contactors due to their high mass-transfer abilities and low energy requirements compared to those of many other reactors (Bollyky, 1981; Charpentier, 1981). Ozone mass transfer efficiency in these contactors is influenced by the ozone concentration in the gas phase, the liquid and gas flow rates, the column water depth, and the size of the bubbles created (Kuo and Yocum, 1982).

One of the main disadvantages of bubble columns is the occurrence of a large degree of liquid phase back-mixing along the column. Therefore, proper modelling is essential for estimating the bubble columns' capabilities accurately (Charpentier, 1981; Deckwer and Schumpe, 1993). However, bubble columns can be modified to overcome their disadvantages and to enhance their efficiency in treating and disinfecting water and wastewater. Gamal El-Din and Smith (2001b) introduced a novel design for the bubble column by utilizing two impinging jets through which gas and liquid enter the contactor under a turbulent flow condition. These researchers showed that this new design is very effective compared to that of conventional bubble columns, and also introduced a one-phase axial dispersion model and a transient backflow cell model to predict the dissolved ozone concentration along the column (Gamal El-Din and Smith, 2001a; Gamal El-Din and Smith, 2001b).

This study aims at characterizing the hydrodynamics of an impinging jet bubble column with mixing nozzles by evaluating the concentration distributions of a tracer dye, the liquid velocity components, and the gas velocity components in the bubble column under different operating conditions. Then, an attempt to predict the longitudinal dispersion coefficients of the bubble column under each operating condition will be performed by analyzing the residence time distribution (RTD) curves. The non-intrusive laser-based techniques briefly described below were used in this study.

4.2 LASER MEASUREMENT TECHNIQUES

Laser-based measuring techniques are popular because they are non-intrusive, directional-sensitive, highly spatial and temporal in resolution, and highly accurate (Albrecht et al., 2002). Some of these measuring techniques are point-wise, such as those using a laser Doppler anemometry (LDA) and a particle dynamics analyzer (PDA), while others such as those using particle image velocimetry (PIV) and planar laser-induced fluorescence (PLIF) are simultaneous flow field measuring techniques. PIV and PLIF techniques are considered to be effective experimental tools for characterizing the hydrodynamics of different reactors.

The laser Doppler anemometer (LDA) is an optical method for flow measurement utilizing the Doppler principle, which states that the coherent light (laser) reflected from a moving particle exhibits a frequency relative to a fixed observer that depend on the known laser light source wavelength and the velocity of the moving particle (Bernard and Wallace, 2002). LDA has been the single most important instrumental technique that has contributed to the investigation of complex flows of fundamental and practical interest (Tropea, 1995). This importance is due to its non-intrusiveness (except for the presence of the seeding particles), directional sensitivity and high accuracy (Bernard and Wallace, 2002). LDA uses monochromatic laser light as a light source. The idea is to have two laser beams crossing in one volume (measuring volume). The interference of the two beams in the measuring volume or the interference of the two scattering waves (due to the moving particle) on the detector creates a fringe pattern. The velocity information is contained in the scattered field due to the Doppler Effect.

The particle dynamics analyzer (PDA) is considered a well-established measuring technique for simultaneous measurements of particle velocity and size. The most accurate PDA configuration is the planar PDA systems (Durst et al., 1997). The basic configurations of PDA systems are similar to those of LDA systems with the difference in number and alignment of detectors, usually two, and the laser beam intersection angles (Albrecht et al., 2002). The phase difference of two signals received at the same time for both detectors is employed to determine the size of the particle (Albrecht et al., 2002; Durst et al., 1997).

The PIV system aims at measuring the displacement of seeded particles over a short time in order to determine the velocity components in an image plane. The particles' displacement is determined through a pulsed light velocimetry in which the positions of the marker particles in a plane are noted at some time step by illuminating through successive pulses of laser light and capturing the images either on film or via a charge-coupled device (CCD) camera (Bernard and Wallace, 2002; Raffel et al., 1998). The experimental set-up of a PIV system normally consists of several subsystems. Most applications add tracer particles to the flow. These particles have to be illuminated in a plane of the flow at least twice within a short time interval, as mentioned above. The scattered light has to be recorded either on a single frame or on a sequence of frames. The displacement of the particle images between pulses can then be determined by evaluating the PIV recordings. A sophisticated post-processing system is required to handle the great amount of data that can be collected by using the PIV technique (Raffel et al., 1998; Stanislas et al., 2000).

The PLIF system is based on obtaining the planar measurements of a scalar concentration field in water. In such a case, a fluorescent dye is mixed and carried as a passive scalar in the flow. During the illumination process of the laser, the dye absorbs incident light at one wavelength and reemits it at a different wavelength. According to the Beer-Lambert law, the reemitted wavelength of the light intensity is proportional to the dye concentration at the measuring point (Bernard and Wallace, 2002). Additional details about the basic principles behind different planar laser measurement techniques can be found in Vancruyningen et al. (1990) and Willert and Gharib (1991).

4.3 EXPERIMENTAL SET-UP

4.2.1 Flow Facility

The experimental set-up used in this study is similar to the one shown in Figure 3.2, which was introduced originally by Gamal El-Din and Smith (2001b). The bubble column (made of clear acrylic) had an inner diameter of 100 mm and a height of 1320 mm. An outer square jacket with 150 mm sides and 1000 mm high (starting from 150 mm above the bottom of the column) was used in this study to minimize any reflection effect. An overflow weir was placed around the top portion of the bubble column for recycling and/or draining purposes. The liquid and gas were introduced into this bubble column through two Kynar Mazzei® venturi injectors with inside diameters of 12.7 mm that were placed 25 mm above the bottom of the column at an intersecting angle of 125°. A slight modification to the bubble column introduced by Gamal El-Din and Smith (2001b) was implemented in this study by adding mixing nozzles to the outlet of the injectors (see Figure 4.1). The distance between the two nozzles was measured to be 40 mm centre to centre. This modification was expected to enhance the momentum of the entering plunging jets and to provide better mixing at the bottom of the column. More details about the original impinging-jet bubble column design and configurations can be found in Gamal El-Din and Smith (2001b).

4.2.2 PIV/PLIF Set-up

The PIV/PLIF set-up used in the hydrodynamic analysis of the ozone contactor included a laser source, charge coupled device (CCD) cameras, and processing units, as shown in Figure 4.2a. An Nd:Yag dual cavity laser was utilized in this study for both the PIV and PLIF experiments. The emitted wavelength of the utilized Nd:Yag laser was 532 nm, with a pulse duration of 10 ns. The period between pulses was set to 1000 μs during PIV measurements and 100 μs during PLIF measurements, with a maximum repetition rate of 8.0 Hz. The measurements were obtained at a time interval of 1000 ms during PIV measurements and 125 ms during PLIF measurements. The CCD cameras were configured to use double frames for PIV measurements (velocity measurements) and a single frame for PLIF measurements (concentration measurements). A FlowMap System Hub® produced by Dantec Dynamics was used to transfer the data to a PC where FlowMap Software® was used for further analysis of the collected data.

The PLIF system was first calibrated by measuring the intensity of 5 different concentrations of Rhodamine 6G (Rh6G) solutions ranging from zero to 400 μg/L at a power level ranging from 50 to 150 mJ. The concentration versus the intensity was plotted to determine the most appropriate calibration curve for this study. The calibration curve obtained for the 150 mJ power gave the highest correlation coefficient (0.88). Therefore, this power level was used during all PLIF measurements.

The PIV measurements were conducted by using two CCD cameras with a double-frame mode for measuring the velocity of both phases (liquid and gas) simultaneously by utilizing special filters. Melamine-formaldehyde (MF) spheres, coated with Rhodium B (RhB), were used as seeding particles to obtain the liquid velocity measurements while gas bubbles represented the seeding particles for the gas velocity measurements. The 2-D velocity vectors were then obtained by employing an interrogation cell of 64 x 64 pixels, which was a subdomain of a 1344 x 1024 pixel viewing area. The interrogation cell was then shifted with 25% overlap, and thus 21 x 21 velocity vectors were obtained in each instantaneous PIV sample. However, for illustration purposes, 11 x 11 velocity vectors maps were produced.

4.2.3 PDA Set-up

The PDA set-up used in this study included a PDA system and the same bubble column used in the PIV/PLIF experiments (see Figure 4.2b). The PDA system utilized during the study, produced by Dantec Dynamics, consisted of a 60X FiberFlow transmitting probe, a FiberPDA 58N70 detector unit, and a BSA P60 flow and particle processor. An Argon-Ion laser was utilized in this study with a beam wavelength of 514.5 nm. A summary of the configuration and operational settings of the PDA system are shown in Table 4.1. Those setting were chosen after exploring a wide range of operational settings to match the bubble column's operational conditions. This system was used to provide the bubble size measurements for the same operational conditions conducted during the PIV/PLIF study.

4.3 MEASUREMENT DESCRIPTION

The PLIF and PIV experimental conditions utilized in this study are provided in Table 4.2. For comparison reasons, the ranges of the liquid and gas flow rates were chosen to be similar to those used by Gamal El-Din and Smith (2001b). Three liquid flow rates (Q_L) were used in this study: 6.3 x 10^{-5} m^3/s, 1.26 x 10^{-4} m^3/s, and 1.89 x 10^{-4} m^3/s. The gas flow rate (Q_G) ranged from 8.3 x 10^{-6} to 1.0 x 10^{-4} m^3/s. The resulting gas to liquid ratio was from 4 to 53%. After a steady state flow condition was reached, a continuous injection of the Rh6G tracer at about 1.4 x 10^{-5} m^3/s was introduced into the system through two injection points at the entrance of each Mazzei injector. Three concentrations of the Rh6G were used to yield a 45 μg/L average concentration when fully mixed with the entering flow (250, 425, and 625 μg/L for Q_L of 6.3 x 10^{-5} m^3/s, 1.26 x 10^{-4} m^3/s, and 1.89 x 10^{-4} m^3/s, respectively). The continuous (step) input of the tracer was chosen over the slug input for this contactor due to the difficulties associated with injecting the tracer manually at the two inlets. The PLIF process of image capturing covered about 2 times the detention time required for the tracer to pass through the system under each operating condition (300 images at 1 s intervals were captured for Q_L of 6.3 x 10^{-5} m^3/s, 130 images at 1 s intervals were captured for Q_L of 1.26 x 10^{-4} m^3/s, and 100 images at 1 s intervals were captured for Q_L of 1.89 x 10^{-4} m^3/s). (Duplicate measurements were applied to reduce the uncertainty associated with the measurements.) The average water temperature was 17 ± 1 °C.

During the PIV experiments, the flow patterns of the system were studied for 1-phase and 2-phase flow conditions for the same experimental conditions shown in Table 4.2. The measurements were taken at the same location where the PLIF measurements were taken. The PIV process of image capturing was taken in 30 duplicated measurements for each experimental condition. The average water temperature was 20 ± 1 °C.

The bubble-sizing measurements were also conducted for the same range of operating conditions shown in Table 4.2. The measurements were conducted around the middle height of the column by using the PDA system. Different acquisition times were used for the bubble size measurements depending on the rate of the bubbles formed in the column. The acquisition time ranged from 100 s to 600 s.

Since the bubble size measurements were conducted, it was thought that estimating the gas hold-up (ε_G) would provide a basis for determining the specific interfacial area (a, m^{-1}), which in turn would provide useful information for characterizing the gas mass transfer efficiency of the contactor. The value of ε_G for each operating condition shown in Table 4.2 was calculated by inserting two tubes through the sides of the bubble column (one was fixed in the mixing zone, which is the zone where the two jets impinged into each other, and the other one was fixed just above the measurement location used for the PIV, PLIF and bubble sizing). The change in the water level in the tubes was observed, and the following equation was applied to determine ε_G:

$$\varepsilon_G = \frac{\Delta h}{\Delta x} \qquad [4.1]$$

where Δh (m) is the difference between the water level in the tubes, and Δx (m) is the axial distance between the measuring points.

4.4 RESULTS AND DISCUSSION

All images captured during the PLIF experiments were converted to 2D concentration fields through the obtained calibration relation by using the FlowMap Software®. A re-sampling of these concentration fields yielded colored contour maps that show the concentration distribution of the tracer along the cross-section of the contactor parallel to the flow direction. A colored contour map representing the concentration distribution at different sampling (image capturing) times for two different liquid flow rates (Q_L of 8.8 x 10^{-5} m^3/s and 1.5 x 10^{-4} m^3/s) without gas injection is shown in Figure

4.3. Both cases resemble the laminar flow (Re of 1000 and 2000 respectively). Therefore, it was expected that the pipe with higher Re will have higher dispersion, as Levenspiel (1999) and others had stated. This expectation is clearly supported by the results shown in Figure 4.3b, as segments of the tracer are reaching the measurement point relatively faster than the segments shown in Figure 4.3a.

Figure 4.4 shows the concentration distribution resulting from using two different gas flow rates (Q_L of 8.3 x 10^{-6} m^3/s and 3.3 x 10^{-5} m^3/s) at a fixed liquid flow rate (Q_L of 1.3 x 10^{-5} m^3/s). The results suggest a lower dispersion effect when a higher gas flow rate was used under the same liquid flow rate. This result can be related to the increased mixing resulting from the higher momentum of the plunging jets (the flow might have been in the transitional region where the dispersion effect decreased again). This expectation is supported by Figure 4.5, as the results show that the dispersion effect decreased as the flow moved toward transitional conditions.

Further analysis of the mixing and the dispersion in the contactor was achieved through velocity measurements obtained for the studied operating conditions by using the PIV system. Figure 4.6 shows the averaged velocity vectors for two different liquid flow rates (Q_L of 6.3 x 10^{-5} m^3/s and 1.3 x 10^{-4} m^3/s) without gas injection. This figure shows that the axial flow is dominating, and, hence, that the flow with the higher axial velocity will exhibit a higher dispersion. In contrast, for the same liquid flow rate, as the gas flow rate increased, the radial mixing increased in both phases (liquid and gas), and, hence, the axial dispersion decreased (Figure 4.7).

In order to evaluate the mixing in the contactor numerically, the following differential equation, introduced by Levenspiel (1999) and representing the dispersion of a conservative tracer (C, μg/L), was considered:

$$\frac{\partial C}{\partial \theta} = \left(\frac{D_L}{uL}\right)\frac{\partial^2 C}{\partial z^2} - \frac{\partial C}{\partial z} \qquad [4.2]$$

where θ is a dimensionless time ($\theta = t/\tau = tu/L$, t is time (s)), $\left({}^{D_L}\!/_{uL}\right)$ is the dispersion number (the inverse of the Peclet number, Pe), D_L is the liquid axial dispersion coefficient (m^2/s), u is the pipe flow average velocity (m/s), L is the axial distance between the tracer input point and measurement point (m), and z is the dimensionless axial distance ($z = (ut + x)/L$, x is the axial distance along the pipe (m)). For a step input of a tracer, the shape of the tracer at the measurement point is S-shaped and referred to as the F-curve. The F-curves normally represent the dimensionless concentration (F), the ratio between the tracer concentration at the measurement point (C, μg/L) to the initial mixed tracer concentration (C_o, μg/L), as a function of time. The shape of the F-curve depends on the boundary conditions of the contactor and the dispersion number $\left({}^{D_L}\!/_{uL}\right)$. The analytical expressions of the F-curves are not available. However, their graphs can be constructed (Levenspiel, 1999). The value $\left({}^{D_L}\!/_{uL}\right)$ can be obtained directly by plotting the experimental data on a probability graph paper or by differentiating the S-shaped response curve and considering the boundary conditions (Levenspiel and Smith, 1957).

The numerical concentration of the Rh6G values obtained by the PLIF system can be extracted for all images under each operating condition and the step response curves (F-curves) at any position of interest can then be plotted. Figure 4.8 shows an F curve obtained from the PLIF experiments for the tracer concentration at the centre of the images captured for $Q_L = 1.26 \times 10^{-4}$ m^3/s and $Q_G = 8.3 \times 10^{-6}$ m^3/s. In order to obtain the dispersion number of the dye under each operating condition, the F-curves were differentiated, and the open vessel condition was assumed since the flow patterns at the boundaries were not disturbed (Levenspiel, 1999). Therefore, the residence time distribution (RTD) curves at any position of interest were obtained for the dimensionless concentration (E_θ) as a function of the dimensionless time (θ). The value of θ (t_i/τ) is the ratio of the data acquisition time (t_i) to the mean residence time (τ.) For discrete tracer data, τ can be determined as follows:

$$\tau = \frac{\sum t_i C_i \Delta t_i}{\sum C_i \Delta t_i} \qquad [4.3]$$

where t_i is the data acquisition time (s), Δt_i is the time step (s), and C_i is the instantaneous (recorded) concentration (μg/L). The dispersion number can be obtained from the RTD curves, which are characterized by τ (Equation 4.3) and the variance (σ_t^2), which can be obtained for discrete tracer test data as follows:

$$\sigma_t^2 = \frac{\sum t_i^2 C_i \Delta t_i}{\sum C_i \Delta t_i} - \tau^2 \qquad [4.4]$$

The value of the dispersion number can be obtained from the dimensionless variance (σ_θ^2), which can be determined as shown below:

$$\sigma_\theta^2 = \frac{\sigma_t^2}{\tau^2} = 2\frac{D_L}{uL} + 8\left(\frac{D_L}{uL}\right)^2 \qquad [4.5]$$

The value of D_L for all operating conditions was determined and correlated with the superficial liquid velocity (u_L) and the superficial gas velocity (u_G) by using a nonlinear regression as follows:

$$D_L = 8.52 \times 10^{-3} u_G^{0.06} u_L^{0.29} \qquad [4.6]$$

A plot of the experimentally-determined versus the predicted D_L, obtained by using Equation 4.6, is shown in Figure 4.9. The obtained correlation of the multiple determination coefficient (R^2) is 0.90, indicating an excellent agreement. According to Equation 4.6, as u_G and u_L increased, D_L also increased. This result agrees with the observations reported by Zhou (1995) and Gamal El-Din and Smith (2001a; 2003). Furthermore, Equation 4.6 yielded much lower D_L values (about 80% lower) compared to those of the impinging jet bubble column studied by Gamal El-Din and Smith (2001b), indicating that a major improvement in the mixing regime resulted from the use of the mixing nozzles.

Samples of the results obtained from the PDA measurements of the bubble sizing are shown in Figures 4.10 and 4.11. The histograms show that most of the bubbles sizes range from 0.0003 to 0.003 m. These figures show that for the same gas flow rate, as the liquid flow rate increased, the bubble sizes decreased. This result can be related to the higher shearing rates exerted by the higher flow rates. Furthermore, when the gas flow rates increased, at a fixed liquid flow rate, higher bubble sizes can be observed. The value of the Sauter mean bubble diameter (d_S, m) was correlated with u_L and u_G as follows:

$$d_S = 3.6 \times 10^{-3} u_G^{0.32} u_L^{-0.19} \qquad [4.7]$$

Figure 4.12 show a comparison between the measured and the calculated d_S. A very good agreement was obtained as the R^2 value was found to be 0.91. The value of d_S obtained by using the nozzles (Equation 4.7) was found to be about 50 to 60% of the d_S for the column without nozzles (Equations 3.18 and 3.19). Therefore, the mass transfer efficiency is expected to be higher for the bubble column with mixing nozzle as the available bubble surface area is higher.

The results obtained from the gas hold-up (ε_G) measurements were collected and correlated with u_L and u_G as follows (R^2 = 0.95):

$$\varepsilon_G = 3.25 u_G^{1.54} u_L^{-0.67} \qquad [4.8]$$

The values of ε_G obtained from Equation 4.8 were found to be comparable to the values of ε_G obtained for the same bubble column without nozzles. This result is due mainly to the high dependence of ε_G on u_G compared to u_L. Since ε_G and d_S have been determined, one can estimate the value of the specific bubble interfacial area (a, m) by using the following equation:

$$a = \frac{6 \cdot \varepsilon_G}{d_S} \qquad [4.9]$$

Substituting Equations 4.7 and 4.8 into Equation 4.9 will yield the following:

$$a = 5.42 \times 10^{3} u_G^{1.22} u_L^{-0.48} \qquad [4.10]$$

The nozzles have enhanced the values of *a* by a factor of 1.5 to 2. This result indicates that the mass transfer efficiency was consequently enhanced. If the value of a local mass transfer coefficient (k_L) of the contactor determined by (Baawain et al., 2007) remains the same for both cases of the bubble column (i.e. with and without nozzles), then the overall mass transfer coefficient (k_La, s^{-1})can be expressed as follows:

$$k_L a = 88.8 u_G^{1.57} u_L^{-0.36} \qquad [4.11]$$

Equation 4.11 indicates that k_La will range from 0.01 s^{-1} to 0.33 s^{-1} for the range of the operational conditions shown in Table 4.2. The corresponding values for the bubble column without nozzles are 0.006 s^{-1} to 0.16 s^{-1}.

4.4 CONCLUSIONS

This study explored the hydrodynamic characteristics of an impinging jet ozone bubble column with mixing nozzles by using non-intrusive laser measuring techniques. A planar laser-induced fluorescence (PLIF) was employed to estimate the concentration distribution of a scalar tracer in the bubble column. The particle image velocimetry (PIV) was used to evaluate the flow pattern of the two phases under different operating conditions. Furthermore, the bubble size distribution was estimated by using the particle sizing method. In order to evaluate the mass transfer efficiency, gas hold-up (ε_G) measurements were also conducted for the studied operating conditions.

The results obtained by using the PLIF system showed that the nozzles affected the dispersion favourably as the axial dispersion coefficient was found to be much lower (about 80% lower) than that of the column without nozzles. The mixing patterns observed by the velocity vectors (obtained by using the PIV system) suggested a considerable lateral mixing due to the increased momentum of the two phase jets exerted by the nozzles. Furthermore, the bubble sizes (obtained by using the PDA system) were found much smaller than the ones formed in conventional bubble columns. The combination of the gas hold-up measurements and the bubble size distributions allowed for the specific interfacial area (*a*) to be determined. Consequently, the overall mass transfer coefficient (k_La) was estimated. It was noted that enhanced mass transfer rates can be obtained by using this column, as high ε_G, a, and k_La values were achieved.

Table 4.1 Summary of PDA configuration and operational settings.

Processor		Optical PDA	
High voltage activation	Automatic	1. Beam system	
Anode current warning	90%	Wavelength	514.5 nm
Calibration mode	Automatic	Focal length	500 mm
40 MHz Frequency shift	Enable	Beam diameter	1.35 mm
		Expander ratio	1.0
Coincidence Group		Beam spacing	20 mm
1. General		Frequency shift	40 MHz
Filter method	Overlapped	2. PDA receiver	
Spherical validation	On	Receiver type	Fiber PDA
2. LDA1		Scattering angle	71°
Record length mode	Auto-adaptive	Receiver focal length	400 mm
Record length	32	Receiver expander ratio	1.0
Maximum record length	256	Fringe direction	Positive
High voltage level	1000 V	Scattering mode	Reflection
Signal gain	30 dB	Aperture mask	Mask C
Anode current limit	1500 μA	Spherical validation	5%
Frequency shift	Fixed	3. Particle properties	
Frequency shift direction	Up	Particle name	Air
3.PDA2		Particle refractive index	1.0
High voltage level	1000 V	3. Medium properties	
3.PDA3		Medium name	Water
High voltage level	1000 V	Medium refractive index	1.334

Table 4.2 Summary of the operating conditions used for the PIV, PLIF and PDA experiments.

Experiment number	Liquid flowrate, $Q_L \times 10^{-5}$ (m^3/s)	Gas flowrate, $Q_G \times 10^{-5}$ (m^3/s)	Superficial liquid velocity, $u_L \times 10^{-3}$ (m/s)	Superficial gas velocity, $u_G \times 10^{-3}$ (m/s)	Gas/ Liquid ratio, Q_G/Q_L
1	6.3	0	8.02	0	0
2	6.3	0.83	8.02	1.01	0.13
3	6.3	1.67	8.02	2.12	0.27
4	6.3	2.50	8.02	3.18	0.40
5	6.3	3.33	8.02	4.24	0.53
6	12.6	0	16.0	0	0
7	12.6	0.83	16.0	1.01	0.07
8	12.6	1.67	16.0	2.12	0.13
9	12.6	2.50	16.0	3.18	0.20
10	12.6	3.33	16.0	4.24	0.26
11	12.6	6.67	24.1	8.48	0.53
12	18.9	0	24.1	0	0
13	18.9	0.83	24.1	1.01	0.04
14	18.9	1.67	24.1	2.12	0.09
15	18.9	2.50	24.1	3.18	0.13
16	18.9	3.33	24.1	4.24	0.18
17	18.9	6.67	24.1	8.48	0.35
18	18.9	10.0	24.1	12.7	0.53

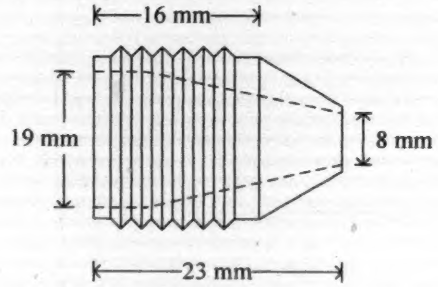

N-8 Mazzei mixing nozzle

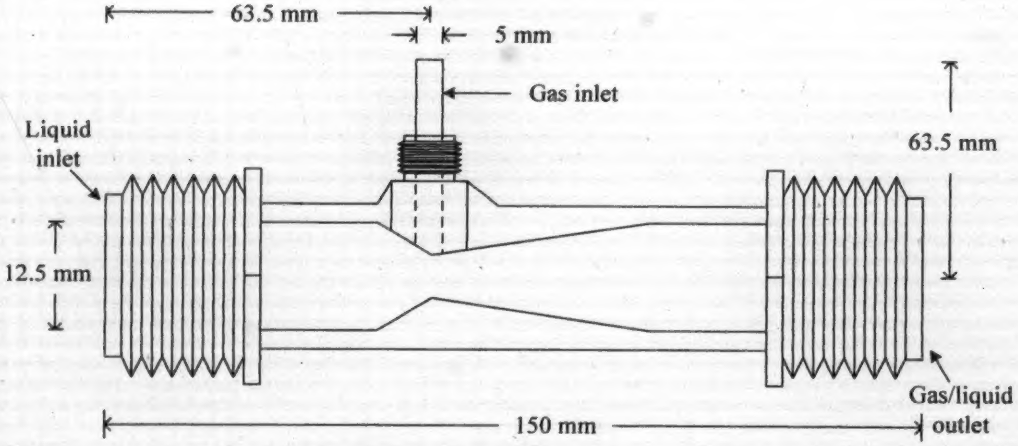

Model 384 Mazzei injector

Figure 4.1 Critical dimensions and geometry of Mazzei injector and nozzle.

(a) PIV setup

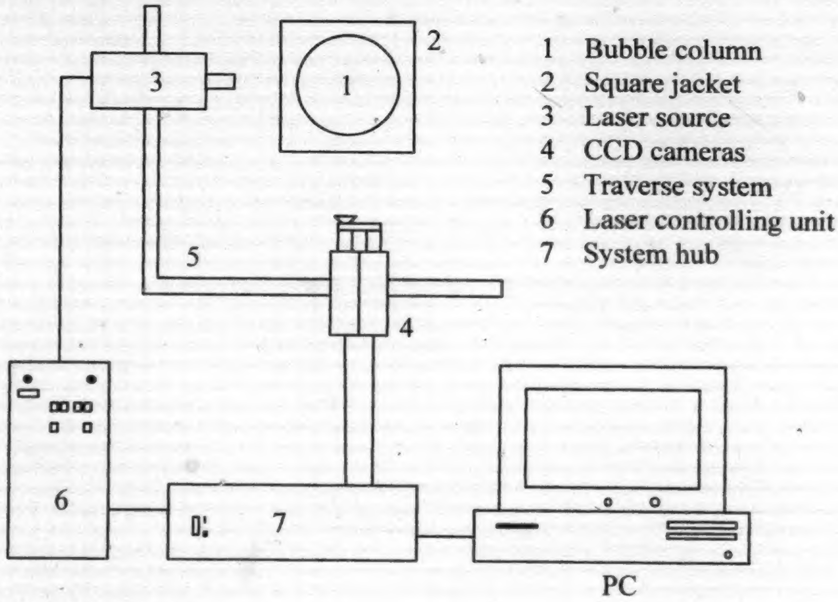

1 Bubble column
2 Square jacket
3 Laser source
4 CCD cameras
5 Traverse system
6 Laser controlling unit
7 System hub

(b) PDA setup

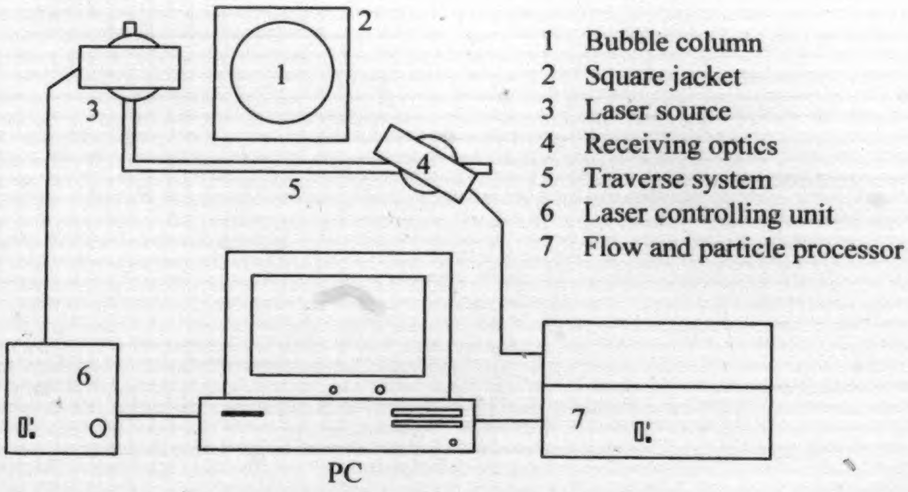

1 Bubble column
2 Square jacket
3 Laser source
4 Receiving optics
5 Traverse system
6 Laser controlling unit
7 Flow and particle processor

Figure 4.2 Experimental setup.

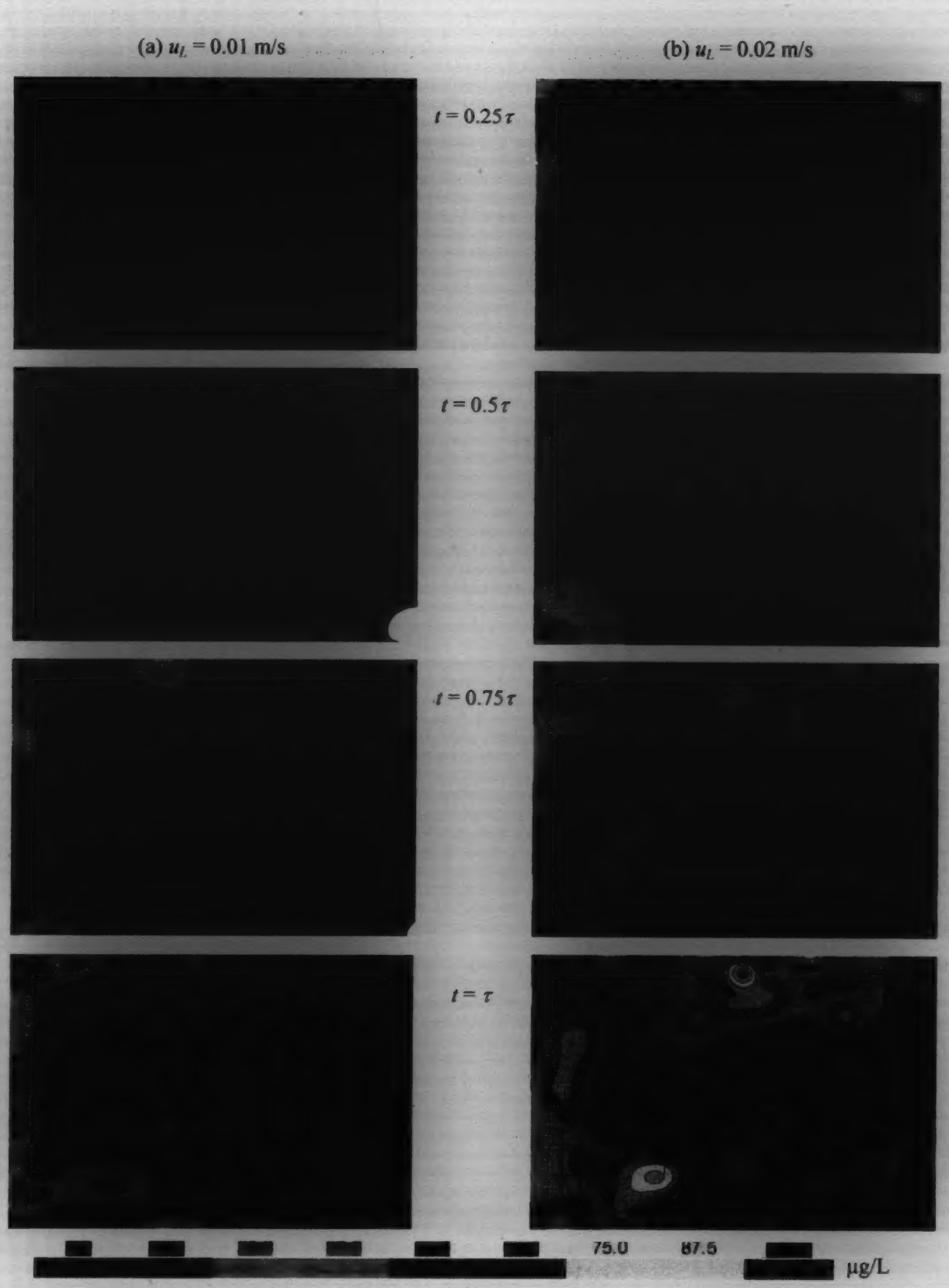

Figure 4.3 PLIF images showing concentration distribution for different liquid flow rates.

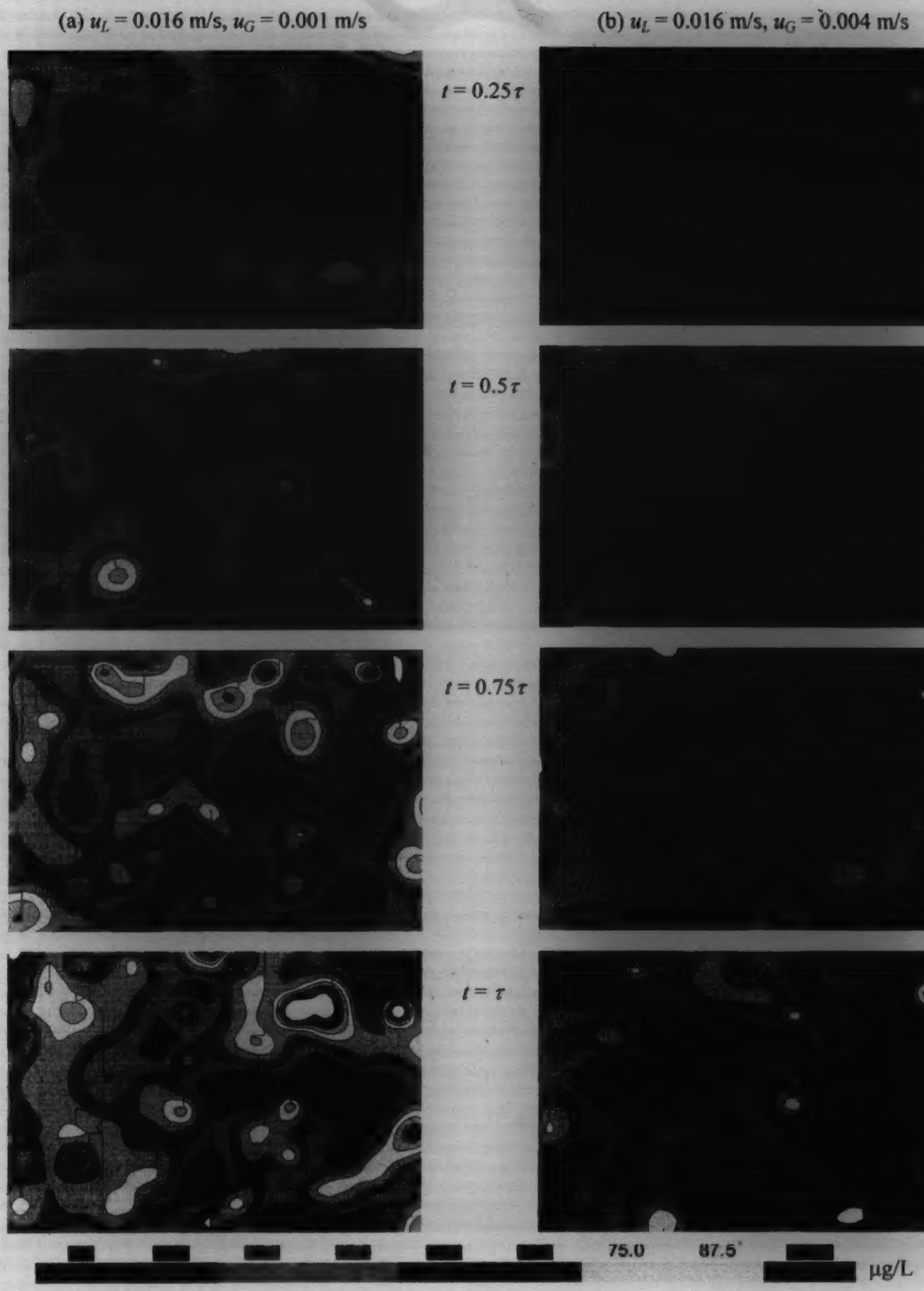

(a) $u_L = 0.016$ m/s, $u_G = 0.001$ m/s

(b) $u_L = 0.016$ m/s, $u_G = 0.004$ m/s

Figure 4.4 PLIF images showing concentration distribution of two different gas flow rates for the same liquid flow rate.

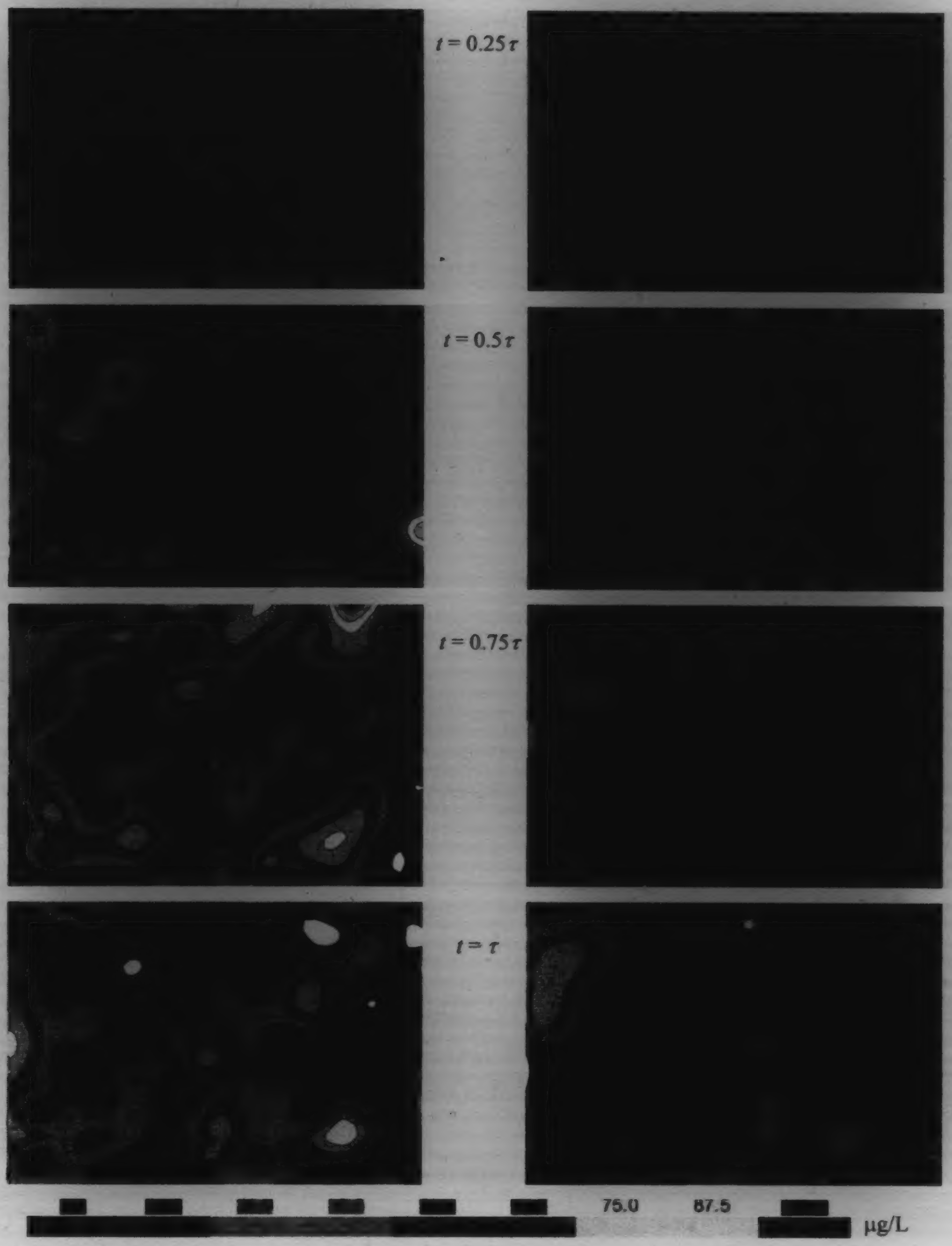

(a) $u_L = 0.008$ m/s, $u_G = 0.002$ m/s

(b) $u_L = 0.024$ m/s, $u_G = 0.002$ m/s

Figure 4.5 PLIF images showing concentration distribution of two different liquid flow rates for the same gas flow rate.

(a) $u_L = 0.008$ m/s

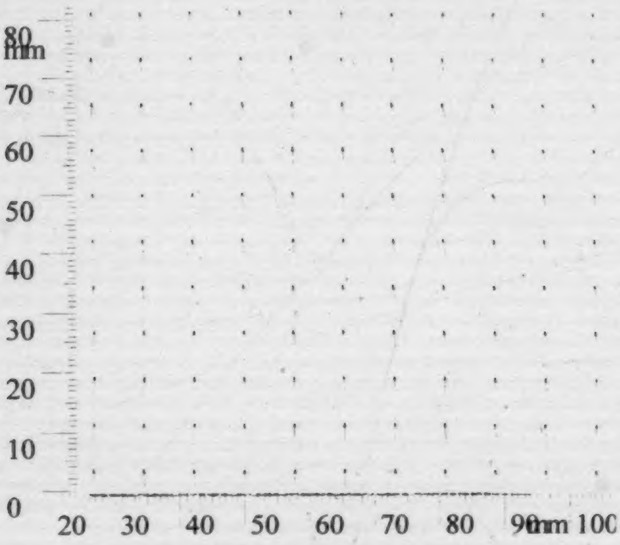

(b) $u_L = 0.016$ m/s

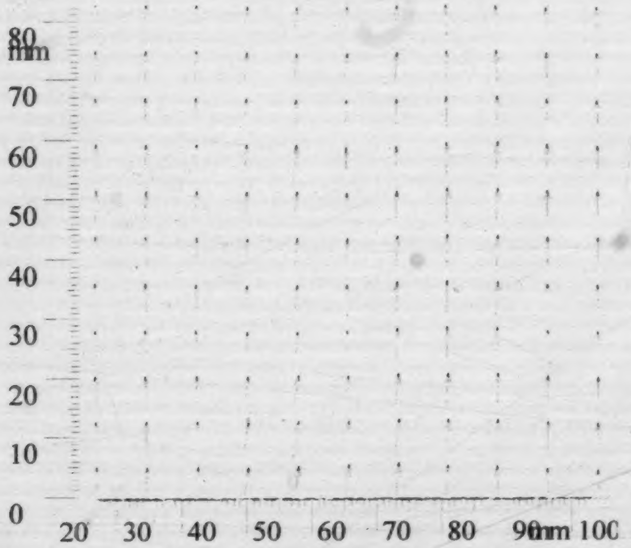

Scale: 5mm = 0.02 m/s

Figure 4.6 Velocity vectors for different liquid flow rates without gas injection.

(a) $u_G = 0.002$ m/s, liquid phase

(b) $u_G = 0.002$ m/s, gas phase

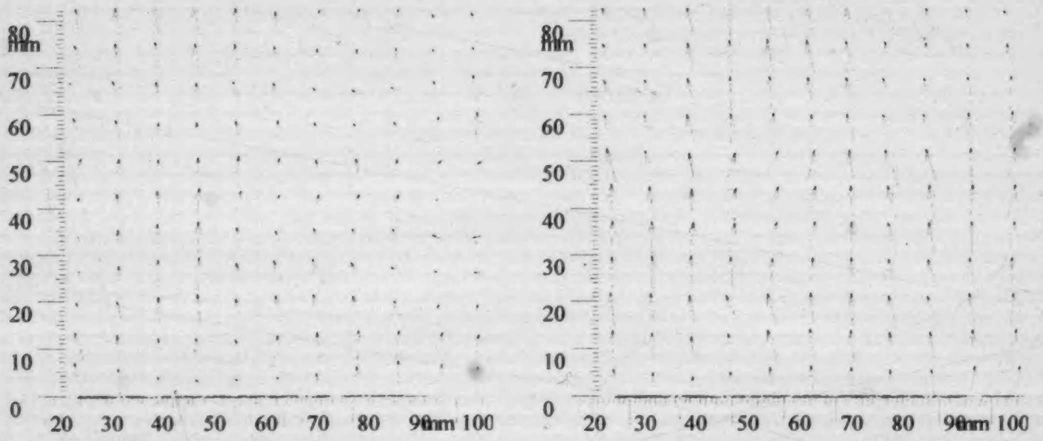

(c) $u_G = 0.008$ m/s, liquid phase

(d) $u_G = 0.008$ m/s, gas phase

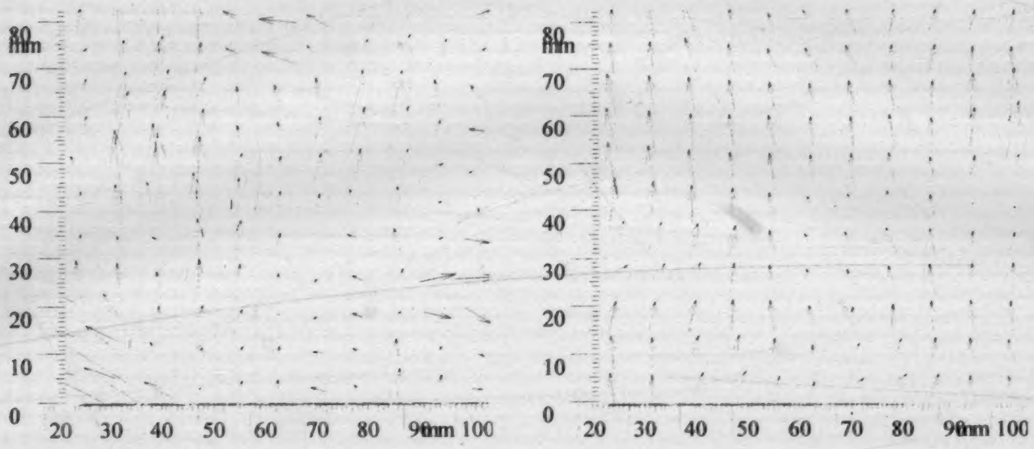

Scale: 5mm = 0.02 m/s for (a) and (c)

Scale: 5mm = 0.2 m/s for (b) and (d)

Figure 4.7 Velocity vectors for liquid and gas phases under different gas flow rates ($Q_L = 1.26 \times 10^{-4}$ m^3/s).

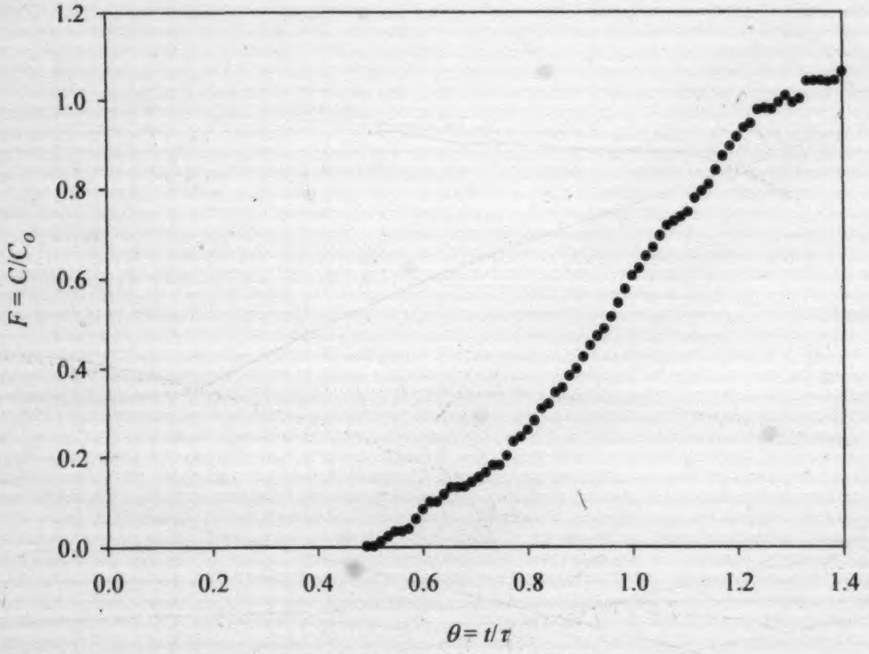

Figure 4.8 Step response curve from PLIF images (u_L = 0.016 m/s, u_G = 0.001 m/s).

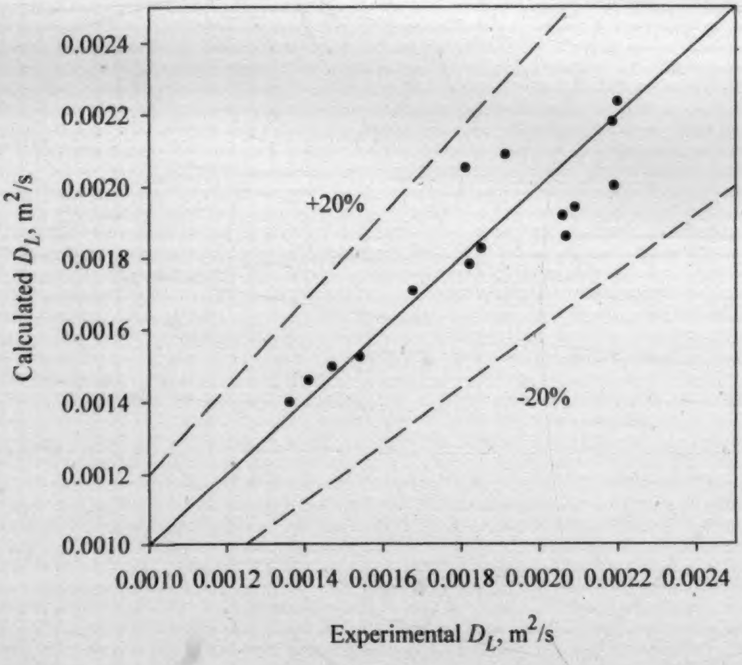

Figure 4.9 Comparison between the predicted and the experimental D_L.

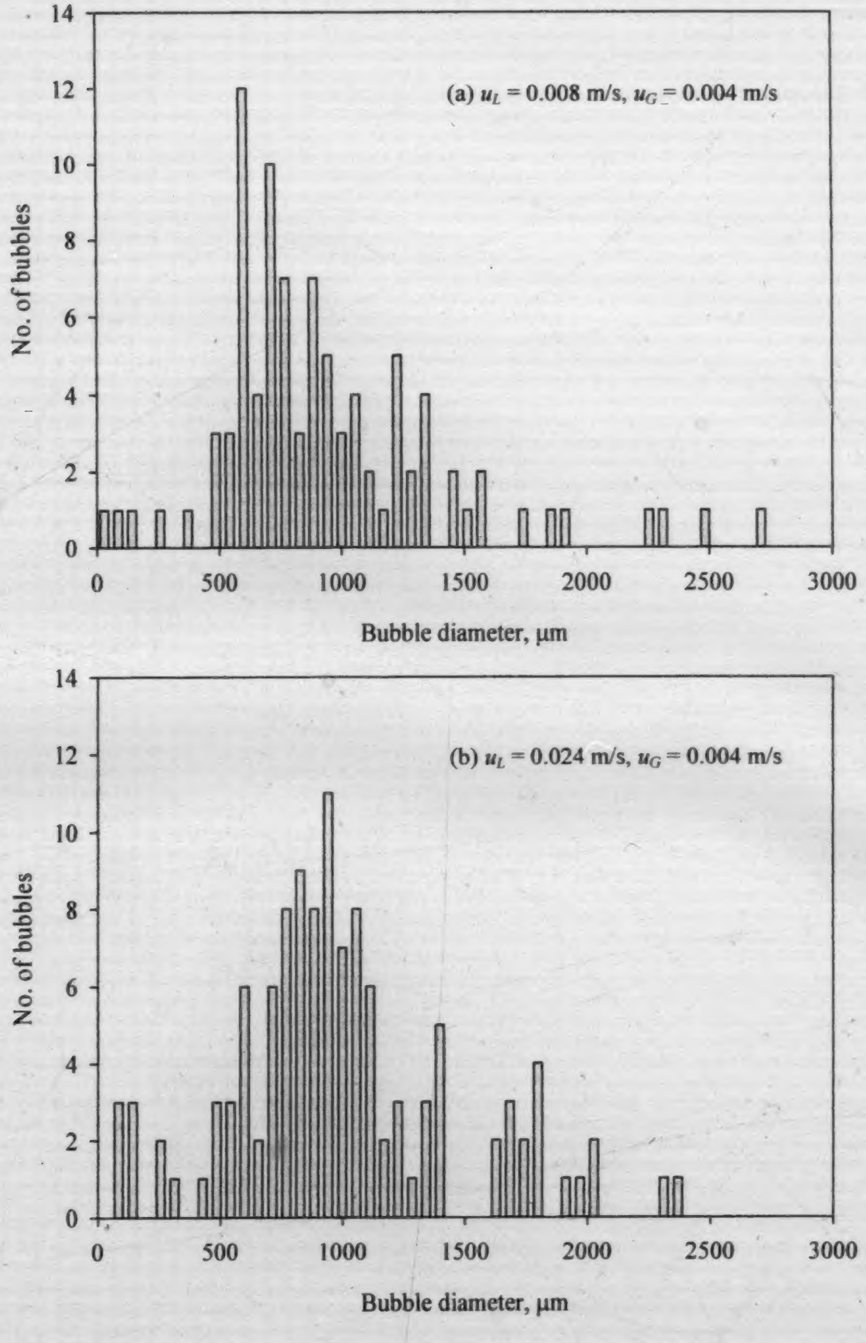

Figure 4.10 Bubble size distributions under different liquid flow rates.

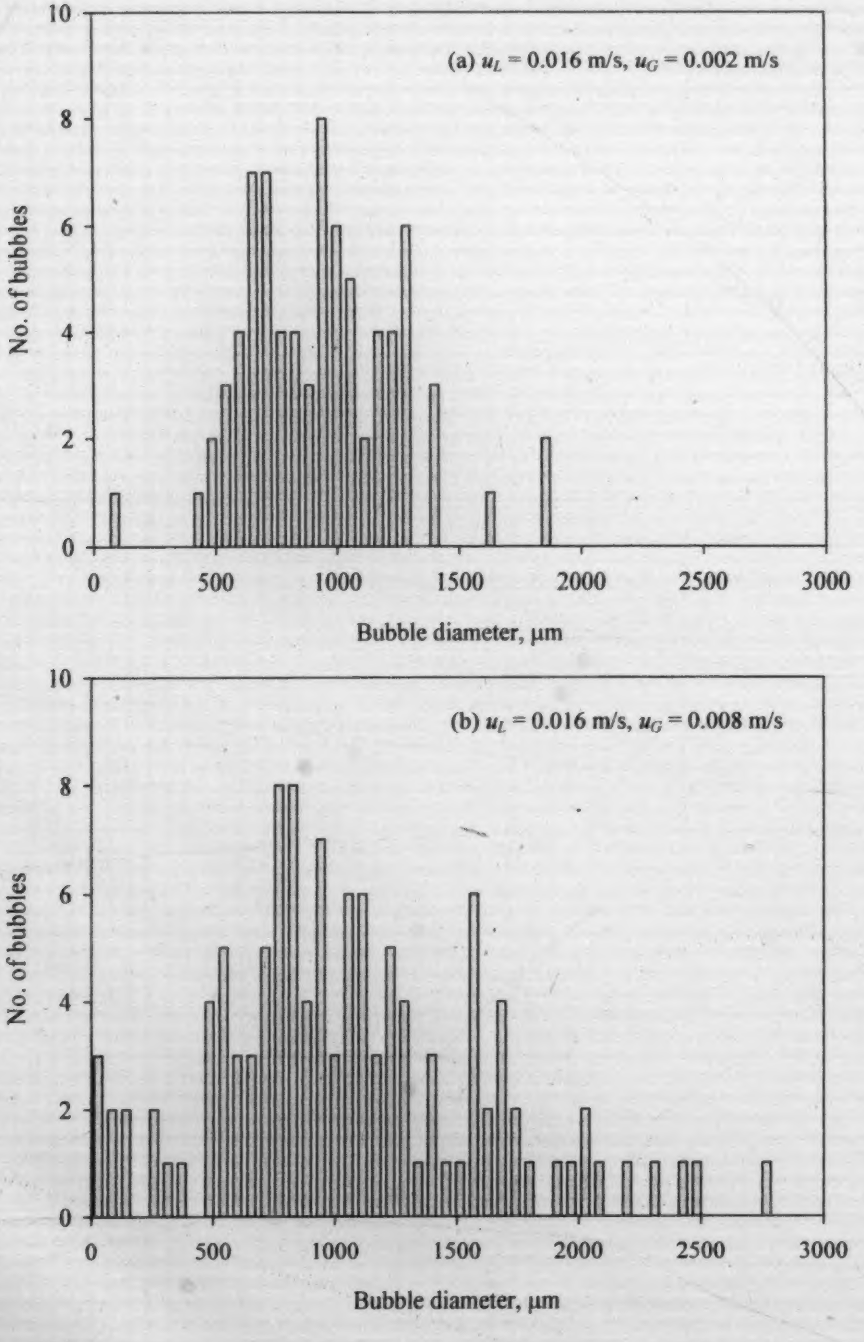

Figure 4.11 Bubble size distributions under different gas flow rates.

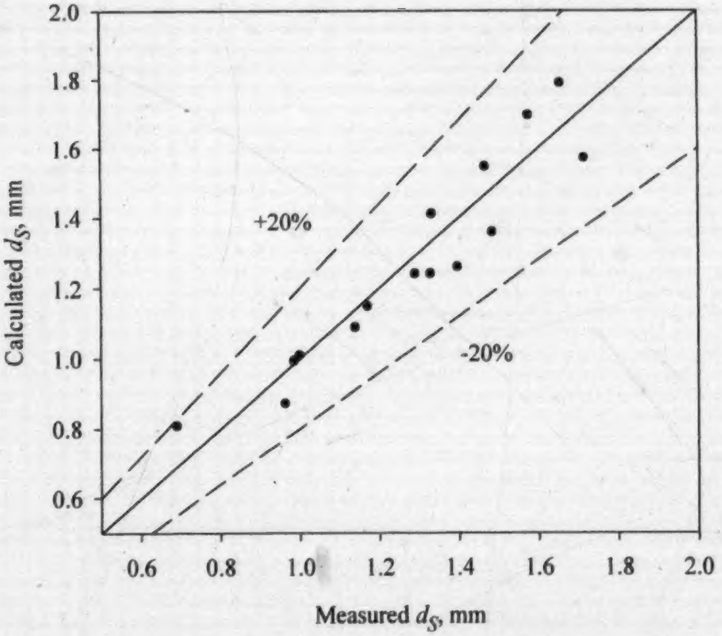

Figure 4.12 Comparison between the predicted and the experimental d_S.

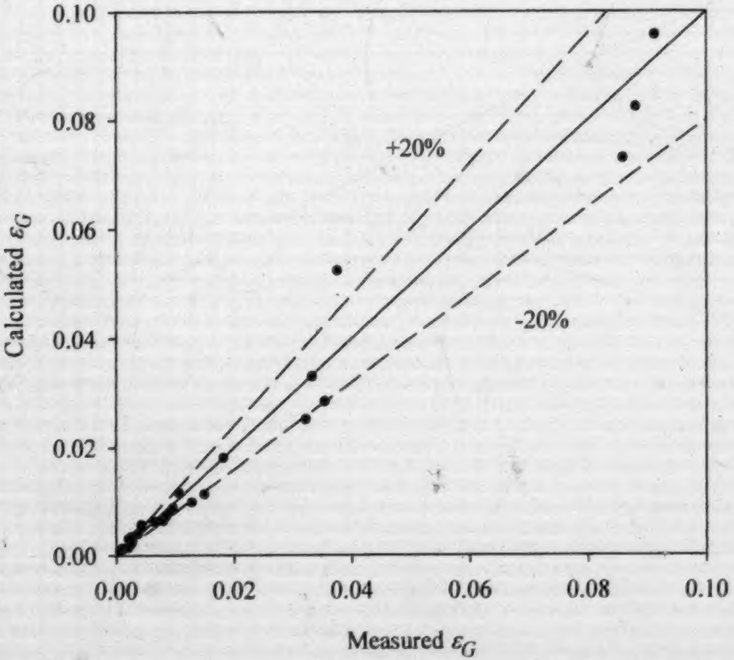

Figure 4.13 Comparison between the predicted and the experimental ε_G.

4.5 REFERENCES

1 Albrecht, H.E., M. Borys, N. Damaschke, and C. Tropea, *Laser Doppler and Phase Doppler Measurement Techniques*. (N. Y: Springer-Velag Berlin Heidelberg, 2002).

2 Baawain, M.B., M. Gamal El-Din, and D.W. Smith, "Impinging-Jet Ozone Bubble Column Modeling: Hydrodynamics, Gas Hold-up, Bubble Characteristics, and Ozone Mass Transfer", *Ozone Sci. & Eng.* (2007).

3 Bernard, P.S., and J.M. Wallace, *Turbulent Flow: Analysis, Measurement and Prediction*. (Hoboken, N. J.: John Wiley & Sons, Inc., 2002).

4 Bollyky, L.J., "The Mass-Transfer of Ozone into Water - Energy-Requirements State of the Art", *Ozone-Science & Engineering*, 3(3): 181-210 (1981).

5 Charpentier, J.-C., *Mass-Transfer Rates in Gas-Liquid Absorbers and Reactors: Advances in Chemical Engineering*. (Toronto: Academic Press, 1981).

6 Deckwer, W.D., and A. Schumpe, "Improved Tools for Bubble Column Reactor Design and Scale-Up", *Chemical Engineering Science*, 48(5): 889-911 (1993).

7 Durst, F., G. Brenn, and T.H. Xu, "A Review of the Development and Characteristics of Planner Phase-Doppler Anemometry", *Meas. Sci. Technol.* , 8: 1203-1221 (1997).

8 Gamal El-Din, M.G., and D.W. Smith, "Development of Transient Back Flow Cell Model (Bfcm) for Bubble Columns", *Ozone-Science & Engineering*, 23(4): 313-326 (2001a).

9 Gamal El-Din, M.G., and D.W. Smith, "Maximizing the Enhanced Ozone Oxidation of Kraft Pulp Mill Effluents in an Impinging-Jet Bubble Column", *Ozone-Science & Engineering*, 23(6): 479-493 (2001b).

10 Gamal El-Din, M.G., and D.W. Smith, "Mass Transfer Analysis in Ozone Bubble Columns", *Journal of Environmental Engineering and Science*, 2(1): 63-76 (2003).

11 Kuo, C.-H., and F.H. Yocum, "Mass Transfer of Ozone into Aqueous Systems", Handbook of Ozone Technology and Applications, Rice, R.G. and A. Netzer, eds. (Ann Arbor, Michigan, U.S.A.: Ann Arbor Science Publishers, 105-141, 1982).

12 Levenspiel, O., *Chemical Reaction Engineering*. (Hoboken, NJ.: J. Wiley & Sons, Inc., 1999).

13 Levenspiel, O., and W.K. Smith, "Notes on the Diffusion-Type Model for the Longitudinal Mixing of Fluids in Flow", *Chem. Eng. Sci.*, 6(4-5): 227-233 (1957).

14 Raffel, M., C. Willert, and J. Kompenhans, *Particle Image Velocimetry: A Practical Guide*. . (N. Y.: Springer-Velag Berlin Heidelberg, 1998).

15 Stanislas, M., J. Kompenhans, and J. Westerweel, *Particle Image Velocimetry: Progress Towards Industrial Application*. (Dordrecht, The Netherlands: Kluwer Academic Publishers, 2000).

16 Tropea, C., "Laser-Doppler Anemometry - Recent Developments and Future Challenges", *Measurement Science & Technology*, 6(6): 605-619 (1995).

17 Vancruyningen, I., A. Lozano, and R.K. Hanson, "Quantitative Imaging of Concentration by Planar Laser-Induced Fluorescence", *Experiments in Fluids*, 10(1): 41-49 (1990).

18 Willert, C.E., and M. Gharib, "Digital Particle Image Velocimetry", *Experiments in Fluids*, 10(4): 181-193 (1991).

19 Zhou, H., "Investigation of Ozone Disinfection Kinetics and Contactor Performance Modelling", Ph.D. , University of Alberta, Edmonton, Alberta, Canada., (1995).

CHAPTER 5

HYDRODYNAMIC CHARACTERIZATION AND MASS TRANSFER ANALYSIS OF AN IN-LINE MULTI-JETS OZONE CONTACTOR

5.1 INTRODUCTION

Designing an effective reactor requires information, knowledge, and experience from different areas including chemical kinetics, fluid mechanics, and mass transfer (Levenspiel, 1999). However, due to the difficulty of accurately estimating the parameters needed for these areas, empirical and semi-empirical relationships are used in designing such reactors. These relationships are not reliable and/or valid over the reactors' wide range of practical applications (Joshi, 2002). Furthermore, recent challenges resulting from the existence of micro-pollutants in drinking water supplies (Petrovic et al., 2003) have increased the need for accurately designed advanced water and wastewater treatment reactors. Hence, a proper design procedure has to be followed in order to reduce the prevailing empiricism associated with conventional water treatment reactors. Joshi and Ranade (2003) suggested the following procedure: (1) identify the desired fluid dynamic characteristics by understanding the process requirements; (2) develop possible reactor configurations/operating protocols to achieve the desired fluid dynamic characteristics; (3) develop quantitative relationships between the reactor configuration and performance; and (4) optimize and fine-tune the final reactor design.

The use of non-intrusive measurement techniques (i.e., techniques resulting in no direct interaction with the flow field) such as the use of laser measurement systems can provide accurate hydrodynamic characteristics for a reactor. Laser measuring techniques are non-intrusive and directional-sensitive and provide accurate and high-resolution measurements (Albrecht et al., 2002). The laser systems used for characterizing reactors' hydrodynamics include the laser Doppler anemometer (LDA), the particle dynamics analyzer (PDA), the particle image velocimetry (PIV), and the planer laser-induced fluorescence (PLIF) (Albrecht et al., 2002; Atkinson et al., 2000). The LDA and PDA systems are commonly used to provide the flow velocity at one point in a flow field (the PDA can also provide a simultaneous measurement of the particles' sizes) (Durst et al., 1997). The PIV system provides simultaneous planar measurements of the flow velocity by measuring the displacement of seeded particles over a relatively short time interval (Atkinson et al., 2000; Bernard and Wallace, 2002; Raffel et al., 1998). The PLIF system is used to obtain a scalar concentration field in water by introducing a fluorescent dye as a passive scalar in the flow. The dye absorbs incident light, during the illuminating process of the laser, at one wavelength and re-emits it at a different wavelength with an intensity proportional to the dye concentration at the measuring point (Bernard and Wallace, 2002).

The objectives of this study are to: (1) characterize the hydrodynamics of an in-line multi-jets ozone contactor by utilizing PLIF laser measurement techniques, (2) evaluate the flow patterns at different locations along the contactor by using PIV laser measurement techniques (3) analyze the mass transfer efficiency of the contactor, and (4) optimize the system's operating conditions.

5.2 EXPERIMENTAL SET-UP

5.2.1 Flow Facility

A pilot-scale ozone contactor is shown in Figure 5.1. The pipe was made of a round clear acrylic glass tube 0.1 m in diameter (d) and 2 m in length (L). The water flow was driven through the system from a 2 m^3 tank via two lines, main stream and side stream, by utilizing centrifugal pumps. The designed water flow rate (Q_L) for this contactor was 0.01 m^3/s with a side stream to main stream (liquid to liquid) ratio ranging from 2.5 to 20%. However, other flow rates were also tested to cover a range of Reynolds number, Re (based on the pipe diameter) of 45000 to 100000. The side stream line had multi jets that employed Mazzei® venturi injectors (model 584) with N-8 Mazzei® nozzles as shown in Figure 5.2. The jets were aligned along the axial direction of the contactor in groups of two opposing jets. The axial distance between any two consecutive jets along the axial direction of the contactor was fixed at 0.15 m. These jets allowed for the gas to be introduced into the system in either injection or suction modes. The end of the pipe had two outlets to allow for recycling or draining of the water. An outer square jacket of 0.15 m sides and 1.5 m length was installed around the pipe to reduce optical distortion. A diffuser with a diameter of 0.003 m was installed at the entry region of the pipe at a position 0.3 m downstream from the first side stream injector. This diffuser was used to inject the tracer for the PLIF runs and the seeding particles for the PIV runs.

When a side jet enters a pipe flow (i.e., a cross flow), the jet can be characterized by using four geometric/flow parameters: the jet diameter D_j (m), the pipe diameter d (m), the jet to pipe velocity ratio r (u_j/u_p), and the pipe flow Reynolds number Re (Forney et al., 1999; Pan and Meng, 2001). The combination of rD_j, known as the jet momentum length ($l_m = D_j u_j / u_p$, m), represents the distance over which the jet travels before it bends over in the cross flow. In the case of a turbulent pipe flow, it is desired that the jet penetrates into the potential core of the pipe flow before the jet turns and aligns with the pipe flow. This regime is referred to as the jet-mixing regime and can be achieved when the dimensionless parameter rD_j/d is within a range from 0.07 to 1.0 (Pan and Meng, 2001; Sroka and Forney, 1989). In the jet-mixing regime, the jet expands quickly in the pipe due to turbulent entrainment and, therefore, creates efficient macromixing (Cozewith and Busko, 1989; Pan and Meng, 2001). If the parameter rD_j/d is greater than 1.0, the jet hits the opposite wall of the pipe, and the impingement helps in creating more efficient micromixing (Tosun, 1987). However, a significant stress on the pipe wall is exerted due to the jet impingement and, thus, such designs are not desirable from a practical point of view (Pan and Meng, 2001). When rD_j/d is smaller than 0.07, the jet attaches to the pipe wall and grows slowly without significant penetration into the pipe flow. This result is undesirable as the resultant mixing will be inefficient.

Two side jet types were used in this study: the tracer/seeding particle injection port (0.003 m diameter) and the 1-phase/2-phase side stream nozzles (N-8 Mazzei® nozzles, 0.008 m diameter). The flow rates through these jets were 7.6 x 10^{-5} m^3/s and 2.5 x 10^{-4} m^3/s (per one nozzle), respectively. The corresponding rD_j/d values for the injection port and the side stream nozzles were 0.24 and 0.35, respectively, which were within the desirable jet-mixing regime.

5.2.2 PIV/PLIF Set-up

The PIV/PLIF set-up used in the hydrodynamic analysis of the contactor consisted of a laser source, charge coupled device (CCD) cameras, and processing units (Figure 5.1). An Nd:Yag dual cavity laser was utilized in this study for both the PIV and PLIF experiments. The emitted wavelength of the utilized Nd:Yag laser was 532 nm with a pulse duration of 10 ns. The period between pulses was set to 1000 μs during PIV measurements and 100 μs during PLIF measurements with a maximum repetition rate of 8.0 Hz. The measurements were obtained at a time interval of 1000 ms during PIV measurements and 125 ms during PLIF measurements. The CCD cameras were configured to use double frames for PIV measurements (velocity measurements) and a single frame for PLIF measurements (concentration measurements). A FlowMap System Hub® produced by Dantec Dynamics was used to transfer the data to a PC where FlowMap Software® was used for sequential analysis of the collected data.

The PLIF system was first calibrated by measuring the intensity of 5 different concentrations of Rhodamine 6G (Rh6G) solutions ranging from zero to 500 μg/L at a power level ranging from 50 to 150 mJ. The concentration versus the intensity was plotted to determine the most appropriate calibration curve for this study. The calibration curve obtained for the 150 mJ power gave the highest correlation coefficient (0.85). Therefore, this power level was used for the PLIF measurements.

The PIV measurements were taken by using two CCD cameras with a double-frame mode for measuring the velocity of both phases (liquid and gas) simultaneously by utilizing special filters. Melamine-formaldehyde (MF) spheres, coated with Rhodamine B

(RhB), were used as seeding particles to obtain the liquid velocity measurements while gas bubbles represented the seeding particles for the gas velocity measurements. The 2-D velocity vectors were then obtained by employing an interrogation cell of 64 x 64 pixels that was a subdomain of a 1344 x 1024 pixel viewing area. The interrogation cell was then shifted with 25% overlap, and, thus, 21 x 16 velocity vectors were obtained in each instantaneous PIV sample. However, for illustration purposes, 13 x 10 velocity vectors maps were produced.

5.2.3 Gas Mass Transfer Set-up

The experimental set-up for the mass transfer of the gas in the pilot-scale multi-jets ozone contactor shown in Figure 5.1 consisted of two dissolved oxygen (DO) probes (model YSI 5750) that were placed 1.37 m apart in the contactor (one upstream of the jets and one downstream of the two-phase jets), two DO meters (YSI 50B model) to obtain DO measurements directly, air and nitrogen gas cylinders. The system was arranged to operate under the suction or injection modes of gas through the Mazzei injectors (Figure 5.2). The gas flow rate during the suction mode was kept constant through each injector by keeping the side stream pressure constant when using any number of injectors and monitoring the flow rates by using gas flow meters. During the injection mode, gas cylinders were used to supply the required amounts of gas by using pressure regulators and gas flow meters.

5.3 MEASUREMENT DESCRIPTION

The PLIF and PIV experimental conditions conducted in this study are summarized in Tables 5.1 and 5.2, respectively. The pressure in the main flow and side stream was kept constant at 69 kPa (10 psi) and 138 kPa (20 psi), respectively, under the operating conditions shown in Tables 5.1 and 5.2. After reaching a steady state flow condition, a continuous injection of a 12.5 mg/L of the Rh6G tracer at about 7.56 x 10^{-5} m^3/s (yielding about 95 μg/L average concentration when fully mixed with the total liquid flow rate (Q_L) of 0.01 m^3/s) was introduced into the system through the injection point at the entrance of the contactor, as shown in Figure 5.1. The continuous (step) input of the tracer was chosen over the slug input for this contactor due to the relatively short theoretical residence time (1.0 to 2.0 s) of the contactor. The effect of increasing Re was studied first by varying Q_L from 7.56 x 10^{-3} to 0.01 m^3/s without side stream injection. The effect of 1-phase (liquid phase) side stream injection was investigated by keeping Q_L at the designed value (0.01 m^3/s) and varying the liquid side stream flow from 2.5 x 10^{-4} m^3/s (for one jet) to about 1.8 x 10^{-3} m^3/s (for eight jets). Then, the system was studied under 2-phase side stream injection by varying the gas flow rate (Q_G) from 5.0 x 10^{-5} m^3/s (for one jet) to 4.0 x 10^{-4} m^3/s (for eight jets). Both the 1-phase and the 2-phase, side jets were tested under opposing (jets released to the contactor facing each others) and alternating (jets released to the contactor from the opposite side but apart with a distance of 0.15 m) alignments. The PLIF process of image capturing covered about 5 times the detention time required for the tracer to pass through the system under each operating condition (duplicate measurements were applied to reduce the uncertainty associated with the measurements).

During the PIV measurements, the flow patterns of the system were studied for 1-phase and 2-phase flow conditions as shown in Table 5.2. The value of Q_L was varied from 7.56 x 10^{-3} to 0.01 m^3/s while Q_G ranged from 5.0 x 10^{-5} m^3/s to 4.0 x 10^{-4} m^3/s. The measurements were taken at several locations along the system (at the pipe end where the PLIF measurement were taken, at the mixing zone of the alternating jets, and at the mixing zone of the opposing jets) in order to evaluate the system's flow patterns. The PIV process of image capturing was taken in duplicate measurements. To avoid contaminating of the water tank with the tracer dye and the seeding particles, the water was not recycled during the PLIF and PIV measurements.

The gas mass transfer measurements were conducted for the wide range of operating conditions as shown in Table 5.3. The DO was first stripped out of the water in the tank by the injection of nitrogen gas until the DO level fell below 0.5 mg/L. The water was then recycled through the system for a few minutes by using both the main and side streams, with no injection of gas, to ensure that a steady state was reached and that the DO level was still below 0.5 mg/L. The gas was then introduced into the system through the Mazzei injectors (Figure 5.2), and the change in DO concentrations was monitored under each operating condition at the two locations. As the flow was recycled to the tank, a pressure drop at the main line to about 41 kPa (6 psi) was observed when the total Q_L was 0.01 m^3/s and to about 36 kPa (5.3 psi) when Q_L wass 7.6 x 10^{-3} m^3/s.

5.4 RESULTS AND DISCUSSION

5.4.1 Reactor's Hydrodynamics

All images captured during the PLIF experiments were converted to 2D concentration fields through the obtained calibration relation by using the FlowMap Software®. A re-sampling of these concentration fields yielded colored contour maps that show the concentration distribution of the tracer along the cross-section of the contactor parallel to the flow direction. A colored contour map representing the concentration distribution at different sampling (image capturing) times for two different liquid flow rates (Q_L of 7.56 x 10^{-3} m^3/s and 0.01 m^3/s) without side stream injection is shown in Figure 5.3. Figure 5.3a (Q_L = 7.56 x 10^{-3} m^3/s) shows that segments of the Rh6G tracer reached the measurement point earlier than those shown in Figure 5.3b (Q_L = 0.01 m^3/s). Furthermore, a higher cross-sectional (radial) mixing can be observed under the higher liquid flow rate as a relatively uniform concentration of the Rh6G dye can be perceived. The concentration distribution for 1-phase (liquid phase) side stream jets at Q_L = 0.01 m^3/s is shown in Figure 5.4. This figure shows color contour maps for 4 opposing and 4 alternating jets. Some tracer segments appear to have passed through the reactor with the opposing 1-phase jets' condition slightly faster than the alternating 1-phase jets' condition. However, a relatively better radial mixing was observed under the opposing jets' condition. Therefore, further analysis is needed to explain the dispersion under these conditions (see next section).

The concentration distribution of 2-phase (liquid and gas phases) side stream jets at Q_L = 0.01 m^3/s and Q_G of 2.0 x 10^{-4} m^3/s is shown in Figure 5.5 for 4 opposing and alternating jets. This figure shows that segments of the tracer have passed through the contactor with the alternating 2-phase jets relatively faster than the opposing 2-phase jets. In contrast, a relatively higher cross-sectional mixing can be observed in the case of the opposing jets. Therefore, it is expected that the 2 opposing jets will exert a lower axial dispersion compared to that of the same number of alternating jets.

The mixing and the dispersion in the contactor could be further analyzed through velocity measurements obtained from the PIV system for the studied operating conditions. Figure 5.6 shows the averaged and radial velocity vectors for two different liquid flow rates (Q_L of 7.56 x 10^{-5} m^3/s and 0.01 m^3/s) taken at the pipe's end (the same location as that of the PLIF measurements). This figure shows that the contactor has not reached a fully developed flow at this stage as the distance from the tracer diffuser to the measurement point is 1.61 m. The required length to reach a fully developed flow, under the given turbulent conditions ($l_d = 4.4d\,\mathrm{Re}^{1/6}$, m), is in the order of 2.85 m and 3.0 m for Q_L of 7.56 x 10^{-3} m^3/s and 0.01 m^3/s, respectively. Furthermore, Figure 5.6 also shows that the random radial movement of the flow velocity in the higher flow was more pronounced. This result explains the relative uniformity in the cross-sectional mixing of such a flow rate compared to that of the lower flow rate shown earlier in Figure 5.3.

The velocity vectors of the liquid-phase in-line multi jets (opposing and alternating), obtained at the mixing zone (the entrance zone of the jets), for Q_L of 0.01 m^3/s are shown in Figure 5.7. A better cross-sectional (radial) mixing can clearly be observed when the opposing liquid-phase jets are used. Each jet penetrates to about 0.04 m ($l_m = rD_i$) from each side before the jets bend, merge into each other, and expand with the cross flow. Similarly, the opposing gas-phase jets exert better cross-sectional mixing than the alternating ones, as Figure 5.8 shows. Furthermore, some backmixing was observed in the opposing jets, which was believed to affect the gas transfer rate favourably.

In order to evaluate the mixing in the contactor numerically, the following differential equation representing the dispersion of a conservative tracer (C, μg/L) was considered (Levenspiel, 1999):

$$\frac{\partial C}{\partial \theta} = \left(\frac{D_L}{uL}\right)\frac{\partial^2 C}{\partial z^2} - \frac{\partial C}{\partial z} \qquad [5.1]$$

where θ is a dimensionless time ($\theta = t/\tau = tu/L$, t is time (s)), $\left({}^{D_L}\!/_{uL}\right)$ is the dispersion number (the inverse of the Peclet number, Pe), D_L is the liquid axial dispersion coefficient (m^2/s), u is the pipe flow average velocity (m/s), L is the axial distance between the tracer input point and measurement point (m), and z is the dimensionless axial distance ($z = (ut + x)/L$, x is the axial distance along the pipe (m)). For a step input of a tracer, the shape of the tracer at the measurement point is S-shaped and referred to as the F-curve. The F-curves normally represent the dimensionless concentration (F), the ratio between the tracer concentration at the measurement point (C, μg/L) to the initial mixed tracer concentration (C_o, μg/L), as a function of time. The shape of the F-curve depends on the boundary conditions of the contactor and the dispersion number $\left({}^{D_L}\!/_{uL}\right)$. The analytical expressions of the F-curves are not available; however, their graphs can be constructed (Levenspiel, 1999). The value $\left({}^{D_L}\!/_{uL}\right)$ can be obtained directly by plotting the experimental data on a probability graph paper as explained below or by differentiating the S-shaped response curve and considering the boundary conditions (Levenspiel and Smith, 1957).

The numerical concentration of the Rh6G values obtained by the PLIF system were extracted for all images under each operating condition, and the step response curves (F-curves) at any position of interest were plotted. An example of an F curve obtained from the PLIF experiments for the tracer concentration at the centre of the images captured for $Q_L = 0.01$ m^3/s (without side injection) is shown in Figure 5.9. In order to obtain the dispersion number of the dye under each operating condition, the probability plot method was employed, as illustrated in Figure 5.10, for $Q_L = 0.01$ m^3/s (without side injection). The standard deviation (σ, s) was obtained from each probability plot as follows:

$$\sigma = \frac{t_{84\%} - t_{16\%}}{2} \qquad [5.2]$$

where $t_{84\%}$ and $t_{16\%}$ are the times corresponding to 84% and 16%, respectively, of the tracer measured at the contactor's outlet. The dispersion number $\left({D_L}/{uL} \right)$ for each operating condition can then be calculated by using the following equation:

$$\frac{D_L}{uL} = \frac{{\sigma_\theta}^2}{2} = \frac{(\sigma / \tau)^2}{2} \qquad [5.3]$$

where σ_θ is the dimensionless standard deviation, and τ is the theoretical detention time of the contactor. In order to validate the findings from the PLIF experiments, the dispersion in the contactor without side stream injection (i.e. the dispersion in a turbulent pipe flow) was compared with the published data. Therefore, the intensity of the dispersion (also referred to as the dispersion parameter, D_L/ud) was determined by multiplying the dispersion number by the geometric factor (L/d). The dispersion parameter is a function of Re (Re = ud/ν, ν is the kinematic viscosity (m^2/s)) and Schmidt number (Sc = ν/D_m, D_m is the molecular diffusivity of the tracer) (Levenspiel, 1999). According to the operating conditions, Re varies from about 45000 to 100000, and Sc varies from 3500 to 5000 as D_m of Rh6G is 2.8×10^{-10} m^2/s (Benes et al., 2001; Hansen et al., 1998). The average water temperature during the PLIF experiments was 9 ± 1 °C. However, Levenspiel (1958; 1999) and Ekambara and Joshi (2003) showed that the effect of Sc (i.e., the effect of molecular diffusion, D_m) can be ignored for turbulent flow conditions (Re > 2300). This phenomenon is illustrated in Figure 5.11, as the values of the dispersion number obtained by several researchers agree with each other at relatively high Re values (especially for Re > 10000). The absolute relative error (ARE) between the dispersion parameter models presented in several research studies (Ekambara and Joshi, 2003; Levenspiel, 1958; Sittel et al., 1968; Taylor, 1954) and the experimental data obtained by Sittel et al. (1968) ranged from 5 to 30% for Re ranging between 10000 to 200000. Furthermore, Figure 5.11 shows a very good agreement between the measured dispersion parameter of the studied contactor and the selected published data for turbulent pipe flow. The absolute relative error (ARE) was within a range of 5 to 20%, which indicates the validity of the obtained PLIF results.

Figure 5.12 shows a plot of D_L as a function of the number of jets, for both 1-phase and 2-phase side jets, under a total Q_L of 0.01 m^3/s. The results show that the contactor with both 1- and 2-phase side injection yielded a higher dispersion coefficient compared to that of the condition without side injection. According to Pan and Meng (2001), the decay of a scalar concentration along the centreline of a jet with a downstream axial distance (x, m) for pipe flow can be written as follows:

$$\xi \sim r^{-0.88}\left(\frac{x}{rD_j}\right)^{-0.67} \qquad [5.4]$$

where ξ is the decay of the mean concentration along the jet centreline when $x > rD_j$. It should be noted that ξ in Equation 5.4 cannot be less than the ratio between the fully mixed concentration in the pipe (C_{mix}) to the initial concentration of the jet inlet (C_i). Hence, when ξ is found to be equal to C_{mix}/C_i, ideal cross-sectional mixing is achieved. According to Equation 5.4, ξ is about 1 % at $x = 1.61$ m (i.e., at the PLIF measurement point) compared to a C_{mix}/C_i of about 0.7%. This result indicates a very good radial mixing. When the first two side jets are used, then ξ at $x = 0.3$ m will be 3 % (about 350 μg/L). However, the tracer-free jets will expand with the flow axial direction and, hence, contribute to the higher dispersion effect. Therefore, as the number of jets increases, the liquid dispersion coefficient increases. As the opposing jets yielded a better mixing effect at the entrance zone (Figures 5.7 and 5.8), their dispersion effect was thus lower compared to that of alternating jet for both 1-phase and 2-phase jets. The dispersion effect of the side jets increases as the number of jets increases in the opposing jets (for both 1- and 2-phase jets). However, the value of D_L approaches a plateau as the number of opposing jets reaches 8. The higher D_L observed in the 2-phase jets compared to that in the 1-phase jets can be related to the axial dispersion of bubbles and, hence, to the axial carrying of some tracer segments.

The dispersion coefficient, D_L, was found to be affected by the superficial gas velocity, (u_G (m/s), the ratio between Q_G to the cross-sectional area of the contactor), at the fixed superficial liquid velocity (u_L (1.21 m/s), the ratio between Q_L to the cross-sectional area of the contactor) for both the opposing and alternating jets. Figure 5.13 shows the experimental results of D_L for different u_G values. The following empirical correlation was used to express D_L in terms of u_G:

$$D_L = \alpha_1 u_G^{\beta_1} \qquad [5.5]$$

where α_1 and β_1 are empirical constants that can be obtained through a non-linear regression analysis. The constants α_l and β_l were found to be 0.40 and 0.43, respectively, for the opposing jets case with a coefficient of multiple determination (R^2) value of 0.99. In the case of alternating jets, α_l and β_l were found to be 0.42 and 0.36, respectively, with R^2 value of 0.92. It can be seen from the Equation 5.5 that D_L increases with u_G. This result agrees with the results obtained by Weiland and Onken (1981) for a co-current gas-liquid contactor with 0.1 m diameter, u_G range of 0.02 to 0.05 m/s, and u_L range of 0.21 to 0.32 m/s. Weiland and Onken (1981) showed that as u_G increased from 0.02 to 0.05 m/s with u_L increasing from 0.21 to 0.32 m/s, D_L increased from 0.01 to 0.02 m^2/s. Roy and Joshi (2006) modelled D_L for a u_L range of 0.2 to 1.6 m/s at a fixed u_G value of 0.045 m/s by using a computational fluid dynamics (CFD) model. Their results showed that D_L decreased from 0.4 to 0.03 m^2/s as u_L increased from 0.2 to 1.6 m/s. The value of D_L was obtained from their results at a u_L of 1.21 m/s (the same u_L used in this study) and a u_G of 0.045 m/s to be around 0.06 m^2/s, which was smaller than the corresponding D_L values obtained from Equation 5.5 (about 0.1 m^2/s for opposing jets and 0.14 m^2/s for alternating jets). The higher value of D_L of the multi-jet contactor was directly related to the injection of the 2-phase jets from several locations along the contactor, which enhanced the axial dispersion of the system.

5.4.2 Gas Mass Transfer

The overall mass transfer coefficient (k_La, s^{-1}) of the contactor, for each operating condition, was determined by solving the following partial differential equation numerically:

$$\frac{\partial C}{\partial t} + u\frac{\partial C}{\partial x} = D_L \frac{\partial^2 C}{\partial x^2} + k_L a(C_s - C) \qquad [5.6]$$

where C is the dissolved oxygen in the system (mg/L), t is time (s), u is the average axial velocity of the liquid (m/s), x is the axial distance along the contactor (m), and C_s is the equilibrium concentration of dissolved oxygen in water (mg/L). The values of C were determined at the described two locations (1.37 m apart) by using the DO probes. The value of u is the ratio of Q_L to the cross-sectional area of the contactor (A = 0.008 m^2). The value C_s in water can be determined as follows:

$$C_s = \frac{P_{O_2}}{H} \qquad [5.7]$$

where P_{O_2} is the partial pressure of the oxygen in the gas phase (kPa), and H is Henry's constant (kPa.L/mg). The value of H can be described as a function of the temperature as follows (Sander, 1999; Wilcock et al., 1977; Wilhelm et al., 1977):

$$H = H_s e^{-1500\left(\frac{1}{T+273.15} - \frac{1}{298.15}\right)} \qquad [5.8]$$

where H_s is the Henry's constant of oxygen at 25 °C (0.41 kPa.L/mg), and T is the water temperature (°C).

Once all the constants are determined, Equation 5.6 can be solved numerically for each operating condition by using the appropriate numerical method. The box method was utilized as it gives a consistent and unconditionally stable solution (Wei and Klette, 2001). It can be expressed as follows:

$$\frac{C_{j-1}^{n+1} - C_{j-1}^{n}}{2\Delta t} + \frac{C_{j}^{n+1} - C_{j}^{n}}{2\Delta t} + \frac{u}{2}\left(\frac{C_{j}^{n} - C_{j-1}^{n}}{\Delta x} + \frac{C_{j}^{n+1} - C_{j-1}^{n+1}}{\Delta x}\right)$$

$$- \frac{D_L}{2}\left(\frac{C_{j}^{n} - C_{j-1}^{n}}{\Delta x^2} + \frac{C_{j}^{n+1} - C_{j-1}^{n+1}}{\Delta x^2}\right) - k_L a\left(C_s - C_j^{n+1}\right) = 0 \qquad [5.9]$$

where C_j^n is the concentration of dissolved oxygen (mg/L) at axial grid node j and temporal time grid node n (j = 1, 2,..., M and n = 0, 1, 2, ..., N-1), Δt is the time step (s), and Δx is the axial distance step (m). Equation 5.9 was solved by combining the results from the PLIF measurements for D_L, the measured DO concentration at the two locations along the contactor, and by providing an initial guess for the value of k_La. The corresponding overall mass transfer coefficient of oxygen (k_La-O_2, s^{-1}) was then calculated by using iteration until the minimum sum of the squared error was achieved. The overall mass transfer coefficient of the ozone (k_La-O_3, s^{-1}) was determined by using the obtained k_La-O_2 by applying the following relationship which was introduced by Danckwert (1970) and validated by Sherwood et al. (1975):

$$\frac{k_La - O_3}{k_La - O_2} = \sqrt{\frac{D_{O_3}}{D_{O_2}}} \qquad [5.10]$$

where, D_{O_3} and D_{O_2} are the molecular diffusivities of ozone and oxygen gases, respectively, in water (1.74 x 10^{-9} and 2.50 x 10^{-9} m^2/s, respectively). The k_La-O_3 values were obtained at 20 °C by applying the following relationship (Roustan et al., 1996):

$$(k_La - O_3)_{20} = (k_La - O_3)_T 1.024^{20-T} \qquad [5.11]$$

where T is the water temperature in the ozone contactor (°C). The value of T ranged from 20 to 23 °C during all DO measurements.

The overall mass transfer coefficient, k_La, was found to be affected favourably by u_G at the fixed u_L value of 1.21 m/s, for both the opposing and alternating jets. As with the case of D_L, the following empirical correlation, proposed by Deckwer et al. (1974), was used to show the effect of u_G on k_La:

$$k_La = \alpha_2 \, u_G^{\beta_2} \qquad [5.12]$$

Figure 5.14 shows the experimental results of the ozone-based k_La for different u_G values. The constants α_2 and β_2 were found to be 1.27 and 0.48, respectively, for the opposing jets case with a R^2 value of 0.98 compared to 2.27 and 0.69, respectively, for the alternating jets with a R^2 value of 0.96. As the gas flow rate is increased (by increasing the number of side jets), the value of k_La increases. This result can be attributed to the expected increase in the gas hold-up. This finding agrees with the findings of Briens et al. (1992) (who used a venturi ozone contactor with $Q_G/Q_L < 1$ and $u_L = 0.95$ m/s, $k_La = 0.97\,u_G^{1.91}$) and Mao et al. (1993) (who used a plunging jet ozone contactor, $Q_G/Q_L < 1$ and u_G ranges from 0.025 to 0.25 m/s, $k_La = 1.17\,u_G^{0.82}$). It should be noted that the multi-jets ozone contactor outperformed the contactors used by theses researchers. Moreover, the use of opposing jets yielded higher k_La values at the same u_G (about 15%). This result can be related to their better radial mixing and, hence, to the lower D_L values, as discussed earlier. Also, the bubble size obtained by using the opposing jets alignment is expected to be less than that obtained from the alternating jets alignment (at the same volume of gas) due to a possible bubble shear-off resulting from the impingement of the entering jets on each other. This result can lead to a higher interfacial area (a, m^{-1}) and, hence, increaes the total value of the k_La.

The effect of u_L and u_G on k_La was also investigated for opposing jets (as they exert a higher mass transfer than that of the alternating jets) by varying the values of Q_L and Q_G and fixing the number of the utilized side jets. The following expression for the ozone-based k_La was obtained for two opposing jets:

$$k_La = 0.8u_G^{0.36}u_L^{0.23} \qquad [5.13]$$

Figure 5.15 shows the obtained regression model (Equation 5.13) versus the experimental calculated k_La for two opposing jets. An excellent agreement is clearly observed with a R^2 value of 0.99. It was found that the mass transfer rate of the ozone increased with both

u_G and u_L. However, the effect of u_G was more pronounced. This result was expected as the gas flow rate was the driving force for such a process with the given range of the operating conditions. This finding agrees with those in several other studies of ozone contactors (Gamal El-Din and Smith, 2003; Huynh et al., 1991; Wang and Fan, 1978; Zhou and Smith, 2000).

The comparison of Equations 5.12 and 5.13 at u_L of 1.21 m/s for a u_G representing 4, 6 and 8 opposing jets (0.025, 0.037, and 0.049 m/s, respectively) shows that the multi jets induce a higher mass transfer rate compared to that of the two opposing jets only when u_G was higher than 0.025 m/s (i.e., when more than 4 opposing jets are used). This result can be related to the decrease of the available space in the mixing zone needed for higher gas mass transfer to occur in the case of two opposing jets with u_G greater than 0.025 m/s. Furthermore, as the value of D_L is higher for 8 opposing jets compared to that for 6 opposing jets, the use of the 6 opposing jets (3 from each side) may yield an enhanced k_La at high u_G values.

5.5 CONCLUSIONS

This chapter investigated the design of a pilot-scale of an in-line multi-jets ozone contacting system. A two-dimensional laser flow map particle image velocimetry coupled with planar laser-induced fluorescence (PIV/PLIF) was used to characterize the hydrodynamics of the contactor under different operating conditions. By using the PIV system, velocity measurements of the two phases (liquid and gas), were taken at different locations along the contactor to examine the flow patterns within the system. The results of velocity vectors, for both phases, at the mixing zone (the entrance zone of the side jets) showed that the opposing jets exerted better radial mixing compared to that of the alternating jets. This finding was supported by the findings obtained from the PLIF measurements as the axial dispersion coefficient resulting from the use of opposing jets was found to be smaller than that of the alternating jets. Furthermore, it was found that as the number of the 2-phase jets increased (i.e., as the gas-flow rate increased), the dispersion coefficient increased due to the dispersion effect of the bubbles.

The results obtained by using the PIV and PLIF systems were coupled with dissolved oxygen measurements, and monitored at two different locations along the contactor (upstream and downstream of the 2-phase side jets) to estimate the overall mass transfer coefficient ($k_L a$) of the system under wide operational conditions. The value of $k_L a$-O_3 was found to increase with the number of jets (i.e., with higher gas-flow rates). Also, higher $k_L a$-O_3 values were observed when opposing jets were used compared to those observed when the same number of alternating jets were used. It was found that when u_G was higher than 0.025 m/s, the use of 6 and 8 opposing jets exerted higher $k_L a$ values than those exerted by the use of two opposing jets with the same u_G value. Hence, the use of 6 to 8 opposing jets is recommended at high gas flow rates for the studied ozone contactor at a liquid flow rate of 0.01 m^3/s.

Table 5.1 Summary of the operating conditions during PLIF experiments.

Experiment number	# of jets	Jet alignment*	Total Q_L ($\times 10^{-3}$ m^3/s)	Side stream Q_L ($\times 10^{-3}$ m^3/s)	Side stream Q_G ($\times 10^{-3}$ m^3/s)
1	-	-	7.56	-	-
2	-	-	8.19	-	-
3	-	-	8.82	-	-
4	-	-	10	-	-
5	1	-	10	0.30	-
6	2	O	10	0.62	-
7	2	A	10	0.62	-
8	3	A	10	0.91	-
9	4	O	10	1.21	-
10	4	A	10	1.21	-
11	5	A	10	1.51	-
12	6	O	10	1.70	-
13	6	A	10	1.70	-
14	8	O	10	1.76	-
15	1	-	10	0.25	0.05
16	2	O	10	0.47	0.10
17	2	A	10	0.47	0.10
18	3	A	10	0.72	0.15
19	4	O	10	0.95	0.20
20	4	A	10	0.95	0.20
21	5	A	10	1.20	0.25
22	6	O	10	1.42	0.30
23	6	A	10	1.42	0.30
24	8	O	10	1.76	0.40

* O = opposing; A = alternating

Table 5.2 Summary of the operating conditions during PIV experiments.

Experiment number	# of jets	Measurement location*	Total Q_L ($\times 10^{-3}$ m^3/s)	Side stream Q_L ($\times 10^{-3}$ m^3/s)	Side stream Q_G ($\times 10^{-3}$ m^3/s)
1	-	E	7.56	-	-
2	-	E	8.19	-	-
3	-	E	8.82	-	-
4	-	E	10	-	-
5	1	E	10	0.30	-
6	2	E	10	0.62	-
7	3	E	10	0.91	-
8	4	E	10	1.21	-
9	5	E	10	1.51	-
10	6	E	10	1.70	-
11	7	E	10	1.73	-
12	8	E	10	1.76	-
13	2	M/O	10	0.62	-
14	2	M/A	10	0.62	-
15	1	E	10	0.25	0.05
16	2	E	10	0.47	0.10
17	3	E	10	0.72	0.15
18	4	E	10	0.95	0.20
19	5	E	10	1.20	0.25
20	6	E	10	1.42	0.30
21	7	E	10	1.67	0.35
22	8	E	10	1.76	0.40
23	2	MO	10	0.47	0.10
24	2	MA	10	0.47	0.10

* E = pipe end; M/O = mixing zone (opposing jets); M/A = mixing zone (alternating jets)

Table 5.3 Summary of the operating conditions during gas mass transfer experiments.

Experiment number	# of jets	Jet alignment*	Liquid flowrate, Q_L (x 10^{-3} m^3/s)	Gas flowrate, Q_G (x 10^{-3} m^3/s)	Gas/ liquid ratio, Q_G/Q_L (%)
1	1	-	10	0.05	0.5
2	2	O	10	0.10	1.0
3	2	A	10	0.10	1.0
4	3	A	10	0.15	1.5
5	4	O	10	0.20	2.0
6	4	A	10	0.20	2.0
7	5	A	10	0.25	2.5
8	6	O	10	0.30	3.0
9	6	A	10	0.30	3.0
11	8	O	10	0.40	4.0
13	2	O	10	0.07	0.7
14	2	O	10	0.13	1.3
15	2	O	10	0.27	2.7
16	2	O	10	0.4	4.0
17	2	O	7.56	0.07	0.92
18	2	O	8.19	0.07	0.85
19	2	O	8.82	0.07	0.79

* O = opposing; A = alternating

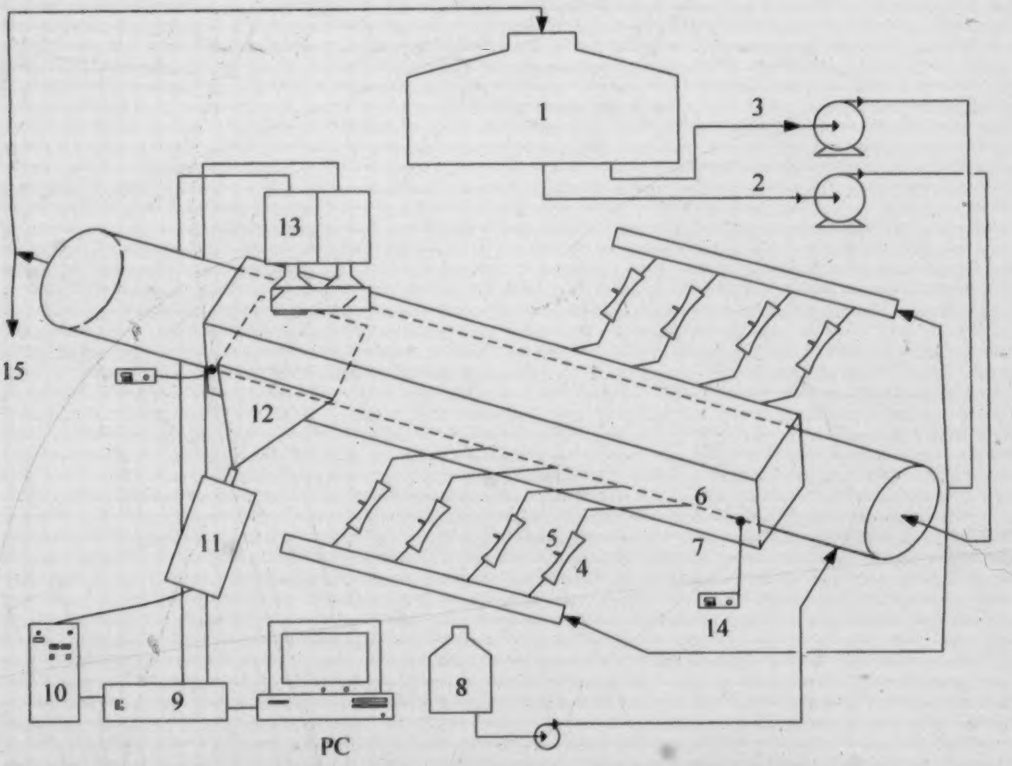

1 Water tank 2 Main line 3 Side stream 4 Mazzei injector
5 Gas inlet 6 Jet nozzle 7 Outer jacket 8 Dye/seeding particles reservoir
9 System hub 10 Laser controlling unit 11 Laser source
12 Laser sheet 13 CCD Camera 14 DO meter 15 To drain

Figure 5.1 Experimental setup.

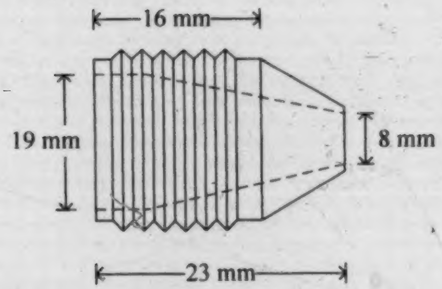

N-8 Mazzei mixing nozzle

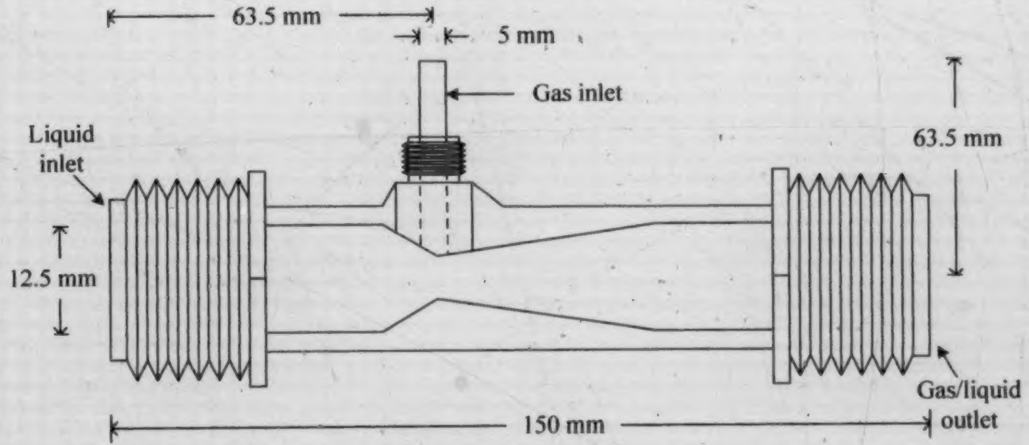

Model 584 Mazzei injector

Figure 5.2 Critical dimensions and geometry of Mazzei injector and nozzle.

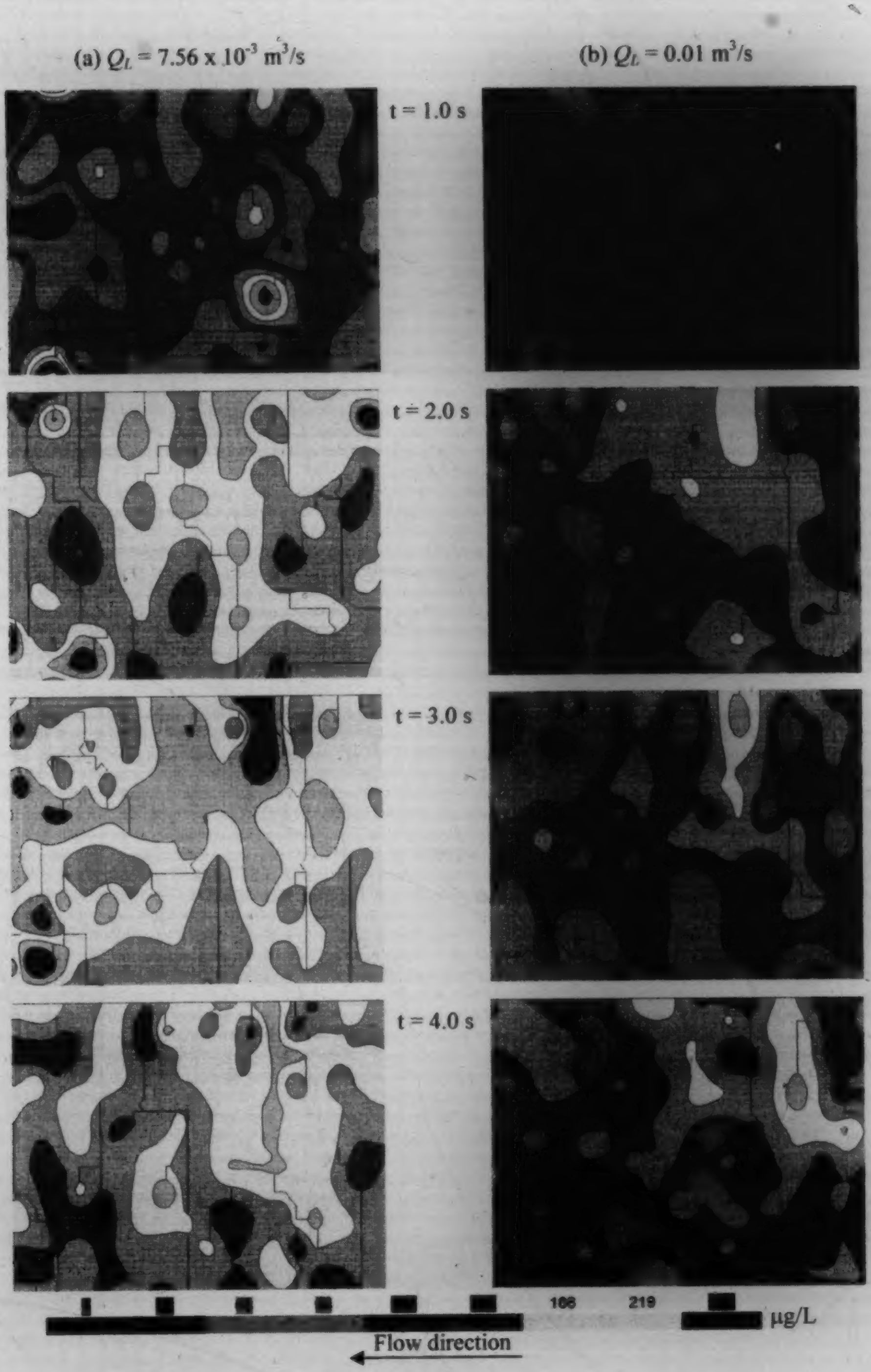

Figure 5.3 PLIF images showing concentration distribution for different liquid flow rates without side stream injection.

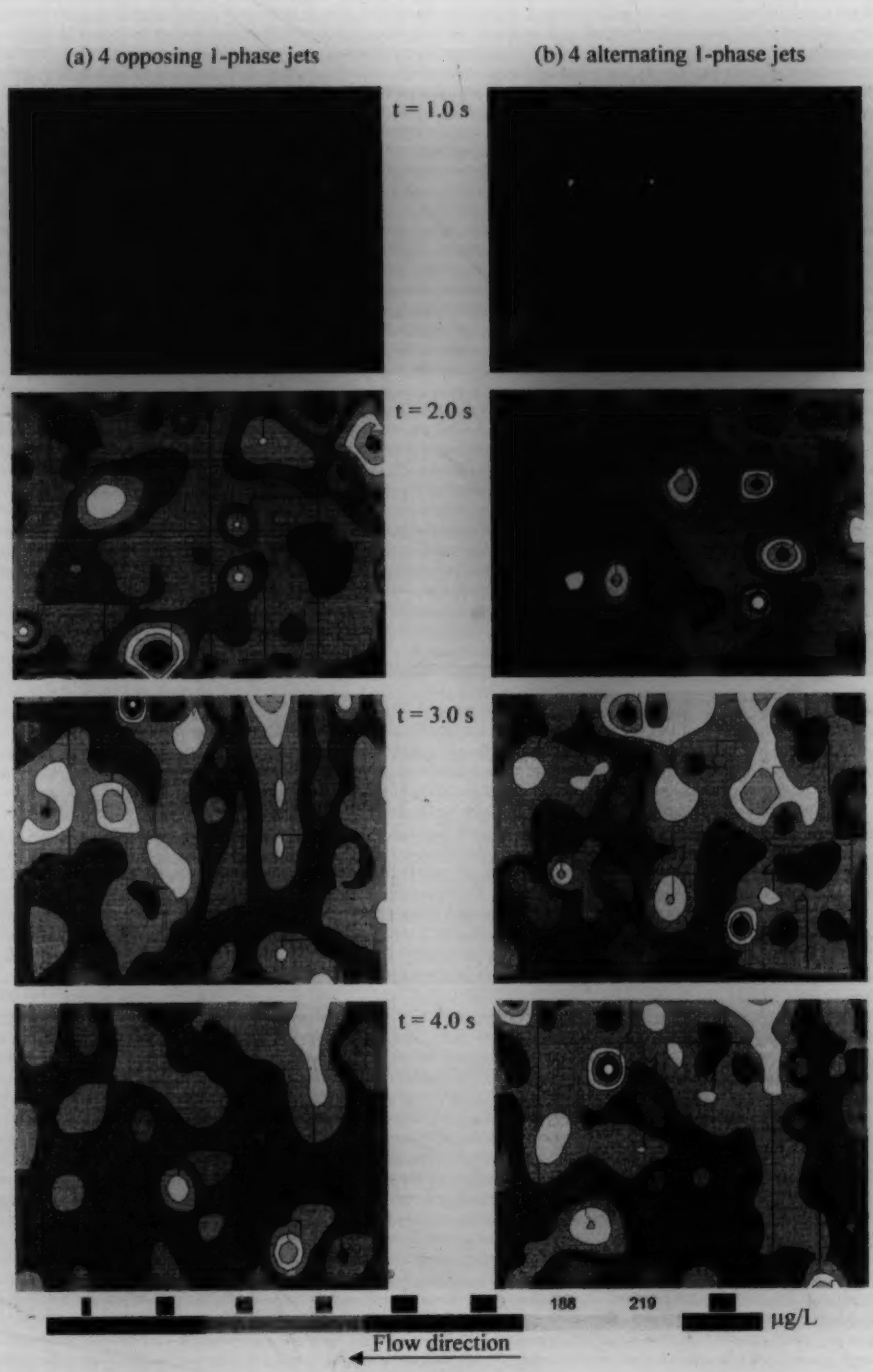

(a) 4 opposing 1-phase jets

(b) 4 alternating 1-phase jets

Figure 5.4 PLIF images showing concentration distribution for 1-phase side stream jets ($Q_L = 0.01$ m^3/s).

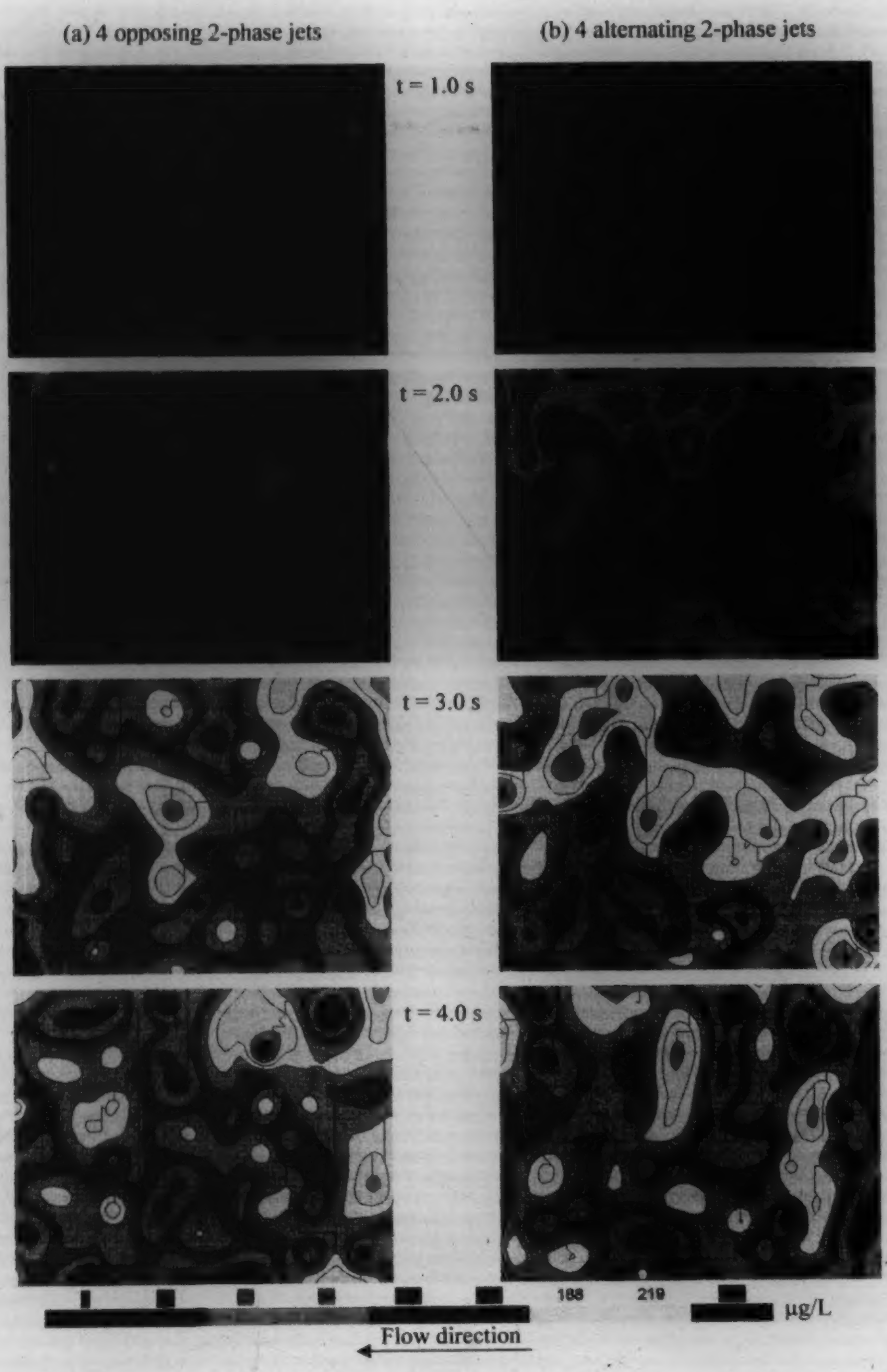

Figure 5.5 PLIF images showing concentration distribution for 2-phase side stream jets ($Q_L = 0.01$ m^3/s, $Q_G = 2.0 \times 10^{-4}$ m^3/s).

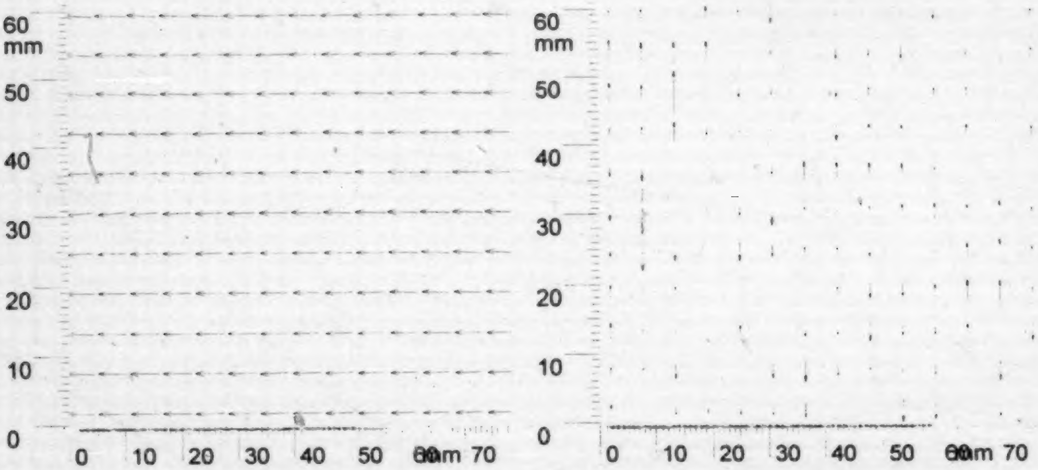

(a) $Q_L = 7.56 \times 10^{-3}$ m^3/s

(b) $Q_L = 7.56 \times 10^{-3}$ m^3/s
(Axial velocity suppressed)

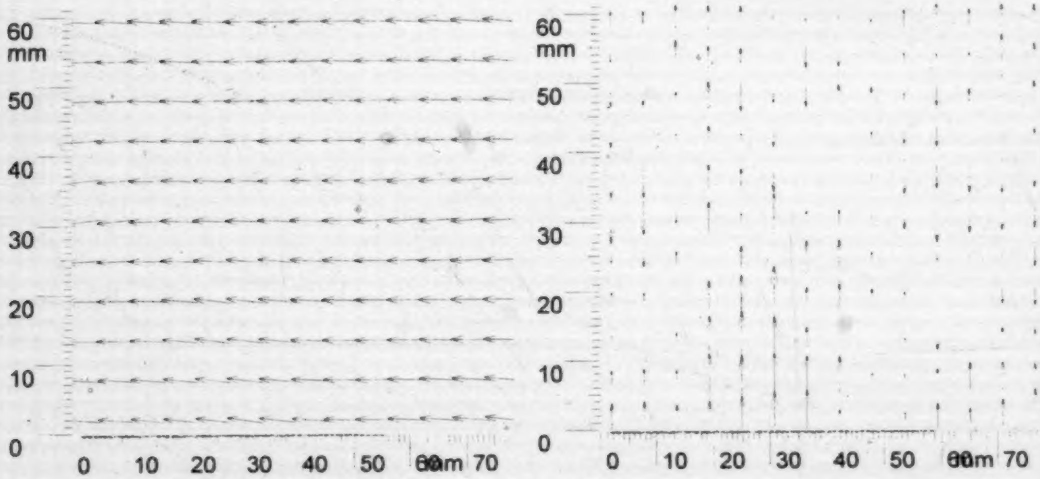

(c) $Q_L = 0.01$ m^3/s

(d) $Q_L = 0.01$ m^3/s
(Axial velocity suppressed)

Scale: 5mm = 1 m/s for (a) and (c)

Scale: 5mm = 0.1 m/s for (b) and (d)

Figure 5.6 Velocity vectors at the contactor end for different pipe flow rates without side stream injection.

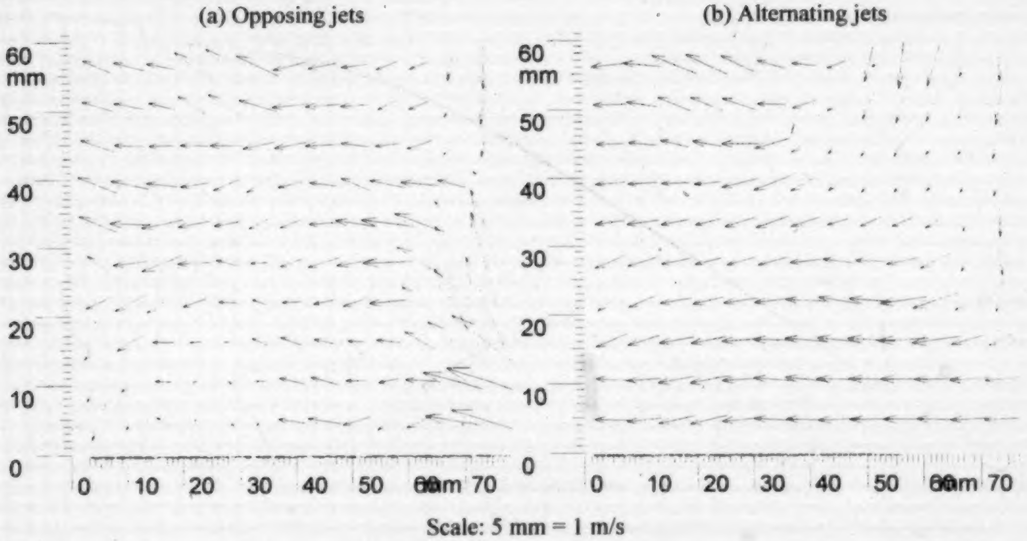

Figure 5.7 Velocity vectors at the mixing zone of the side stream injection for liquid-phase jets (without gas injection).

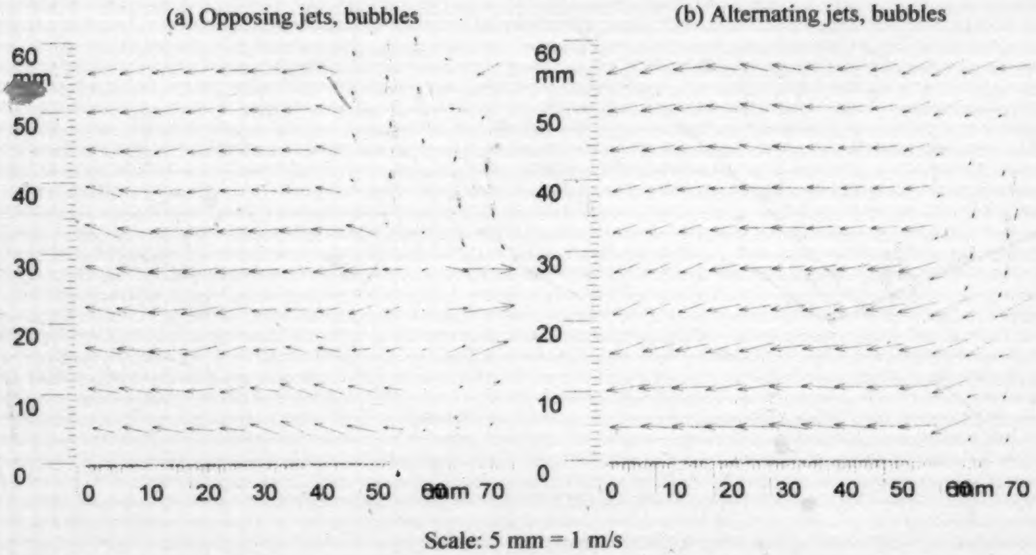

Figure 5.8 Velocity vectors at the mixing zone of the side stream injection for gas-phase jets.

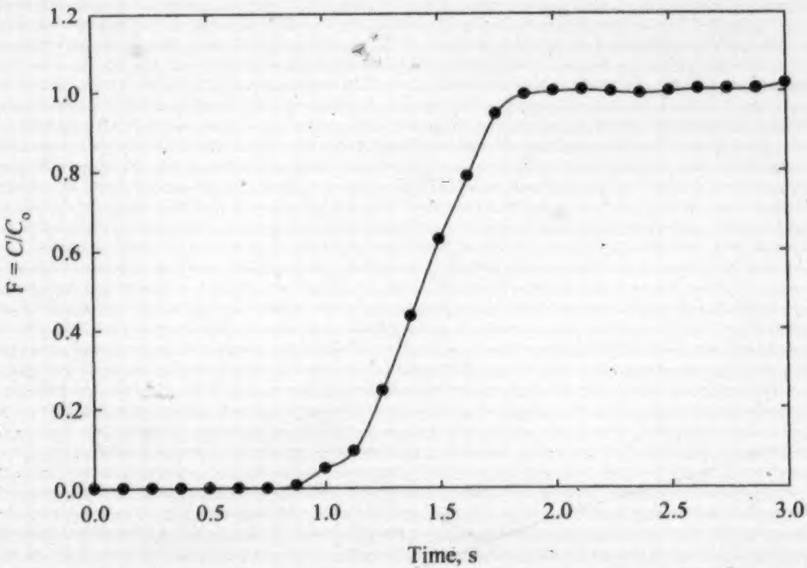

Figure 5.9 Step response curve from PLIF images ($Q_L = 0.01$ m^3/s, no side jets).

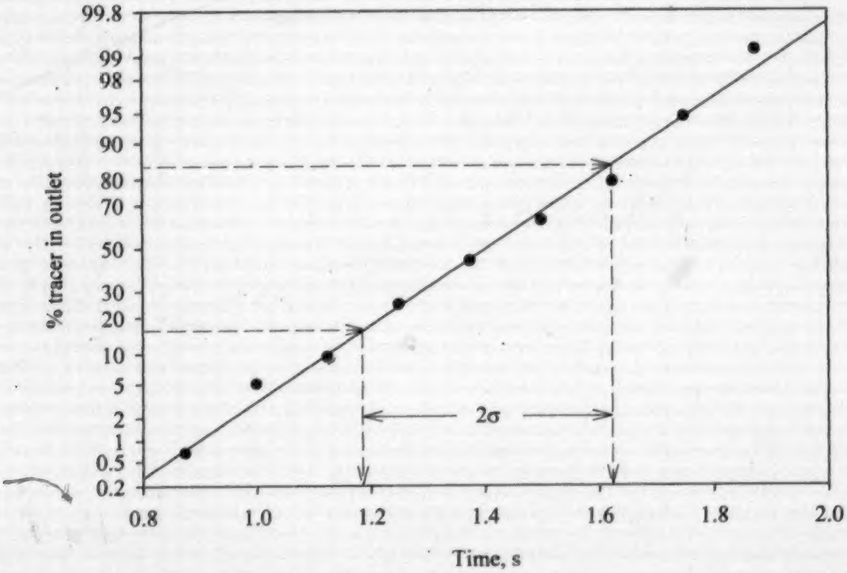

Figure 5.10 Probability plot of the step response signal ($Q_L = 0.01$ m^3/s, no side jets).

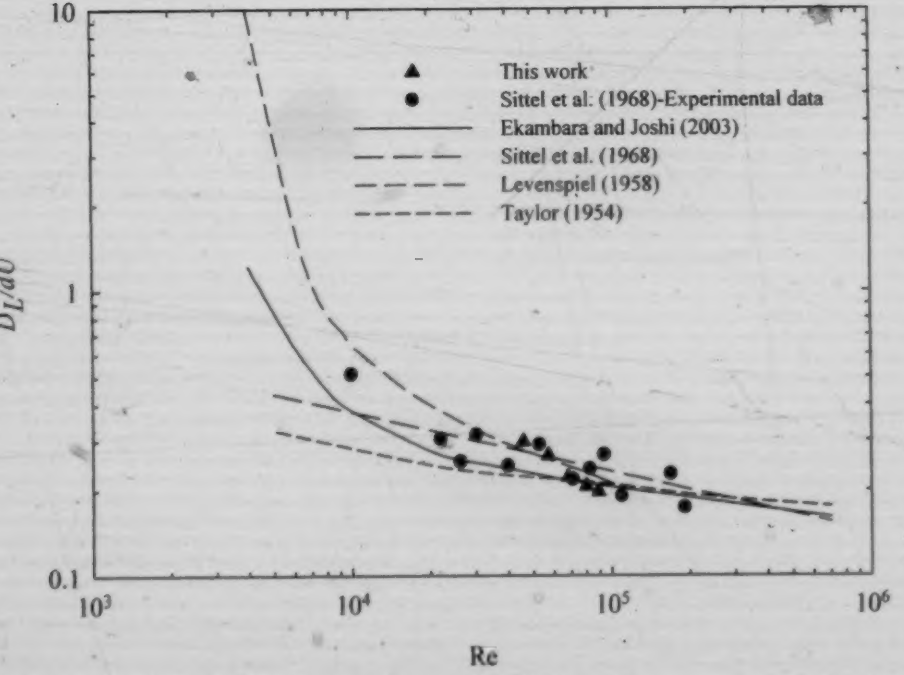

Figure 5.11 Comparison between the measured dispersion parameter and published data for turbulent pipe flows.

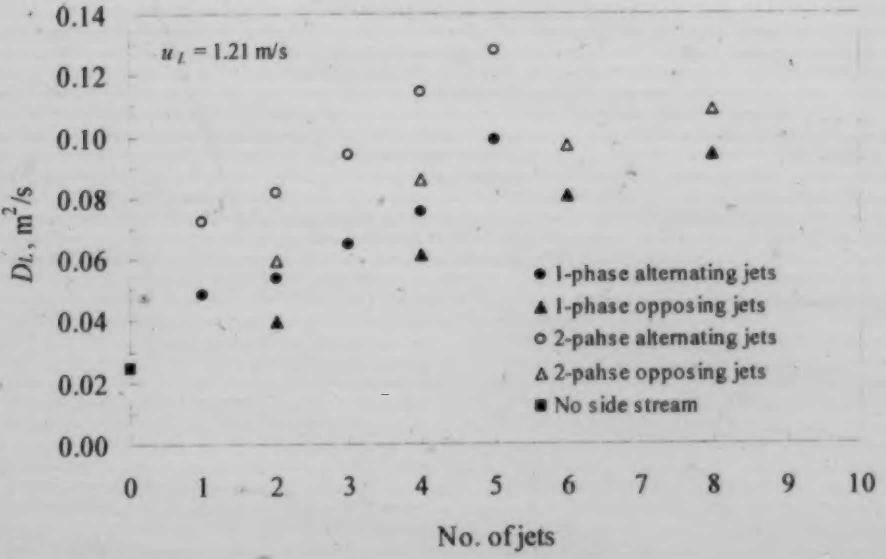

Figure 5.12 Liquid dispersion coefficient versus number of side jets for different phases and jet alignments.

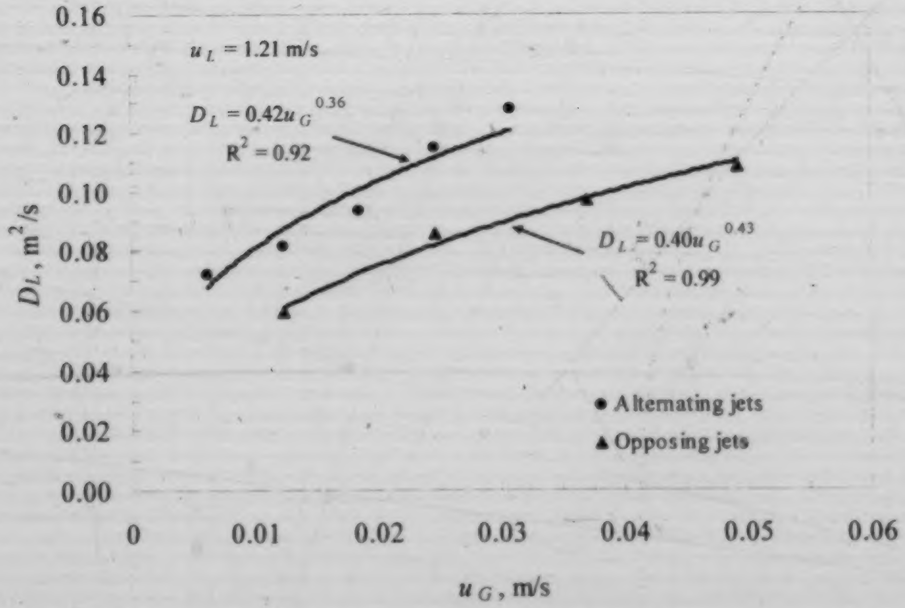

Figure 5.13 Liquid dispersion coefficient versus superficial gas velocity for alternating and opposing jets.

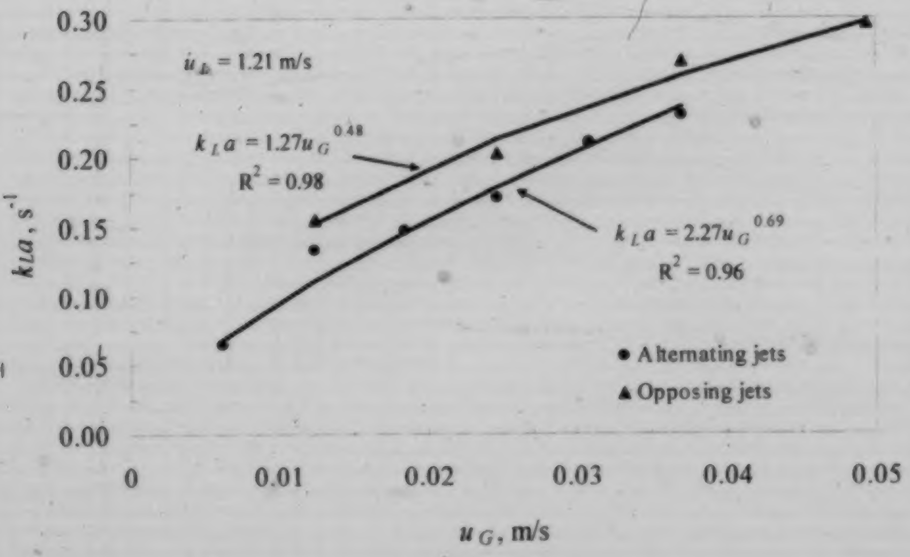

Figure 5.14 Overall mass transfer coefficient for alternating and opposing jets.

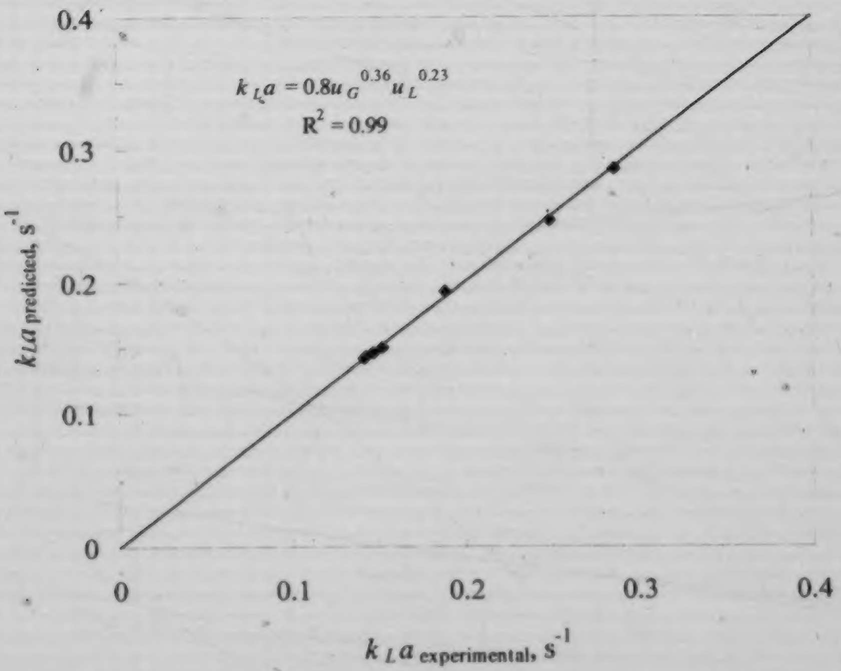

Figure 5.15 Experimental versus predicted overall mass transfer coefficient for 2 opposing jets.

5.6 REFERENCES

1. Albrecht, H.E., M. Borys, N. Damaschke, and C. Tropea, *Laser Doppler and Phase Doppler Measurement Techniques*. (N. Y: Springer-Velag Berlin Heidelberg, 2002).
2. Atkinson, J.F., J.V. Benschoten, and C.Y. Cheng, *Development of Particle Image Technology for Water Treatment Studies*. (Denver: AWWA Research Foundation, U.S.A., 2000).
3. Benes, M., J. Hudecek, P. Anzenbacher, and M. Hof, "Coumarin 6, Hypericin, Resorufins, and Flavins: Suitable Chromophores for Fluorescence Correlation Spectroscopy of Biological Molecules", *Collect. Czech. Chem. Commun.*, 66(6): 855-869 (2001).
4. Bernard, P.S., and J.M. Wallace, *Turbulent Flow: Analysis, Measurement and Prediction*. (Hoboken, N. J.: John Wiley & Sons, Inc., 2002).
5. Briens, C.L., L.X. Huynh, J.F. Large, A. Catros, J.R. Bernard, and M.A. Bergougnou, "Hydrodynamics and Gas-Liquid Mass-Transfer in a Downward Venturi-Bubble Column Combination", *Chem. Eng. Sci.*, 47(13-14): 3549-3556 (1992).
6. Cozewith, C., and M. Busko, "Design Correlations for Mixing Tees", *Ind. Eng. Chem. Res.*, 28(10): 1521-1530 (1989).
7. Danckwerts, P., *Gas-Liquid Reaction*. (New York: McGraw-Hill, 1970).
8. Deckwer, W.D., R. Burckhart, and G. Zoll, "Mixing and Mass Transfer in Tall Bubble Columns", *Chem. Eng. Sci.*, 29: 2177-2188 (1974).

9. Durst, F., G. Brenn, and T.H. Xu, "A Review of the Development and Characteristics of Planner Phase-Doppler Anemometry", *Meas. Sci. Technol.* , 8: 1203-1221 (1997).

10. Ekambara, K., and J.B. Joshi, "Axial Mixing in Pipe Flows: Turbulent and Transition Regions", *Chem. Eng. Sci.*, 58(12): 2715-2724 (2003).

11. Forney, L.J., Z. Feng, and X. Wang, "Jet Trajectories of Transverse Mixers at Arbitrary Angle in Turbulent Tube Flow", *Chem. Eng. Res. Des.*, 77(A8): 754-758 (1999).

12. Gamal El-Din, M., and D.W. Smith, "Mass Transfer Analysis in Ozone Bubble Columns", *J. Environ. Eng. Sci.* , 2(1): 63-76 (2003).

13. Hansen, R.L., X.R. Zhu, and J.M. Harris, "Fluorescence Correlation Spectroscopy with Patterned Photoexcitation for Measuring Solution Diffusion Coefficients of Robust Fluorophores", *Analyt. Chem.*, 70(7): 1281-1287 (1998).

14. Huynh, L.X., C.L. Briens, J.F. Large, A. Catros, J.R. Bernard, and M.A. Bergougnou, "Hydrodynamics and Mass-Transfer in an Upward Venturi Bubble Column Combination", *Canad. J. Chem. Eng.*, 69(3): 711-722 (1991).

15. Joshi, J.B., "Reduction of Empiricism through Flow Visualization and Computational Fluid Dynamics", *Chem. Eng. Technol.* , 25(3): 321-328 (2002).

16. Joshi, J.B., and V.V. Ranade, " Computational Fluid Dynamics for Designing Process Equipment: Expectations, Current Status, and Path Forward", *Ind. Eng. Chem. Res.* , 42: 1115-1128 (2003).

17. Levenspiel, O., "Longitudinal Mixing of Fluids Flowing in Circular Pipes", *Ind. Eng. Chem.*, 50(3): 343-346 (1958).

18. Levenspiel, O., *Chemical Reaction Engineering*. (Hoboken, NJ.: J. Wiley & Sons, Inc., 1999).

19. Levenspiel, O., and W.K. Smith, "Notes on the Diffusion-Type Model for the Longitudinal Mixing of Fluids in Flow", *Chem. Eng. Sci.*, 6(4-5): 227-233 (1957).

20. Mao, W.P., G.M. Evans, and G.J. Jameson, "Mass Transfer Study in a Plunging Jet Bubble Column", *5th Australasian Heat and Mass Transfer Conference*, The University of Queensland, Brinsbane Australia. (1993).

21. Pan, G., and H. Meng, "Experimental Study of Turbulent Mixing in a Tee Mixer Using Piv and Plif", *AIChE J.*, 47(12): 2653-2665 (2001).

22. Petrovic, M., S. Gonzalez, and D. Barcelo, "Analysis and Removal of Emerging Contaminants in Wastewater and Drinking Water ", *TrAC-Trends Anal. Chem.* , 22(10): 685-696 (2003).

23. Raffel, M., C. Willert, and J. Kompenhans, *Particle Image Velocimetry: A Practical Guide.* . (N. Y.: Springer-Velag Berlin Heidelberg, 1998).

24. Roustan, M., R.Y. Wang, and D. Wolbert, "Modeling Hydrodynamics and Mass Transfer Parameters in a Continuous Ozone Bubble Column", *Ozone-Science & Engineering*, 18(2): 99-115 (1996).

25. Roy, S., and J.B. Joshi, "Effect of Liquid Velocity on Axial Mixing in Gas-Liquid Dispersions: A Cfd Simulation", *Chem. Eng. Tech.*, 29(9): 1034-1041 (2006).

26. Sander, R., "Compilation of Henry's Law Constants for Inorganic and Organic Species of Potential Importance in Environmental Chemistry", (Mainz: http://www.henrys-law.org, 1999).

27. Sherwood, T.K., L.P. Robert, and R.W. Charles, *Mass Transfer* (New York: McGraw-Hill, 1975).

28. Sittel, C.N., Threadgi.Wd, and K.B. Schnelle, "Longitudinal Dispersion for Turbulent Flow in Pipes", *Ind. Eng. Chem. Fund.*, 7(1): 39-& (1968).

29. Sroka, L.M., and L.J. Forney, "Fluid Mixing with a Pipeline Tee - Theory and Experiment", *AIChE J.*, 35(3): 406-414 (1989).

30. Taylor, G., "The Dispersion of Matter in Turbulent Flow through a Pipe", *Proc. Roy. Soc. (London)* 223(1155): 446-468 (1954).

31. Tosun, G., "A Study of Micromixing in Tee Mixers", *Ind. Eng. Chem. Res.*, 26(6): 1184-1193 (1987).

32. Wang, K.B., and L.T. Fan, "Mass Transfer in Bubble Columns Packed with Motionless Mixers", *Chem. Eng. Sci.*, 33: 945-952 (1978).

33. Wei, T., and R. Klette, "Finite Difference Methods for Linear Shape from Shading", (Auckland, The University of Auckland: http://citr.auckland.ac.nz/techreports/2001/CITR-TR-110.pdf, 2001).

34. Weiland, P., and U. Onken, "Fluid Dynamics and Mass Transfer in an Airlift Fermentor with External Loop", *Ger. Chem. Eng.*, 4: 42-50 (1981).

35. Wilcock, R.J., R. Battino, and E. Wilhelm, "Solubility of Gases in Liquids .10. Solubility of He,Ne,Ar,Kr,N2,O2,Co,Co2,Ch4,Cf4, and Sf6 in Cyclooctane at 289 to 313 K", *J. Chem. Therm.*, 9(2): 111-115 (1977).

36. Wilhelm, E., R. Battino, and R.J. Wilcock, "Low-Pressure Solubility of Gases in Liquid Water", *Chem. Rev.*, 77(2): 219-262 (1977).

37. Zhou, H.D., and D.W. Smith, "Ozone Mass Transfer in Water and Wastewater Treatment: Experimental Observations Using a 2d Laser Particle Dynamics Analyzer", *Water Res.*, 34(3): 909-921 (2000).

CHAPTER 6

THE EFFECT OF TWO INCLINED CIRCULAR PLUNGING JETS ON AIR ENTRAINMENT IN AN AERATION TANK*

6.1 INTRODUCTION

Liquid plunging jets are moving columns of liquid (water) that pass through some gaseous headspace before impinging on the free surface of the receiving liquid (Figure 6.1). At the intersection of the plunging jet and the liquid surface, free-surface instabilities develop, and gas entrainment may be observed. This aeration system is preferred over conventional aeration systems as it does not require an air compressor, it is simple in construction and operation, and it is free of operational difficulties such as clogging of air diffusers (Ohkawa et al., 1986). Therefore, many studies have been conducted on characterizing the flow of plunging water jets by utilizing a vertical or inclined nozzle (Bin, 1993; Chanson et al., 2004; Cummings and Chanson, 1997; Ito et al., 2000; Kusabiraki et al., 1990; Ohkawa et al., 1986; Vandesande and Smith, 1976).

In order for the gas entrainment to take place, the jet impact velocity has to exceed a characteristic velocity (the onset or threshold velocity) that is a function of the plunging flow conditions (Bin, 1993; Cummings and Chanson, 1999). Other factors controlling the mechanisms of air entrainment include the physical properties of the liquid, the design of the jet nozzle (e.g. the nozzle diameter (d_o) and nozzle length (L_n)), the distance from the jet outlet to the liquid surface (L_j), thw jet angle (α), and the turbulence of the jet (Bin, 1993; Chanson et al., 2004; Cummings and Chanson, 1997; Kusabiraki et al., 1990; Ohkawa et al., 1986). For small jet velocities (at the nozzle outlet) that are larger than the threshold velocity (the onset velocity), air is entrained in the form of individual air bubbles, while large packets of air are entrained and broken up subsequently in the shear flow at higher jet velocities (Bin, 1993; Chanson et al., 2004). When the distance from the pipe outlet to the water surface (L_j) is short, the surface of the water jet is not disturbed by the shear forces induced by the surrounding air, and, thus, many small bubbles are generated and dispersed in the whole water body. If L_j is long, the surface of the water jet becomes highly disturbed, and relatively large bubbles are generated and dispersed in a localized region in the water beneath the pipe exit. These two patterns occur simultaneously for an intermediate distance. Furthermore, the nozzle length to diameter (L_n/d_o) ratio is an important factor in nozzle design (Bin, 1993; Burgess and Molloy, 1973; Ohkawa et al., 1986; Vandesande and Smith, 1976). For practical reasons, Ohkawa et al. (1986) recommended the use of a relatively small L_n/d_o ratio (much smaller than 50).

---

* A version of this chapter has been published. Baawain, M.S., M. Gamal El-Din, and D.W. Smith, *WIT Trans. of Eng. Sci.*, 50: 229-240 (2005).

Air entrainment by plunging liquid jets in water bodies has potential applications in many chemical and wastewater treatment processes. Examples of such processes include mineral-processing flotation cells, confined plunging jet reactors, plunging jet bioreactors, and small-scale activated sludge systems (Evans et al., 1996; Jakubowski et al., 2003; Ohkawa et al., 1986; Yamagiwa et al., 1991; Yamagiwa et al., 1996). This process, referred to as plunging jet entrainment and aeration, has also been studied by researchers interested in natural systems such as self-purification (re-aeration) of rivers and waterfalls (Baylar and Bagatur, 2006; Bin, 1993; Davoust et al., 2002; Evans et al., 1997; Oguz, 1998; Soh et al., 2005).

When aeration systems are used in wastewater treatment plants, the ultimate goal is to obtain a high mass transfer of oxygen by generating the most effective bubbles (i.e., bubbles with small diameter and long residence time) and avoiding significant solid break-up. The process of oxygen mass transfer to water with time (*t*) can be expressed by using the following equation (by assuming a constant volume in the system, a constant equilibrium concentration of oxygen in the liquid phase, and a negligible effect of free surface transfer):

$$\frac{dC}{dt} = k_L a(C_s - C) \qquad [6.1]$$

where C is the dissolved oxygen concentration in water (mg/L), k_La is the overall mass transfer coefficient (s^{-1}), and C_s is the saturation (equilibrium) concentration of oxygen in water. The determination of k_La is very important for the design and performance evaluation of gas-liquid mass transfer processes.

This study explores the air entrainment resulting from the use of two inclined circular plunging jets intersecting at the surface of water tank, in contrast to the commonly used vertical jets. The aim is to utilize particle image velocimetery (PIV), which is a well established non-intrusive measuring technique that can provide simultaneous measurements of the velocity components of different phases of fluids (Atkinson et al., 2000; Raffel et al., 1998; Stanislas et al., 2000) to evaluate the two-phase jet velocity components in the tank. In addition to evaluating the impingement angle, this study evaluated the effect of different jet nozzle sizes, free jet lengths, and jet outlet velocities on the air entrainment rate, bubble plume penetration depth, gas hold-up and bubble diameter.

6.2 EXPERIMENTAL SET-UP

6.2.1 Flow Facility

The air entrainment experiments were conducted in two stages. During the first stage, the entrained air flow rate was determined by using the experimental set-up shown in Figure 6.2a. This set-up consisted mainly of a clear walled tank, a nozzle, and a bubble trap. The inside dimensions of the glass tank had a width of 0.67 m, a length of 0.67 m, and a depth of 0.67 m. An overflow weir was located on one side to maintain a constant depth in the tank. The water overflow drained into a storage barrel and was re-circulated by using an electric pump, which also provided a means of varying the discharge by using a flow meter. Water was directed by the pump to the inclined (or vertical) circular jet mounted above the water surface of the tank by using a special rack that allowed for changing L_j (up to 0.5 m) and α (from 0^o to 90^o). The jet nozzles were made of copper with an inlet diameter (d_n) of 0.025 m and a cylindrical length (L_n) of 0.015 m. The nozzle outlet diameters (d_o) used in this study ranged from 2.5 x 10^{-3} to 0.01 m, yielding an aspect ratio (L_n/d_o) from 1.5 to 6. The flow rate of the entrained gas collected in the trap (0.3 m width, 0.2 m length, and 0.5 m depth) was measured by using an air flow meter.

The second stage of the experiments was conducted by using the experimental set-up shown in Figure 6.2b. Two inclined circular nozzles were used instead of one after removing the bubble trap used in the previous stage. Two measuring tapes were secured to the tank horizontal and vertical sides in order to monitor the depth and width of the bubble plumes.

6.2.2 PIV Set-up

The experimental set-up for the PIV measurements is shown in Figure 6.3. The flow facility is identical to the one shown in Figure 6.2b. The PIV system consisted of a laser source, two charge coupled device (CCD) cameras, a traverse system and processing units. This study used an Nd:Yag dual cavity laser with a power level of 100 mJ. The emitted wavelength of the Nd:Yag laser was 532 nm with a pulse duration of 10 ns. The time between pulses was set to 100 μs with a maximum repetition rate of 8.0 Hz. The two CCD cameras were configured to use double frames for PIV measurements (velocity measurements) of the two phases (water and air). Melamine-formaldehyde (MF) spheres, coated with Rhodium B (RhB), were used as seeding particles during the liquid velocity measurements. A FlowMap System Hub from Dantec Dynamics was used to record and transfer the data to a PC where FlowMap software was used to analyze the images and export the resulting files to a desired format for further analysis. Two PIV measurements were conducted simultaneously: one for obtaining the liquid jet velocity components and the second for measuring the air (bubble) jet velocity components. Measurements were taken at different locations along the bubble plumes by using the traverse system. The images of the bubble plumes captured by the CCD camera were also used to estimate the average bubble size under each experimental condition.

6.3 MEASUREMENT DESCRIPTION

The conducted runs for the entrained air flowrates are summarized in Table 6.1. The water temperature was observed to be 16 °C ± 1 °C. The liquid flowrate (Q_L) was varied from 6.3×10^{-5} to 3.15×10^{-4} m^3/s. The angle at which the jets plunged the surface (α) ranged from 60° to 80°. The vertical distance from the jets' outlet to the free water surface (H) was varied from 0.05 to 0.55 m. The range of H and α used in this study resulted in a free jet length (L_o) ranging from 0.05 to 0.58 m.

A summary of the PIV and plume characterizing runs is provided in Table 6.2. The monitored water temperature during all experiments was 23 °C ± 1 °C. The value of Q_L was varied from 3.2×10^{-5} to 1.26×10^{-4} m^3/s, with α of 67.5°, 75° (the resulting angles between the two jets (θ) were 45° and 30°, respectively) and 90°. The vertical distance from the jets outlet to the free water surface (H) was varied from 0.05 to 0.11 m. The range of H and α used in this study resulted in a free jet length (L_o) ranging from 0.05 to 0.13 m.

The mean outlet jet velocity ($u_o = \dfrac{Q_L}{(\pi d_o^2/4)}$, m/s) has to be greater than the threshold value (u_e) at which gas entrainment inaugurates. A rough estimate of u_e in m/s can be obtained by using the following relationship (Bin, 1993):

$$u_e = 5L_o^{0.534} \tag{6.2}$$

Equation 6.2 is valid for L_o ranging from 0.015 to 0.4 m. The required u_e for this study ranged from 1.0 to 3.7 m/s for the entrained air flowrate measurements and from 1.0 to 1.7 m/s for the PIV measurements. The used u_o was always more than the required u_e in order to ensure air entrainment in the tank under every experimental condition throughout the course of this study. In addition to satisfying the threshold velocity criterion, the water temperature ranged from 16 °C (for the entrained air flowrate measurements) to 23 °C (for the PIV measurements) (i.e. the kinematic water viscosity was 1.13×10^{-6} and 9.34×10^{-7} m^2/s, respectively) and at the mentioned flow rates and nozzle diameters, the diameter-based Reynolds number (Re_d) was greater than 1.71×10^4, indicating turbulent flow conditions, which are favourable for air entertainment (Bin, 1993).

Some parameters of interest such as the maximum penetration depth (z_p), the width of the bubble plume, and the height and the width of the two-phase mixture (gas and water) due to the air entrainment were observed by using a digital photographic technique and by eye inspection utilizing the measuring tapes fixed to the sides of the tank. The height and width of the two-phase mixture were used to estimate the gas hold-up (ε_G) as follows:

$$\varepsilon_G = \frac{\left(\frac{W_{L-G}}{W_L}\right)\left(H_{L-G} - H_L\right)}{H_{L-G}} \qquad [6.3]$$

where W_{L-G} is the width of the two-phase mixture (m), W_L is the inside width of the tank under no air entrainment (m), H_{L-G} is the height of the two-phase mixture (m), and H_L is the inside depth of the tank under no air entrainment (m). Once ε_G is obtained and the average bubble diameter (d_b) was obtained from the CCD camera images, the specific interfacial area ([illegible]) of the bubbles was determined by using the following relationship (Jakubowski et al., 2003):

$$a = \frac{6}{d_b}\left(\frac{\varepsilon_G}{1-\varepsilon_G}\right) \qquad [6.4]$$

6.4 RESULTS AND DISCUSSION

6.3.1 Air entrainment measurements

The results of the air entrainment ratio (Q_G/Q_L) for different operating conditions are summarized in Table 6.3. The expected factors affecting (Q_G/Q_L) are the basic system parameters such as the jet outlet velocity (u_o), jet length (L_o), jet angle (α), nozzle diameter (d_o), and the physical properties of the liquid phase. The results showed that increasing the nozzle outlet velocity and (L_o/d_o) ratio (either by increasing L_o or decreasing d_o) led to an increased (Q_G/Q_L) ratio. Such an increase can be related to the increase in the turbulence (as u_o increased) and the surface roughness (as L_o/d_o increased) of the plunging jet. In order to evaluate the impact of these factors on the entrainment ratio, many researchers have developed different empirical expressions ranging from very simple ones neglecting the jet velocity to ones classifying different regions for air entrainment according to the velocity of the jet (Bin, 1993; Ohkawa et al., 1986). Bin (1993) suggested a general expression valid for the different regions of air entrainment resulting from the use of one vertical plunging jet:

$$\frac{Q_G}{Q_L} = 0.04Fr^{0.28}\left(\frac{L_o}{d_o}\right)^{0.4} \qquad [6.5]$$

$$Fr = \frac{u_o^2}{gd_o} \qquad [6.6]$$

where Fr is the dimensionless Froude number, and g is the acceleration due to gravity (g = 9.81 m/s^2). Equation 6.5 is valid for water jets with $L_o/d_o \leq 100$, $L_n/d_o \geq 10$, and $0.04Fr^{0.28}(L_o/d_o)^{0.4} \geq 10$. Similarly, the results shown in Table 6.3 were expressed as follows by adding an additional term to account for the jet angle:

$$\frac{Q_G}{Q_L} = 0.03Fr^{0.23}\left(\frac{L_o}{d_o}\right)^{0.49}(\sin\alpha)^{-0.83} \qquad [6.7]$$

The values of (Q_G/Q_L) obtained from Equation 6.7 were plotted against the experimental results, as Figure 6.4 illustrates. A very good agreement can clearly be observed with a coefficient of multiple determination (R^2) value of 0.94. Furthermore, the entrainment ratio obtained by using Equation 6.7 was comparable to the ratio obtained by Ohkawa et al. (1986) for an inclined nozzle with d_o of 0.008 to 0.02 m, L_o of 0.03 to 0.15 m, u_o of 2.0 to 13.0 m/s, α of 30 to 60°, and L_n/d_o ratio of 5.0. However, their expression requires the determination of three entrainment regions and an intricate process to determine the jet velocity ranges defining these regions. The accuracy in their final expression of Q_G/Q_L was found to be $\pm 30\%$ while the general expression provided by Equation 6.7 is applicable to all entrainment regions and covers wider ranges of L_n/d_o, L_o/d_o and u_o. Furthermore, Equation 6.7 accounts for an α range that Ohkawa et al. (1986) did not study (60 to 80°). Both Equation 6.7 and the expression provided by Ohkawa et al. (1986) show that inclined nozzles with a short L_n/d_o ratio provide a small Q_G/Q_L ratio compared to a long L_n/d_o ratio (Equation 6.6). However, practical use would in many cases require the use of a short L_n/d_o ratio.

6.3.2 Velocity measurements

All PIV measurements obtained for the velocity components of the two-phase flow conditions were taken below the region of the break-up length (z_b) (the length after which bubbles start to be formed in the water body) of the two-phase jets. The measurements were taken below z_b because of the inability of the scattered laser sheet to reach the CCD cameras. Therefore, the CCD cameras were moved up and down by utilizing the traverse system to overcome this problem. Measurements of the lateral (radial) distributions (x) of water and the bubble jets' velocity components were taken at different axial positions (z). At each z, the axial velocity (v) was normalized by its centreline value (v_m), and plotted against the normalized lateral distance (x/d_0). The data shown in Figure 6.5 is a result of using the same value of Re_d and varying d_o and α. Figure 6.5a, representing the gas phase, shows a fairly good agreement with the Gaussian distribution. However, as d_o decreased (i.e., as the water jet velocity increased), the deviation from the Gaussian distribution increased. The negative values of v/v_m in the region of $x/d_o > 2$ could be attributed to the fact that bubbles rise up when their buoyancy force overcomes the impingement force. On the other hand, the water phase jet, shown in Figure 6.5b, showed a very good agreement with the Gaussian distribution in the region of $x/d_o < 2$. This finding is supported by the observations made by Iguchi et al. (1998) and McKeogh and Ervine (1981). The negative values observed as x/d_o increased further were related to the effect that the rising bubbles had exerted on the surrounding liquid.

6.3.3 Penetration depth

The performance of the aeration process resulting from air entrainment due to plunging jets is highly affected by the residence time of the entrained bubbles. Therefore, the residence time is related to the bubble penetration depth (z_p) into the aeration tank. During all experimental conditions (Table 6.2), the penetration depth was always less than the water depth in the tank.

Figure 6.6a illustrates that under the same turbulence condition and different α, as d_o increases, z_p also increases. This figure also shows that under the same d_o, z_p at $\alpha = 75^o$ (i.e., $\theta = 30^o$) is greater than the ones related to the other two cases ($\alpha = 67.5^o$ and $\alpha = 90^o$). Figure 6.6b shows the variation of z_p with the water jet outlet velocity for $d_o = 5.0 \times 10^{-3}$ m and different α values. The results show that as the jet outlet velocity increased, z_p also increased. For a specific velocity, the highest z_p was obtained when $\alpha = 75^o$ and the L_o/d_o ratio was relatively small. The relatively high z_p value under $\alpha = 75^o$ ($\theta = 30^o$) could be related to the combined energy of the two plunging jets, which intersected at the surface of the water without much dissipation. In the case of $\alpha = 67.5^o$, the intersecting jets could have dissipated the energy as the angle of intersection was too wide.

Ohkawa et al. (1986) suggested a generalized correlation for z_p of one inclined water jet:

$$z_p = c_1 (u_o d_o)^{c_2} (L_o / d_o)^{c_3} (\sin\alpha)^{c_4} \qquad [6.8]$$

where c_1, c_2, c_3, and c_4 are empirical constants that can be determined experimentally. The values of c_1, c_2, c_3, and c_4 were found to be 10.5, 0.54, -0.56, and 1.39, respectively, for two inclined plunging jets compared to 5.5, 0.73, -0.26, and 1.11, respectively, for the one inclined plunging jet that Ohkawa et al. (1986) studied. The combination of two inclined plunging jets yielded a higher penetration depth for the same values of u_o, d_o, L_o and α. The excellent agreement between the measured z_p and the z_p calculated by using Equation 6.8, can be observed in Figure 6.7 ($R^2 = 0.96$).

6.3.4 Gas hold-up and mass transfer coefficient

Gas hold-up (ε_G) is another important parameter in evaluating gas-liquid mass transfer. ε_G was obtained by using the measured parameters and applying them to Equation 6.3. As d_o increased (the outlet velocity decreased for the same Re_d), ε_G decreased (see Figure 6.8a). This result can be explained by the reduced amount of bubbles entrained under such conditions. In contrast, for the same d_o, ε_G increased as the outlet velocity increased, as shown in Figure 6.8b. This result was expected, as for the same nozzle diameter, increasing the jet outlet velocity increased the turbulence further (the initial experimental condition was turbulent with $Re_d > 1.7 \times 10^4$). Hence, the free-surface instabilities will increase and, therefore, lead to more air entrainment and, eventually, higher gas hold-up.

In order to correlate ε_G with the characteristic parameters of the inclined plunging jet, the following correlation (for one inclined plunging jet) developed by Kumagai and Endoh (1983) was considered for comparison purposes:

$$\varepsilon_G = c_1 u_o^{c_2} L_o^{c_3} d_o^{c_4} (\sin\alpha)^{c_5} \qquad [6.9]$$

where c_1, c_2, c_3, c_4, and c_5 are experimentally determined empirical constants. The values of c_1, c_2, c_3, c_4, and c_5 were found to be 1.9, 2.45, 0.97, 1.55 and 0.2, respectively, for two inclined plunging jets, compared to 2.0, 2.0, 0.35, 1.65, and 0.2, respectively, for the one inclined plunging jet that Kumagai and Endoh (1983) evaluated. Figure 6.7 shows a comparison between the measured and calculated ε_G values for the studied inclined jets. A good match can clearly be observed ($R^2 = 0.86$).

The average bubble diameter (d_b) resulting from the combination of two inclined plunging jets was evaluated for each operating condition by using the CCD images captured during the PIV runs. The value of d_b ranged from 0.001 to 0.002 m, which was smaller than the reported range of a vertical or inclined single plunging jet (0.002 to 0.003 m (Bin, 1993)). This difference is related to the shearing off of the bubbles exerted by the intersecting jets. Another non-linear regression was conducted to correlate d_b (m) with the jets' characteristic parameters. The following regression was obtained:

$$d_b = 1.12 u_o^{-0.34} (L_o / d_o)^{0.26} (\sin\alpha)^{-0.02} \qquad [6.10]$$

Equation 6.10 was plotted against the measured d_b values in Figure 6.10. The results showed a very good agreement (R^2 of 0.88).

After ε_G and d_b were determined, the specific interfacial area (a) was calculated by using Equation 6.4. It should be noted that the relative increase in ε_G and decrease in d_b resulting from the use of two inclined jets will lead to higher a values. Therefore, enhanced gas transfer efficiency (i.e., a higher overall mass transfer coefficient (k_La)) can be expected when a system of multiple two-inclined jets were applied compared to the use of a series of one vertical or inclined jet systems.

6.5 CONCLUSIONS

This study explored the air entrainment resulting from the use of two inclined circular plunging jets intersecting at the surface of a water tank at different angles and with nozzle diameters in comparison to the vertical plunging jets. Particle image velocimetery (PIV) was used to measure the lateral and axial velocities of the two-phase jets. The images captured during the PIV process by using the charge coupled device (CCD) cameras were used to estimate the average bubble size (d_b) under each operating condition. Other important parameters such as the maximum penetration depth, the width of the bubble plume, and the height and the width of the two-phase mixture (gas and water) due to the air entrainment were also measured.

The PIV measurements of the normalized axial velocity for the gas and water jets were plotted against the normalized lateral distance. The results of both phases showed good agreement with the Gaussian distribution and agree with the results in the literature. The variation from the Gaussian distribution could be related to the amount of bubbles, which may have blocked the CCD camera from capturing the scattered laser sheet.

The bubble penetration depth was measured to evaluate the jet combination that would provide the longest bubble residence time. The results obtained under the same turbulence condition and different plunging angles (α) showed that as the nozzle diameter (d_o) increased, the penetration depth (z_p) also increased. Also, under the same d_o, z_p at $\alpha =$

75° (θ = 30°) was found to be higher than the ones obtained under other cases (α = 67.5° and α = 90°). Furthermore, the combination of two inclined jets yielded a higher z_p compared to that yielded by one inclined jet.

Gas hold-up (ε_G) was found to decrease as d_o was increased. This result was related to the reduced amount of bubbles entrained under such conditions (a lower Re_d). On the other hand, when same d_o was used, ε_G increased as the outlet velocity increased. Furthermore, the value of d_b was found to be smaller than the reported range of a vertical or inclined single plunging jet. This result can be related to the shearing off of the bubbles exerted by the intersecting jets. The values of ε_G and d_b suggested higher gas transfer rates as the resulting specific interfacial area (a) was higher than that of a one-vertical or one-inclined jet system.

Table 6.1 Summary of the operating conditions for entrained air flow rate runs.

Run #	Q_L x 10^{-4} (m^3/s)	d_o x 10^{-3} (m)	α (deg)	H x 10^{-2} (m)	Run #	Q_L x 10^{-4} (m^3/s)	d_o x 10^{-3} (m)	α (deg)	H x 10^{-2} (m)
1	1.26	5.0	80	6.0	25	0.63	2.5	80	6.0
2	1.58	5.0	80	6.0	26	0.63	2.5	75	6.5
3	1.89	5.0	80	6.0	27	0.63	2.5	67.5	8.0
4	2.52	5.0	80	6.0	28	0.63	2.5	60	10
5	1.26	5.0	75	6.5	29	0.63	2.5	75	5.0
6	1.58	5.0	75	6.5	30	0.63	2.5	75	11
7	1.89	5.0	75	6.5	31	0.63	2.5	75	16
8	2.52	5.0	75	6.5	32	0.95	2.5	75	5.0
9	1.26	5.0	67.5	8.0	33	0.95	2.5	75	11
10	1.58	5.0	67.5	8.0	34	0.95	2.5	75	15.5
11	1.89	5.0	67.5	8.0	35	1.89	7.5	80	6.0
12	2.52	5.0	67.5	8.0	36	1.89	7.5	75	6.5
13	1.26	5.0	60	10	37	1.89	7.5	67.5	8.0
14	1.58	5.0	60	10	38	1.89	7.5	60	10
15	1.89	5.0	60	10	39	1.89	7.5	75	15
16	2.52	5.0	60	10	40	1.89	7.5	75	25
17	1.58	5.0	75	8.0	41	1.89	7.5	75	47
18	1.58	5.0	75	10	42	1.89	7.5	75	55
19	1.58	5.0	75	22	43	3.15	10	80	6.0
20	1.58	5.0	75	31	44	3.15	10	75	6.5
21	1.58	5.0	80	9.8	45	3.15	10	67.5	8.0
22	1.58	5.0	75	9.7	46	3.15	10	60	10
23	1.58	5.0	67.5	9.2	47	3.15	10	75	12
24	1.58	5.0	60	8.7	48	3.15	10	75	20

Table 6.2 Summary of the operating conditions for PIV runs.

Run #	Q_L x 10^{-4} (m^3/s)	d_o x 10^{-3} (m)	α (deg)	H x 10^{-2} (m)
1	0.32	2.5	90	5.0
2	0.32	2.5	75	7.0
3	0.32	2.5	67.5	8.5
4	0.63	5.0	90	5.0
5	0.63	5.0	75	7.0
6	0.63	5.0	67.5	8.5
7	0.95	5.0	90	5.0
8	1.26	5.0	90	5.0
9	0.95	5.0	75	7.0
10	1.26	5.0	75	7.0
11	0.63	5.0	75	8.6
12	0.95	5.0	75	8.6
13	1.26	5.0	75	8.6
14	0.63	5.0	75	11.2
15	0.95	5.0	75	11.2
16	1.26	5.0	75	11.2
17	0.95	5.0	67.5	8.5
18	1.26	5.0	67.5	8.5
19	0.95	7.5	90	5.0
20	0.95	7.5	75	7.0
21	0.95	7.5	67.5	8.5
22	1.26	10	90	5.0
23	1.26	10	75	7.0
24	1.26	10	67.5	8.5

Table 6.3 Summary of the air entrainment results.

d_o x 10^{-3} (m)	α (deg)	u_o (m/s)	L_o/d_o	Q_G/Q_L	d_o x 10^{-3} (m)	α (deg)	u_o (m/s)	L_o/d_o	Q_G/Q_L
5	80	6.4	12.2	0.37	2.5	80	12.8	24.4	0.87
5	80	8.0	12.2	0.45	2.5	75	12.8	26.9	1.12
5	80	9.6	12.2	0.50	2.5	67.5	12.8	34.6	1.25
5	80	12.8	12.2	0.54	2.5	60	12.8	46.2	1.37
5	75	6.4	13.5	0.44	2.5	75	12.8	20.7	0.87
5	75	8.0	13.5	0.50	2.5	75	12.8	45.6	1.25
5	75	9.6	13.5	0.58	2.5	75	12.8	64.2	1.50
5	75	12.8	13.5	0.59	2.5	75	19.3	20.7	1.08
5	67.5	6.4	17.3	0.50	2.5	75	19.3	45.6	1.33
5	67.5	8.0	17.3	0.55	2.5	75	19.3	64.2	1.66
5	67.5	9.6	17.3	0.62	7.5	80	4.3	8.1	0.25
5	67.5	12.8	17.3	0.65	7.5	75	4.3	9.0	0.33
5	60	6.4	23.1	0.56	7.5	67.5	4.3	11.5	0.42
5	60	8.0	23.1	0.60	7.5	60	4.3	15.4	0.50
5	60	9.6	23.1	0.66	7.5	75	4.3	20.7	0.46
5	60	12.8	23.1	0.81	7.5	75	4.3	34.5	0.58
5	75	8.0	16.6	0.55	7.5	75	4.3	64.2	0.75
5	75	8.0	20.7	0.60	7.5	75	4.3	75.9	0.87
5	75	8.0	45.6	0.90	10	80	4.0	6.1	0.30
5	75	8.0	64.2	1.10	10	75	4.0	6.7	0.35
5	80	8.0	19.9	0.60	10	67.5	4.0	8.7	0.40
5	75	8.0	20.1	0.60	10	60	4.0	11.5	0.45
5	67.5	8.0	19.9	0.60	10	75	4.0	12.4	0.47
5	60	8.0	20.1	0.60	10	75	4.0	20.7	0.62

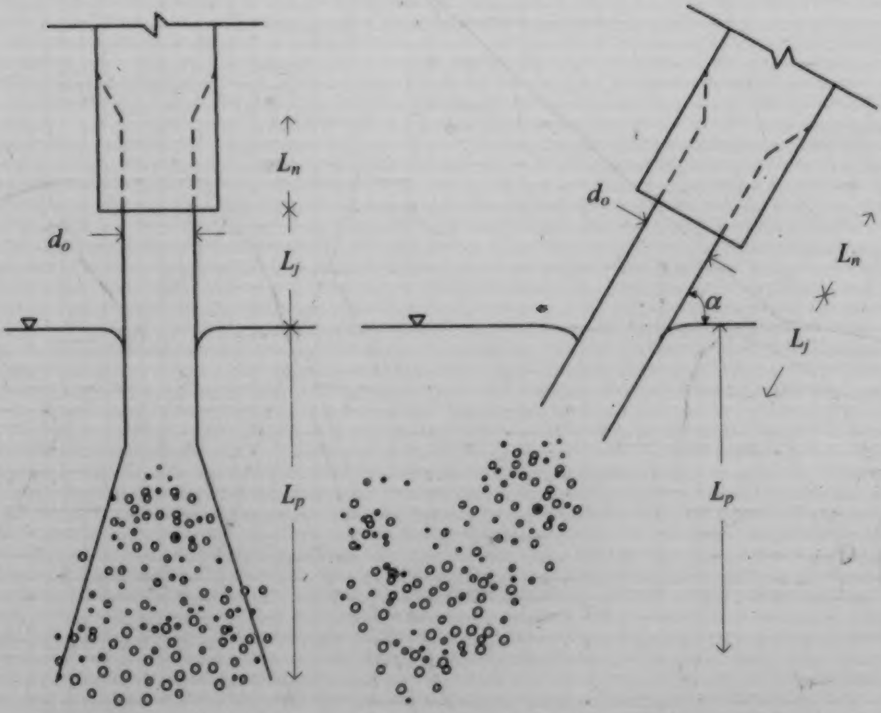

Figure 6.1 Schematic of characteristic lengths of plunging jets.

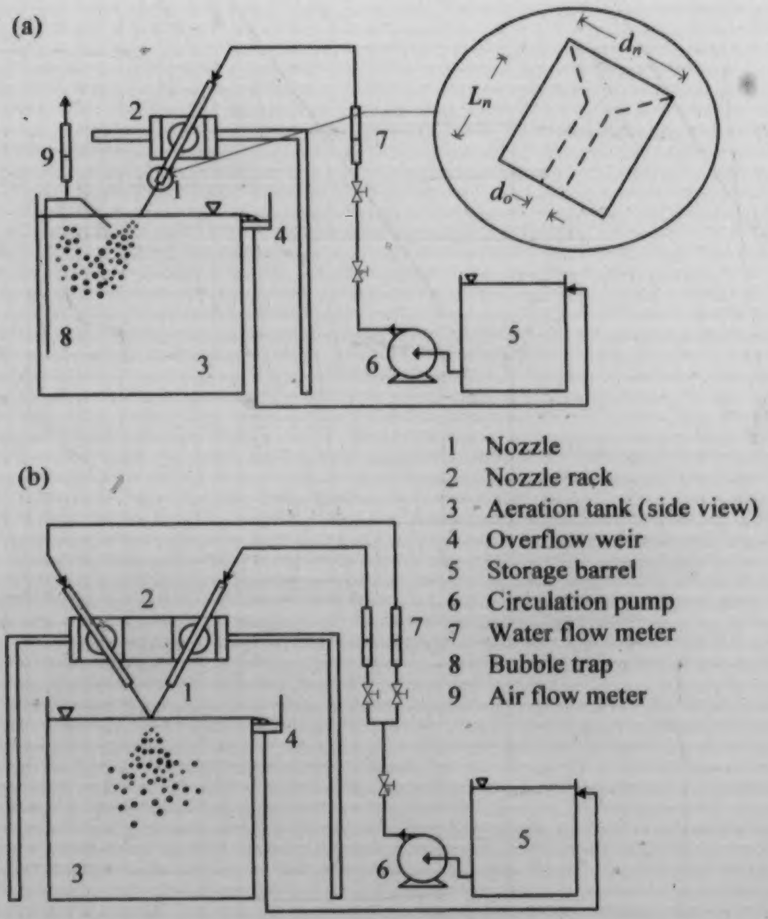

Figure 6.2 Experimental setup (flow facility).

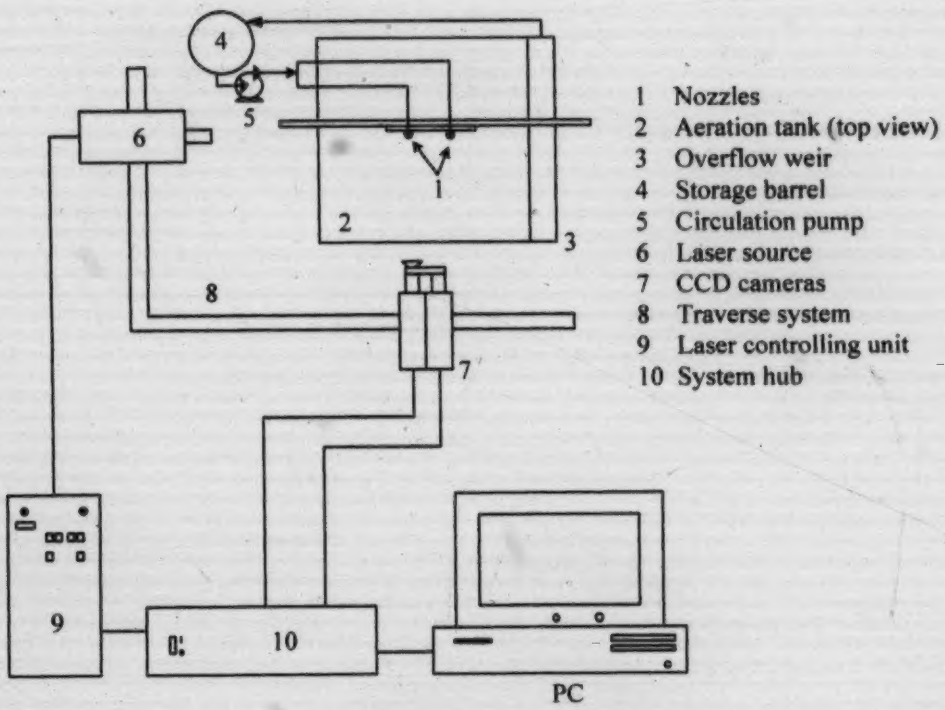

Figure 6.3 PIV Setup.

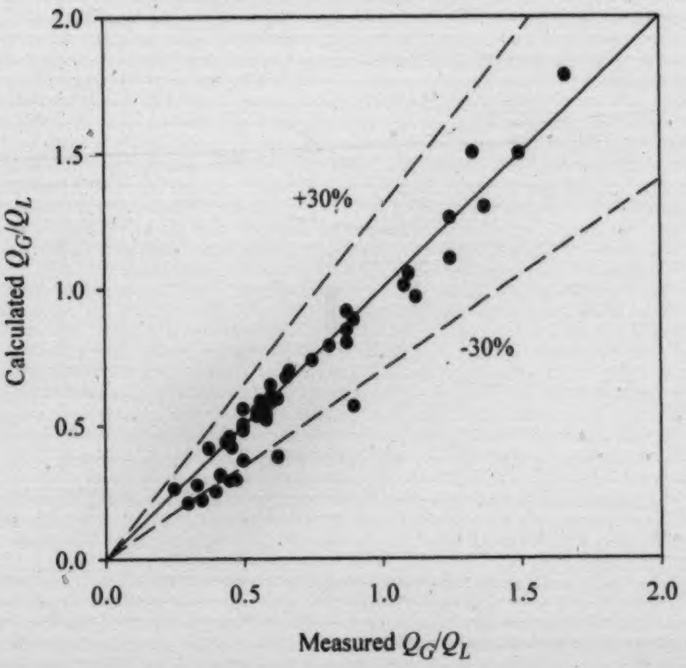

Figure 6.4 Comparison between measured and calculated air entrainment ratio.

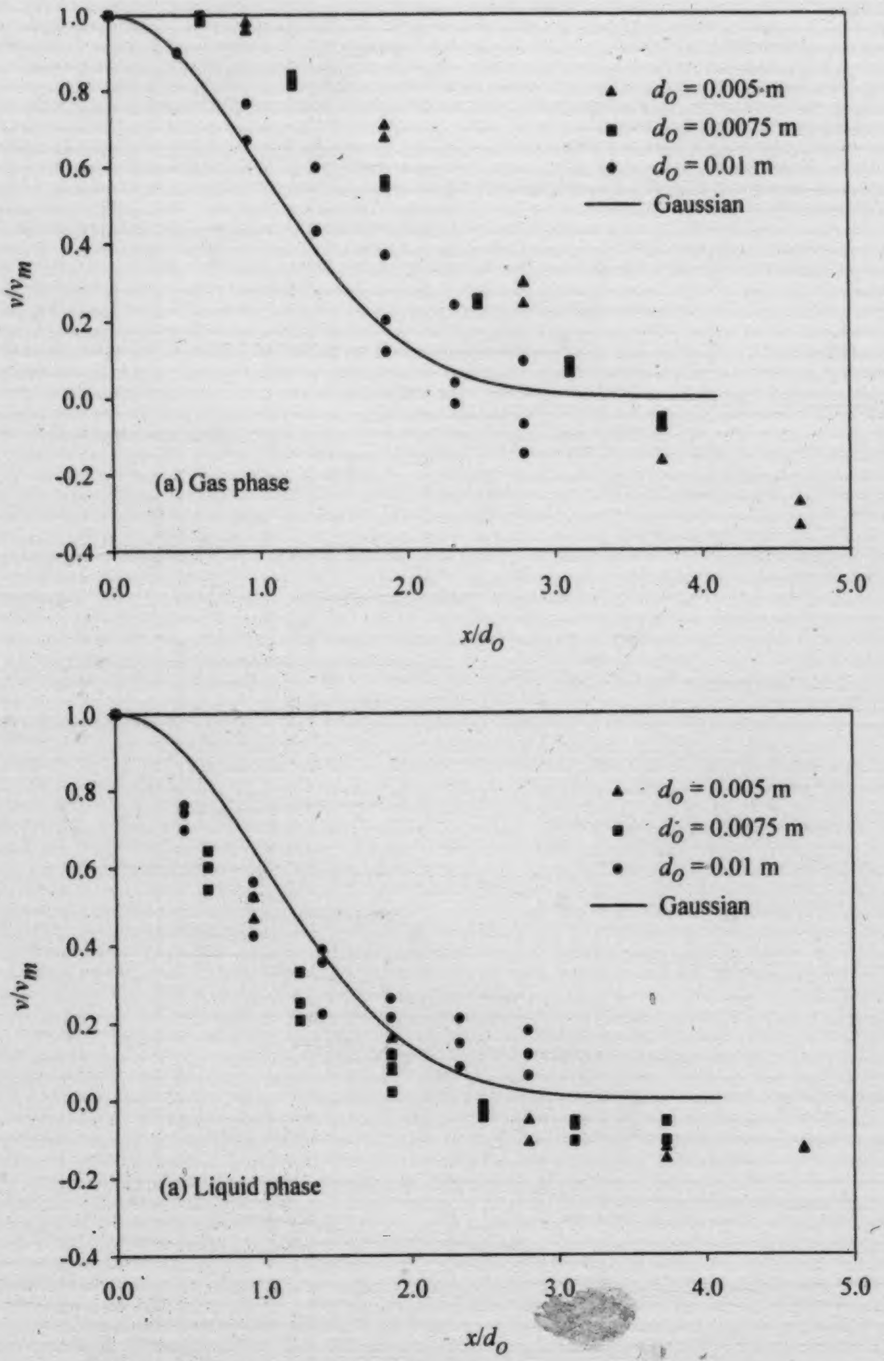

Figure 6.5 Lateral distributions of the axial mean velocity.

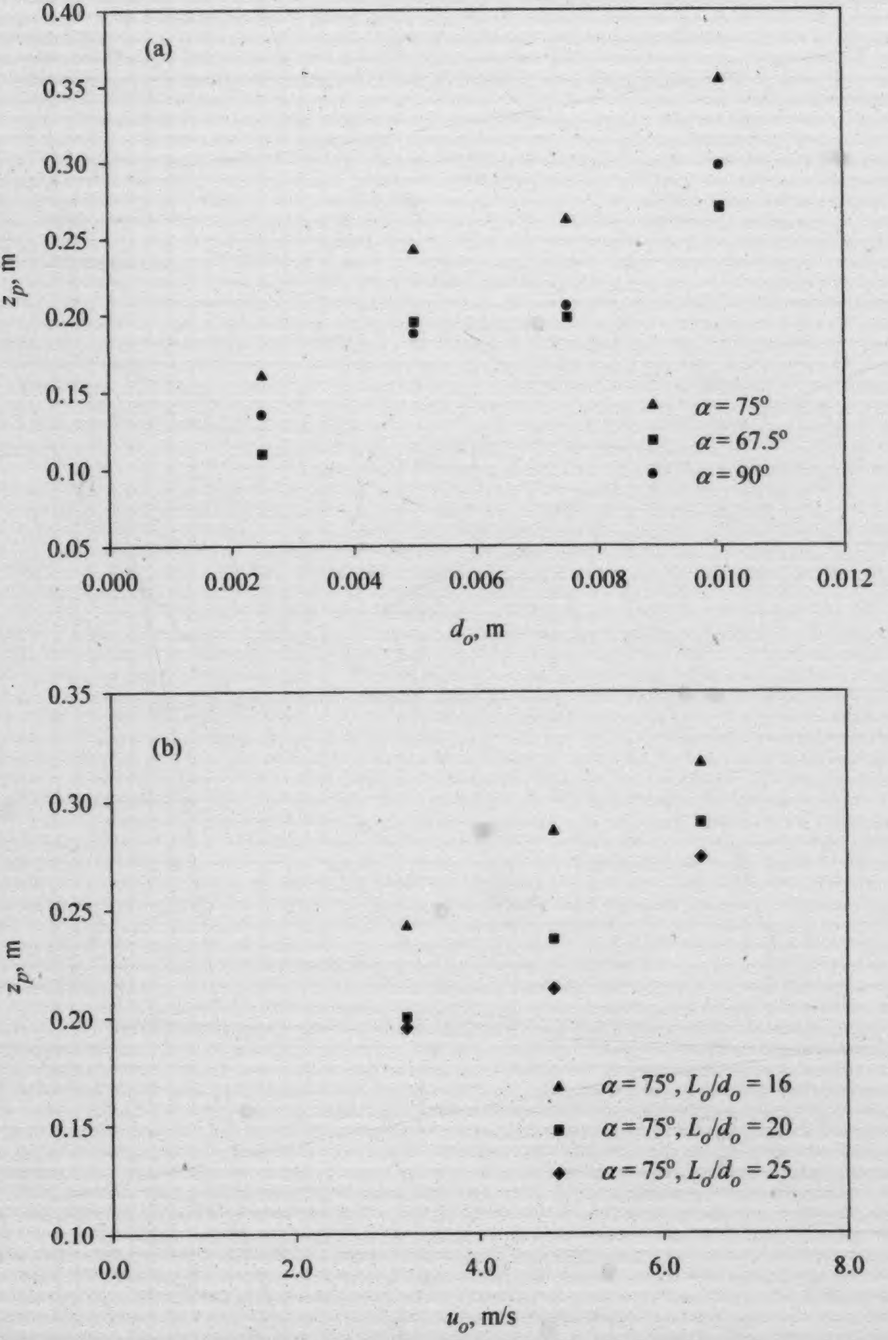

Figure 6.6 Variation of penetration depth with nozzle diameter and outlet velocity.

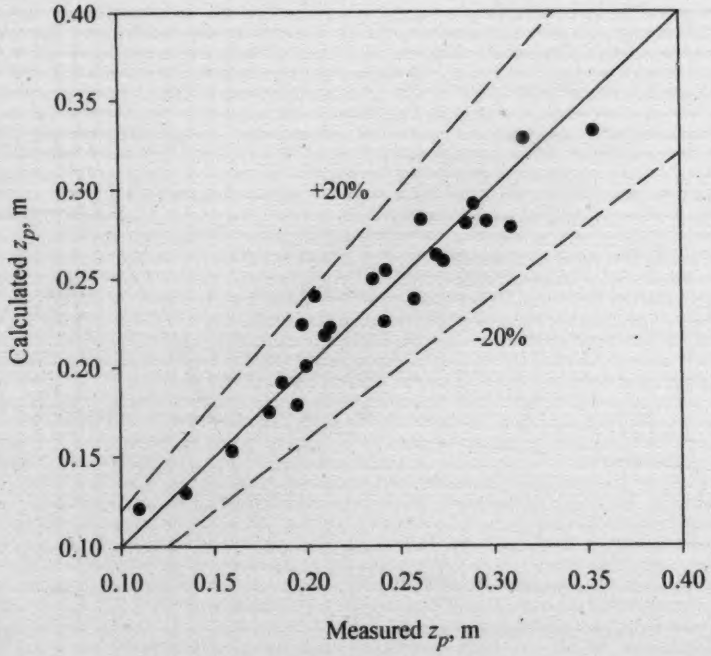

Figure 6.7 Comparison between measured and calculated penetration depth.

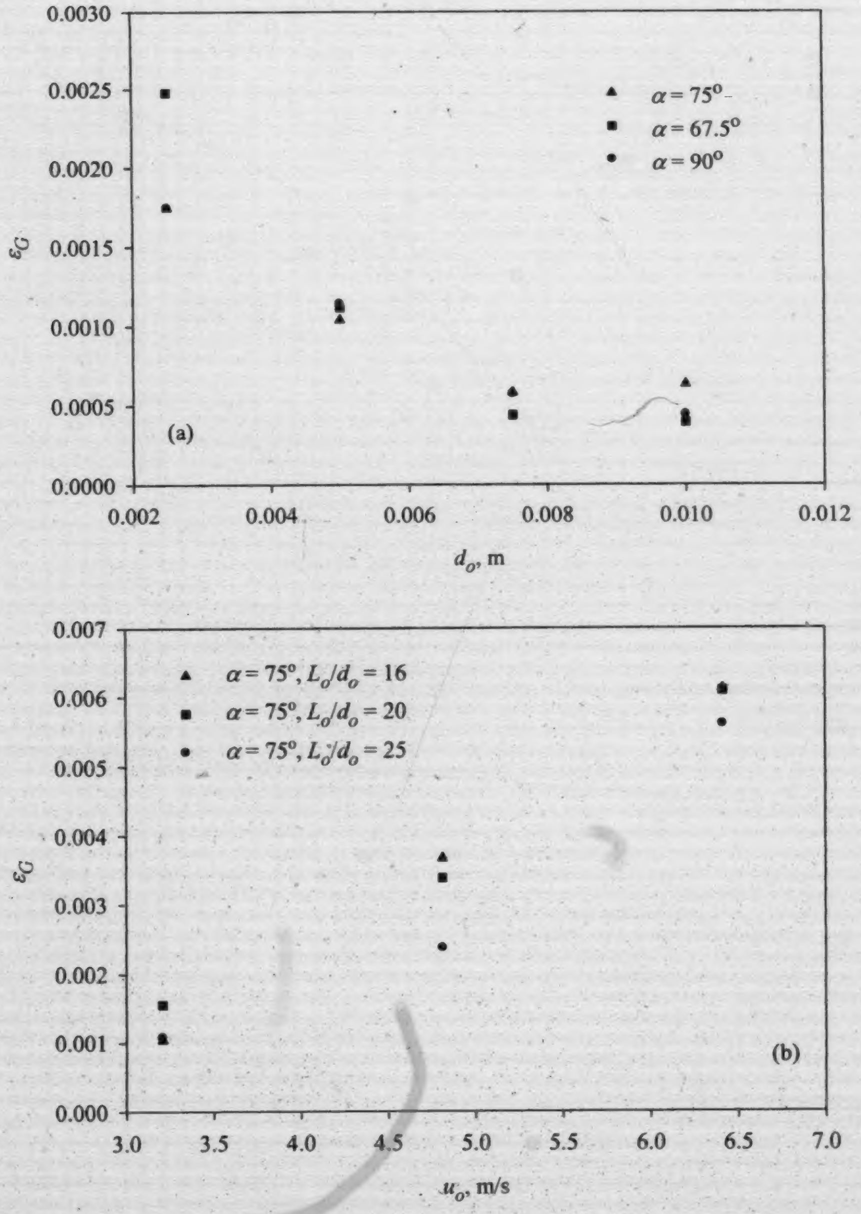

Figure 6.8 Variation of the gas hold-up with nozzles diameter and outlet velocity.

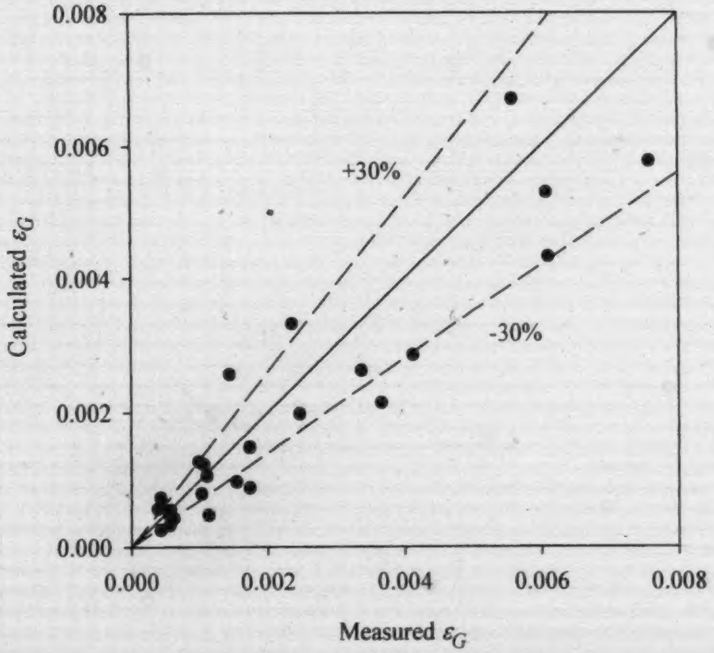

Figure 6.9 Comparison between measured and calculated gas hold-up.

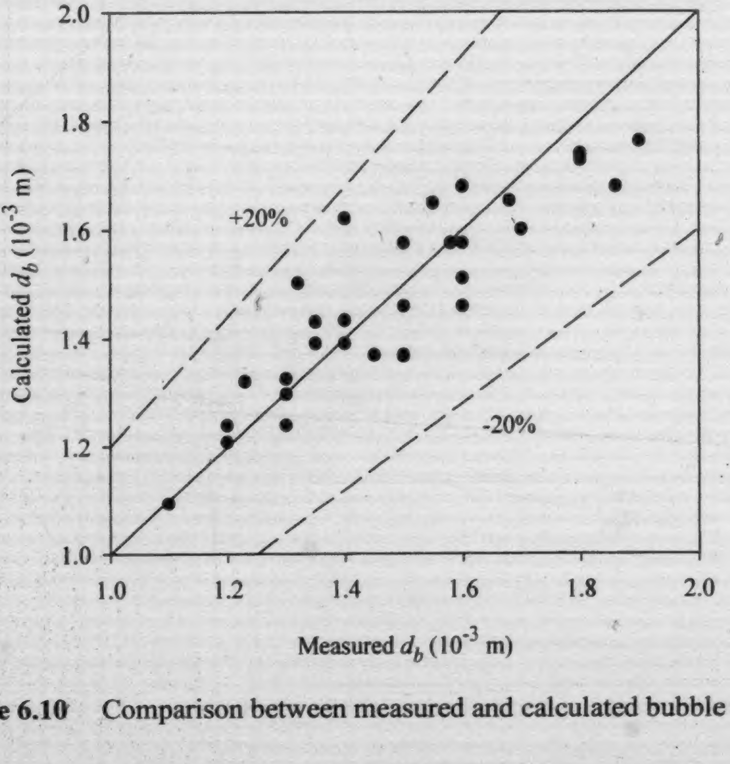

Figure 6.10 Comparison between measured and calculated bubble diameter.

6.6 REFERENCES

1. Atkinson, J.F., J.V. Benschoten, and C.Y. Cheng, *Development of Particle Image Technology for Water Treatment Studies*. (Denver: AWWA Research Foundation, U.S.A., 2000).

2. Baylar, A., and T. Bagatur, "Experimental Studies on Air Entrainment and Oxygen Content Downstream of Sharp-Crested Weirs", *Water and Environment Journal*, 20(4): 210-216 (2006).

3. Bin, A.K., "Gas Entrainment by Plunging Liquid Jets", *Chemical Engineering Science*, 48(21): 3585-3630 (1993).

4. Burgess, J.M., and N.A. Molloy, "Gas Absorption in Plunging Liquid Jet Reactor", *Chemical Engineering Science*, 28(1): 183-190 (1973).

5. Chanson, H., S. Aoki, and A. Hoque, "Physical Modelling and Similitude of Air Bubble Entrainment at Vertical Circular Plunging Jets", *Chemical Engineering Science*, 59(4): 747-758 (2004).

6. Cummings, P.D., and H. Chanson, "Air Entrainment in the Developing Flow Region of Plunging Jets .1. Theoretical Development", *Journal of Fluids Engineering-Transactions of the Asme*, 119(3): 597-602 (1997).

7. Cummings, P.D., and H. Chanson, "An Experimental Study of Individual Air Bubble Entrainment at a Planar Plunging Jet", *Chemical Engineering Research & Design*, 77(A2): 159-164 (1999).

8. Davoust, L., J.L. Achard, and M. El Hammoumi, "Air Entrainment by a Plunging Jet: The Dynamical Roughness Concept and Its Estimation by a Light Absorption Technique", *International Journal of Multiphase Flow*, 28(9): 1541-1564 (2002).

9. Evans, G.M., G.J. Jameson, and C.D. Rielly, "Free Jet Expansion and Gas Entrainment Characteristics of a Plunging Liquid Jet", *Experimental Thermal and Fluid Science*, 12(2): 142-149 (1996).

10. Evans, G.M., G.J. Jameson, and C.D. Rielly, *Air Bubble Entrainment in Free-Surface Turbulent Shear Flows*. (London: Academic Press, 1997).

11. Iguchi, M., K. Okita, and F. Yamamoto, "Mean Velocity and Turbulence Characteristics of Water Flow in the Bubble Dispersion Region Induced by Plunging Water Jet", *International Journal of Multiphase Flow*, 24(4): 523-537 (1998).

12. Ito, A., K. Yamagiwa, K. Tajima, M. Yoshida, and A. Ohkawa, "Maximum Penetration Depth of Air Bubbles Entrained by Vertical Liquid Jet", *Journal of Chemical Engineering of Japan*, 33(6): 898-900 (2000).

13. Jakubowski, C.A., B.W. Atkinson, P. Dennis, and G.M. Evans, "Ozone Mass Transfer in a Confined Plunging Liquid Jet Contactor", *Ozone-Science & Engineering*, 25(1): 1-12 (2003).

14. Kumagai, M., and K. Endoh, "A Note on the Relationship between Gas Entrainment Curve and Its Starting Velocity", *Journal of Chemical Engineering of Japan*, 16(1): 74-75 (1983).

15. Kusabiraki, D., M. Murota, S. Ohno, K. Yamagiwa, M. Yasuda, and A. Ohkawa, "Gas Entrainment Rate and Flow Pattern in a Plunging Liquid Jet Aeration System Using Inclined Nozzles", *Journal of Chemical Engineering of Japan*, 23(6): 704-710 (1990).

16. McKeogh, E.J., and D.A. Ervine, "Air Entrainment Rate and Diffusion Pattern of Plunging Liquid Jets", *Chemical Engineering Science*, 36(7): 1161-1172 (1981).

17. Oguz, H.N., "The Role of Surface Disturbances in the Entrainment of Bubbles by a Liquid Jet", *Journal of Fluid Mechanics*, 372: 189-212 (1998).

18. Ohkawa, A., D. Kusabiraki, Y. Shiokawa, N. Sakai, and M. Fujii, "Flow and Oxygen-Transfer in a Plunging Water Jet System Using Inclined Short Nozzles and Performance-Characteristics of Its System in Aerobic Treatment of Waste-Water", *Biotechnology and Bioengineering*, 28(12): 1845-1856 (1986).

19. Raffel, M., C. Willert, and J. Kompenhans, *Particle Image Velocimetry: A Practical Guide*. . (N. Y.: Springer-Velag Berlin Heidelberg, 1998).

20. Soh, W.J., B.C. Khoo, and W.Y.D. Yuen, "The Entrainment of Air by Water Jet Impinging on a Free Surface", *Experiments in Fluids*, 39(3): 496-504 (2005).

21. Stanislas, M., J. Kompenhans, and J. Westerweel, *Particle Image Velocimetry: Progress Towards Industrial Application*. (Dordrecht, The Netherlands: Kluwer Academic Publishers, 2000).

22. Vandesande, E., and J.M. Smith, "Jet Break-up and Air Entrainment by Low Velocity Turbulent Water Jets", *Chemical Engineering Science*, 31(3): 219-224 (1976).

23. Yamagiwa, K., Y. Ohmae, M.H. Dahlan, and A. Ohkawa, "Activated-Sludge Treatment of Small-Scale Waste-Water by a Plunging Liquid Jet Bioreactor with Cross-Flow Filtration", *Bioresource Technology*, 37(3): 215-222 (1991).

24. Yamagiwa, K., Y. Oohira, S. Takesono, M. Yoshida, and A. Ohkawa, "Simultaneous Removal of Organic Carbon and Nitrogen by a Plunging Liquid Jet Bioreactor with Crossflow Filtration Operated under Zone-Limited Aeration", *Journal of Chemical Engineering of Japan*, 29(3): 464-469 (1996).

CHAPTER 7

COMPUTATIONAL FLUID DYNAMICS MODELLING OF DISSOLVED OXYGEN IN A RECYCLED WATER POND

7.1 INTRODUCTION

Recycled water (RCW) ponds are used to centralize the collection of tailings water to ensure an adequate supply of cooling water required for the production of synthetic oil. The water entering the RCW ponds is generally high in suspended solids (SS) because of unsettled fine tailings. To avoid scouring the bottom of the ponds, the inlets are usually designed to dissipate the energy of the entering water jets in the form of spray aeration. Such designs not only reduce bottom scour but also mitigate short-circuiting, thus leading to lower concentrations of SS in the pond's effluent. However, the intensive aeration process raises the level of the dissolved oxygen (DO) in the RCW pond up to saturation levels. As a result, carbon steel pipelines, used to supply RCW from the pond to the processing units, may be subjected to increased rates of corrosion as the concentration of the oxidant, in this case oxygen, increases (Kuch, 1988; Stratmann and Muller, 1994; Tomoe et al., 1999). Recent research work has shown that reduced concentrations of dissolved oxygen will reduce the rate of carbon steel corrosion (Kawai et al., 2003; Padma et al., 2001). Therefore, a modelling technique is needed to explore the options for reducing the DO levels in such ponds.

This chapter reports on the modelling of DO in a RCW pond, located at the Syncrude Oil Sands operation in northern Alberta, Canada, which undergoes an extensive aeration process due to its inlet configurations. The ultimate goal of this research project was to find a solution that would lower the DO concentration in the RCW pond. Subsequently, the corrosion effect on the carbon steel pipeline delivering the water to a remote mine site could be minimized. The study involved the following stages: (1) developing a computational fluid dynamics (CFD) model that would simulate the DO levels in the RCW pond; (2) validating the CFD model's results by comparing them with field data measurements; and (3) utilizing the CFD model to predict the RCW pond's DO levels for a new inlet configuration (a submerged inlet).

7.2 MODEL FORMULATION

Many researchers have investigated the modelling of DO in lakes, ponds, and reservoirs. However, the majority of these efforts focussed on the variation of DO with depth and hence used one-dimensional models only (Bell et al., 2006; Ginot and Herve, 1994; Imteaz et al., 2003; Snodgrass and Dalrymple, 1985; Stefan et al., 1995). 1D-models were used because the complexity of the governing equations of multidimensional problems in addition to the computational requirements needed for solving such equations. Also, the high number of parameters controlling the DO in water bodies limits the application of the multidimensional models. However, some research work has been conducted to explore the use of 2D and 3D models in simulating DO in different water bodies (Boegman et al., 2001; Choa et al., 2005; Harza, 2003; Sullivan and Rounds, 2005). It was concluded that computational fluid dynamics (CFD) modelling appeared to be a promising technique when good calibration measurements are available. The CFD models can solve the governing equations simultaneously and provide spatial and temporal representation of the solved problem. In addition, a good visualization of the results can be obtained by using this modelling technique.

The governing equations to be solved for the RCW pond by the CFD model are the Navier-Stokes (momentum and continuity) and the mass conservation equations for incompressible fluids. The Navier-Stokes equations (in Cartesian form) for incompressible fluids are

$$\frac{\partial u_i}{\partial t}+\frac{\partial (u_i u_j)}{\partial x_i}=-\frac{1}{\rho}\frac{\partial p}{\partial x_i}+\frac{\partial \tau_{ij}}{\partial x_j}+g_i \qquad [7.1]$$

$$\frac{\partial u_i}{\partial x_i}=0 \qquad [7.2]$$

$$\tau_{ij}=\nu_L\left(\frac{\partial u_i}{\partial x_j}+\frac{\partial u_j}{\partial x_i}\right) \qquad [7.3]$$

where t is the time (s), x_i or x_j (i and j = 1, 2, 3) are the Cartesian coordinates ("x_1, x_2, x_3" or "x, y, z", m), u_i or u_j ("u_1, u_2, u_3" or "u, v, w") are the Cartesian components of the fluid velocity (m/s), ρ is the fluid density (kg/m^3), p is the static pressure (Pa), τ_{ij} is the stress tensor for incompressible flows (m^2/s^2), g_i or (g_1, g_2, g_3) are the Cartesian components of the gravitational acceleration (note that both g_1 and g_3 equal zero, while g_2 equals 9.81 m/s^2), and ν_L is the fluid kinematic viscosity (m^2/s). The mass conservation equation (also know as the transport equation) of the DO concentration (C_{DO}, mg/L) in the same fluid can be written as

$$\frac{\partial C_{DO}}{\partial t}+\frac{\partial (u_i C_{DO})}{\partial x_i}=\frac{\partial}{\partial x_i}\left(D\frac{\partial C_{DO}}{\partial x_i}\right)+S \qquad [7.4]$$

where D is the diffusivity coefficient of DO (m^2/s), and S is the source(s) or sink(s) of *DO* (mg/L·s). The above equations can be solved numerically by using the finite volume approach within the CFX Solver™ 10.0. The turbulence in the pond can be modelled by using the well-know k-ε model, where k is the turbulence kinetic energy (m^2/s^2), and ε is the dissipation rate (m^2/s^3). A detailed description of the k-ε model can be found elsewhere (Bernard and Wallace, 2002; Davidson, 2004).

Dissolved oxygen in lakes, ponds and reservoirs is controlled by oxygen sources and sinks. DO sources include (1) DO in the entering flows where the inlet design might play a major factor, (2) reaeration from the atmosphere due to wind action at the water surface, and (3) DO production due to photosynthesis processes if phytoplankton exists in the water body (Antonopouls and Gianniou, 2003; Banks, 1975; Snodgrass, 1983). On the other hand, DO sinks include oxygen losses due to (1) biological degradation of organic compounds represented by biochemical oxygen demand (BOD), (2) aerobic decomposition of sediments at the pond's bottom, represented by sediment oxygen demand (SOD), and (3) respiration of phytoplankton if it exists in the water body (Gelda et al., 1995; Stefan and Fang, 1994; Truax et al., 1995). Since no phytoplankton was observed in the RCW pond, photosynthesis and respiration processes were eleminated as they were not applicable for this study.

The RCW pond under investigation receives water from two lakes used as settling basins for water and fine tailings resulting from oil sand extraction. Both lakes are in near anaerobic condition, as recent measurements showed that the DO levels are in the range of 0 to 0.4 mg/L. The flow rates from Lake 1 to the RCW pond range from 2.5 to 5.0 m^3/s with a temperature range of 1.0 °C (during winter) to 25 °C (during summer). The pond receives flow rates from Lake 2 ranging from 2.2 to 4.0 m^3/s, with a similar temperature range as in Lake 1. Two additional inlets contribute about 1 to 1.8 m^3/s of water to the pond. One of them is operational only during summer, with an average flow rate of about 0.8 m^3/s. The fourth inlet is used to recycle the retrieved (condensed) cooling water from a nearby refinery (about 1.0 m^3/s year around). The pond's surface area of is about 1.5 x 10^5 m^2 with a variable depth ranging from 0.4 to 4.8 m, with a mean depth of 2.3 m according to a field depth survey. The average theoretical hydraulic retention time (HRT) is estimated to be around 18 h. The RCW is delivered to the processing units at a flow rate range of 6.0 to 7.0 m^3/s (using two outlets), with an average flow rate of 6.5 m^3/s.

7.2.1 Inlets' Boundary Conditions

The water delivered, under high turbulent conditions, from both lakes to the RCW pond is dissipated at the inlets to avoid scouring the bottom of the pond. The inlets were designed as shown in Figure 7.1 to divert and spray the water jets in air before they enter the pond. This feature, in turn, leads to the intensive aeration process of the entering waters and hence raises the levels of DO concentration dramatically inside the RCW pond. This aeration process (Figure 7.1) occurs in a few seconds. Hence, the effect of BOD and SOD can be safely ignored. Consequently, the rate of the DO concentration (C_{DO}) over time (t) resulting from each inlet can be expressed as

$$\frac{dC_{DO}}{dt} = k_L a\left(C_{DO}^{sat} - C_{DO}\right) \qquad [7.5]$$

where k_La is the overall mass transfer coefficient (s^{-1}), and C_{DO}^{sat} is the DO saturation concentration (mg/L). The value of k_La can be expressed as a function of the overall mass transfer coefficient at 20 °C (k_La_{20}) and the water temperature (T, °C):

$$k_La = k_La_{20}\theta_1^{T-20} \qquad [7.6]$$

where θ_1 equals 1.024 (Stefan and Fang, 1994). The k_La_{20} (s^{-1}) can be represented by (Bin, 1993)

$$k_La_{20} = 0.003\left(\frac{Q^2}{gd_o^5}\right)^{0.85}\left(\frac{g^2}{\nu_{L20}}\right)^{1/3}\left(\frac{L_j}{d_o}\right)^{0.5} \qquad [7.7]$$

where Q is the flow rate (m^3/s), d_o is the initial water jet diameter (m), L_j is the length of the water jet (m), and $\nu_{L_{20}}$ is the kinematic viscosity of water at 20 °C (m^2/s). Equation 7.7 is valid for a relatively low modified Froude number ($Fr_o' = \frac{Q^2}{gd_o^5}$) ranging up to 200 with an estimated error of $\pm 20\%$ (Bin, 1993). The Fr_o' for the RCW inlets condition ranges from 0.1 to 6.9 as d_o equals 0.9 m for inlets 1, 3, and 4, and 1.8 m for inlet 2 (Q ranges from 0.8 to 7.0 m^3/s). The value of L_j ranges from 2.5 to 8 m for inlet 1. A regression obtained for L_j as a function of Q for inlet 1 is shown in Figure 7.2 with a R^2 value of 0.99. Since the design of inlets 3 and 4 is similar to that of inlet 1, it was assumed that the same regression can be used to obtain their L_j values. The value of L_j for inlet 2 should range from 1.5 to 2 m according to the regression shown in Figure 7.2 ($R^2 = 0.97$). However, field observations suggested that the value obtained from the regression had to be multiplied by a factor of 5. This factor was used to account for the effective jet length resulting from four pentagon-shaped concrete columns, used to dissipated the energy of the entering water jet (in addition to the initial free jet length as shown in Figure 7.1).

The DO saturation concentration (C_{DO}^{sat}) in Equation 7.5 can be determined by calculating the mean sea level DO concentration for fresh water ($C_{DO}^{s_o}$), which can be written as (Bell et al., 2006)

$$C_{DO}^{s_o} = 0.0043T^2 - 0.36T + 14.48 \qquad [7.8]$$

Then, the C_{DO}^{sat} can be expressed as (Thomann and Mueller, 1987)

$$C_{DO}^{sat} = C_{DO}^{s_o} P \left[\frac{\left[1 - \left({P_{wv}}/{P} \right)\right](1 - \theta P)}{(1 - P_{wv})(1 - \theta)} \right] \qquad [7.9]$$

where P is the atmospheric pressure (atm), P_{wv} is the water vapour pressure (atm), and θ is a dimensionless correcting factor. The values of P can be obtained from Environment Canada (2006) while P_{wv} and θ can be calculated by using the following equations (Thomann and Mueller, 1987):

$$P_{wv} = \exp\left(11.8571 - \frac{3840.7}{273.15 + T} + \frac{216961}{(273.15 + T)^2} \right) \qquad [7.10]$$

$$\theta = 0.000975 - 1.426 \times 10^{-5} T + 6.436 \times 10^{-8} T^2 \qquad [7.11]$$

Once the constants $k_L a$ and C_{DO}^{sat} are determined, Equation 7.5 can be integrated for DO ranging from C_{DO}^{in} (at $t = 0$) to C_{DO} (for any time t) to yield

$$C_{DO} = C_{DO}^{sat} - \left(C_{DO}^{sat} - C_{DO}^{in} \right) \cdot e^{-k_L a \cdot t} \qquad [7.12]$$

The time (t) in Equation 7.12 ranges from 0.5 to 1.5 s for inlets 1, 3, and 4 and from 2 to 3 s for inlet 2 (depending on the flow rate at each inlet). Field observations of the DO concentration at the outflows of inlets 1 and 2 agreed very well with Equation 7.12, as depicted by Table 7.1. Equation 7.12 could not be applied to inlet 3 as no data were collected for the initial DO concentration as the field measurements were taken from September 2005 until May 2006. However, since this inlet is close to inlets 1 and 2 where the water is almost saturated with DO, and the flow rate is relatively low, the effect of disregarding this inlet might not be significant under current conditions. Also, inlet 4 was not included in the DO model developed for the RCW pond due to the lack of DO concentration measurements at this location because of safety concerns. According to Equation 7.12, inlet 4 can deliver water with a DO concentration that ranges from 1 mg/L to 4 mg/L (for an initial DO range of 0 to 3 mg/L). Therefore, due to possible short circuiting, this inlet might contribute to lower DO readings than expected in winter (when microbial activity is relatively slow; i.e., the DO level is high) and to higher DO readings than expected in summer (when microbial activity is relatively high; i.e., DO level is low).

7.2.2 Surface Boundary Condition

An additional source for DO in the RCW pond is related to the reaeration at the free water surface of the pond due to wind action. Therefore, the boundary condition at this water surface can be described by the oxygen flux due to the reaeration process and the losses of oxygen corresponding to the carbonaceous biochemical oxygen demand (CBOD) as follows:

$$\frac{dC_{DO}}{dt} = \frac{k_s}{h}\left(C_{DO}^{sat} - C_{DO}\right) - k_d L_{CBOD} \qquad [7.13]$$

where k_s is the reaeration coefficient (m/s), h is the average water depth (m), k_d is the pseudo 1st decay coefficient of organic matter (s^{-1}), and L_{CBOD} is the CBOD concentration (mg/L). The value of k_s depends on the wind velocity (U) and the water temperature (T), many researchers have stated. Different cited representations of k_s as a function of U (m/s) and T (°C) have been evaluated (Antonopouls and Gianniou, 2003; Fang and Stefan, 1995; Gelda et al., 1996; Gualtieri, 2006). Although most of these relationships yield similar values of k_s (m/s), the following representation was chosen as it combines both U and T in one equation (Bell et al., 2006; Stefan and Fang, 1994):

$$k_s = 2.611\times10^{-7}U^{1.64}\left(0.1065e^{-0.0627T} + 0.00495\right)^{-0.5} \qquad [7.14]$$

The wind velocity (U), measured at 10 m above the water surface, can be obtained from Environment Canada (2006) while the water temperature (T) was obtained whenever DO measurements in the RCW pond were conducted. Table 7.2 summarizes the field measurements and data collected during the course of this study. This data was used in running and validating the CFD model developed to simulate DO concentrations in the RCW pond under current and suggested inlet conditions.

Some additional measurements were collected at inlets 1 and 2 from June to September 2005, but unfortunately, the outlet measurements were missing. Hence, these measurements could not be used in modelling the pond's current inlet conditions. However, they provided a good basis for modelling DO under the suggested inlet condition given that the CFD model successfully simulated the current condition.

The second part of Equation 7.13 is related to the CBOD, which is exerted by the presence of microorganisms that can derive the energy from organic carbon substances oxidation. The CBOD of the RCW pond was measured (by using a standard CBOD test) over time in order to fit the following theoretical equation (Thomann and Mueller, 1987) with the experimental results:

$$L_{CBOD} = L_o e^{-k_d \cdot t} \qquad [7.15]$$

where L_o is the ultimate CBOD concentration (mg/L). Figure 7.3 shows the experimental results and the model (Equation 7.15). The values obtained for L_o and the pseudo 1st order decay coefficient at 20 °C (k_{d20}) were found to be 50.8 mg/L and 0.32 d^{-1}, respectively, with R^2 of 0.97. Since the CBOD reaction is mediated by microorganisms, the value of k_d is a function of the water temperature (T) according to the following equation:

$$k_d = k_{d_{20}} \theta_2^{T-20} \qquad [7.16]$$

The value of θ_2 equals 1.13 for T ranging from 4 to 20 °C and 1.047 for $T \geq 20$ °C (Fang and Stefan, 1995). Equation 7.13 can now be integrated for DO ranging from C_{DO}^{in} (at t = 0) to C_{DO} (for any time t) to give

$$C_{DO} = C_{DO}^{sat} - \frac{k_d L_o}{\left({k_s}/{h}\right) - k_d} e^{-k_d \cdot t} + \frac{k_d L_o + \left[\left({k_s}/{h}\right) - k_d\right]\left(C_{DO}^{in} - C_{DO}^{sat}\right)}{\left({k_s}/{h}\right) - k_d} e^{-\frac{k_s}{h}t} \qquad [7.17]$$

The time (t) in Equation 7.17 was set to be the theoretical hydraulic retention time (HRT) of the RCW pond. Although the average HRT was estimated to be around 18 h, several values of the HRT were used to simulate different scenarios of the RCW pond according to the applied flow rates and pond depths.

7.2.3 Bottom Boundary Condition

The boundary condition at the bottom of the RCW pond can be described by (Bell et al., 2006)

$$\frac{dC_{DO}}{dt} = -\frac{SOD}{h} \qquad [7.18]$$

where *SOD* is the sediment oxygen demand (g/m^2·d). The SOD, which represents the DO required for aerobic decompositions at the surface layer of the bottom deposits in direct contact with the water, can be determined experimentally by utilizing in-situ devices as explained by Thomann and Mueller (1987) and Truax et al. (1995). However, due to some safety concerns, the experimental procedure was simulated by collecting a sample of sediments and water from the RCW pond and observing the change in the DO concentration over time at 20 °C. The experiment was conducted in a 1-L chamber with a diameter of 0.08 m. Typically, the change of DO over time in SOD experiments is linear after an initial stabilization period of about 20 minutes (Truax et al., 1995; Wood, 2001). The sediment oxygen demand at 20 °C (SOD_{20}) in g/m^2·d can be calculated by using the following relationship (Doyle and Lynch, 2005; Wood, 2001):

$$SOD_{20} = 0.024\frac{V_s}{A_s}(-b) \qquad [7.19]$$

where V_s is the volume of the water in the chamber (= 0.5 L), A_s is the surface area of the sediment layer (= 5.0×10^{-3} m^2), and b is the slope of the regression line obtained from the SOD test (mg/L·h). The value of b was found to be -0.11 mg/L·h as shown in Figure 7.4, with R^2 of 0.87. Hence, SOD_{20} was determined to be 0.26 g/m^2·d. The typical range for SOD_{20} for water bodies with a sandy bottom is 0.2 to 1.0 g/m^2·d and 0.05 to 0.1 g/m^2·d for mineral soils (Thomann and Mueller, 1987). The value of the SOD for the RCW pond sediment which is a mixture of sand and clay particles (Czarnecki et al., 2005), clearly agrees with the typical range cited in the literature. The SOD can then be corrected for the water temperature by

$$SOD = SOD_{20}\theta_3^{T-20} \qquad [7.20]$$

The value of the constant θ_3 is 1.065 for $T \geq 10$ °C and 1.13 for $T<10$ °C (Fang and Stefan, 1995). The effect of SOD is normally negligible when the water temperature drops below 5 °C (Thomann and Mueller, 1987).

After the SOD value is determined, Equation 7.18 can be integrated for DO ranging from C_{DO}^{in} (at $t = 0$) to C_{DO} (for any time t) as follows:

$$C_{DO} = C_{DO}^{in} - \frac{SOD}{h}t \qquad [7.21]$$

The time (t) in Equation 7.21 was set to be the theoretical hydraulic retention time (HRT) of the RCW pond. Since the HRT for a pond with an average depth of 2.3 m is 18 h, the value calculated for the term "$\frac{SOD}{h}t$" was found to range from 0.04 to 0.08 mg/L when ranging the temperature from 5 to 20 °C. This value is less than 1% of the measured DO concentrations at the current inlets outflow (see Table 7.1). Therefore, the DO deficiency in the pond due to SOD can be ignored when modelling the current DO levels. However, the SOD effect might be significant if the DO levels are reduced under different inlet designs and/or configurations.

7.3 CFD MODEL

In order to model the DO concentration in the RCW pond, CFX-Pre™ 10.0 was used to introduce the DO concentration in the entering fluid (water) as a specific concentration with units of kg/m^3 (1 kg/m^3 is equivalent to 1000 mg/L). Then a fluid domain (water) was created for the 3D region with the reference pressure obtained from Environment Canada (2006) for each specific case. No buoyancy effect was considered as the lake is relatively shallow with a short HRT (Fischer et al., 1979). Since the water enters into the pond from two different lakes (i.e., the water temperature is variable) and the RCW pond is relatively large (i.e., the water velocity is small in the pond, away from the inlets), the thermal energy model (which considers internal energy only, i.e., assumes the flow energy is small) was used to simulate the heat transfer in the pond. The well-known k-ε turbulence model was used in this model along with the transport equation with a DO kinematic diffusivity (molecular diffusion coefficient) value of 2.09×10^{-9} m^2/s (Sherwood et al., 1975).

The CFD model was initialized before introducing the inlet, outlet and boundary conditions by setting the water velocity inside the pond at an initial value of zero, to be automatically updated as the numerical simulations proceeded (the model was later run under steady state conditions to provide an initial guess for the transient mode used in this model). The static pressure, temperature, and DO concentration were set at initial values of 97 kPa (Environment Canada, 2006), 274 K and 1.0 mg/L, respectively, and then updated automatically as the numerical simulations proceeded.

Average mass flow rates of 3300 kg/s for inlet 1, 3200 kg/s for inlet 2, 3250 kg/s for outlet 1, and 3250 kg/s for outlet 2 were used. For the inlets, the flow direction was set to be normal to boundary, and the turbulence intensity was set to be 5% (medium intensity). Appropriate temperature values were used according to the field measurements. The 2D surfaces for inlets 1 and 2 were treated as walls with a free slip and a DO flux value that was represented by Equation 7.12. The top surface was also treated as a wall with a free slip and an expression for the DO flux value equivalent to Equation 7.17. The bottom surface was used to represent the SOD by treating it as a wall with no slip and a DO flux value by using Equation 7.21 (not activated for current conditions). All other 2D regions (default) were treated as walls with no slip and zero DO flux.

A transient simulation type was chosen to model the RCW pond under current inlet conditions. A total time equivalent to the HRT was used for the time duration option with a time step of 1000 s starting at time equal to zero. The simulations were carried out by using a high-resolution advection scheme with a 2nd-order backward Euler transient scheme. The convergence process was controlled by using a maximum value of three timescale coefficient loops. The convergence criterion was the root mean square (RMS) residual with a value of 1.0×10^{-7}. After all conditions had been successfully introduced into the system, the solving procedure was started by utilizing CFX-Solver™ 10.0.

Different ranges and combinations of mass flow rates, water depths, water temperatures and DO levels were then used to cover possible inlet conditions. The results were then obtained and analyzed by using CFX-Post™ 10.0. These results were compared with some field DO data to validate the developed CFD model.

7.4 RESULTS AND DISCUSSION

7.4.1 Current Inlet Conditions

The developed CFD model for the current inlet conditions was run for all data shown in Table 7.2. A sample of the results, shown in Figure 7.5, was obtained for the measurements conducted on December 21, 2005 (see Table 7.2) with zero DO concentrations at inlet 1 and 1.1 mg/L at inlet 2. The DO concentration is shown for an XY plane at a water depth of 1.3 m from the water surface (at the level of the outlets). The simulation results showed that the DO concentration at the outlets is about 8.9 mg/L, which is very close to the measured value of 8.6 mg/L obtained for the same region (Table 7.2). The difference between the modelled and the measured DO values might be attributed to neglecting inlet 4 from the CFD model. Because the water is discharged (about 1.0 m^3/s) from inlet 4 at a temperature of around 30 ^oC, the maximum concentration of such water entering the pond cannot exceed 7.60 mg/L, which is the saturation concentration according to Equation 7.8. Therefore, the CFD model can be expected to slightly overestimate the measured outlet DO value due to possible short-circuiting from inlet 4 under such conditions.

All CFD simulation results obtained for the data summarized in Table 7.2, by using an average flow rate of 6.5 m^3/s and an average pond depth of 2.3 m, were plotted against the measured ones as shown in Figure 7.6. A very good agreement between the simulated and the relevant field data can be observed. The error involved in the prediction is within ± 20% (similar to the error associated with estimating the k_La values; Equation 7.7). Higher deviations between the simulated and measured data can be observed for DO values less than 5 mg/L and greater than 10 mg/L. These deviations can be related to the exclusion of inlet 4 from this model due to lack of information. The water entering from inlet 4 can result in lower DO measurements at the outlet for cold water conditions (e.g. in the wintertime) as discussed above. On the other hand, the short circuiting of the water discharged from inlet 4 can increase the outlet DO measurements for warm water conditions, in which the consumption of DO is higher due to the increased rate of biodegradation activities.

Different ranges of mass flow rates and water depths were tested for the data shown in Table 7.2 to cover possible scenarios. Figure 7.7 shows the CFD prediction of the outlet DO concentration for flow rates ranging from 5.0 to 7.0 m^3/s and two water depths (the average and the maximum water depths, 2.3 and 4.8 m, respectively, according to the field survey). For a water depth of 2.3 m, the results showed that the outlet's predicted DO level increased as the flow rate increased. This finding can be explained by the decrease in the HRT as the flow rate increased; therefore, less time for the biodegradation activities (i.e., less DO consumptions) was provided. On the other hand, the HRT increased as the water depth increased, and hence, allowed for more time for higher DO consumption due to the biodegradation activities. Consequently, the predicted DO concentration for the deeper pond is lower than the shallow one for the same flow rate.

7.4.2 Submerged Inlet Condition

After the developed CFD model had simulated current conditions successfully, it was possible to evaluate the DO concentration inside the RCW pond under different conditions without the need for extensive field and/or laboratory work. A reduction in the DO level inside the pond could be obtained by utilizing an existing, but not in use, submerged inlet designed for a hydroturbine system that was not in service. The inlet area is made of concrete to prevent scouring. Therefore, this inlet appeared to be an ideal solution as it would reduce (1) the extensive aeration problem (caused by the current inlets), (2) the scouring problem, and (3) the cost of designing and constructing a new inlet.

The developed CFD model was run for all data shown in Table 7.2 by keeping the pond surface activated (for atmospheric reaeration), activating the submerged inlet and the bottom of the pond (for SOD), and deactivating inlet 1, inlet 1 surface, inlet 2 and inlet 2 surface. To compare the results of this case with the previous results, a sample of the CFD simulations obtained for the new submerged inlet condition, for December 21, 2005, is illustrated in Figure 7.8. The flow rate was set to be 6.5 m^3/s while the inlet DO concentration and temperature were calculated by using a mass balance approach to be 0.55 mg/L and 2.5 °C, respectively. The simulation results showed that the outlet's DO concentration was about 0.25 mg/L compared to the measured value of 8.6 mg/L obtained for the same region under the current inlet's condition (97% reduction).

A further comparison between the CFD results obtained for the submerged inlet and the current inlet conditions is shown in Figure 7.9 for three different dates: 31 October 2005, 19 January 2006, and 17 April 2006. The results showed that the expected outlet DO concentration for the new submerged inlet condition was less than 2.0 mg/L for the three dates. The results from the current inlet conditions yielded outlet DO concentrations of 8.8 mg/L, 8.2 mg/L, and 5.0 mg/L for the three dates, respectively. Therefore, the use of a submerged inlet will significantly reduce the DO level inside the RCW pond.

The outlet DO concentrations resulting from the CFD model simulations for all data shown in Table 7.2 are summarized in Figure 7.10 (average *Q* and *h* were used, 6.5 m^3/s and 2.3 m, respectively). Although all the predicted outlet DO levels were much lower when using the submerged inlet than the current inlets, there are some concerns about some dates (31 October 2005, 14 November 2005, and 9 February 2006) where the predicted outlet DO concentration is 2.0 mg/L or higher. Crosschecking with Table 7.2 showed that the wind velocity played an important role in elevating the DO concentration in the pond. This finding agrees with the theoretical basis (see Equation 7.14). Other observed parameters of relatively high importance are the temperature and the DO concentration of the entering water.

The effect of different ranges of the wind velocity, water temperature, and initial DO concentration was investigated by utilizing the developed CFD model. Figure 7.11

shows the results of varying the wind velocity on the outlet DO concentration for different combinations of inlet water temperatures and DO values. The water flow rate and depth were set to be 6.5 m^3/s and 2.3 m, respectively. The outlet DO concentration was found to increase as the wind velocity increased, regardless of the inlet DO and temperature values. However, for the same wind velocity, the outlet DO concentration increased as the inlet DO concentration increased, and as the temperature decreased. Under such a condition, the DO flux from the atmosphere remained constant (as it is a function of the wind velocity) and the biodegradation process decreased with a decrease in the temperature (i.e., with less oxygen consumption). The highest outlet DO range resulted when the water temperature and the inlet DO concentration were set to 5 °C and 3 mg/L, respectively. The effects of varying the flow rate and the water depth were also investigated by using the developed CFD model. For the same wind velocity and flow rate, the outlet DO concentration was found to decrease as the water depth increased. This result was likely due to the increased HRT, which allowed extra time for more oxygen consumption during the biodegradation process.

The CFD model was then utilized to predict the monthly outlet DO concentration over the year based on the monthly averaged measured temperature (temperature data was found for one full year, with an average of three measurements per month), and the monthly averaged wind velocity and pressure at the study area as obtained from Environment Canada (2006). The CFD model was run by using an average flow rate of 6.5 m^3/s and an average water depth of 2.3 m. The monthly variation of the outlet DO concentration, as predicted by the developed CFD model is shown in Figure 7.12. According to the obtained results, the outlet DO values can always be expected to be less than the entering DO values. Very low outlet DO values can be expected between May and September as the microorganims activities are quite high and thus consume most of the DO available. The consumption of the DO can be expected to decrease gradually from October to December as the water temperature cools down (i.e., the biodegradation process slows down). Then, the DO consumption starts to increase gradually from January to April as the water gets warmer. The maximum monthly averaged inlet DO concentration is 2.0 mg/L (see Table 7.2). Therefore, the maximum expected outlet DO concentration as depicted in Figure 7.12 is around 1.8 mg/L from November to January, which is less than 25% of the measured outlet DO value for the same period under the current inlet conditions (Table 7.2).

7.5 CONCLUSIONS

This study aimed at modelling the dissolved oxygen (DO) in a recycled water (RCW) pond, located at the Syncrude Oil Sands operation in northern Alberta, Canada, which has high DO levels due to an extensive aeration process resulting from its inlet configurations. The study started by developing a computational fluid dynamics (CFD) model in order to simulate the DO levels in the RCW pond under the current inlet configurations. Then, the obtained results were compared to some field data measurements to validate the developed CFD model.

It was then run for an existing, but not in use, submerged inlet with a concrete inlet region (to minimize bottom scouring). The obtained results showed a considerable reduction in the DO concentration in the RCW pond when the flow rate and the water depth were set to 6.5 m^3/s and 2.3 m, respectively. Further modelling results showed that the DO concentration in the pond increased with an increase in the wind velocity (increased surface reaeration) and inlet DO concentration, and a decrease in the water temperature (a decreased oxygen consumption due to a decreased biodegradation process). The CFD simulations showed that as the water depth increased for the same flow rate, wind velocity, water temperature, and inlet DO concentration, the outlet DO concentration decreased. This result can be related to the increase in the HRT, which provided more time for the biodegradation process and, hence, for higher oxygen consumption, and to the layer volume to be aerated.

The CFD model was then employed to predict the average monthly values of the pond's outlet DO by using the available data for the wind velocity, pressure, water temperature, averaged flow rate, and water depth. For the maximum average inlet DO concentration, the maximum averaged outlet DO concentration was found to be around 1.8 mg/L from November to January, which is less than 25% of the measured outlet DO values for the same period under the current inlet conditions. Therefore, it is recommended that all the current inlets should discharge their flows through the submerged inlet in order to minimize the outlet DO concentration of the RCW pond and to reduce the carbon steel pipeline maintenance.

Table 7.1 Measured and predicted DO levels at the outflow of the current inlets.

Date (dd/mm/yr)	P^* (kPa)	Measured				Predicted	
		Inlet 1 outflow		Inlet 2 outflow		Inlet 1 outflow	Inlet 2 outflow
		DO (mg/L)	T (°C)	DO (mg/L)	T (°C)	DO (mg/L)	DO (mg/L)
24-6-05	97	7.6	19.2	6.9	18.0	8.3	7.2
1-2-06	95	10.6	4.1	9.4	5.5	10.8	8.3

* Environment Canada (2006), Fort McMurray Station A (about 10 km from the study area). Assumption made that these values would not vary significantly at the study area.

Table 7.2 Summary of data collected for the RCW pond.

Date (dd/mm/yr)	U_{wind}^* (m/s)	P^* (kPa)	Inlet 1		Inlet 2		Outlet	
			DO (mg/L)	T (°C)	DO (mg/L)	T (°C)	DO (mg/L)	T^{**} (°C)
11-10-05	2.8	96.6	0.1	8.8	1.8	9.3	6.1	10.5
17-10-05	1.2	96.3	0.0	7.5	3.1	8.2	7.2	11.0
24-10-05	1.3	97.1	0.0	6.2	4.1	6.7	9.5	6.8
31-10-05	3.4	96.9	0.1	4.5	3.4	5.5	11.1	4.5
07-11-05	1.6	96.8	0.0	3.3	3.6	4.9	10.8	3.4
14-11-05	3.7	98.1	0.0	0.8	4.4	4.7	10.8	2.9
21-12-05	2.0	95.8	0.0	1.9	1.1	3.1	8.6	3.3
28-12-05	1.2	96.0	0.0	2.3	0.8	3.4	9.0	3.4
06-1-06	2.5	96.3	0.0	2.0	0.4	3.8	8.3	4.0
12-1-06	1.9	96.4	0.1	1.4	0.4	3.9	8.0	4.8
19-1-06	0.9	97.0	0.0	2.1	0.7	3.9	7.6	3.5
9-2-06	7.9	98.1	0.0	5.0	5.0	0.1	10.4	5.8
21-2-06	1.8	96.5	0.0	5.0	0.1	5.3	7.8	6.6
06-3-06	2.3	96.8	0.0	7.5	0.7	4.4	8.5	6.3
22-3-06	4.1	98.4	0.0	5.0	0.1	4.2	8.9	5.6
03-4-06	3.3	96.9	0.0	7.1	0.1	6.3	6.6	8.6
17-4-06	2.3	96.5	0.0	13.4	0.4	8.4	5.6	11.8
01-5-06	3.4	97.0	0.0	19.1	1.5	11.6	4.2	17.4
15-5-06	2.9	97.7	0.0	18.9	1.9	15.2	3.2	21.7

* Environment Canada (2006), Fort McMurray Station A (about 10 km from the study area). Assumption made that these values would not vary significantly at the study area.

** The increase in the outlet temperature over the inlet temperatures might be due a possible short-circuiting of relatively hot water entering from inlet 4.

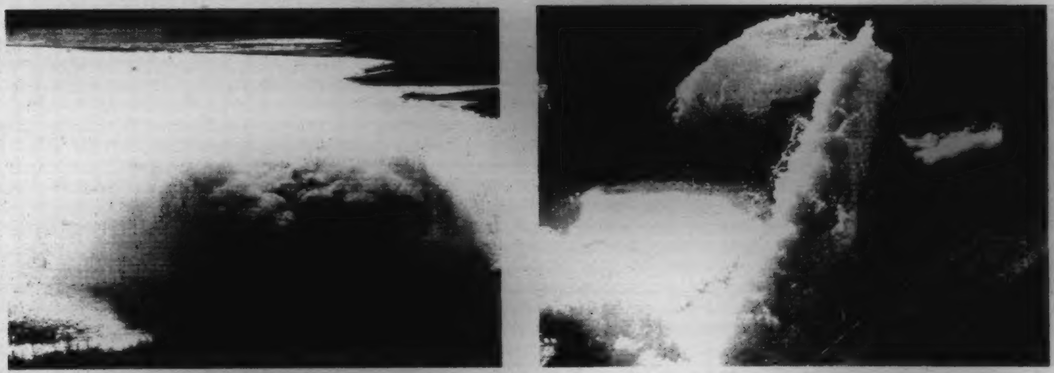

Figure 7.1 Current inlet configurations of the RCW pond.

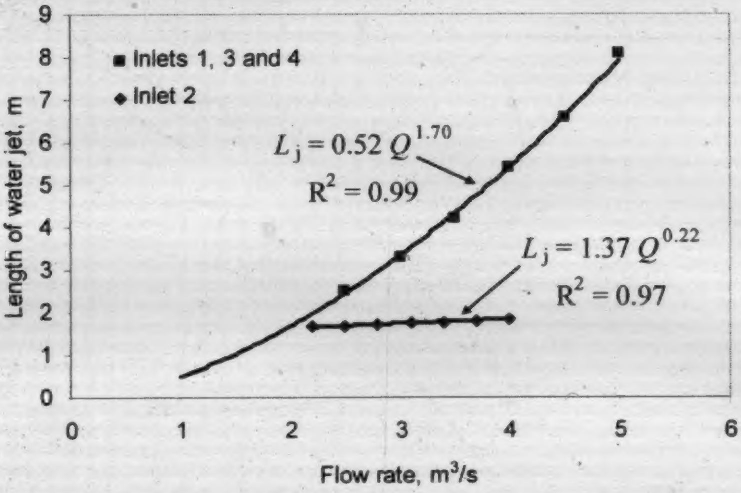

Figure 7.2 Variation of free water jets at the inlets of the RCW pond.

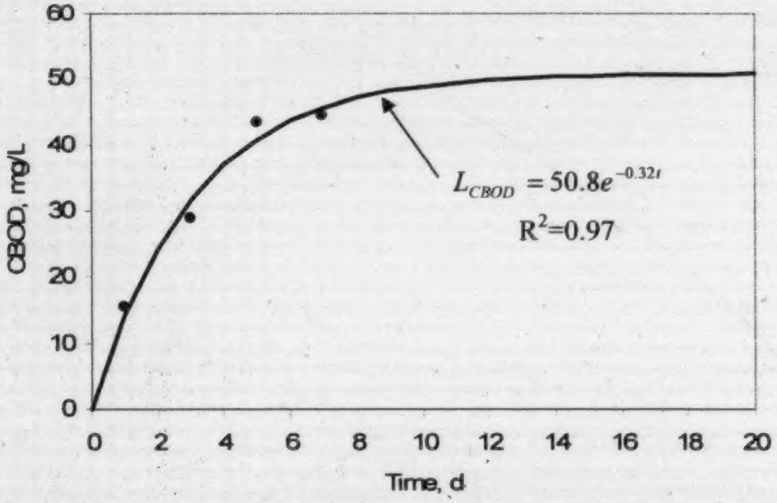

Figure 7.3 Carbonaceous biochemical oxygen demand test results.

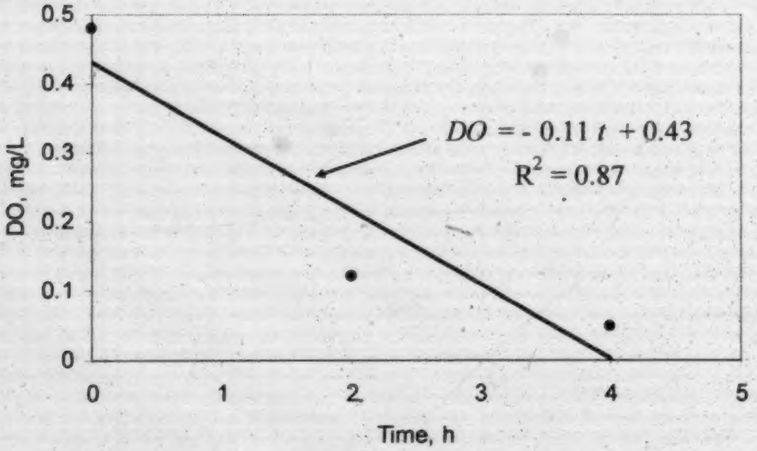

Figure 7.4 Sediment oxygen demand test results.

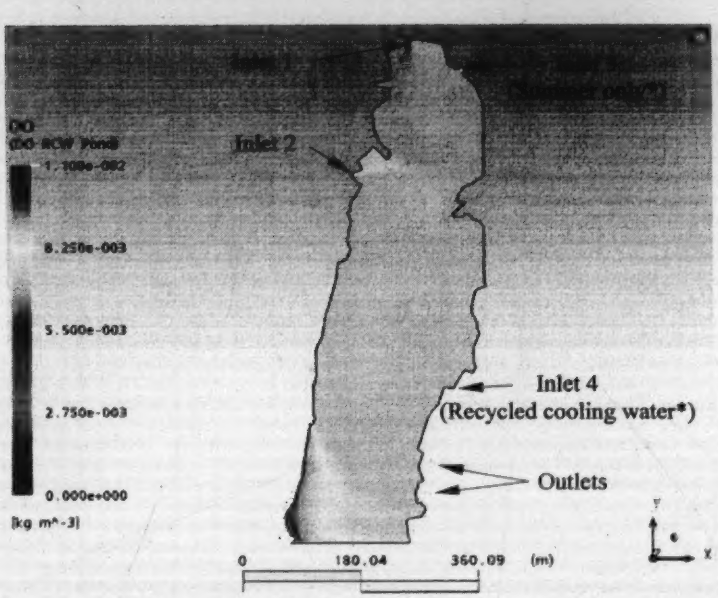

* Inlets 3 and 4 were not included in the CFD model due to lack of data and their low flow rates

Figure 7.5 CFD simulation of DO for current inlet conditions (21-12-05).

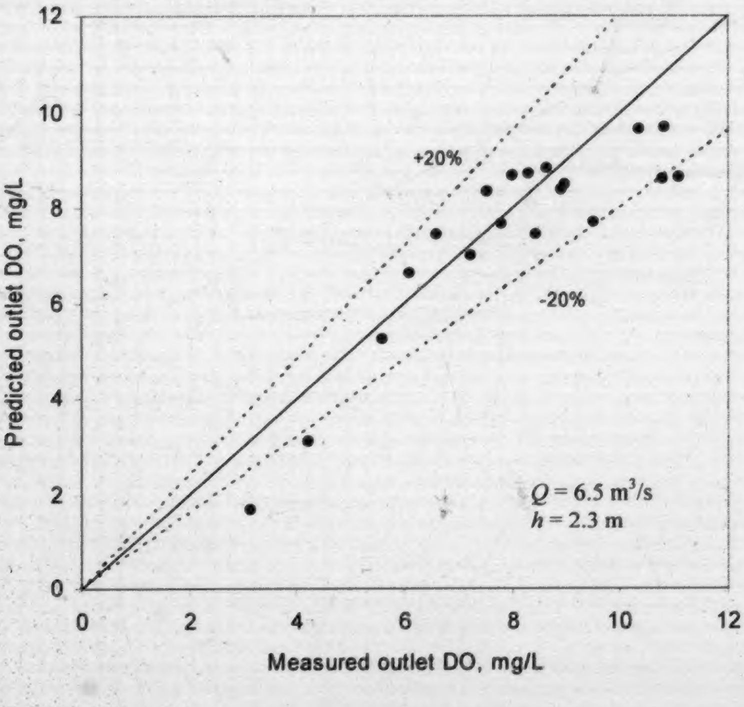

Figure 7.6 CFD simulations versus measured outlet DO for current inlet conditions.

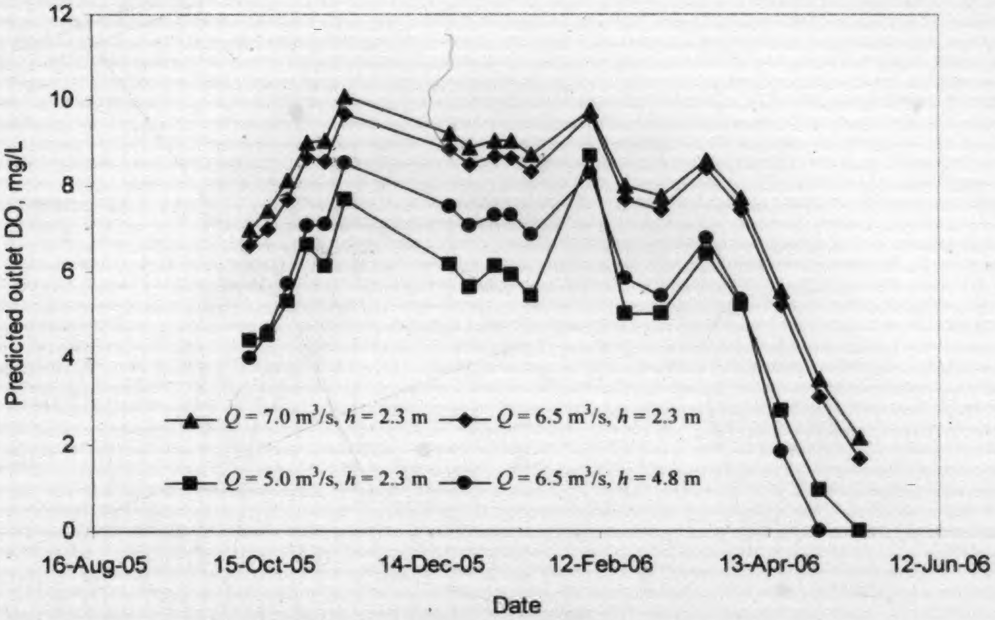

Figure 7.7 Predicted outlet DO concentrations with time under current inlet conditions for different flow rates and water depths.

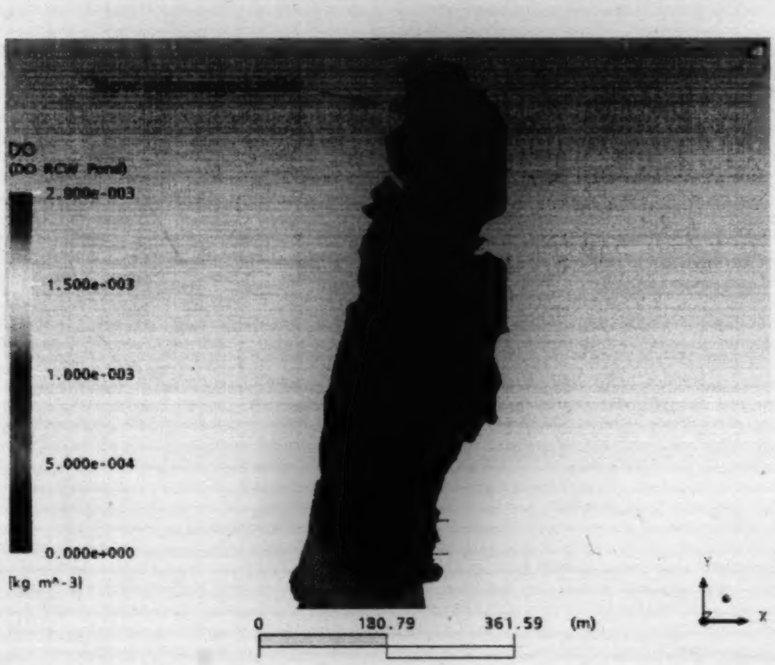

Figure 7.8 CFD model results of DO for the submerged inlet (21-12-05).

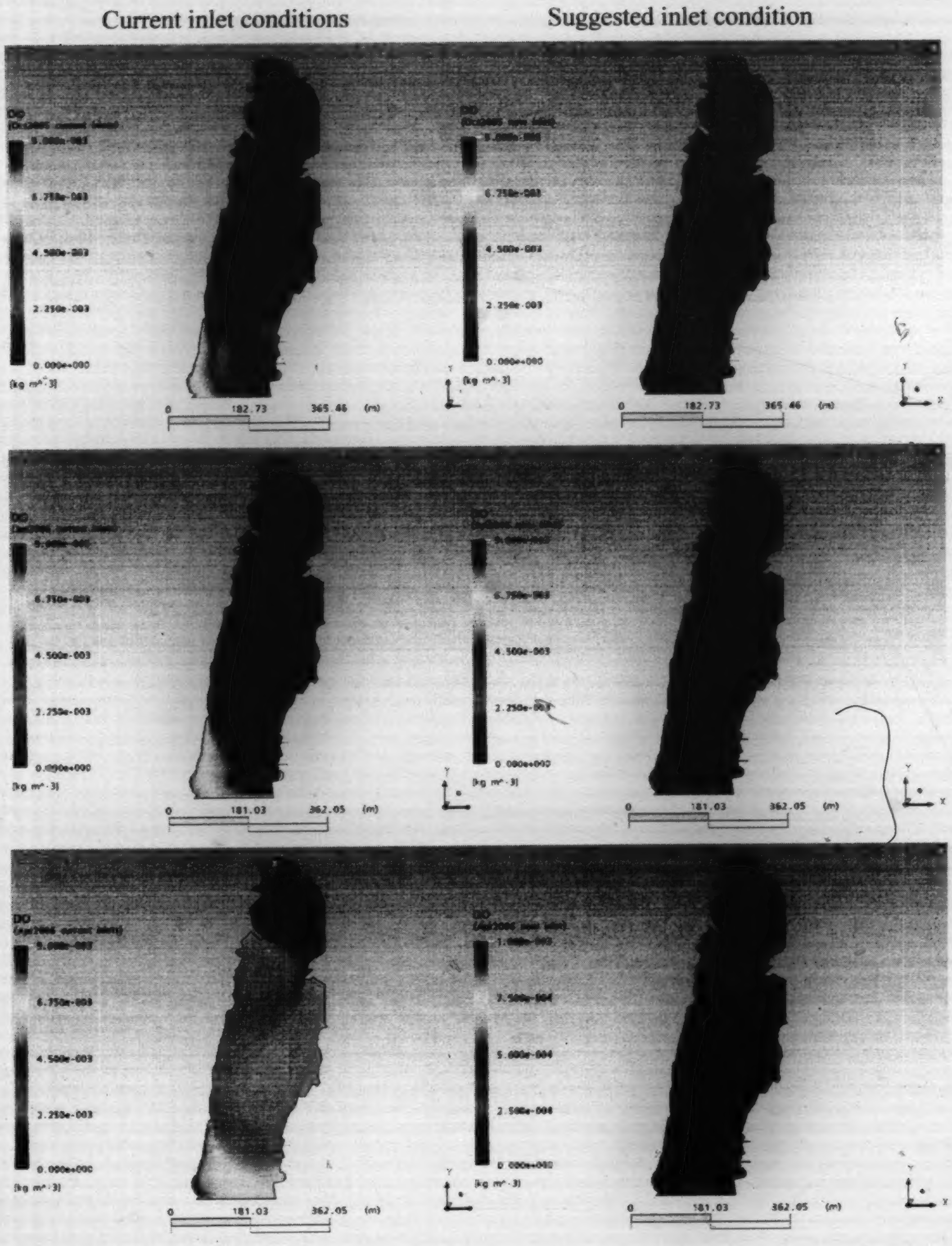

Current inlet conditions

Suggested inlet condition

Figure 7.9 Comparison between CFD model of DO under current and submerged inlet conditions.

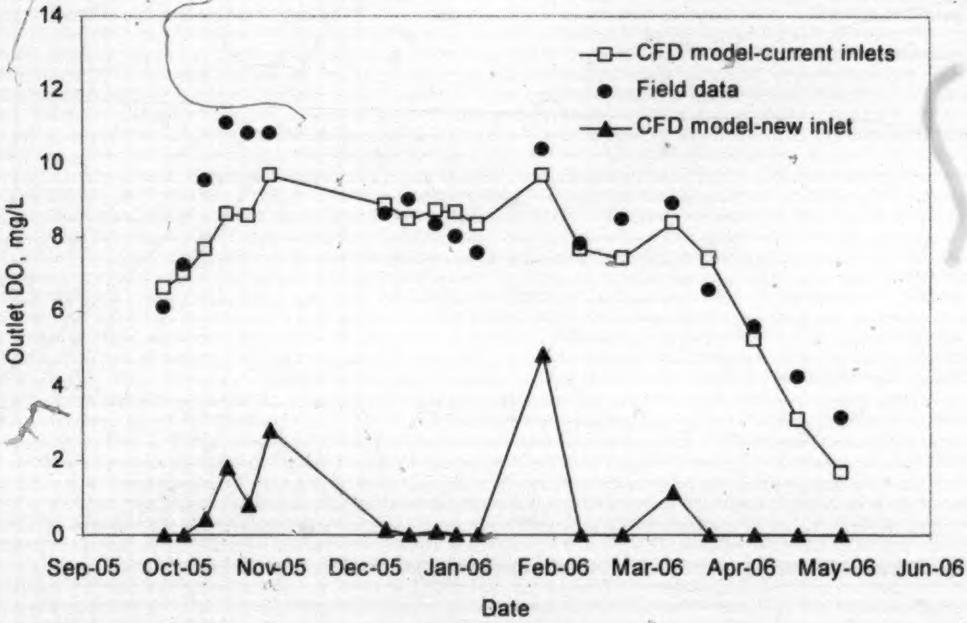

Figure 7.10 Outlet DO concentration versus time under different inlet conditions for average Q of 6.5 m^3/s and h of 2.3 m.

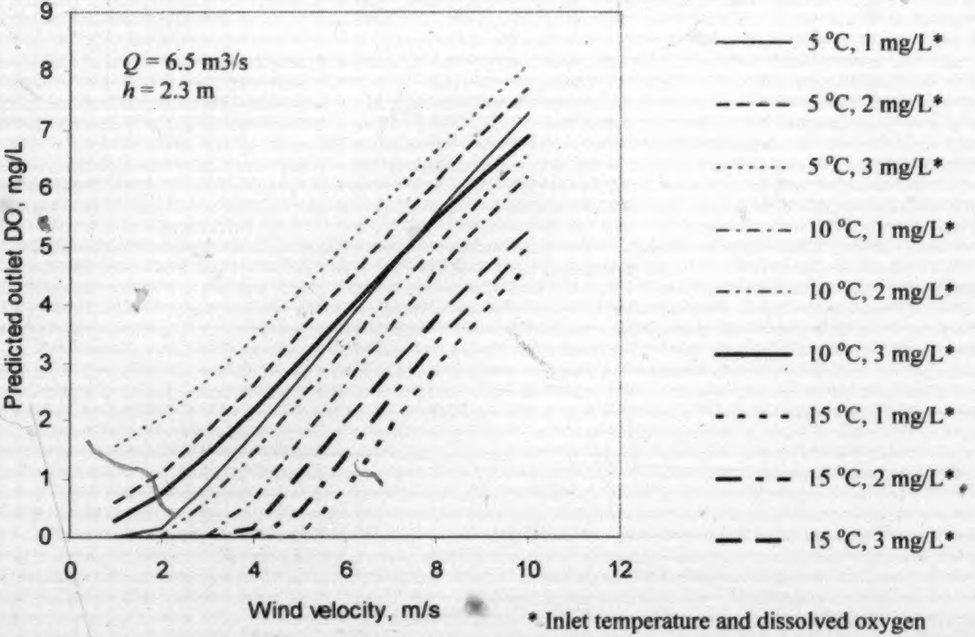

Figure 7.11 Predicted outlet DO concentrations versus wind velocity at different inlet temperatures and DO levels for submerged inlet condition.

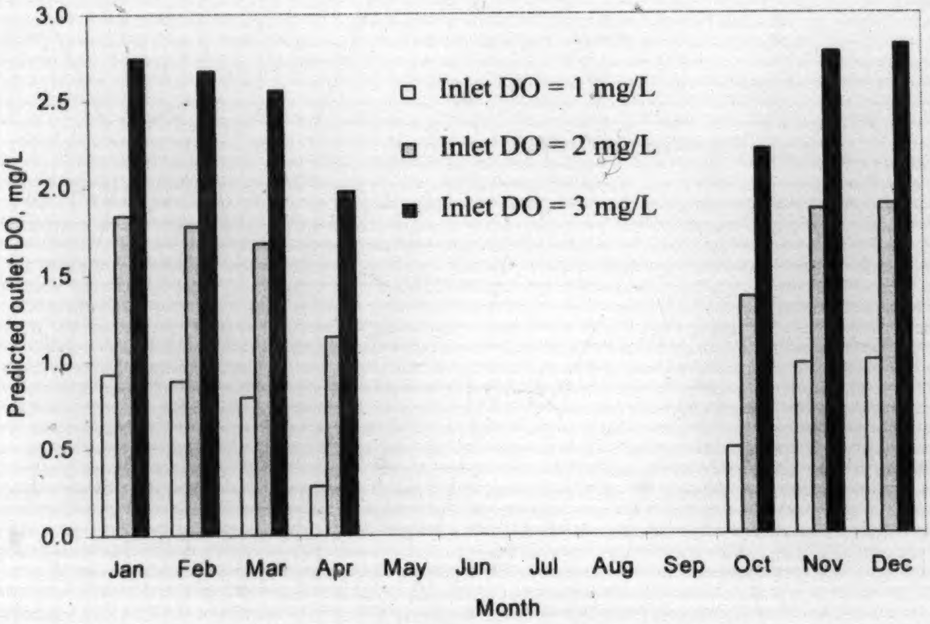

Figure 7.12 Monthly outlet DO prediction for submerged inlet condition using *Q* of 6.5 m^3/s and *h* of 2.3 m.

7.6 REFERENCES

1. Antonopouls, V.Z., and S.K. Gianniou, "Simulation of Water Temperature and Dissolved Oxygen Distribution in Lake Vegoritis, Greece", *Ecological Modelling*, 160: 39-53 (2003).
2. Banks, R.B., "Some Features of Wind Action on Shallow Lakes", *Journal of the Environmental Engineering Division*, 101(5): 813-827 (1975).
3. Bell, V.A., D.G. George, R.J. Moore, and J. Parker, "Using a 1-D Mixing Model to Simulate the Vertical Flux of Heat and Oxygen in a Lake Subject to Episodic Mixing", *Ecological Modelling*, 190: 41-54 (2006).
4. Bernard, P.S., and J.M. Wallace, *Turbulent Flow: Analysis, Measurement, and Prediction*. (New Jersey: John Wiley & Sons, Inc, 2002).
5. Bin, A.K., "Gas Entrainment by Plunging Liquid Jets", *Chemical Engineering Science*, 48(21): 3585-3630 (1993).
6. Boegman, L., M.R. Loewen, P.F. Hamblin, and D.A. Culver, "Application of a Two-Dimensional Hydrodynamic Reservoir Model to Lake Erie ", *Canadian Journal of Fisheries and Aquatic Science*, 58: 858-869 (2001).
7. Choa, X., Y. Jia, F.D.J. Shields, and S.S.Y. Wang, "Development and Application of a Three Dimensional Water Quality Model for a Shallow Oxbow Lake", *US-China Workshop on Advanced Computational Modelling in Hydroscience and Engineering*, Oxford, Mississippi, U.S.A. (2005).
8. Czarnecki, J., B. Radoev, L.L. Schramm, and R. Slavchev, "On the Nature of Athabasca Oil Sands", *Advances in Colloid and Interface Science*, 114: 53-60 (2005).

9. Davidson, P.A., *Turbulence: An Introduction for Scientists and Engineers*. (New York, U.S.A.: Oxford University Press Inc., 2004).

10. Doyle, M.C., and D.D. Lynch, "Sediment Oxygen Demand in Lake Ewauna and the Klamath River, Oregon, 2003", U.S. Geological Survey Scientific Investigations, ed., 14p, 2005).

11. Environment Canada, "Climate Data Online", 2006).

12. Fang, X., and H.G. Stefan, "Interaction between Oxygen-Transfer Mechanisms in Lake Models", *Journal of Environmental Engineering-Asce*, 121(6): 447-454 (1995).

13. Fischer, H.B., E.J. List, R.C.Y. Koh, J. Imberger, and N.H. Brooks, *Mixing in Inland and Coastal Waters*. (USA: Academic Press, 1979).

14. Gelda, R.K., M.T. Auer, and S.W. Effler, "Determination of Sediment Oxygen-Demand by Direct Measurement and by Inference from Reduced Species Accumulation", *Marine and Freshwater Research*, 46(1): 81-88 (1995).

15. Gelda, R.K., M.T. Auer, S.W. Effler, S.C. Chapra, and M.L. Storey, "Determination of Reaeration Coefficients: Whole-Lake Approach", *Journal of Environmental Engineering-Asce*, 122(4): 269-275 (1996).

16. Ginot, V., and J.C. Herve, "Estimating the Parameters of Dissolved-Oxygen Dynamics in Shallow Ponds", *Ecological Modelling*, 73(3-4): 169-187 (1994).

17. Gualtieri, C., "Verification of Wind-Driven Volatilization Models", *Environmental Fluid Mechanics*, 6(1): 1-24 (2006).

18. Harza, M.W., "Panama Lakes Water Quality Modeling Study": ACP Report 50050, 181p, 2003).

19. Imteaz, M.A., T. Asaeda, and D.A. Lockington, "Modelling the Effects of Inflow Parameters on Lake Water Quality", *Environmental Modeling & Assessment*, 8(2): 63-70 (2003).

20. Kawai, N., K. Wada, H. Hirano, T. Naganuma, M. Sueyoshi, H. Nakui, I. Saito, and S. Asakura, "Critical Concentration of Dissolved Oxygen to Form Protective Iron Oxides under Combined Water Treatment Conditions", *Corrosion Engineering Science and Technology*, 38(4): 286-290 (2003).

21. Kuch, A., "Investigations of the Reduction and Reoxidation Kinetics of Iron(Iii) Oxide Scales Formed in Waters", *Corrosion Science*, 28(3): 221-231 (1988).

22. Padma, S., S.N. Veena, A.L. Rufus, V.S. Sathyaseelan, S. Velmurugan, and S.V. Narasimhan, "Corrosion of Carbon Steel and Monel-400 in Edta Based Steam Generator Cleaning Formulations", *Materials and Corrosion-Werkstoffe Und Korrosion*, 52(10): 771-780 (2001).

23. Sherwood, T.K., L.T. Robert, and R.W. Charles, *Mass Transfer*. (New York, U.S.A.: McGraw-Hill, Inc., 1975).

24. Snodgrass, W.J., "Reaeration and Vertical Diffusion of Lake Oxygen", *Journal of Environmental Engineering-Asce*, 109(6): 1419-1423 (1983).

25. Snodgrass, W.J., and R.J. Dalrymple, "Lake-Ontario Oxygen Model .1. Model Development and Application", *Environmental Science & Technology*, 19(2): 173-179 (1985).

26. Stefan, H.G., and X. Fang, "Dissolved-Oxygen Model for Regional Lake Analysis", *Ecological Modelling*, 71(1-3): 37-68 (1994).

27. Stefan, H.G., X. Fang, D. Wright, J.G. Eaton, and J.H. McCormick, "Simulation of Dissolved-Oxygen Profiles in a Transparent, Dimictic Lake", *Limnology and Oceanography*, 40(1): 105-118 (1995).

28. Stratmann, M., and J. Muller, "The Mechanism of the Oxygen Reduction on Rust-Covered Metal Substrates", *Corrosion Science*, 36(2): 327-359 (1994).

29. Sullivan, A.B., and S.A. Rounds, "Modeling Hydrodynamics, Temperature, and Water Quality in Henry Hagg Lake, Oregon, 2000-03", Investigations, U.S.G.S.S., ed., 38p, 2005).

30. Thomann, R.V., and J.A. Mueller, *Principles of Surface Water Quality Modeling and Control*. (New York, U.S.A.: Harper Collins Publishers Inc, 1987).

31. Tomoe, Y., M. Shimizu, and Y. Nagae, "Unusual Corrosion of a Drill Pipe in Newly Developed Drilling Mud During Deep Drilling", *Corrosion*, 55(7): 706-713 (1999).

32. Truax, D.D., A. Shindala, and H. Sartain, "Comparison of 2 Sediment Oxygen-Demand Measurement Techniques", *Journal of Environmental Engineering-Asce*, 121(9): 619-624 (1995).

33. Wood, T.M., "Sediment Oxygen Demand in Upper Klamath and Agency Lakes, Oregon, 1999", Investigations, U.S.G.S.W.-R., ed., 13p, 2001).

CHAPTER 8

CFD APPLICATION IN MODELING AND IMPROVING THE PERFORMANCE OF A STORAGE RESERVOIR USED AS A CONTACT CHAMBER FOR MICROORGANISM INACTIVATION*

8.1 INTRODUCTION

The most important requirement for water treatment plant performance is the production of pathogen free water as the microbiological safety of drinking water is of paramount importance to public health. The most effective way of removing the pathogenic microorganisms is by using microorganism inactivation processes (traditionally referred to as disinfection) such as chlorination (for viruses, bacteria, and some protozoans) or ozonation (for all microorganisms).

A microorganism inactivation regime using chemical methods can be characterized by its CT or Ct_{10} which is a product of the chemical concentration (C) multiplied by the amount of effective contact time (t_{10}) the water is in contact with the chemical (Hart and Vogiatzis, 1982). This concept was promulgated under the U.S. Surface Water Treatment Rule (SWTR) (USEPA, 1989). The logarithmic inactivation has been shown to be proportional to the value of Ct_{10} and the rate constant for the inactivation of a particular microorganism (k') according to the first-order Chick-Watson law (AWWA, 1999; Gyurek and Finch, 1998; Li et al., 2001; von Gunten et al., 2001):

---

* A version of this chapter has been published. Baawain M.S., M. Gamal El-Din, and D.W. Smith, *J. Env. Eng. Sci.* 5(2): 151-162 (2006).

$$\log\left(N/N_0\right) = k'Ct \qquad [8.1]$$

where N and N_0 are the number of microorganisms at time t and $t = 0$, respectively. As the integral Ct_{10} value is not easily determined in non-ideally behaving reactors during water treatment, Ct_{10} determination is performed with a conservative approach. The chemical concentration (C) from a step or a slug concentration change is measured at the outlet of the reactor and then multiplied by the contact time (t_{10}) that is determined from the residence time distribution obtained through tracer or mixing studies and defined as the amount of time at which 10% of the tracer has to be passed through the reactor or the contact chamber (Johnson et al., 1998).

Microorganism inactivation chemical dosage generally depends on water quality parameters that exert a chemical demand. For example, the chemical demand of chlorine, which is the difference between the amount of the chlorine injected into the water and the amount of chlorine remaining at the end of a specified contact period, is affected by the presence of organic matter and other oxidizable contaminants in the treated water as they use up chlorine (AWWA, 1999; Kiely, 1998). Therefore, chlorine demand can be very low for finished water and is at its highest level for raw water. Chlorine consumption or decay is generally characterized by first-order decay kinetics (Chambers et al., 1995; Powell et al., 2000).

Microorganism inactivation efficiency is also a function of the hydraulic efficiency of contact chambers. This efficiency depends on flow characteristics within the contact chamber such as flow backmixing, bypassing, and short-circuiting (AWWA, 1999). Thus, some portions of the treated water (i.e., water parcels) will remain in the chamber for a longer time than others, and the contact time with the microorganism inactivation chemical will vary between different regions within the chamber. In the Ct_{10} concept, the time component is used to account for the hydraulics of the contact chamber. A plug-flow regime is considered to be the ideal flow regime through a contact chamber (AWWA, 1999). Therefore, from the inlet to the outlet, fluid in a plug flow reactor will travel as if through a frictionless pipe, mixing completely in the transversal and vertical directions without any longitudinal dispersion or mixing. Consequently, all the contents of the reactor are exposed to the chemical for the maximum amount of time. At the other end of the spectrum, the completely-mixed flow regime (the liquid that enters a reactor is perfectly and instantaneously mixed with all the fluid in the system) is considered the worst condition for microorganism inactivation contact time but ideal for chemical mixing when first injected to the water. However, if several completely mixed reactors (10 or more) are put in series, they can simulate a plug-flow system since in each reactor all fluid parcels are having the same contact time (Chapra, 1997).

Microorganism inactivation can also be limited by the mass transfer efficiency which is considered the controlling factor that dictates the overall performance of gaseous disinfectant, such as ozone, contact chambers (Gamal El-Din and Smith, 2002; Zhou et al., 1994). A proper design of the gas sparging device for introducing the gaseous chemical into the liquid in the contactors is needed to ensure enough turbulence and mixing in the liquid phase and hence achieve high mass transfer rates (Gamal El-Din and Smith, 2003). Several mathematical and stochastic models have been developed to simulate the performance of microorganism inactivation processes that apply gaseous disinfectant such as ozone (Do-Quang et al., 2001; Do-Quang et al., 2000; Gujer and von Gunten, 2003; Zhou and Smith, 1995).

Several numerical models have been developed to simulate the flow conditions and microorganism inactivation process in contact chambers. Falconer and Ismail (1997) used a two-dimensional semi-time-centered implicit the Quadratic Upstream Interpolation for Conservative Kinematics (QUICK) scheme to model the transport of a tracer in a scaled physical model of a chorine contact tank. They observed good agreement of their model with laboratory measurements in the compartments of the tank where the flow was relatively uniform over the depth. Wang and Falconer (1998) tried to simulate the flow conditions in chlorine treatment tanks using different numerical models but did not model chlorine concentrations in these tanks. They found that *k-ε* model is more appropriate model to describe flow regimes when compared to other numerical methods such as 3rd order upwind scheme and Smagorinsky model. Peplinski and Ducoste (2002) developed a computational fluid dynamics (CFD) model to evaluate contactor hydraulics under model input uncertainty. They predicted the effluent residence time distribution (RTD) curve and analyzed the sensitivity of the effluent RTD using Monte Carlo probabilistic techniques. They found that the effluent RTD was most sensitive to uncertainty in turbulence Schmidt number and the selected turbulence model.

8.1.1 Storage Tanks as Contact Chambers

Storage tanks in water distribution systems are integral parts of these systems, providing storage for drinking water, fire-fighting needs, and industry requirements

(AWWA, 1999). When they are located on-site at the end of a water treatment plant, they can be used as microorganism inactivation contact chambers. When they are properly configured, they can provide extended contact time between water and the microorganism inactivation chemical(s) added. Thus, storage reservoirs are a potential venue for additional microorganism inactivation at the end of the water treatment train.

Some experimental studies have examined the use of physical models as an effective means of studying the hydraulics within full-scale rectangular storage basins (Hoff, 1986; Liem, 1994). These physical models have been used to observe the influence of internal basin geometry on microorganism inactivation efficiency in terms of mixing and contact time. The first objective of these experiments was to simulate effectively the hydraulics of the studied storage basins. Then, these models were used to study the effects of different configurations, in terms of internal basin geometry, and to assess the dependence of hydraulic performance on various design parameters such as the use and the arrangement of baffle walls in the storage basins, and operational parameters such as water depth and discharge. The hydraulic efficiency of each tank configuration could be determined effectively using tracer studies (Bishop et al., 1993). From these studies, the effective contact time (t_{10}) could be obtained and used to determine Ct_{10} and the corresponding microorganism inactivation credit. This approach is considered to be a relatively accurate method of evaluation for microorganism inactivation efficiency (Regli, 1989; Teefy and Singer, 1990).

Modeling the hydraulics of storage reservoirs has gained considerable attention during the past decade. Boulos et al. (1996) evaluated the hydraulic mixing and chlorine residual in two water treatment reservoirs. They used a continuously flow stirred tank reactor (CFSTR) approach to predict the t_{10} of the reservoirs. They found that the actual t_{10} was less than 50% of the predicted one. They related this difference to the occurrence of short-circuiting between the inlets and the outlets of the reservoirs. Grayman et al. (1996) developed system models, such as a simple CFSTR and a four-compartment model, and a basic CFD model to describe water quality and mixing in water treatment reservoirs. They found that their models have shown good agreement at some portions of the reservoirs but there were some deviations at other portions especially toward the top centre of the reservoirs. Hannoun et al. (1998) used hydraulic modeling based on a CFD approach to optimize contact time in reservoirs. They managed with the use of CFD and by changing the configurations of baffles in the reservoirs to increase the t_{10} to the theoretical detention time (τ) ratio (t_{10}/τ) from less than 0.15 to about 0.66. Ta and Brignal (1998) used the CFD technique to evaluate the effect of changing the inlet and the outlet configurations to maximize the residence time. They used a manifold inlet arrangement, a submerged baffle inlet, and a central outlet arrangement. They concluded that the manifold inlet gave better residence time compared to the other two arrangements. Crozes et al. (1999) conducted extensive research to improve the Ct_{10} for storage reservoirs and used a CFD approach to model their results. They observed that the t_{10}/τ ratio could be improved from 0.2 for poor baffled reservoirs to 0.8 for proper baffled reservoirs. Their CFD predictions were within 13% (on average) of the measured values for t_{10}/τ.

8.1.2 Study Objectives

This study was conducted to simulate the performance of an existing storage tank when used as a chlorine contact basin for additional microorganism inactivation credit. Computational fluid dynamics (CFD) modeling approach was utilized to simulate the performance of two scaled-down physical models of the existing storage tank. Hurtig (2003) conducted two tracer (i.e., mixing) studies in these two physical models to explore the storage reservoir hydraulics using a step input of Rhodamine WT as a conservative tracer. To investigate the effects of the internal geometry of the tanks (in terms of the baffle configuration) on the tank hydraulics, the storage tank models were equipped with a number of baffles, ranging from one to nine. The aim of these mixing studies was to improve the contact time in the storage tank in order to achieve an efficient microorganism inactivation process. The physical models were scaled-down models of an existing storage tank located on-site at E. L. Smith Water Treatment Plant, Edmonton, Alberta, Canada. The CFD models were developed using the CFX® 5.6 software from ANSYS, Inc. This study also aimed at developing a number of CFD models for other reservoir configurations for further investigations of t_{10} improvement.

8.2 CFD MODEL

The experimental results used in this study were obtained from the tracer tests conducted by Hurtig (2003). These tests were carried out in a number of scaled-down physical models of a storage tank located at E. L. Smith Water Treatment Plant. The full-scale reservoir was scaled down using Froude number and the resultant length scale, L_s

(full-scale length to pilot-scale length), was 47.46. Time, velocity and discharge scales were $L_s^{0.5}$, $L_s^{0.5}$, and $L_s^{2.5}$, respectively (Hurtig, 2003). In all experiments, the reservoir model was filled with tap water to a constant level using a constant head tank located at the outlet of the basin. The inflow and the outflow were attempted to be held at constant rates throughout each experiment. A jet tank was used to supply enough tap water to each model for the duration of the experiment. The conservative tracer dye (Rhodamine WT) was well mixed in the jet tank to ensure a uniform concentration inside the tank. Once the concentration within the jet tank was homogeneous, the tracer solution was introduced to the model (Hurtig, 2003).

Two schemes of the experimental work (a reservoir with one baffle wall and another one with nine baffle walls) conducted by Hurtig (2003) were simulated in this study. Then, different inlet configurations were used to assess their effect on the effective contact time (t_{10}). The inlet configurations used in the CFD simulations were as follows:

- Same inlet size as the experimental work (D_{in} = 32 mm),
- One larger inlet (D_{in} = 44 mm),
- One smaller inlet (D_{in} = 20 mm), and
- Seven small inlets (D_{in} = 6 mm each).

Initially, a similar geometry of the original studied reservoir was created (CFX-Build®). Figure 8.1 shows the reservoir's dimensions and the locations of its inlet and outlet. The depth of water inside the reservoir physical model was 82 mm and the height to the centers of the inlet and outlet was 50 mm from the bottom of the reservoir (Hurtig, 2003). The reservoir dimensions used in the software were in millimeters within the global model tolerance (minimum distance between two geometry entities) of 0.005 mm. After the reservoir's geometry had been well characterized, the flow region to be modeled was identified as a 3D region. Then, 2D regions of interest, where certain boundary conditions have to be defined in CFX-Pre®, including the inlet region, the outlet region, and the top surface of the reservoir (the reservoir is ventilated from above to keep atmospheric pressure on the top surface). All other 2D regions (around baffle and side walls and reservoir bottom) were considered as default walls (i.e., with no slip or velocity equals to zero at the walls). Inflated boundaries from the default regions (inflating triangular elements from the surface of the wall to generate prismatic elements into the fluid domain) with five layers, geometry expansion factor of 1.3 at a maximum thickness of 20 mm, and mesh surface with maximum edge thickness of 30 mm were used in creating a finite-volume mesh. Inflation near the wall boundaries allows for layers with flat wedge-shaped elements that provide a smaller mesh length scale in the direction perpendicular to the wall and therefore, providing better resolution of the velocity field near the wall, where it changes hastily. On the other hand, the mesh elements will be tetrahedral away from the inflated region.

After building the geometry of the reservoir, flow characteristics and conditions have to be introduced to the CFD model (CFX-Pre®) at the previously identified 2D regions. Two options were available for introducing the problem to the software. The first one was to model two fluids; water inside the tank and the fluid entering the tank (water mixed with Rhodamine WT). This method needs the volume fraction of fluids entering the tank and the volume fraction leaving the tank or the pressure at the outlet. It was known that the volume fraction, at the inlet, was equal to one for the water mixed with

Rhodamine WT and zero for the water inside the tank. Meanwhile, the initial volume fraction inside the tank was equal to zero for the water mixed with Rhodamine WT and one for water inside the tank. However, the volume fraction of the two fluids at the outlet was not known. Thus, only the static pressure could be introduced in such case at the outlet. The pressure at the outlet of the existing reservoir was not measured (the reservoir was connected to a water distribution network) but can be roughly estimated. The other option was to introduce the tracer material (Rhodamine WT) in the entering fluid (American Water Works Association (AWWA)) as a specific concentration. This method required the water mass flow rate (in kg/s) and the concentration of Rhodamine WT at the inlet and either the pressure or water mass flow rate at the outlet. The mass flow rate at the outlet was known to be equal to the entering mass flow rate which is equal to 0.18 kg/s which was equivalent to a flow rate of 10.3 L/min (1.72×10^{-4} m^3/s) used by Hurtig (2003). Thus, the second option had less uncertainty in the boundary conditions. In both options, the top surface was treated as a wall with free slip and zero flux.

The volume fraction approach could be used by creating a new material, representing Rhodamine WT, and entering it as another fluid into the CFX-Pre®. The properties of the Rhodamine WT fluid, such as density (ρ_{rw}), molecular mass (M_{rw}) and dynamic viscosity (μ_{rw}), were entered into the CFX-Pre®. These properties were obtained from the Material Safety and Data Sheet (MSDS) for Rhodamine WT or online (Risk Reactor, 2004). Rhodamine WT properties are: M_{rw} of 567 g/mole, ρ_{rw} of 1030 ± 50 kg/m^3 at 25°C and μ_{rw} of 1.8×10^{-3} kg/m.s.

The concentration approach could be used by entering Rhodamine WT as a new variable with specific value option and a unit of kg/m^3 (equivalent to mg/L or ppm). Then when creating the domain, a transport equation with a kinematic diffusivity (diffusion coefficient) of 3.6 x 10^{-10} m^2/s (Shilton, 2001) was used.

The governing equations to be solved were the Navier-Stokes (momentum and continuity), and the mass conservation equations for incompressible fluids. The following equations adopt Einstein convention that whenever the same index appears twice in any term, summation over the range of that index is implied. Accordingly, Navier-Stokes equations (in Cartesian form) for incompressible fluids reduce from the general form to:

$$\frac{\partial u_i}{\partial t} + \frac{\partial (u_i u_j)}{\partial x_i} = -\frac{1}{\rho}\frac{\partial p}{\partial x_i} + \frac{\partial \tau_{ij}}{\partial x_j} + g_i \qquad [8.2]$$

$$\frac{\partial u_i}{\partial x_i} = 0 \qquad [8.3]$$

$$\tau_{ij} = \nu\left(\frac{\partial u_i}{\partial x_j} + \frac{\partial u_j}{\partial x_i}\right) \qquad [8.4]$$

where t is the time, x_i or x_j (i and j = 1, 2, 3) are the Cartesian coordinates (x_1, x_2, x_3) or (x, y, z), u_i or u_j (u_1, u_2, u_3) or (u, v, w) are the Cartesian components of the velocity, ρ is the liquid density, p is the static pressure, τ_{ij} is the stress tensor for incompressible flows, g_i or (g_1, g_2, g_3) are the Cartesian components of the gravitational acceleration (note that both g_1 and g_3 equal zero, while g_2 equals 9.81 m/s^2), and ν is the liquid kinematic viscosity. Mass conservation equation of concentration (C) in the same fluid can be written as:

$$\frac{\partial C}{\partial t} + \frac{\partial (u_i C)}{\partial x_i} = \frac{\partial}{\partial x_i}\left(D\frac{\partial C}{\partial x_i}\right) + S \qquad [8.5]$$

where D is the diffusivity coefficient for the material of concentration C, and S is the source or sink of C. The above equations were solved numerically using the finite volume approach within the CFX solver®.

The volume fraction and concentration approaches used steady state simulations and Shear Stress Transport (SST) k-ω turbulence model, where k is the turbulence kinetic energy and ω is the specific dissipation rate. In the SST k-ω turbulence model, the dissipation rate (ε) in the well-known k-ε model was replaced by k-ω and therefore, the eddy kinematic viscosity (ν_t) becomes proportional to the ratio between k and ω (Bernard and Wallace, 2002).

A physical time scale of 30 seconds and 120 iterations, to obtain a solution after one-hour simulation (to match the one-hour time frame used for the experiment), with root mean square (RMS) error of 10^{-6} were used in the simulations. Two monitoring points were applied; one for the tracer concentration or volume fraction of Rhodamine WT at the outlet and another one for flow velocity at the outlet.

Two initial runs, one using the volume fraction approach and the other using the concentration approach, were conducted to obtain numerical solutions that were compared with the experimental results to determine which of the two approaches is more suitable for this case. The volume fraction approach did not work as CFX-Solver® was always terminating the run due to some fluid return from the outlet back to the reservoir. The concentration option did not show any problems at the solving stage, and thus was chosen to continue the research project.

The same procedure was followed for the simulation of the reservoir with nine baffle walls in terms of geometry building and flow conditions introduced as shown in Figure 8.2. In the case of one baffle wall reservoir, Rhodamine WT concentration used at the inlet was 0.238 kg/m^3 (238 ppb) compared to 0.345 kg/m^3 (345 ppb) for the case of nine baffle wall reservoir as used by Hurtig (2003) in both cases. Also, in all models, the concentration values were obtained at the reservoir's outlet to compare with the relevant experimental or modeled results. The input and the output conditions along with the assumptions used in the CFD models developed in this study are shown in Table 8.1.

8.3 RESULTS AND DISCUSSION

The following section presents and discusses some of the results obtained from the CFD models simulating the original and modified physical models conducted by Hurtig (2003). The results shown are in terms of Rhodamine WT concentrations along the reservoir over an XY plane that is 50 mm high from the reservoir's bottom, velocity vectors at the inlet region, and the variation of the Rhodamine WT concentration, with time, at the reservoir's outlet. This is followed by presenting the results obtained from the CFD models' simulations when different inlet configurations were used.

8.3.1 Results of CFD Models' Simulations

The one-baffle-wall reservoir design was quite basic and expected to exhibit short-circuiting and poor mixing of the Rhodamine WT tracer. Figure 8.3 shows the velocity vectors in the entering flow region from two different views on planes that are at the centerline of the inlet; one is an XY plane (top view) and the other one is a YZ plane (side view). The top view shows the entering jet heading forward without much lateral dispersion (i.e., mixing) as the baffle wall (not shown in this figure) was relatively far from the inlet (see Figure 8.1). The side view shows that the location of the inlet was at the upper half of the reservoir depth and therefore the jet was lacking good vertical mixing. These vectors explain the distribution of the tracer material (Rhodamine WT) in the reservoir. The jet flow was the main driving force of the fluid (i.e., the water mixed with Rhodamine WT) entering the reservoir until it hit the baffle wall where it was expected to deflect heading to the outlet and part of the flow headed back to the first compartment of the reservoir. This phenomenon is depicted in Figure 8.4 that presents the Rhodamine WT concentration on an XY plane, at the same height of the inlet and the outlet (50 mm above the bottom of the reservoir), one hour after the release of the water mixed with Rhodamine WT into the reservoir. Figure 8.4 also shows the occurrence of two dead zones in the first and second compartments.

The velocity vectors of the inflow, in the entry region of the baffled (nine baffles were used) reservoir model, are shown in Figure 8.5 (same locations of XY and YZ planes as in the previous case were used). As shown in the top view, the entering jet headed forward with more lateral dispersion than in the previous case (reservoir with one baffle) as the baffle wall (not shown in this figure) was very close to the inlet (see Figure 8.2). This increased level of lateral mixing could lead to a uniform Rhodamine WT concentration profile in the lateral direction. Also, Figure 8.5 shows that there was a better vertical mixing of the jet than that in the reservoir with one baffle wall. Again, this higher level of vertical mixing could lead to a uniform Rhodamine WT concentration profile in the vertical direction. Figure 8.6 shows Rhodamine WT concentration on an XY plane (50 mm above the bottom of the reservoir) one hour after the release of the water mixed with Rhodamine WT into the reservoir. As shown in Figure 8.6, the dye was well mixed in all regions, i.e., the flow could be assumed to follow an ideal plug flow regime. This could be attributed to the influent flow rate, the increased lateral and vertical mixing at the inlet region, and the arrangement of the baffle walls within the reservoir.

The concentration (C) of Rhodamine WT at the outlet of the two reservoir models (a reservoir with one baffle wall and a reservoir with nine baffle walls) was calculated by the CFD model one hour, with a time step of 30 seconds, after the release of the water mixed with Rhodamine WT into the reservoir. The concentration ratio (C/C_o) was then calculated, where C_o is the concentration at the inlet (initial concentration), to compare with Hurtig (2003) experimental results. The calculated C/C_o obtained from the CFD models for the two reservoirs and the experimental C/C_o measured by Hurtig (2003) are depicted in Figure 8.7. A good agreement between the experimental and simulated concentration profiles exists, thus indicating the suitability of the used CFD models. The experimental and simulated t_{10} (corresponding to $C/C_o = 0.1$) of the one-baffle-wall reservoir was less than eight minutes, i.e., lower than 25% of the theoretical detention time (τ) of the one-baffle-wall reservoir, which was about 35 minutes. This indicated the existence of regions of short-circuiting within the reservoir and is in agreement with the CFD model simulation results shown in Figure 8.4. The experimental and simulated t_{10} of the nine-baffle-wall reservoir was slightly higher than 25 minutes, which is about 80% of τ (32 minutes in this case due to the decrease in volume caused by the baffle walls). This is a great improvement in t_{10} compared to the t_{10} of the existing design (one-baffle-wall reservoir). This enhancement in t_{10}/τ ratio (~ 0.8) is in agreement with the results of Hannoun et al. (1998) and Crozes et al. (1999) who managed to achieve t_{10}/τ up to 0.66 and 0.8, respectively.

The minor differences between the CFD simulated concentration profiles and the experimental observations were expected as it was virtually impossible to obtain a perfect simulation due to many reasons such as the difficulties in maintaining exactly the same flow rate at both the inlet and outlet (during the experiment) and thus the top surface could not be kept at constant level. Also, there could have been experimental tracer concentration measurement error and any difference between the exact location at which the tracer samples were collected during the mixing study and the CFD simulation location. In addition, the software has its own approximations in terms of the governing equations and the models used to solve for turbulence effects could also contribute to some differences between both CFD modeling results and the experimental observations.

8.3.2 Effect of Different Inlet Configurations

After successfully simulating both reservoir physical models, the CFD model of the nine-baffle-wall reservoir design was chosen for further investigation for a possible performance improvement, in terms of t_{10}, by using different inlet configurations. Three models were developed for the nine-baffle-wall physical reservoir model; the first model had an inlet diameter of 44 mm instead of the 32 mm inlet diameter, the second model had an inlet diameter of 20 mm, and the third model had seven inlets each with 6 mm diameter. In the third model, the seven inlets were placed at three different depths; two inlets at depth 30 mm, three inlets at depth 40 mm, and two inlets at depth 50 mm. The same flow conditions, as for the nine-baffle-wall reservoir model with one 32 mm inlet, were used (mass flow rate of 0.18 kg/s and Rhodamine WT concentration of 0.345 kg/m^3). In the case of the seven inlets, the flow rate was equally divided between the inlets.

The flow velocity at the inlet region in the case of the large inlet (D_{in} = 44 mm) would be lower than that in the original design and hence, the kinetic energy would be less. Thus, it was expected to have less mixing with this configuration. Meanwhile, the use of a reservoir with a smaller inlet diameter (D_{in} = 20 mm) would lead to a higher velocity than both the two cases of 32 mm and 44 mm inlets. In turn, this would help in providing better mixing due to the higher kinetic energy. In the case of the reservoir with seven inlets (D_{in} = 6 mm), the inlets probably acted as multiple diffusers that provided higher initial lateral and vertical mixing in the first compartment, compared to the one-inlet reservoir models, due to the impingement of the entering jets on the first baffle wall and on each other.

The simulated C/C_o profiles of Rhodamine WT, at the outlets of the nine-baffle-wall reservoir models with different inlet configurations, are shown in Figure 8.8. As expected, the reservoir with the largest inlet diameter (D_{in} = 44 mm) exhibited the lowest t_{10} even though the inflow had a lower kinetic energy, and thus, a lower mixing level than those of the reservoir model with D_{in} = 32 mm. Although the kinetic energy and the mixing level were higher in the reservoir model with D_{in} = 22 mm, the traveling distance from the inlet to the first baffle wall might be too short for the kinetic energy to die off and thus, the flow would have a similar kinetic energy as in the original reservoir model

(D_{in} = 32 mm) after impinging on the first baffle. As a result, the two reservoir models with D_{in} = 32 and 22 mm had identical t_{10}. The reservoir model with seven small inlets exhibited a longer t_{10} compared to the reservoir models with one inlet. As C/C_o of Rhodamine WT at the outlet of the reservoirs with one inlet reached almost 100% after one hour of the release of the water mixed with Rhodamine WT into the reservoir, C/C_o reached only 75% for the reservoir with seven small inlets and t_{10} in this case was about 30 minutes which (about 94% of the theoretical detention time of 32 minutes). This could be a result of the higher initial lateral and vertical mixing in the first compartment, compared to the one-inlet reservoir models.

8.3.3 Effect of a New Arrangement of Baffle Walls

As constructing nine baffle walls in the existing reservoir might be quite costly, the use of a lower number of baffle walls arranged in a way that might enhance the effective contact time would be a good alternative. Therefore, a CFD model was developed for a reservoir with a new arrangement of five baffle walls as shown in Figure 8.9. In this case, Rhodamine WT concentration used at the inlet was 0.345 kg/m^3 similar to that used for the case of the nine-baffle-wall reservoir CFD models.

The new designed reservoir was modeled using two CFD models; the first model used one inlet with a diameter of 32 mm, and the second CFD model used seven inlets each with a diameter of 6 mm. Figure 8.10 shows Rhodamine WT concentration on an XY plane, at the same height of the inlet and the outlet (50 mm above the bottom of the reservoir) of the one-inlet reservoir model, one hour after the release of the water mixed with Rhodamine WT into the reservoir. Zones of short-circuiting existed in the reservoir, however, C/C_o in these regions was still more than 80% except for a very small zone where C/C_o was about 50%. The effect of inlet configuration on Rhodamine WT simulated concentration profiles at the outlet of two new reservoir designs (one inlet with D_{in} = 32 mm and seven inlets with D_{in} = 6 mm each) is depicted in Figure 8.11. The reservoir model with seven inlets had a higher t_{10} (about 18 minutes equivalent to 65% of the theoretical detention time of 33 minutes for this reservoir with five baffle walls) than that of the one inlet (about 15 minutes). Therefore, the one-inlet design with the new arrangement of five baffle walls almost doubled t_{10} of the original one-baffle-wall reservoir model.

8.4 CONCLUSIONS AND RECOMMENDATIONS

Storage reservoirs at the end of water treatment facilities could be retrofitted for possible use as contact chambers for additional microorganism inactivation. However, poorly baffled or unbaffled storage tanks might exhibit short-circuiting, thus leading to a short effective contact time (t_{10}). This study applied the computational fluid dynamics (CFD) modeling approach to simulate some experimental studies conducted to t_{10} in an existing storage reservoir. Results of two scaled-down physical models were chosen for developing CFD models that could accurately predict the hydrodynamics and thus, t_{10} of contact chambers. The CFD model simulations resulted in conservative tracer concentration profiles that were in excellent agreement with the experimental profiles. The CFD reservoir model that yielded the highest t_{10} was further investigated by changing the inlet configuration for possible improvement in t_{10}. Varying the diameter of the reservoir's inlet did not show any significant influence on t_{10}. However, the use of seven small inlets enhanced t_{10} substantially (almost tripled the effective contact time).

Furthermore, the use of multiple small inlets, instead of one large inlet, was evaluated to investigate the effect on t_{10}. Although the increase in the effective contact time was quite substantial (from about eight minutes to about 27 minutes) by increasing the number of baffle walls from one to nine, the cost of constructing the nine walls is an issue that might limit the practicality of such a design. On the other hand, the one-inlet reservoir design with the five baffle wall arrangement almost doubled t_{10} of the original one-baffle-wall reservoir model. As a result, to improve the performance of storage tanks in terms of having higher t_{10} with the lowest cost, baffle wall arrangement has to be considered. Also, the use of inlets with different angles, heights above the tank bottom, and diameters might improve the initial mixing conditions in the first compartment thus leading to higher t_{10}. Further work should examine the use of small baffles downstream of each inlet and the change of each inlet's angle (i.e., from 0 to 90^0).

Table 8.1 Input and output conditions and assumptions used for the CFD models.

	One-baffle-wall reservoir	Nine-baffle-wall reservoir	Proposed reservoir design
Inlet			
Mass flow rate	0.18 kg/s	0.18 kg/s	0.18 kg/s
Tracer concentration	0.238 kg/m^3	0.345 kg/m^3	0.345 kg/m^3
Outlet	Total flow was conserved for all reservoirs models		
Turbulence model	*k-ω* model was used for all reservoir models		
Assumptions	Reservoir walls (including reservoir base): non slip condition (velocity at the wall equals zero) Reservoir top surface (water surface): slip condition applied (to simulate free surface condition)		

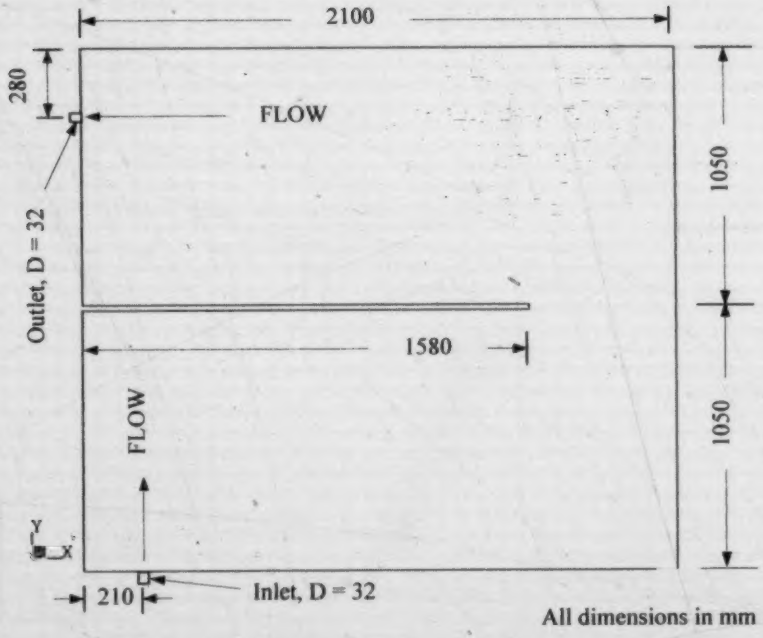

Figure 8.1 A plan view of the original reservoir design; a reservoir with one baffle wall (after Hurtig (2003)).

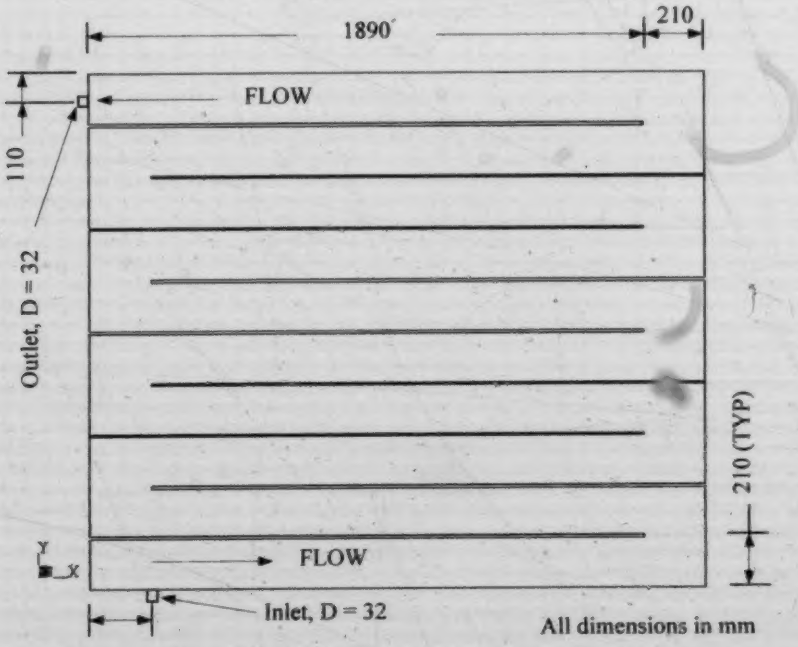

Figure 8.2 A plan view of the modified reservoir design; a reservoir with nine baffle walls (after Hurtig (2003)).

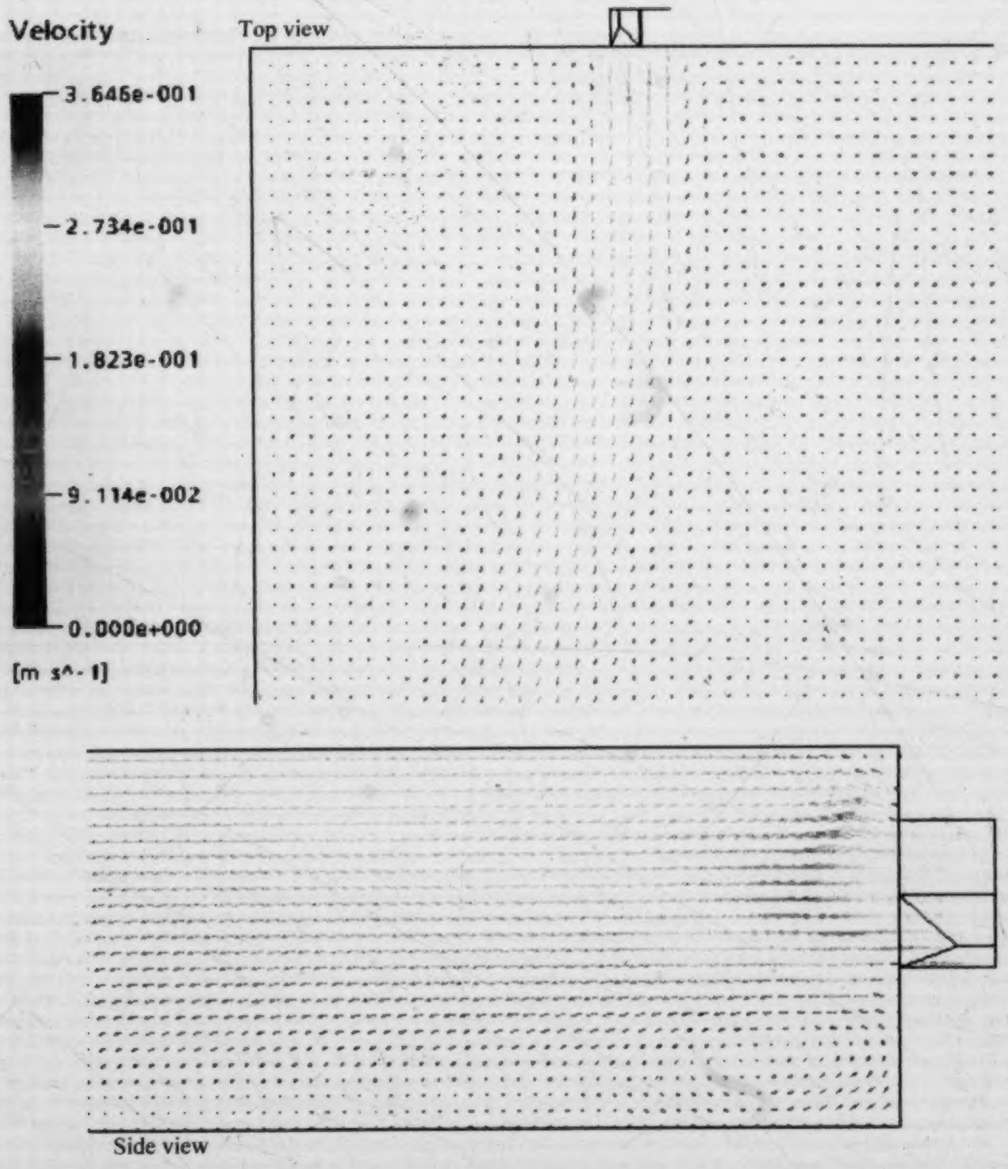

Figure 8.3 Velocity vectors in the influent flow region of the one-baffle-wall reservoir model.

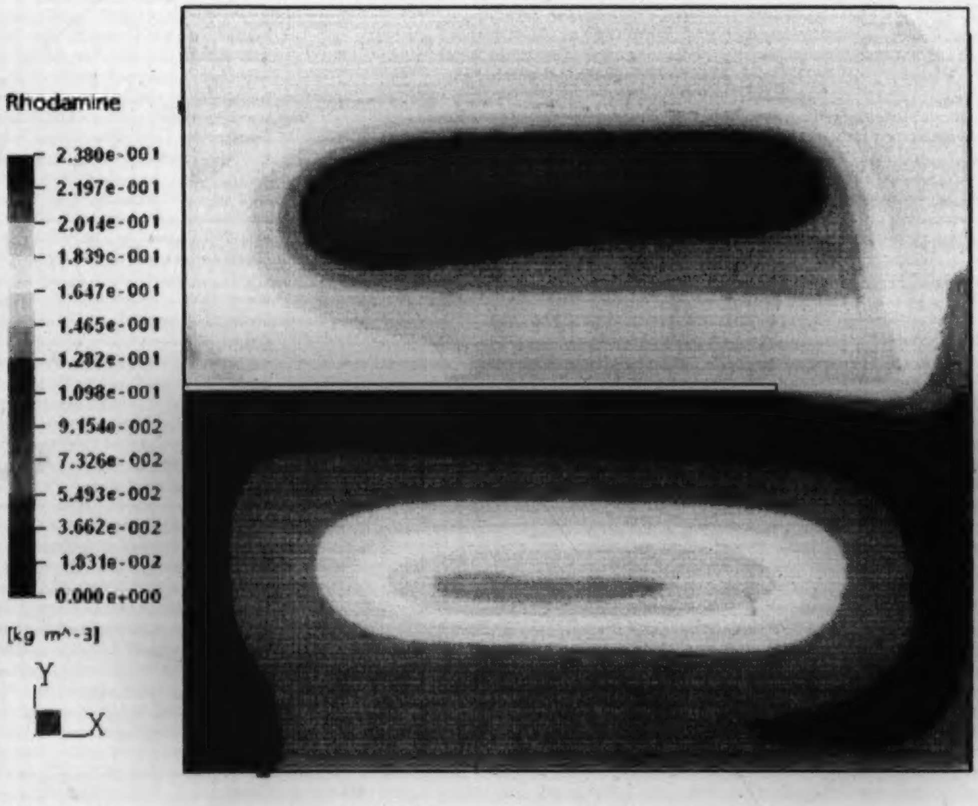

Figure 8.4 Rhodamine WT concentration distribution on an XY plane at 50 mm above the bottom of the one-baffle-wall reservoir model.

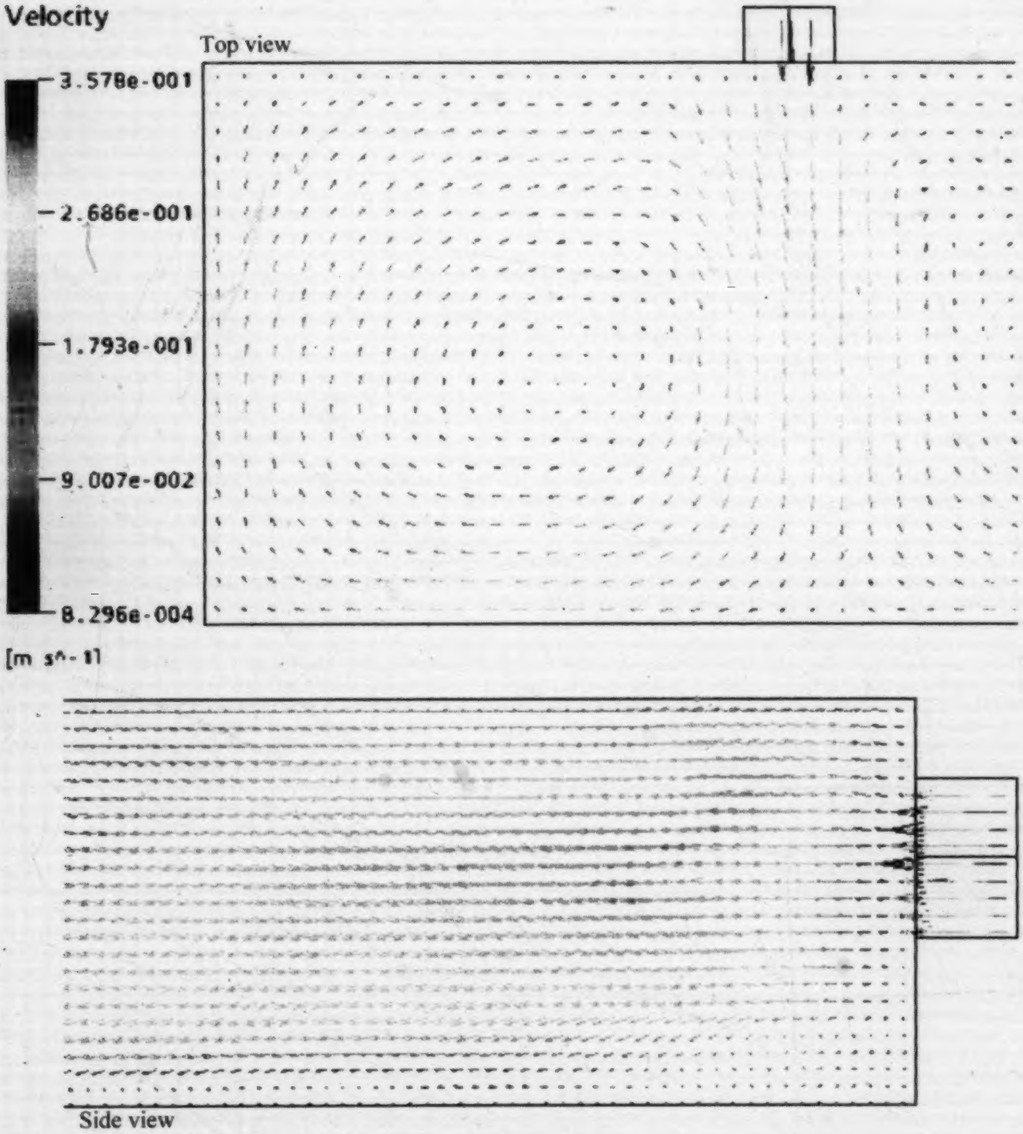

Figure 8.5 Velocity vectors in the influent flow region of the nine-baffle-wall reservoir model.

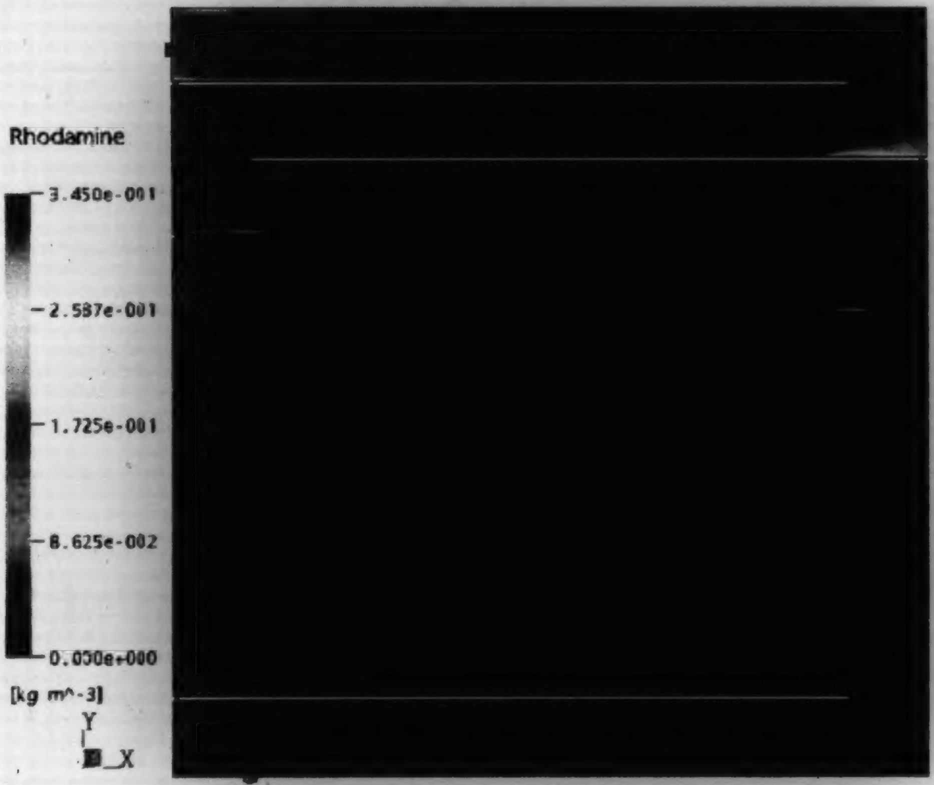

Figure 8.6 Rhodamine WT concentration distribution on an XY plane at 50 mm above the bottom of the nine-baffle wall reservoir model.

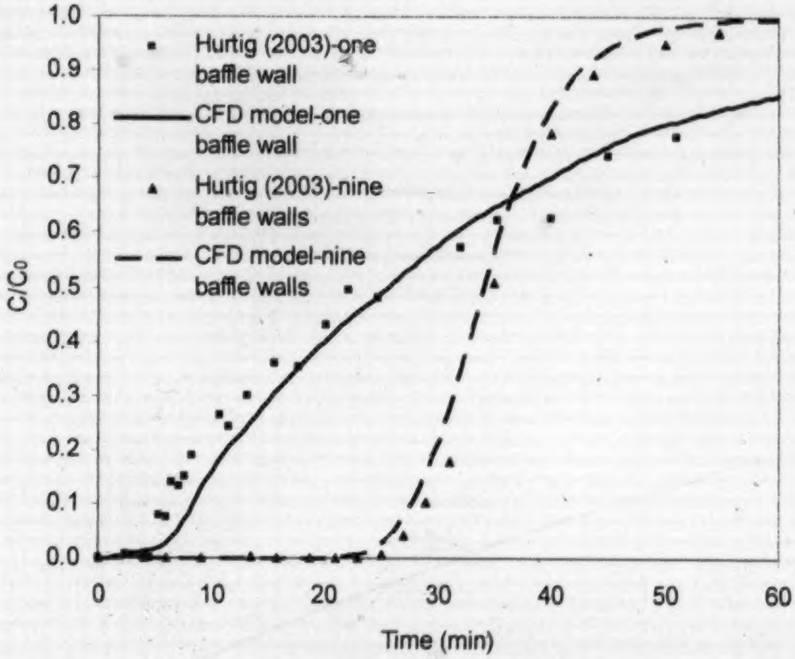

Figure 8.7 Rhodamine WT experimental and simulated concentration profiles at the outlet of the reservoir models.

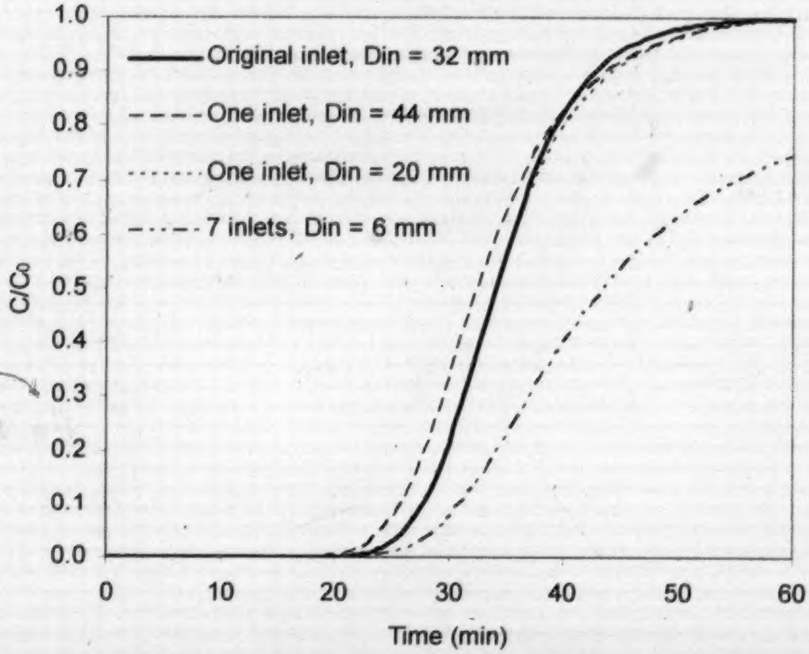

Figure 8.8 Effect of inlet configuration on Rhodamine WT simulated concentration profiles at the outlet of the nine-baffle-wall pilot-scale reservoir.

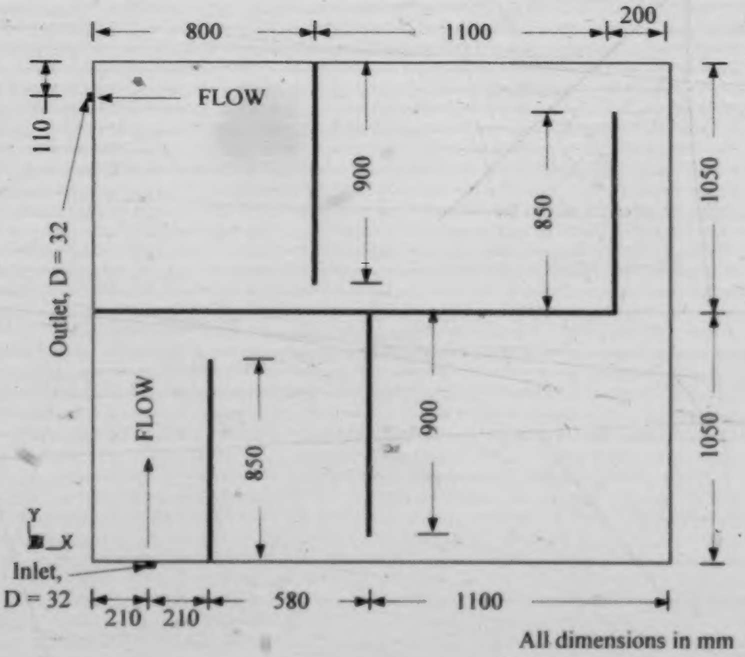

Figure 8.9 A plan view of a proposed reservoir design; with a new arrangement of five baffle walls.

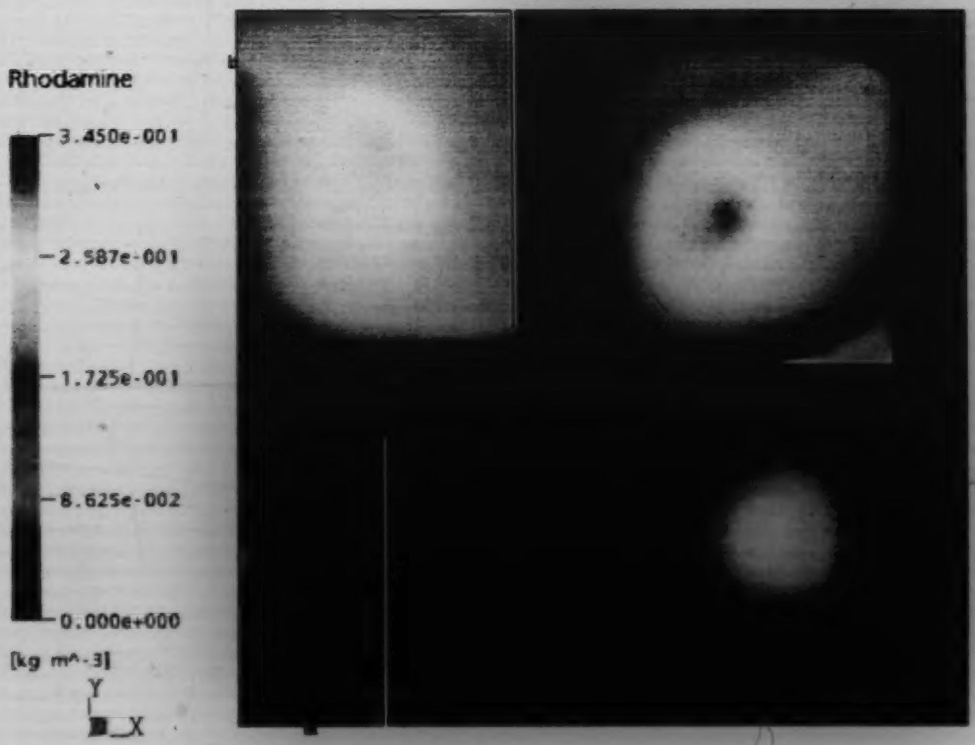

Figure 8.10 Rhodamine WT concentration distribution on an XY plane at 50 mm above the bottom of the proposed one-inlet reservoir design.

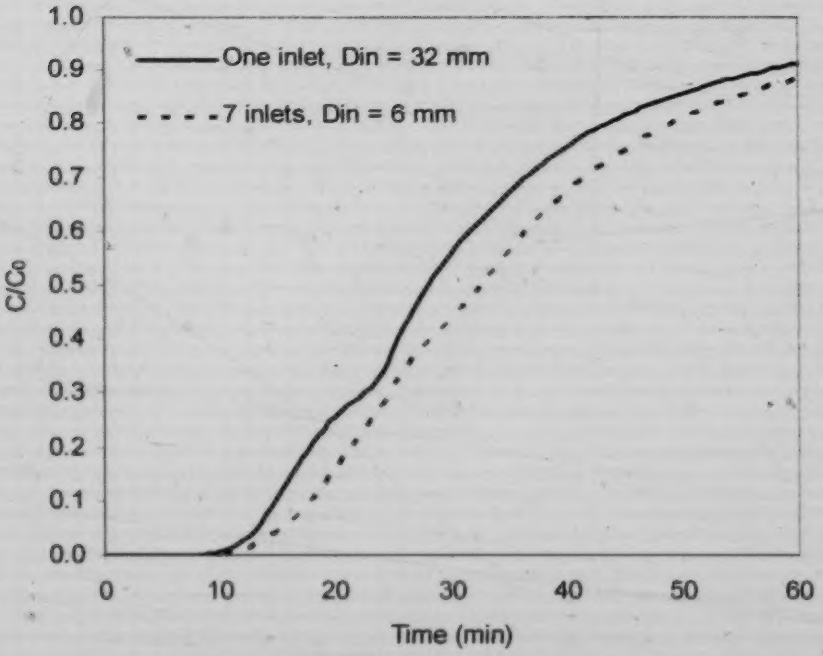

Figure 8.11 Effect of inlet configuration on Rhodamine WT simulated concentration profiles at the outlet of two proposed reservoir designs.

8.5 REFERENCES

1. American Water Works Association (AWWA), Guidance Manual for Compliance with the Filtration and Disinfection Requirements for Public Water Systems Using Surface Water Sources. (Denver, Colorado: Malcolm Prince Inc. and HDR Engineering Inc. , 1990).
2. AWWA, Water Quality and Treatment: A Handbook of Community Water Supplies. (New York: McGraw Hill Inc, 1999).
3. Bernard, P.S., and J.M. Wallace, *Turbulent Flow: Analysis, Measurement, and Prediction*. (New Jersey: John Wiley & Sons, Inc, 2002).
4. Bishop, M.M., J.M. Morgan, B. Cornwell, and D.K. Jamison, "Improving the Disinfection Detention-Time of a Water-Plant Clearwell", *Journal American Water Works Association*, 85(3): 68-75 (1993).
5. Boulos, P.F., W.M. Grayman, R.W. Bowcock, J.W. Clapp, L.A. Rossman, R.M. Clark, R.A. Deininger, and A.K. Dhingra, "Hydraulic Mixing and Free Chlorine Residual in Reservoirs", *Journal American Water Works Association*, 88(7): 48-59 (1996).
6. Chambers, V.K., J.D. Creasey, and J.S. Joy, "Modeling Free and Total Chlorine Decay in Potable Water Distribution-Systems", *Journal of Water Supply Research and Technology-Aqua*, 44(2): 60-69 (1995).
7. Chapra, S.C., *Surface Water-Quality Modeling*. (Boston: WCB/McGraw Hill Companies Inc, 1997).

8. Crozes, G., J. Hagstorm, M. Clark, J. Ducoste, and C. Bueus, *Improving Clearwell Design for Ct Compliance*. (Denver, Co., USA.: American Water Works Association Research Foundation (AWWARF), 1999).

9. Do-Quang, Z., A. Cockx, and J.M.R. Laine, M. , "Applying Cfd Modeling in Order to Enhance Water Treatment Reactors Efficiency: Example of the Ozonation Process. " *Water Science and Technology: Water Supply* 1(4): 125-130 (2001).

10. Do-Quang, Z., M. Roustan, and J.P. Duguet, "Mathematical Modeling of Theoretical Cryptosporidium Inactivation in Full-Scale Ozonation Reactors", *Ozone-Science & Engineering*, 22(1): 99-111 (2000).

11. Falconer, R.A., and A. Ismail, "Numerical Modeling of Tracer Transport in a Contact Tank", *Environment International*, 23(6): 763-773 (1997).

12. Gamal El-Din, M., and D.W. Smith, "Theoretical Analysis and Experimental Verification of Ozone Mass Transfer in Bubble Columns", *Environmental Technology* 23: 135-147 (2002).

13. Gamal El-Din, M., and D.W. Smith, "Mass Transfer Analysis in Ozone Bubble Columns", *Journal of Environmental Engineering and Science*, 2(1): 63-76 (2003).

14. Grayman, W.M., R.A. Deininger, A. Green, P.F. Boulos, R.W. Bowcock, and C.C. Godwin, "Water Quality and Mixing Models for Tanks and Reservoirs", *Journal American Water Works Association*, 88(7): 60-73 (1996).

15. Gujer, W., and U. von Gunten, "A Stochastic Model of an Ozonation Reactor", *Water Research*, 37(7): 1667-1677 (2003).

16. Gyurek, L.L., and G.R. Finch, "Modeling Water Treatment Chemical Disinfection Kinetics", *Journal of Environmental Engineering-Asce*, 124(9): 783-793 (1998).

17. Hannoun, I.A., P.F. Boulos, and E.J. List, "Using Hydraulic Modeling to Optimize Contact Time", *Journal American Water Works Association*, 90(8): 77-87 (1998).

18. Hart, F.L., and Z. Vogiatzis, "Performance of Modified Chlorine Contact Chamber", *Journal of the Environmental Engineering Division-Asce*, 108(3): 549-561 (1982).

19. Hoff, J.C., "Inactivation of Microbial Agents by Chemical Disinfectants", Water Engineering Research Laboratory (Office of Research and Development). ed.: U.S. Environmental Protection Agency, 1986).

20. Hurtig, K.I., "Hydraulic Modelling of Storage Tanks in Water Distribution Systems", M.Sc., University of Alberta, Edmonton, Alberta, (2003).

21. Johnson, P., N. Graham, M. Dawson, and J. Barker, "Determining the Optimal Theoretical Residence Time Distribution for Chlorine Contact Tanks", *Journal of Water Services Research and Technology-Aqua*, 47(5): 209-214 (1998).

22. Kiely, G., *Environmental Engineering*. (London, U.K.: McGraw-Hill, International Editions, 1998).

23. Li, H., L.L. Gyurek, G.R. Finch, D.W. Smith, and M. Belosevic, "Effect of Temperature on Ozone Inactivation of Cryptosporidium Parvum in Oxidant Demand-Free Phosphate Buffer", *Journal of Environmental Engineering-Asce*, 127(5): 456-467 (2001).

24. Liem, L.E., "Analysis of Residence Time Distributions in Water Treatment Processes as Related to the Ct Concept", M.Sc., University of Alberta, Edmonton, Alberta, (1994).

25. Peplinski, D.K., and J.J. Ducoste, "Modeling of Disinfection Contactor Hydraulics under Uncertainty", *Journal of Environmental Engineering-Asce*, 128(11): 1056-1067 (2002).

26. Powell, J.C., N.B. Hallam, J.R. West, C.F. Forster, and J. Simms, "Factors Which Control Bulk Chlorine Decay Rates", *Water Research*, 34(1): 117-126 (2000).

27. Regli, S., "How and Whys of Cts", *AWWA Annual Conference* Los Angeles, California. (1989).

28. Risk Reactor, "Fluorescent Tracers for Water and Oil Based Systems", 2004).

29. Shilton, A., "Studies into the Hydraulics of Waste Stabilisation Ponds", PhD Massey University New Zealand, (2001).

30. Ta, C.T., and W.J. Brignal, "Application of Computational Fluid Dynamics Technique to Storage Reservoir Studies", *Water Science and Technology*, 37(2): 219-226 (1998).

31. Teefy, S.M., and P.C. Singer, "Performance and Analysis of Tracer Tests to Determine Compliance of a Disinfection Scheme with the Swtr", *Journal American Water Works Association*, 82(12): 88-98 (1990).

32. USEPA, "Drinking Water; National Primary Drinking Water Regulations; Filtration, Disinfection; Turbidity, Giardia Lamblia, Viruses, Legionella, and Heterotrophic Bacteria; Final Rule", U. S. Environmental Protection Agency, ed.: Federal Register 54 (124), 27486-27541., 1989).

33. von Gunten, U., A. Driedger, H. Gallard, and E. Salhi, "By-Products Formation During Drinking Water Disinfection: A Tool to Assess Disinfection Efficiency?" *Water Research*, 35(8): 2095-2099 (2001).

34. Wang, H., and R.A. Falconer, "Numerical Modeling of Flow in Chlorine Disinfection Tanks", *Journal of Hydraulic Engineering-Asce*, 124(9): 918-931 (1998).

35. Zhou, H.D., and D.W. Smith, "Evaluation of Parameter-Estimation Methods for Ozone Disinfection Kinetics", *Water Research*, 29(2): 679-686 (1995).

36. Zhou, H.D., D.W. Smith, and S.J. Stanley, "Modeling of Dissolved Ozone Concentration Profiles in Bubble-Columns", *Journal of Environmental Engineering-Asce*, 120(4): 821-840 (1994).

CHAPTER 9

GENERAL CONCLUSIONS AND RECOMMENDATIONS

9.1 GENERAL CONCLUSIONS

This work explored the mixing effect resulting from multiple single- and two-phase jets entering different water and wastewater treatment units. The work consisted of experimental and modelling studies. The experimental work involved the use of particle image velocimetry (PIV) and planer laser-induced fluorescence (PLIF) to study three two-phase flow water systems: an impinging-jets bubble column, an inline multi-jets ozone contactor, and an inclined surface plunging jets aeration system. The modelling utilized three different modelling approaches (the use of an artificial neural network (ANN), a steady-state and transient backflow cell model (BFCM), and computation fluid dynamics (CFD)) to characterize four types of water treatment units: ozone bubble columns, an impinging jets bubble column, a recycled water pond, and a storage reservoir. The experimental and modelling results were presented in Chapters 2 to 8.

Chapter 2 demonstrated the validity of the artificial neural network (ANN) modelling approach in predicting key parameters required for designing and evaluating ozone bubble columns. Three multi-layer perceptron (MLP) artificial neural network (ANN) models were used to simulate and predict the overall mass transfer coefficient (k_La, s^{-1}), gas hold-up (ε_G), and Sauter mean bubble diameter (d_S, m) in different ozone bubble columns. The three models used the following input parameters: cross-sectional area (A_{cs}, m^2), water height in the bubble column (H_{bc}, m), ozone diffuser diameter (d_{dif}, m), diffuser pore size (d_{pore}, m), flow direction, superficial liquid velocity (u_L, m/s), and superficial gas velocity (u_G, m/s). The developed MLP-ANN models predicted the k_La, ε_G, and d_S values in the training and validation data sets with the coefficient of multiple determination (R^2) values that exceeded 0.98 with an average absolute relative error (*AARE*) of less than 13%. The results obtained from the ANN models were then used to determine the local mass transfer coefficient (k_L, m/s). The results showed excellent agreement between the modelled and the measured k_L values ($R^2 = 0.85$, $AARE = 20\%$).

Chapter 3 presented a transient back flow cell model, which is easy to formulate and solve. It was used to evaluate the hydrodynamic behaviour of an impinging-jet ozone bubble column under a wide range of operating conditions. This approach can be very useful for modelling deep ozone bubble columns when the number of cells in-series is chosen carefully for optimum predictions of the hydrodynamic behaviour of the ozone contactors under various operating conditions. A steady-state back flow cell model was developed to analyze the dissolved ozone concentration profiles measured in the bubble column under varied gas and liquid flow rates. The impinging-jet bubble column increased the ability to transfer ozone into the liquid phase compared to the ability of other contactor designs.

Chapter 4 illustrated the hydrodynamics and ozone mass transfer efficiency of a pilot-scale impinging jets bubble column with mixing nozzles. The PIV/PLIF system was used to examine the mixing patterns exerted by two inclined impinging jets coupled with mixing nozzles. The PIV system showed an increase in the backmixing effect in the two phases (liquid and gas) when the gas flow rate increased. The liquid axial dispersion coefficient (D_L, m^2/s), obtained from analyzing the PLIF results, was found to increase when the gas flow rate was increased at a fixed liquid flow rate. The value of D_L was found to increase with the liquid flow rate under a laminar flow and to decrease when a transient flow was used. Bubble size measurements were conducted in this contactor using a particle dynamics analyzer (PDA). The results obtained for d_S (using the PDA system) and ε_G (by using the pressure difference along the column height) suggested that this contactor had a higher specific interfacial area (a, m^{-1}) and k_La values compared to those of conventional bubble columns.

In Chapter 5, the design of a pilot-scale of an in-line multi-jets ozone contactor was investigated by using the PIV/PLIF system. Velocity measurements of the two phases (liquid and gas), by using the PIV system, were taken at different location along the contactor to examine the resulting mixing patterns. The results from the velocity vectors showed that the opposing jets exerted better radial mixing compared to that of the alternating jets. Furthermore, the tracer concentration measurements obtained by the PLIF system exhibited lower D_L values when the opposing jets were used compared to those obtained from the alternating ones. As the number of the 2-phase jets increased (i.e., as the gas flow rate increased), the value of D_L was found to increase due to the increase in the bubbles' dispersion effect. The results obtained by using the PIV and PLIF systems were then combined with dissolved oxygen measurements to estimate the system's k_La under wide range of operational conditions. The value of k_La was found to increase with the number of jets (i.e., with higher gas flow rates) for both the opposing and alternating jets alignments. However, higher k_La values were observed when the opposing jets were used than when the same number of alternating jets were used. The use of 6 to 8 opposing jets was found to yield higher k_La values compared to those yielded by other combinations.

Chapter 6 presented the properties of the bubble plumes resulting from the use of two inclined circular plunging jets intersecting at the surface of a water tank. The PIV system was used to measure the velocity of the two-phase plunging jets. The results of the normalized axial velocity for the gas and water jets showed a good mixing effect in the aeration tank. The results obtained under the same turbulence condition and different plunging angles (α) showed that as the nozzle diameter (d_o, m) increased, the penetration depth (z_p, m) also increased. Furthermore, under the same d_o, z_p at $\alpha = 75^\circ$ was found to be higher than the ones obtained under other cases ($\alpha = 67.5^\circ$ and $\alpha = 90^\circ$). The combination of two inclined jets yielded a higher z_p compared to that yielded by one inclined jet. The value of ε_G was found to decrease as d_o increased for the same liquid flow rate. The captured images of the bubble plumes, obtained by using the PIV system, showed a lower bubble mean diameter (d_b, m) compared to that of the vertical plunging jets systems.

Chapter 7 presented a study aimed at modelling the dissolved oxygen (DO) in a recycled water (RCW) pond. The pond had high DO levels due to an extensive aeration process resulting from its inlet configurations. A CFD model was used to simulate the DO concentration in the RCW pond under the current inlet configurations and a new proposed submerged inlet configuration. The results showed a very good agreement between the simulated and the measured outlet DO concentrations. The CFD model of the submerged inlet configuration showed a considerable reduction in the outlet DO concentration compared to the current inlet configurations utilizing the same operational conditions. The CFD model was then tested for different ranges of the water flow rate, water depth, inlet DO concentration, temperature, and wind velocity. Fr the maximum average inlet DO concentration, the outlet DO concentration using the current inlet configurations was found to be reduced by more than 75% when using the submerged inlet configuration.

Chapter 8 presented another CFD model utilized to characterize a storage reservoir used as a chamber for microorganisms inactivation. The CFD model was used to simulate two tracer studies conducted, in scaled-down physical models of an existing storage tank, to investigate the effect of the tank configuration on the reactor's effective contact time (t_{10}). One of the scaled-down physical models of the storage tank was equipped with one baffle wall at the middle length, and the other was equipped with nine baffle walls distributed evenly along the reservoir length. A comparison between the experimental and modelled tracer concentration profiles showed an excellent agreement. The developed CFD model was then applied to different reservoir configurations to improve the t_{10} value. The use of seven small inlets and nine baffle walls extended the t_{10} value from about eight minutes to about 30 minutes (for a theoretical detention time, τ, of 32 minutes). Furthermore, using fewer baffle walls with different inlet arrangements enhanced the t_{10} considerably.

The overall conclusion drawn from this work is the significance of the modern analytical tools like PIV and PLIF in the accurate evaluation of unit operations and processes. Moreover, the use of newer modelling approaches (ANN, BFCM, and CFD) allows for a better prediction of the performance of the reactor systems.

9.2 RECOMMENDATIONS

In this work, different experimental and modelling methods have been used to explore the applications of 1- and 2-phase multiple mixing jets entering several environmental engineering reactors. Based on the achieved results and the drawn conclusions, the following recommendations can be made for future research:

- For the conventional bubble columns, although the ANN models provided good predictions of some key parameters (k_La, ε_G and d_S), two more ANN models are needed to predict the axial liquid and gas dispersion coefficients (D_L and D_G, respectively) in order to be able to evaluate the ozonation process in the two phases inside the bubble columns.
- In order generalize the findings obtained by the steady-state and transient BFCM, the modelling approaches should be applied to different sizes of ozone bubble columns under wide operational conditions.
- For the impinging-jets ozone bubble column with mixing nozzles and the in-line multi-jets ozone contactors, further experimental studies are needed to generalize the findings achieved in this work by using the PIV/PLIF system (for hydrodynamics characterization), and the PDA system (for bubble size distribution) to evaluate the scale up issue of these contactors. A CFD model of the hydrodynamics for each ozone contactor can then be developed and calibrated with the experimental results obtained from the PIV/PLIF and PDA systems. Once successfully calibrated, Each CFD models can be used to optimize the operating conditions and configurations that yield maximum liquid-gas mixing for each contactor. Furthermore, mass transfer and gas hold-up studies are required to

evaluate the efficiency of ozonation process inside these contactors under the optimized conditions. Then, the ozonation contactors, under optimized conditions, can be tested to treat different types of wastewaters. Comprehensive CFD models for all contactors can then be developed to describe the performance of the ozonation treatment for selective and complete destruction of different organic constituents in the wastewater samples. Such models can incorporate literature data for reaction kinetics, experimental ozone gas mass transfer, and the experimental PLIF and PDA results.

- For the aeration tank, further work is needed to evaluate the mixing resulted from the incline surface plunging jets in the aeration tank using the PLIF system for different operating conditions. Also, a mass transfer study is needed to evaluate the k_La of this tank under wide range of plunging jets' sizes and operational conditions.